UPC CTTC

DNS of multiphase flows: study of atomization and free-surface phenomena

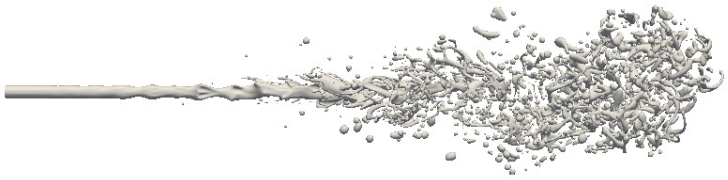

Centre Tecnològic de Transferència de Calor
Departament de Màquines i Motors Tèrmics
Universitat Politècnica de Catalunya

Eugenio Schillaci
Doctoral Thesis

DNS of multiphase flows: study of atomization and free-surface phenomena

Eugenio Schillaci

TESI DOCTORAL

presentada al

Departament de Màquines i Motors Tèrmics
E.T.S.E.I.A.T.
Universitat Politècnica de Catalunya

per a l'obtenció del grau de

Doctor per la Universitat Politècnica de Catalunya

Terrassa, October 2017

DNS of multiphase flows: study of atomization and free-surface phenomena

Eugenio Schillaci

Directors de la Tesi

Dr. Joaquim Rigola Serrano

Dr. Néstor Vinicio Balcázar Arciniega

Tutor

Dr. Assensi Oliva Llena

Tribunal Qualificador

Dr. Antonio Leucona Neumann
Universidad Carlos III

Dr. Jose Miguel Corberán Salvador
Universitat Politècnica de Valencia

Dr. Carlos D. Pérez-Segarra
Universitat Politècnica de Catalunya

Fra il gruppetto ad un tratto si fece largo una giovane signora ...
Era lei, la creatura bramata da sempre che veniva a prenderlo: strano che cosí giovane com'era si fosse arresa a lui; l'ora della partenza del treno doveva esser vicina.
Giunta faccia a faccia con lui sollevó il velo e cosí, pudica ma pronta ad esser posseduta, gli apparve piú bella di come mai l'avesse intravista negli spazi stellari.

Il fragore del mare si placó del tutto.

Giuseppe Tomasi di Lampedusa, Il Gattopardo.

Acknowledgements

I want to use these few lines to thank all the people that has contributed, in one way or another, to the development of this thesis, and that have helped me by making more pleasant the complex path of thinking and creating a doctoral thesis.

First of all, I want to thank Prof. Assensi Oliva, head of *Heat and Mass Transfer Technological Center* (CTTC), for trusting me since my arrival in the department, and for giving me the possibility, both technical and financial, of developing my doctoral Thesis. A mention goes to the directors of this Thesis, Prof. Joaquim Rigola Serrano and Dr. Néstor Vinicio Balcázar Arciniega, for their valuable support and assistance. A big hug goes to Lluís Jofre, who was my first guide within the department and an inspiration for part of the ideas that are now part of this Thesis. Thank you for being such an effective colleague in the work that we developed together. Additionally, I would like to mention the collaboration with other CTTC fellows, Oscar Antepara and Federico Favre, that helped me to develop some important parts of this thesis.

This work has been financially supported by the Ministerio de Economía y Competitividad, Secretaría de Estado de Investigacíon, Desarrollo e Innovacíon, Spain (ENE-2014-60577-R, ENE2015-70672-P) and by Termo Fluids S.L. The author acknowledges financial support in form of a doctoral scholarship (FI Grant, 2014-FI-B01232) provided by AGAUR (Generalitat de Catalunya), the computer resources at MareNostrum III and IV, with technical support provided by BSC (RES-FI-2016-1-0023, RES-FI-2017-2-0015) and at FinisTerrae II, with support by CESGA (RES-FI-2016-2-0028, RES-FI-2016-3-0015).

Quiero agradecer los que han sido mis amigos durante mi estancia en Catalunya, entre Barcelona y Terrassa. Los compañeros del CTTC, con los que he compartido un ambiente de trabajo muy agradable y inspirador. Entre ellos, una mención especial al Octavi, por montarme siempre los ordenadores mas rapidos y eficientes (o casi). Los chilenos, Willy y Hermes, y los otros compañeros de piso de Carrer Prat de la Riba. Gianluca, por ser buena persona no obstante su violencia aparente (si scherza eh, attenzione). Los amigos del grupo de Aigues Obertes en el Club Natació Terrassa, por haber compartido conmigo la pasión para el deporte, que se ha convertido en addición y en la mejor manera par canalizar el stress del trabajo. Los amigos de los muchos Erasmus de estos años, entre ellos Giacomo, con el que tengo mucha afinidad, y que confia siempre en mi, y Giulia (ti voglio bene), por no criticarme demasiado, a pesar de su pasion por la polemica. Un abrazo a todos los *Malakas*, por ser la gente mas positiva del mundo.

Un bacio alla mia grande amica/sorella Martina, che pensa sempre che mi dimentichi di lei, ma che dovrebbe sapere che l'affettuosità non è il mio forte. Un abbraccio a tutti gli altri amici lontani, Archis, Stefano, Massimo, Lucio, sperando di poter passare, in futuro, altri bei momenti insieme.

Voglio ringraziare ancora una volta, ed immensamente, i miei genitori, per il loro appog-

gio, comprensione ed amore incondizionale durante tutti questi anni di assenza. Un bacio a mio fratello, Giuseppe, ed a mia sorella, Mia, con l'augurio che la sua esperienza universitaria possa essere fruttuosa e divertente.

Abstract

The present thesis focuses on the numerical analysis of some diverse physical set-up that involve the interaction of two –or three immiscible and incompressible phases. The simulations are carried out by means of finite-volume algorithms developed on the in-house Computational Fluid Dynamics platform TermoFluids, and they are intended to give detailed insights on the physics of the analyzed phenomena by carrying out Direct Numerical Simulations (DNS). In the context of multiphase flows —Computational Multi-Fluid Dynamics (CMFD) field—, DNS means that all the interfacial and turbulent scales of the phenomenon must be fully resolved.

This work begins from acquiring the experience accumulated by former Phd students within the *Heat and Mass Transfer Technological Center* (CTTC) research group on the numerical simulation of two-phase flow, Lluís Jofre and Nestor Balcázar. Their work consisted in the development and implementation of an unstructured multiphase solver, based on the the most versatile techniques for following the interface in multiphase flows. The methods chosen were the Level-Set and the Volume-of-Fluid methods, whose advantages in comparison to similar technique are listed in detail in Chapter 1. Consequently, such techniques were developed and tested within the pre-existing unstructured code TermoFluids, leading to early publications in important papers of the Computational Fluid Dynamics field. My work consisted initially in the use of these codes to simulate engineering problems involving multiphase flows. At the same time, the integration of classic techniques with additional tools has become necessary to improve the efficiency and the stability of the simulations, and the basic discretization algorithms have undergone modifications or additions to adapt to particular situations, such as free-surface or atomizing flows. The five chapters in which this thesis has been divided, which are following described briefly, resume the research activity carried out in this framework. Chapter 1 is the introduction, while Chapters 2 to 5 reflect the content of the three main research papers which resulted from this work. In particular, Chapters 3 and 4, reflect the content of a single research paper, but they have been separated and extended to better expose the proposed concepts. Finally, in Chapter 6 the final conclusions are reported, together with some considerations above future work.

In Chapter 1, a general overview of the engineering applications and the computational methods related to multiphase flows is proposed. The various types of physics analyzed in this work and the numerical approaches applied here to carry out efficient simulations are introduced. After presenting the state-of-the-art on CMFD models, the text legitimizes the choice of the interface-capturing methods, and, in particular, the level-set method for the simulation of the applications analyzed here. Following, the differential equations that regulate the physics of multiphase flow are introduced, together with their discrete form on unstructured meshes.

In Chapter 2, a low-dissipation convection scheme for the stable discretization of multiphase flow by means of interface-capturing schemes is analyzed. The hybrid form of the

convective operator proposed incorporates localized low-dispersion characteristics to limit the growth of spurious flow solutions. Moreover, in comparison to pure-dissipative schemes, the discretization aims at minimizing the differences in kinetic energy preservation with respect to the continuous governing equations. This property plays a fundamental role in the case of flows presenting significant levels of turbulence. The low-dissipation discrete framework is analyzed in detail and, in order to expose the advantages with respect to commonly used methodologies, its conservation properties and accuracy are extensively studied, both theoretically and numerically. The simulation of a turbulent 2D coaxial jet with the low-dissipation convection scheme demonstrates its capability of solving correctly the two-phase turbulent problems, avoiding, at the same time, the disruptive phenomenon of the spurious currents, which is detrimental when using pure conservative schemes.

In Chapter 3, all the work carried out on the simulation of two-phase flow with the aid of Adaptive Mesh Refinement (AMR) strategies is described. In this framework, the multiphase solver is coupled to the AMR tool developed by Oscar Antepara, Phd student of CTTC. The model is globally addressed at improving the representation of interfacial and turbulent scales in general multiphase flows. It is first applied to the simulation of simple multiphase phenomena, as 2D and 3D rising bubbles, to demonstrate the convergence of the method and the important computational savings in comparison to static mesh computations. However, its adoption becames essential in the simulation of instability and break-up phenomena, where the necessity of representing accurately the complex structures that appear at the interface, as ligaments and droplets, make the simulation particularly expensive in terms of computational cost. Some remarkable examples are the simulation of 3D break-up phenomena, introduced with some basic tests and then deepened in Chapter 4. In all the analyzed cases, the refinement criteria are designed to ensure the proper representation of the characteristic lengths, by achieving the required mesh definition in each part of the domain. The discretization, built on a finite-volume basis, accounts for a divergence-free treatment of the refined/coarsened cells, that ensures the correct transport of mass, momentum and kinetic energy, which are key factor in the correct resolution of turbulence, as explained in Chapter 2.

As introduced before, in Chapter 4, we analyze in detail the results obtained from the simulation of 3-D atomizing phenomena. They include the coaxial jet case, characterized by the parallel injection of high speed liquid and gas fluxes, and the liquid spray case, characterized by the injection of a liquid inside a still air chamber. On the one side, the simulation of the coaxial jet set-up serves as a further validation of for the numerical framework introduced in this work. On the other hand, in the analysis on the liquid spray set-up, we want to propose some additional insights to the related literature, by studying numerically the atomization regime as function of different jet inlet parameters.

In Chapter 5, an original single-phase scheme for the DNS of free-surface problems on 3-D unstructured meshes is presented. The scheme is based on a novel treatment of the interface for the deactivation of the light-phase, allowing the optimization of the classic two-phase model for the cases in which the influence of the lighter phase is negligible. Consequently,

the model is particularly addressed at analyzing problems involving the movement of free-surfaces, as the evolution of waves on the sea surface, and their interaction with fixed and moving obstacles. The deactivation of the light phase is carried out by imposing the appropriate pressure at the surface boundary, and, unlike similar approaches, without the need to treat near-interface velocities. The method is validated against various analytical and experimental references, demonstrating its potential on both hexahedral and unstructured meshes. Finally, some practical cases of application are proposed, as the evaluation of stresses on an object due to the action of a dam-break event, and the interaction of linear waves with an oscillating water column device. In the same Chapter we describe the procedure to couple the single-phase model to the Immersed Boundary Method, developed on TermoFluids by former Phd student Federico Favre. The method is aimed at representing the interaction of a solid moving with prescribed velocity and the free-surface flow. The most significant example consists in the simulation of a sliding wedge into a liquid basin, validated by measuring the magnitude of the waves resulting from the solid-fluid impact.

Contents

1

Introduction

The current chapter introduces the physical and engineering contexts covered by this thesis. In the first part, the work is placed in the background of the research center in which it has been developed, the Heat and Mass Transfer Technological Center (CTTC) of the Polytechnic University of Catalonia (UPC), and it is related to the efforts made by other researchers on the same investigation line. Next, the main themes covered by the following chapters are briefly highlighted.

In the second part, we present the governing equations and the numerical models employed in this work, which constitute the basis on which the original contributions provided here are built.

1.1 Background and Outline

A large number of complex engineering applications and physical phenomena require the analysis of the interaction between immiscible phases, consisting of two or more phases incapable of being mixed to form a homogeneous substance. Consequently, the flows considered exhibit phase separation at a scale well above the molecular level. The case of phases separated by interfaces, also referred to as interfacial flow, is found in a large variety of physical and biological phenomena, ranging from the prediction of atmospheric conditions to the study of blood flow, and in many engineering applications: some remarkable examples are the movement of gaseous bubbles inside a liquid phase, the motion and break-up of waves, as well as their interaction with solid boundaries, and the atomization of liquid jets.

The issues related to the direct numerical simulation (DNS) of multiphase flows —subcategory of the biggest field of the Computational Multi-Fluid Dynamics (CMFD)— are a topic of great interest and lively debate in the scientific community –a general overview can be found in Tryggvason et al. [1]. Indeed, understanding the flow in these situations not only involves the study of velocity and pressure in the different phases, i.e., resolution of mass and momentum balances, but also of the dynamics of the interface separating them. Therefore, its correct representation and coupling to the equations of fluid motion add several complexities to the solution of the problem, as pointed out by Gorokhovski and Herrmann [2]. The

method for the representation of the interface represents the biggest deal and many possible solutions have been proposed in the last decades. For instance, in the interface-tracking methods the interface is represented as a moving boundary or by means of particles, while in the interface-capturing methods, chosen in this work due to their higher versatility, the interface is represented by means of a scalar function advected by the velocity field. One of the earliest and most complete classification of interface-tracking —and capturing schemes is provided by Scardovelli and Zaleski [3].

When attempting to study numerically the physics of multiphase flow, different kinds of numerical issues need to be tackled, depending on the kind of flow analyzed. To make a general example, we can consider the case of the injection of a high-speed liquid into an air chamber, attributable to the atomization process inside a fuel injection device or to a pharmaceutical spray. After the injection, the liquid jet rapidly develops instabilities at the interface, that lead to the liquid column collapse and the spreading of small structures in the form of droplets and ligaments [4], as shown in the picture of Fig. 1.1 which reports an experimental image of the phenomenon. A detailed numerical analysis of this phenomenon would allow the measurement of the distribution of the droplets' size after the pulverization process is completed, and its control could serve to optimize the final use of the device. However, a correct numerical simulation requires a significant computational effort, since the mesh adopted must have a minimum local size that correctly represents all the interfacial scales. In case of turbulent flow, all convective scales must also be represented in order to avoid undesired numerical dissipation. Several thousands of CPUs may be needed to perform such kinds of simulations [5]. Other kind of issues may rise when using interface-capturing schemes to deal with the movement of the interface. For example, the properties of the discrete operators influence the presence and the magnitude of unphysical currents that may affect the proper representation of the considered flow [6]. The same operators must be built in such a way to guarantee the conservation of discrete properties, including both primary –as mass and momentum– and secondary ones –as kinetic energy and vorticity. In fact, their proper representation is a key step if a correct resolution of turbulent phenomena is requested.

Another important challenging field of application of multiphase flows consists in the simulation of sea-surface or similar free-surface phenomena. Some examples may be the study of waves propagation on a sea-surface and their interaction with solid objects, which can be constituted, for example, by fixed –or floating electric power generation units, as in the case of the Oscillating Water Column (OWC) device —see Fig. 1.2. The efficient numerical simulation of these set-up, which include the total Fluid-Structure Interaction coupling between fluids and solid, could allow the design and optimization of these devices for different marine environments. Another example is the simulation of the impact of a solid body with a free-surface, and the analysis of the *tsunami* waves generated by the event.

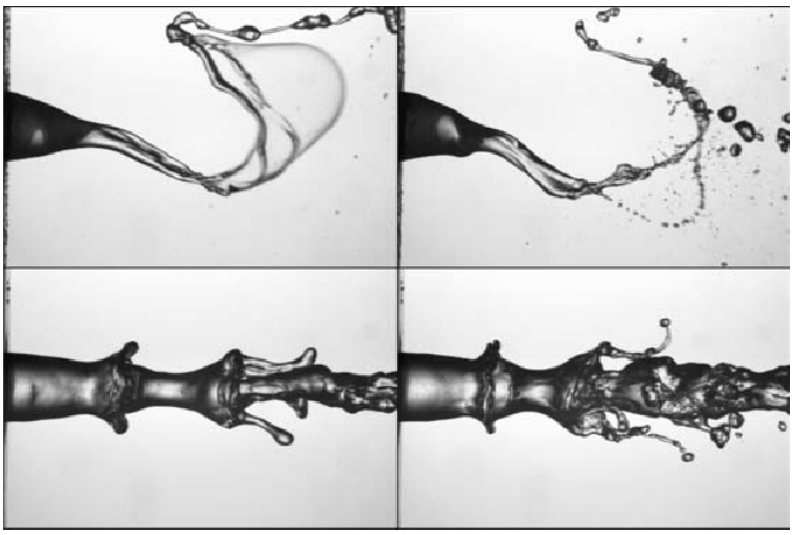

Figure 1.1: Breakup regimes of a slow dense liquid jet by a fast light coaxial stream. Picture extracted from reference by Marmottant and Villermaux [4].

Figure 1.2: Picture of a floating Oscillating Water Column (OWC) device for the extraction of mechanical energy from sea waves. Installation by Ocean Energy [7].

1.1.1 CTTC Background

This work was carried out in the Heat and Mass Transfer Technological Center, Centre Tecnológic de Transferéncia de Calor (CTTC), of the Universitat Politécnica de Catalunya – BarcelonaTech (UPC), situated in Terrassa (Barcelona).

The research activities of the center are focused on two main lines. The first one, in which this work can be placed, is dedicated to the mathematical formulation, numerical resolution and experimental validation of fluid dynamics and heat and mass transfer phenomena. Some issues in this line are: natural and forced convection, direct numerical simulations (DNS) and turbulence modeling (LES, RANS) of single-phase flows, combustion, multiphase flows (free surface flow, two-phase flow, solid-liquid phase change), radiation, porous media, numerical algorithms and solvers, moving and unstructured grids, high performance computing (parallelization). The second line is dedicated to thermal and fluid dynamic optimization of thermal system and equipment. A further description of the work carried out in CTTC can be found in the website [8].

The unstructured CFD algorithms described in this thesis are developed on the TermoFluids software [9]. That platform collects state-of-the-art numerical and physical models developed by current and former CTTC members to perform accurate scientific analysis of engineering problems. TermoFluids has been designed to run on modern parallel supercomputers, and it has demonstrated good scalability up to 100k cores. Parallelization of TermoFluids is achieved via distributed memory model paradigm using standard MPI. The development of the code has been a source of scientific publications in the most prominent scientific journals of the field. An exhaustive list can be found in the website of TermoFluids [9].

This work begins from acquiring the experience accumulated by former Phd students within the CTTC research group on the direct numerical simulation of two-phase flow, Lluís Jofre and Nestor Balcázar. Their work, which is resumed in their Phd Thesis [10, 11], consisted in the development and implementation of an unstructured multiphase solver based on the most versatile techniques for following the interface in multiphase flows. The chosen techniques where the Level-Set (LS) and the Volume-of-Fluid (VOF) ones, whose characteristics and advantages in comparison to similar methods are detailed in the following sections. Consequently, these models were implemented and tested on TermoFluids, leading to quality publications in important papers of the CFD field [12, 13, 14, 15, 16]. Recently, the methods developed by CTTC for the simulation of multiphase flow have demonstrated high reliability on a wide range of applications as bubbly flows [15, 17, 18, 19], free-surface flows [20] and break-up phenomena [21, 22]. In the development on this thesis, it was also fundamental the collaboration with other current and former Phd students at CTTC, as Oscar Antepara and Federico Favre.

Figure 1.3: Main venue of the CTTC, situated in Terrassa (Barcelona). The new part of the building, completed in 2012, expanded the usable area for academic research and technology transfer. However, the building itself served for the testing and development of systems and bioclimatic architecture criteria [8].

High Performance Computing

As previously explained, the direct numerical simulation of certain types of multiphase flow may require the analysis of detailed phenomena that happen at several different length-scales. Regardless of how efficient are the numerical techniques applied, the representation of such domain by means of finite-volume methods requires the employment of heavy computational resources. Consequently, the numerical algorithms used in this framework need to work efficiently on parallel computers, namely, supercomputers –or clusters. The TermoFluids code developed by CTTC have been recently tested on up to 1024 CPUs when using VOF algorithms [14]. In PRACE Project No. 2014112666, the Navier-Stokes equations regulating the gravity driven bubbly flows were solved by means of the Conservative Level-Set method by using up to 3072 CPUs [18, 23, 24]. In PRACE Project No. 2016153612, recently obtained from our group, the *Direct Numerical Simulation of Bubbly Flows with Interfacial Heat and Mass Transfer* will be carried out. Most of the numerical simulations reported in this work, have been carried out on the the computer resources at CTTC own cluster, named Joan Francesc Fernandez (JFF) after the recently disappeared professor of computer science and numerical analysis that brought the first computer to the faculty. In its third generation form, built in 2013, JFF includes 40 nodes; each node has 2 AMD Opteron with 16 Cores per CPU linked with 64 Gigabytes of RAM memory and an infiniband QDR 4X network interconnection between nodes with latencies of 1.07 microseconds with a 40Gbits/s bandwith.

The most expensive simulations, regarding the physics of atomizing sprays and jets, have been performed thanks to the funds provided by Red Española de Supercomputaciòn (RES), to which we accessed towards participating in competitive projects. The simulations have

Figure 1.4: Third generation form of the Joan Francesc Fernandez (JFF) cluster for HPC, placed in CTTC [8].

been performed on the computer resources at MareNostrum III, with technical support provided by Barcelona Supercomputing Center (BSC, research project: RES-FI-2016-1-0023), at the magnificent recently born MareNostrum IV (RES-FI-2017-2-0015), currently the most powerful cluster in Spain —see Fig. 1.5(a)—, and at FinisTerrae II —see Fig. 1.5(b)—, with support by Centro de Supercomputaciòn de Galicia (CESGA, research projects: RES-FI-2016-2-0028, RES-FI-2016-3-0015). Further details above the cited competitive projects are given in Appendix C.

1.1.2 Outline of the Thesis

All the topics covered in this thesis concern the resolution of numerical issues related to the DNS of multiphase flow phenomena. My experience consisted initially in the use of TermoFluids code to simulate engineering problems involving two-phase set-up. However, during the development of the work, I often found the necessity of integrating the original techniques with additional tools to adapt the solver to particular types of physics. This led to the addition of new features to TermoFluids and to the introduction of original contributions to the state-of-the-art of the interested research field. Some example are the application of dynamic meshes to multiphase flows or the development of new discrete operators and strategies.

The various results that have been obtained during my Phd are listed below, specifying the contribution given in each chapter of the current thesis

- In Chapter 2, a hybrid convective operator for the discrete Navier-Stokes equations is presented, applicable to general turbulent multiphase flow. The discrete operator aims at minimizing the differences in kinetic energy preservation with respect to the

(a) MareNostrum IV

(b) FinisTerrae II

Figure 1.5: (a) Mare Nostrum IV (MN4) supercomputer, installed in Torre Girona chapel, Barcelona. The general purpose element, provided by Lenovo, accounts for 48 racks with more than 3,400 nodes with next generation Intel Xeon processors and a central memory of 390 Terabytes [25] (b) FinisTerrae II is installed in Santiago da Compostela, Spain. Renewed in 2016, it is composed of 306 computing nodes, each of these has two Haswell 2680v3 processors, 128 GB memory and a 2TB disc [26].

continuous governing equations. This property plays a fundamental role in the case of flows presenting significant levels of turbulence. At the same time, the hybrid form of the convective operator proposed in this work incorporates localized low-dispersion characteristics to limit the growth of spurious currents.

- In Chapter 3, a strategy for the application of adaptive meshes to multiphase flow is proposed, in order to concentrate dynamically the mesh density in the zones of the flow where a small characteristic length is needed. In this way, the computational resources are optimized in interfacial flows as rising bubbles —see Fig. 1.6— and atomization cases. The discretization, built on a finite-volume basis, accounts for a divergence-free treatment of the refined/coarsened cells, that ensures the correct transport of mass, momentum and kinetic energy

- The numerical framework described in this work is employed to carry out the simulation of 3-D break-up phenomena, in order to obtain physical insights on these kinds of flow. In particular, the two analyzed cases are the air-assisted atomization of liquid jets and the injection of a high velocity liquid jet inside still air chambers, as the one depicted in Fig. 1.7. Both cases are described in a dedicated section, correspondent to Chapter 4.

- In Chapter 5, free-surface flows are studied. A single-phase model is proposed, which specifies and optimizes the two-phase solver for the free-surface case, and adds the possibility to consider the interaction with fixed or mobile objects. The scheme is applied to the numerical simulation of different set-up in the marine engineering field, as the subaerial landslide inside a water basin reported in Fig. 1.8. A possible industrial application of the model is shown in Appendix A, where we study the hydrodynamic behavior of an Oscillating Water Column device.

In the final Conclusions, given in Chapter 6, I resume briefly the results obtained in the various Chapters of this work. Finally, I will express my opinion above the additional arrangements that need to be implemented in the future, in order to further extend the area of applicability of the numerical framework presented in this work.

1.2 Governing equations

In this section, the differential equations that govern the movement of the fluid are introduced, described by means of the renown Navier-Stokes equations. Next, the equation that describe the tracking of the interface is presented, giving a general overview of the numerical approaches adopted in the recent past to model its behavior.

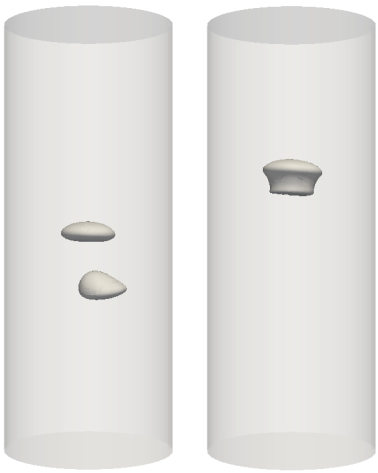

(a) (b)

Figure 1.6: Simulation of the merging process between rising bubbles, carried out with Adaptive Mesh refinement techniques. Details in Sec. 3.3.2

Figure 1.7: Simulation of a water jet inside a still air chamber, characterized by Reynolds number, $\mathrm{Re}_l = 3400$, and Ohnesorge number, Oh$= 0.01$. Further details in Chapter 4

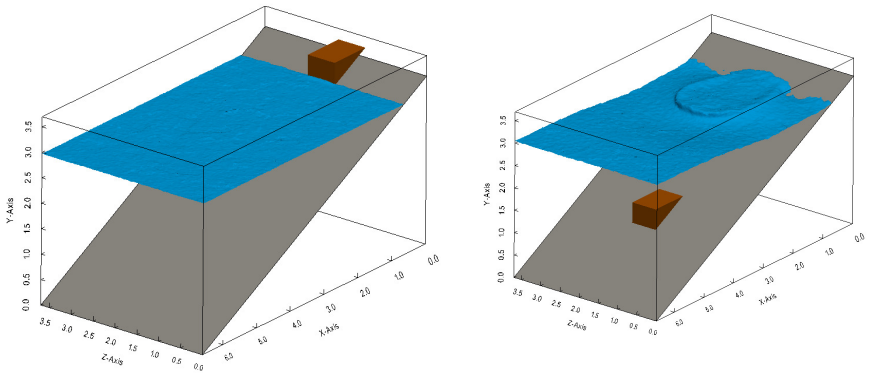

(a) (b)

Figure 1.8: Screenshots of the DNS simulation of a landslide event inside a water basin performed in this work. Further details are reported in Sec. 5.4

1.2.1 Momentum equations

The movement of the Newtonian fluids analyzed in this work is described by means of classic Navier-Stokes equations. In particular, interfacial flows are governed by the mass and momentum equations in the variable-density incompressibility limit, written in divergence form as [12, 27]

$$\nabla \cdot \mathbf{u} = 0, \tag{1.1}$$

$$\frac{\partial(\rho \mathbf{u})}{\partial t} + \nabla \cdot (\rho \mathbf{u}\mathbf{u}) = -\nabla p + \nabla \cdot [\mu(\nabla \mathbf{u} + \nabla^{\mathsf{T}} \mathbf{u})] + \rho \mathbf{g} + T_\sigma, \tag{1.2}$$

where $\mathbf{u}$ and p represent velocity and pressure, $\rho \mathbf{g}$ accounts for the gravitational acceleration, and T_σ is the interfacial surface tension force evaluated as

$$\mathbf{T}_\sigma = \sigma \kappa \mathbf{n}_\Gamma \delta(\mathbf{x} - \mathbf{x}_\Gamma), \tag{1.3}$$

with σ the constant surface tension coefficient, κ and $\mathbf{n}_\Gamma$ the curvature and unit normal vector of the interface, respectively, and $\delta(\mathbf{x} - \mathbf{x}_\Gamma)$ the Dirac delta function concentrating the force in the interface region. The peculiarity of this system of equations is found in the evaluation of density ρ, and dynamic viscosity μ, since they are calculated according to the location of the interface Γ, interpolating them from the properties of each phase k by means of phase-volume fraction values C_k written as

$$\rho = \sum_k C_k \rho_k \quad \text{and} \quad \mu = \sum_k C_k \mu_k. \tag{1.4}$$

The scalar field C_k, indicating the presence of phase k, can be updated in time according to different interface modelization approaches, introduced in detail in the following section.

1.2.2 Interface modelization

The location of the interface determines a discontinuity in density and viscosity, as well as in other physical variables, and is considered to be, in three-dimensions (3-D), a smooth surface that links the different phases by transferring momentum between them. In the case of negligible phase change, an interface evolves according to the velocity field as

$$\frac{d\mathbf{x}_\Gamma}{dt} = \mathbf{u}(\mathbf{x}_\Gamma, t), \tag{1.5}$$

where $\mathbf{x}_\Gamma$ refers to the points on the interface between phases. As introduced in the work by Scardovelli and Zaleski [3], many different methods exist to numerically solve Eq. 1.5, but they can be distributed into two main groups differing in the way in which the detection of the interface is globally conceived. Each group appears to be particularly suitable for the simulation of specific cases.

The first group collects the approaches in which the interface between fluids is tracked as it moves (interface-tracking methods). For instance, in the Arbitrary Lagrangian Eulerian (ALE) technique [28], the tracking is done by means of a moving (Lagrangian) grid that follows the interface, while the fluid evolves on a fixed stationary (Eulerian) mesh. Another example is the Front Tracking (FT) method [29], in which the individual interfaces are represented by sets of connected marker points. Generally, these methodologies are not efficient in the simulation of complex vortical flows, in which significant distortions of the interface topology may occur [2].

The strategies corresponding to the second main group (interface-capturing methods) are characterized by a scalar function that embeds the moving interface on a fixed grid. The interface-capturing approaches, which are adopted in this work, employ only one set of equations to describe the different phases instead of utilizing one for each subdomain k. This methodology allows the spatial discretization of the entire domain on a single static grid, while the interface is captured by means of scalar functions. The main advantage is that large interface distortions, e.g., interface breakage and reconnection due to strong swirling flows, are properly handled, avoiding the necessity to continuously adapt the mesh to a varying interface topology, as pointed out again by Gorokhovski and Herrmann [2] in the context of multiphase jets.

The two main interface-capturing options are the Volume-of-Fluid (VOF) [13, 14, 30, 31] and Level-Set (LS) [12, 32, 33] methods. These two approaches mainly differ in the choice of the scalar fields C_k, also referred to as indicator functions, used to capture the motion of each phase k within the domain. The indicator function is advected by means of a transport equation, which in the hypothesis of immiscibility of fluids and divergence-free

velocity fields, i.e., $\nabla\cdot\mathbf{u}=0$, reads

$$\frac{\partial C_k}{\partial t}+\nabla\cdot(C_k\mathbf{u})=0, \tag{1.6}$$

where a unique velocity field, i.e., $u^k=\mathbf{u}$, has been considered for all phases. In the VOF method, the advected function is the phase-volume fraction C_k, defined as the portion of volume filled by each phase k, and expressed as

$$C_k(\mathbf{x},t)=\frac{1}{V_\Omega}\int_\Omega H(\mathbf{x}-\mathbf{x}_\Gamma)d\mathbf{x}, \tag{1.7}$$

where H is the Heaviside function. Due to the discontinuity of the color function, a method must be found to maintain the sharpness of the interface when it is advected. The main option is to reconstruct the interface before the advection step by means of a Piecewise Linear Interface Calculation (PLIC) scheme, on which many of the advanced modern algorithms are based —in [13, 16] the method is extended to 3D unstructured meshes. The obtainment of the C_k scalar values by means of solving Eq. 1.6 provides closure to the evaluation of the varying density and dynamic viscosity properties, Eq. 1.4, across the whole domain, and at the same time provides the interface topology required for the evaluation of capillary stresses. As detailed in previous works by Jofre aet al. [13, 14], the VOF method provides an implicit volume-preserving formulation, however, due to its geometrical nature, the process of advancing volume fraction values in time can be rather time-consuming when good accuracy is required [16]. Moreover, despite ensuring mass conservation, the accurate evaluation of interface properties, such as curvature, is complex due to the discontinuous nature of the volume fraction scalar field advected by the VOF method [34].

In the LS method, C_k is a regularized level-set function where the interface is defined as the set of points for which the function equals 0.5. Particularly, following the method proposed by Balcázar et al. [12], C_k is evaluated for each phase as

$$C_k(\mathbf{x},t)=\frac{1}{2}\left[\tanh\left(\frac{d(\mathbf{x},t)}{2\varepsilon}\right)+1\right], \tag{1.8}$$

where $d(\mathbf{x},t)$ is the signed distance function from the interface and ε is a parameter controlling the interface thickness. Due to the continuity of the level-set function, the values of viscosity and density of the fluids in contact vary smoothly across the interface. This enhances the numerical stability of the algorithm, albeit it is an artificial continuous representation of the sharp interface separating the different phases.. Moreover, unlike VOF, LS ensures the possibility of extracting interface characteristics without supplementary efforts. In order to maintain the interface sharp, C_k is re-initialized after the advection step according to the following equation

$$\frac{\partial C_k}{\partial \tau}+\nabla\cdot C_k(1-C_k)\mathbf{n}=\nabla\cdot\varepsilon\nabla C_k, \tag{1.9}$$

where τ is the re-initialization pseudo-time. The main drawback of the standard LS method [32] is that it is not strictly conservative, as the volume bounded by the interface contour is not conserved exactly when advected and re-initialized. However, several strategies have been proposed recently to minimize this drawback [12, 16, 33], under the name of Conservative Level Set (CLS) methods, demonstrating high reliability on a wide range of applications as bubbly flows [15, 17, 18, 19], free-surface flows [20] and break-up phenomena [21, 22, 35, 36].

In the tests performed in this thesis, the method mainly used for the tracking of the interface was the CLS developed by [11, 12]. Indeed, CLS demonstrated higher stability for a wide range of situations in comparison to VOF, even with coarse meshes. This is probably due to the smoothing of properties at the interface which avoids the presence of steep density gradients, and the consequent appearance of detrimental spurious currents. However, the numerical techniques presented in this work are thought to be coupled with other interface-capturing methods. Indeed, in some of the numerical tests proposed in Chapter 2, the VOF scheme is employed.

1.3 Numerical model

In this work, a finite-volume discretization of Navier-Stokes and CLS equations on collocated unstructured meshes is used [11, 12]. Technical details on the discretization and implementation of the methods are detailed in Balcázar et al. [11, 12]. However, for the sake of completeness, the schemes adopted in the context of the present methodology are reviewed in next section. The most important geometric features, as well as the simplified explanation of the level-set function are presented in Fig. 1.9(b) for the case of Cartesian meshes —which constitutes the basis for the quad/octree hierarchical refinement process, described in Chap. 3—, and in Fig. 1.9(c) for a general unstructured mesh. In the description of the discretized equations, the following notation is used

c	refers to a cell value
f	refers to a face value
nb	refers to a cell value of the neighbor cell that share a face with c
A_f	face surface
V_c	cell volume
A_c	total cell surface
$\mathbf{n}_f$	face normal vector
$\hat{\mathbf{n}}_f$	outward face normal vector

Finally, face normal mass flux, M_f, and velocity at cell face, $\mathbf{u}_f$, are related as follows

$$M_f = \rho_f \mathbf{u}_f \cdot \mathbf{n}_f A_f. \tag{1.10}$$

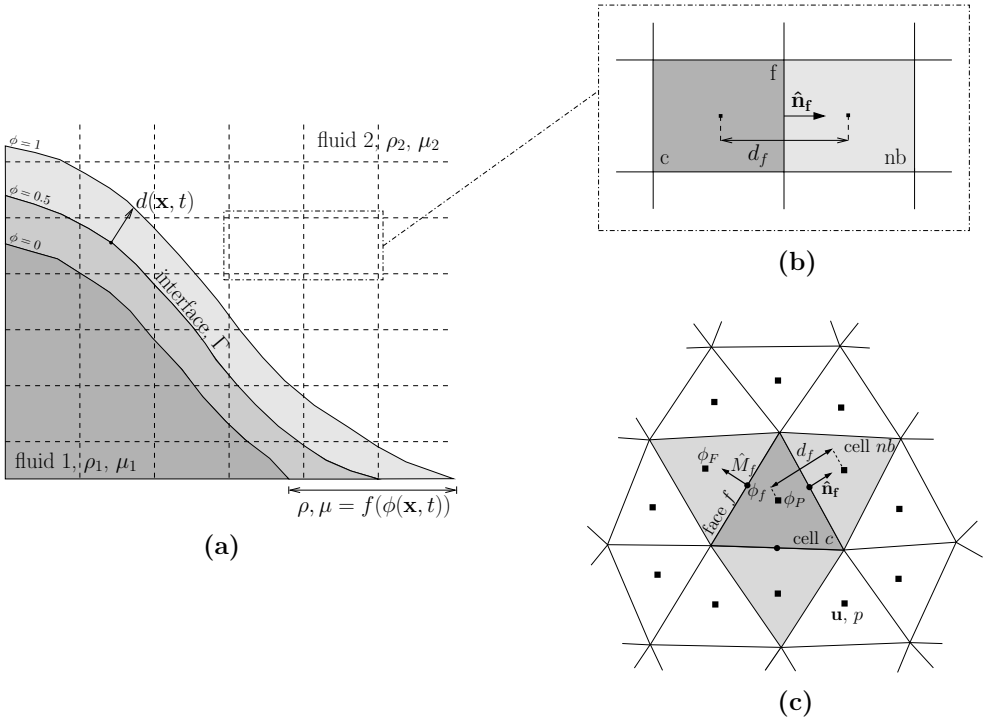

Figure 1.9: (a) Level-set driven distribution of the physical properties; fluid 1 and fluid 2 are separated by a variable density –and viscosity region in which $\phi(\mathbf{x},t)$ ranges from 0 to 1. (b) Schematics of the collocated scheme geometrical features in a Cartesian mesh. (c) Geometrical features on a general tetrahedral unstructured mesh.

1.3.1 Interface-capturing scheme

Following [11, 12], the advection of $\phi(\mathbf{x},t)$ is carried out by integrating Eq. 1.6 over the control volume (CV) corresponding to cell c, and applying the divergence theorem to the second term

$$\int_{V_c} \frac{\partial \phi(\mathbf{x},t)}{\partial t} dV + \int_{\partial V_c} \phi(\mathbf{x},t)\mathbf{u}\cdot\mathbf{n}_f dS = 0. \tag{1.11}$$

The equation is integrated in time according to a Total Variation Diminishing (TVD) third order Runge-Kutta (RK3) explicit time scheme [37] —a first-order advancement scheme is here shown for simplicity. The further discretization of the surface integral over cell faces

yields the following expression [11, 12]

$$\frac{\phi_c^{n+1}-\phi_c^n}{\Delta t}\,V_c+\sum_{f\in F(c)}\hat{U}_f^n A_f\phi_f^n=0, \tag{1.12}$$

where $\hat{U}_f^n A_f=\hat{M}_f^n/\rho_f$ is the face velocity per unit area. The advected value of the level set function, ϕ_f^n, is evaluated according to a TVD flux limiter scheme [38] —adapted to the context of 3D unstructured meshes by [11, 12]—, in order to enhance the accuracy and stability of the solution. Next, the level-set function is re-initialized in order to maintain its thickness and to keep it as a signed distance function. As in the previous case, Eq. (1.9), is integrated over cell CV, and the divergence theorem is applied to the convective and diffusive terms [11, 12]

$$\int_{V_c}\frac{\partial\phi(\mathbf{x},t)}{\partial\tau}dV+\int_{\partial V_c}\phi(\mathbf{x},t)(1-\phi(\mathbf{x},t)\mathbf{n}_{\tau=0}\cdot\mathbf{n}_f dS=\int_{\partial V_c}\varepsilon\nabla\phi(\mathbf{x},t)\cdot\mathbf{n}_f dS. \tag{1.13}$$

Next, the equation is rewritten by advancing the solution in pseudo-time according to an explicit scheme, and discretizing compressive and diffusive terms over cell faces as [11, 12]

$$\frac{\phi_c^{n+1}-\phi_c^n}{\Delta\tau}\,V_c+\sum_{f\in F(c)}\phi_f^n(1-\phi_f^n)\mathbf{n}_{\tau=0}\cdot\mathbf{n}_f A_f=\sum_{f\in F(c)}\varepsilon\nabla\phi_f\cdot\mathbf{n}_f A_f. \tag{1.14}$$

In the numerical implementation, the face value terms are evaluated by means of a central difference (CD) scheme [11, 12]. The pseudo-time step, $\Delta\tau$, is evaluated according to a CFL-like criterion dominated by the diffusive effect, $\Delta\tau=C_\tau\,\min\{\Delta h_c^2/\varepsilon\}$ [11, 12]. The ε parameter, which controls the thickness of the interface, is evaluated as $\varepsilon=C_\varepsilon\Delta h_c$, with Δh_c as the characteristic cell size [11, 12]. Both $C_\varepsilon\simeq 0.5$ and $C_\tau\simeq 0.05$ are evaluated empirically from preliminary tests and adjust to the particular type of flow. A small ε, lead to a thin interface that sharply defines the separation between the two phases. However, in order to avoid numerical instabilities caused by the sudden jump of pressure, ε cannot be too small in comparison to the characteristic mesh length [11, 12].

1.3.2 Fluid motion equations

The discrete velocity field is obtained from the solution of continuity and momentum conservation equations. Navier-Stokes equations for momentum conservation, Eqs. 1.2, are solved applying a classic fractional step projection method [39], along with an explicit time advancement scheme. For the sake of simplicity a first order scheme is here shown, while a higher order scheme [37] is used in simulations. The projection method introduces the predicted velocity concept to avoid the direct relation between velocity and pressure

$$\frac{\rho^{n+1}\mathbf{u}^{n+1}-\rho^{n+1}\mathbf{u}^p}{\Delta t}=-\nabla p^{n+1}, \tag{1.15}$$

$$\rho^{n+1}\mathbf{u}^p=\rho^n\mathbf{u}^n-\Delta t\left[\nabla\cdot(\rho^n\mathbf{u}^n\mathbf{u}^n)-\nabla\cdot[\mu^n(\nabla\mathbf{u}^n+\nabla^\intercal\mathbf{u}^n)]-\mathbf{S}^{n+1}\right]. \tag{1.16}$$

In this work, a collocated scheme is adopted, whose main geometrical features are highlighted in Fig. 1.9(b) for a Cartesian mesh and in Fig. 1.9(c) for a generic unstructured one. Consequently, velocity and pressure are evaluated at cell centers, while mass fluxes and other face variables require specific interpolations. In the first step of the discretization process, Eqs. 1.16 are integrated over the cell CV, applying the divergence theorem and discretizing over cell faces. The following discrete equation is obtained

$$\begin{aligned}\mathbf{u}^p = &\frac{\rho_c^n \mathbf{u}_c^n}{\rho_c^{n+1}} + \frac{\Delta t}{\rho_c^{n+1}}\mathbf{S}^{n+1} \\ &+ \frac{\Delta t}{\rho_c^{n+1} V_c}\left[\sum_{f\in F(c)} -\psi_f^n \hat{M}_f^n + \mu_f^n\left[(\mathbf{u}_{nb}^n - \mathbf{u}_c^n)\frac{A_f}{d_f} + \nabla^T \mathbf{u}_f^n \cdot \hat{\mathbf{n}}_f A_f\right]\right],\end{aligned} \tag{1.17}$$

where $\hat{M}_f^n$ is the face normal mass flow, ψ_f^n is the convected face velocity and d_f is the normal-projected distance between the centroids of cells c and nb. Next, the divergence operator is applied to Eq. 1.15 and the incompressibility constraint, Eq. 1.1, is introduced. Hence, the equation is integrated over the CV, and the divergence theorem is applied. The discretization over cell faces yields the following discrete Poisson equation,

$$\sum_{f\in F(c)} \frac{\hat{M}_f^p}{\rho_f^{n+1}} = \Delta t \sum_{f\in F(c)} \frac{1}{\rho_f^{n+1}}(p_{nb}^{n+1} - p_c^{n+1})\frac{A_f}{d_f}, \tag{1.18}$$

where the unknown is the pressure field, p_c^{n+1}, and $\hat{M}_f^p$ is the predicted face normal mass flow. In its final form, this linear system is rearranged by introducing the cell coefficient a_c, the neighbor coefficients a_{nb}, and the source term b as

$$p_c^{n+1} a_c = \sum_{f\in F(c)} p_{nb}^{n+1} a_{nb} + b, \tag{1.19}$$

$$a_c = \sum_{f\in F(c)} a_{nb}, \quad a_{nb} = \Delta t \frac{A_f}{W_f \rho_f^{n+1}}, \quad b = -\sum_{f\in F(c)} \frac{\hat{M}_f^p}{\rho_f^{n+1}}, \tag{1.20}$$

The updated pressure field is obtained by solving the equation by means of an iterative Preconditioned Conjugate Gradient (PCG) solver [40]. In the last step, the centered velocity is calculated by discretizing again Eq. 1.15 over cell c and introducing p_c^{n+1}.

$$\mathbf{u}_c^{n+1} = \mathbf{u}_c^p - \frac{\Delta t}{V_c \rho_c^{n+1}} \sum_{f\in F(c)} p_f^{n+1} \hat{\mathbf{n}}_f A_f. \tag{1.21}$$

As introduced before, face variables —$\hat{M}_f^p$, $\mathbf{u}_f^n$, μ_f^{n+1}, ρ_f^{n+1}, p_f^{n+1}— are evaluated by using the interpolations from cell values suggested by [41], aimed at ensuring mass-conservation

and minimizing the error in kinetic-energy discrete balance. Following this idea, density, predictor velocity, pressure, and mass flux at face f are calculated as

$$\rho_f^{n+1} = \frac{1}{2}(\rho_c^{n+1} + \rho_{nb}^{n+1}), \;\; \mathbf{u}_f^p = \frac{1}{2}(\mathbf{u}_c^p + \mathbf{u}_{nb}^p), \;\; p_f^{n+1} = \frac{1}{2}(p_c^{n+1} + p_{nb}^{n+1}), \tag{1.22}$$

$$\hat{M}_f^p = \rho_f^{n+1}\mathbf{u}_f^p \cdot \hat{\mathbf{n}}_f A_f. \tag{1.23}$$

Finally, evaluation of the mass flux at face f, $\hat{M}_f^{n+1}$, needs to be studied in detail in order to exactly conserve mass. Thus, taking again the divergence of Eq. 1.15 and discretizing over a cell c, gives

$$\sum_{f\in F(c)} \hat{M}_f^{n+1} - \sum_{f\in F(c)} \hat{M}_f^p = -\Delta t \sum_{f\in F(c)} (p_{nb}^{n+1} - p_c^{n+1})\frac{A_f}{d_f}, \tag{1.24}$$

which may be rearranged in the following form

$$\sum_{f\in F(c)} \left[\hat{M}_f^{n+1} - \hat{M}_f^p + \Delta t(p_{nb}^{n+1} - p_c^{n+1})\frac{A_f}{d_f}\right] = 0. \tag{1.25}$$

Different possibilities exist to solve this under-determined system of equations. For example, the strategy chosen in this work is to set to zero each face summand — it is a more restrictive condition, but at the same time provides an easier formulation. Then, the mass flux at face f is expressed as

$$\hat{M}_f^{n+1} = \hat{M}_f^p - \Delta t(p_{nb}^{n+1} - p_c^{n+1})\frac{A_f}{d_f}. \tag{1.26}$$

At this point, if the predictor mass flux is evaluated by means of Eq. 1.23 and $\mathbf{u}^p$ is substituted using Eq. 1.21, Eq. 1.26 may be rewritten (similarly as [12]) as

$$\hat{M}_f^{n+1} = \rho_f^{n+1}\frac{1}{2}(\mathbf{u}_c^{n+1} + \mathbf{u}_{nb}^{n+1})\cdot\hat{\mathbf{n}}_f A_f - \Delta t(p_{nb}^{n+1} - p_c^{n+1})\frac{A_f}{d_f} \tag{1.27}$$

$$+ \frac{\rho_f^{n+1}\Delta t}{2}\left[\frac{1}{\rho_c^{n+1}V_c}\sum_{f\in F(c)} p_f^{n+1}\hat{\mathbf{n}}_f A_f + \frac{1}{\rho_{nb}^{n+1}V_{nb}}\sum_{f\in F(nb)} p_f^{n+1}\hat{\mathbf{n}}_f A_f\right]\cdot\hat{\mathbf{n}}_f A_f.$$

Regardless of the interface-capturing method adopted, the mass flux resulting from Eq. 1.27 is used to advect the phase volume fractions, C_k, through the transport equation, Eq. 1.6 —Eq. 1.12 in discrete form.

The low-dispersion convection scheme presented by Schillaci et al. [22], and extensively described in Chapter 2, properly designed for turbulent two-phase flows, is used for the evaluation of convected face velocities, ψ_f^n.

Source terms, $\mathbf{S}^{n+1}$, are evaluated by using volumetric approaches. In particular, a model based on the continuum surface force (CSF) method proposed by Brackbill et al. [42] is chosen for the evaluation of surface tension. The discretization of this force on 3-D unstructured meshes has been recently extended by [12, 16, 18].

1.3.3 Time-step evaluation

The time step used for the advancement of the Navier-Stokes equations and the advection of the volume fraction can be evaluated according to the two different criteria following listed. The CFL method is used when the contribution of the source terms to the physics of the problem is considered important (e.g. gravity driven bubbly-flows). Instead, the SAT method is employed when the flow is dominated by convective and diffusive phenomena.

CFL method In most of the proposed tests, a CFL method is used for the determination of the time step, where convective, diffusive and source terms contributions are taken into account. The latter considers both gravity and surface tension forces, through, respectively, Δt_{grav} and Δt_{surf}. Hence, the complete expression for Δt reads as [12]

$$\begin{aligned}\Delta t &\leq \min\{\Delta t_{\text{conv}}, \Delta t_{\text{visc}}, \Delta t_{\text{grav}}, \Delta t_{\text{surf}}\} \\ &\leq \min\left\{\frac{\Delta h}{|\mathbf{u}_c|}, \frac{\Delta h^2 \rho_c}{\mu_c}, \left(\frac{\Delta h}{|\mathbf{g}|}\right)^{\frac{1}{2}}, \left(\frac{\rho_g + \rho_l}{4\pi\sigma}\right)^{\frac{1}{2}} \Delta h^{\frac{3}{2}}\right\},\end{aligned} \tag{1.28}$$

where Δt_{grav} has a convective-like form, and Δt_{surf} follows the scheme proposed by [42].

SAT method In the case of high-Reynolds-number flow, if the equations of fluid motion, Eqs. 1.1 and 1.2, are explicitly integrated in time — which is generally less expensive than using implicit methods [43] —, the time step value is limited by the stability of the convective term. Therefore, applying stability theory to the matrix resulting from multiplying the discrete convective operator by time step, $\Delta t\, \mathbf{C}(\rho\mathbf{u})$, the region of absolute stability can be determined on the complex plane by imposing

$$\Delta t |\lambda_i^C| \leq 1 \qquad \forall i = 1, ..., m, \tag{1.29}$$

with $\lambda_i^C \in \mathbb{I}$ the eigenvalues of the $m \times m$ convective operator matrix.

The solution of large eigenvalue problems is extraordinary time-consuming, particularly in the case of Eq. 1.29, since $\mathbf{C}(\rho\mathbf{u})$ changes every time step. In fact, the calculation of the eigenvalues requires an amount of computational resources similar to that of solving the discrete system. Thus, this is not a real option. Instead, as proposed in Trias and Lehmkuhl [44], a more practical approach is to bound them by means of the Gershgorin circle theorem [45], written as

$$|\lambda_i^C - c_{ii}| \leq \sum_{j \neq i} |c_{ij}| \qquad \forall i = 1, ..., m, \tag{1.30}$$

where c_{ii} and c_{ij} are, respectively, the diagonal and off-diagonal elements of the discrete convective matrix defined in Eqs. 2.20 and 2.21. Hence, the maximum time step within the

stability region results from considering the largest eigenvalue in Eq. 1.30, defined as

$$|\lambda^C_{max}| \leq max\left[|c_{ii}| + \sum_{j\neq i}|c_{ij}|\right] \qquad \forall i = 1,...,m. \tag{1.31}$$

1.3.4 Solution algorithm

In summary, the complete algorithm for the resolution of the equations of fluid motion and advancement/re-initialization of the level-set function consists in the following steps:

1. Calculate the predicted , u^p_f, from Eq. (1.17).
2. Update the pressure field, p^{n+1}, by iteratively solving Eq. (1.18).
3. Evaluate the centered velocity, u^{n+1}_f, as given by Eq. (1.21).
4. Evaluate the new mass fluxes, $\hat{M}^{n+1}_f$, by applying Eq. (1.27).
5. Advect and re-initialize $\phi(\mathbf{x},t)$ according to Eqs. (1.12) and (1.14).

1.3.5 Solid Interaction

In some of the cases analyzed in this work, and reported in Chapter 5, the interaction of the flow with a third solid phase with prescribed velocity is taken into account. The interaction between flow and solid is solved by means of a second-order direct forcing Immersed Boundary Method (IBM), described in detail by Favre et al. [46]. The IBM method introduces a specific treatment of the Navier-Stokes equations at the interface between solid and fluids. In particular, we consider the following NS equation in discrete form

$$\frac{\mathbf{u}^p - \mathbf{u}^n}{\Delta t} = \mathrm{RHS}^n + \vec{f} \tag{1.32}$$

where RHS includes convective, diffusive and source terms and $\vec{f}$ is an additional source term used to consider the effects of the solid motion on the fluid. The forcing term is evaluated as

$$\vec{f} = \frac{U_s - \mathbf{u}^p}{\Delta t} - \mathrm{RHS}^n \tag{1.33}$$

where U_s is directly prescribed in the nodes interiors to the solid body or must follow a particular second-order interpolation [47] for the forcing points that coincide with the interface between solid and fluids.

Bibliography

[1] G. Tryggvason, R. Scardovelli, S. Zaleski, Direct numerical simulations of gas–liquid multiphase flows, Cambridge University Press, 2011.

[2] M. Gorokhovski, M. Herrmann, Modeling primary atomization, Annual Review of Fluid Mechanics 40 (2008) 343–366.

[3] R. Scardovelli, S. Zaleski, Direct numerical simulation of free-surface and interfacial flow, Annual Review of Fluid Mechanics 31 (1999) 567–603.

[4] P. Marmottant, E. Villermaux, On spray formation, Journal of Fluid Mechanics 498 (2004) 73–111.

[5] J. Shinjo, A. Umemura, Simulation of liquid jet primary breakup: Dynamics of ligament and droplet formation, International Journal of Multiphase Flow 36 (2010) 513–532.

[6] S. Zahedi, M. Kronbichler, G. Kreiss, Spurious currents in finite element based level set methods for two-phase flow, International Journal for Numerical Methods in Fluids 69 (2012) 1433–1456.

[7] Webpage: www.oceanenergy.ie.

[8] Webpage: www.cttc.upc.edu.

[9] Termo fluids s.l., webpage: www.termofluids.com.

[10] L. Jofre Cruanyes, Numerical simulation of multiphase immiscible flow on unstructured meshes, Ph.D. thesis, Universitat Politècnica de Catalunya, 2014.

[11] N. V. Balcázar Arciniega, Numerical simulation of multiphase flows: level-set techniques, Ph.D. thesis, Universitat Politècnica de Catalunya, 2014.

[12] N. Balcázar, L. Jofre, O. Lehmkuhl, J. Castro, J. Rigola, A finite-volume/level-set method for simulating two-phase flows on unstructured grids, International Journal of Multiphase Flow 64 (2014) 55–72.

[13] L. Jofre, O. Lehmkuhl, J. Castro, A. Oliva, A 3-D volume-of-fluid advection method based on cell-vertex velocities for unstructured meshes, Computers & Fluids 94 (2014) 14–29.

[14] L. Jofre, R. Borrell, O. Lehmkuhl, A. Oliva, Parallel load balancing strategy for volume-of-fluid methods on 3-D unstructured meshes, Journal of Computational Physics 282 (2015) 269–288.

[15] N. Balcázar, O. Lehmkuhl, J. Rigola, A. Oliva, A multiple marker level-set method for simulation of deformable fluid particles, International Journal of Multiphase Flow 74 (2015) 125–142.

[16] N. Balcázar, O. Lehmkuhl, L. Jofre, J. Rigola, A. Oliva, A coupled volume-of-fluid/level-set method for simulation of two-phase flows on unstructured meshes, Computers & Fluids 124 (2016) 12 –29.

[17] N. Balcázar, O. Lehmkuhl, L. Jofre, A. Oliva, Level-set simulations of buoyancy-driven motion of single and multiple bubbles, International Journal of Heat and Fluid Flow 56 (2015) 91–107.

[18] N. Balcázar, J. Rigola, J. Castro, A. Oliva, A level-set model for thermocapillary motion of deformable fluid particles, International Journal of Heat and Fluid Flow 62 (2016) 324–343.

[19] E. Gutiérrez, N. Balcázar, E. Bartrons, J. Rigola, Numerical study of taylor bubbles rising in a stagnant liquid using a level-set/moving-mesh method, Chemical Engineering Science 164 (2017) 158 – 177.

[20] E. Schillaci, L. Jofre, N. Balcázar, O. Lehmkuhl, A. Oliva, A level-set aided single-phase model for the numerical simulation of free-surface flows on unstructured meshes, Computers & Fluids 140 (2016) 97–110.

[21] E. Schillaci, O. Lehmkuhl, O. Antepara, A. Oliva, Direct numerical simulation of multi-phase flows with unstable interfaces, Journal of Physics: Conference Series 745 (2016).

[22] E. Schillaci, L. Jofre, N. Balcázar, O. Antepara, A. Oliva, A low-dissipation convection scheme for the stable discretization of turbulent interfacial flow, Computers & Fluids 153 (2017) 102–117.

[23] N. Balcázar, J. Castro, J. Rigola, A. Oliva, Dns of the wall effect on the motion of bubble swarms, Procedia Computer Science 108 (2017) 2008–2017.

[24] N. Balcázar, O. Lehmkuhl, J. Castro, A. Oliva, DNS of the Rising Motion of a Swarm of Bubbles in a Confined Vertical Channel, Springer International Publishing, Cham, pp. 125–131.

[25] Webpage: www.bsc.es.

[26] Webpage: www.cesga.es.

[27] C. S. Peskin, Numerical analysis of blood flow in the heart, Journal of computational physics 25 (1977) 220–252.

[28] H. H. Hu, N. A. Patankar, M. Zhu, Direct numerical simulations of fluid–solid systems using the arbitrary lagrangian–eulerian technique, Journal of Computational Physics 169 (2001) 427–462.

[29] S. O. Unverdi, G. Tryggvason, A front-tracking method for viscous, incompressible, multi-fluid flows, Journal of computational physics 100 (1992) 25–37.

[30] C. W. Hirt, B. D. Nichols, Volume of fluid (VOF) method for the dynamics of free boundaries, Journal of Computational Physics 39 (1981) 201–225.

[31] P. Liovic, M. Rudman, J.-L. Liow, D. Lakehal, D. Kothe, A 3D unsplit-advection volume tracking algorithm with planarity-preserving interface reconstruction, Computers & Fluids 35 (2006) 1011–1032.

[32] S. Osher, J. A. Sethian, Fronts propagating with curvature-dependent speed: algorithms based on Hamilton-Jacobi formulations, Journal of Computational Physics 79 (1988) 12–49.

[33] E. Olsson, G. Kreiss, A conservative level set method for two phase flow, Journal of Computational Physics 210 (2005) 225–246.

[34] K. Ito, T. Kunugi, S. Ohno, H. Kamide, H. Ohshima, A high-precision calculation method for interface normal and curvature on an unstructured grid, Journal of Computational Physics 273 (2014) 38–53.

[35] O. Desjardins, V. Moureau, H. Pitsch, An accurate conservative level set/ghost fluid method for simulating turbulent atomization, Journal of Computational Physics 227 (2008) 8395–8416.

[36] O. Desjardins, J. McCaslin, M. Owkes, P. Brady, Direct numerical and large-eddy simulation of primary atomization in complex geometries, Atomization and Sprays 23 (2013).

[37] S. Gottlieb, C.-W. Shu, Total variation diminishing runge-kutta schemes, Mathematics of computation of the American Mathematical Society 67 (1998) 73–85.

[38] P. K. Sweby, High resolution schemes using flux limiters for hyperbolic conservation laws, SIAM journal on numerical analysis 21 (1984) 995–1011.

[39] A. Chorin, A numerical method for solving incompressible viscous flow problems, Journal of Computational Physics 2 (1967) 12–26.

[40] J. R. Shewchuk, An introduction to the conjugate gradient method without the agonizing pain, 1994.

[41] L. Jofre, O. Lehmkuhl, J. Ventosa, F. X. Trias, A. Oliva, Conservation properties of unstructured finite-volume mesh schemes for the Navier-Stokes equations, Numerical Heat Transfer, Part B: Fundamentals 65 (2014) 53–79.

[42] J. Brackbill, D. B. Kothe, C. Zemach, A continuum method for modeling surface tension, Journal of Computational Physics 100 (1992) 335–354.

[43] R. Verstappen, A. Veldman, Direct numerical simulation of turbulence at lower costs, Journal of Engineering Mathematics 32 (1997) 143–159.

[44] F. Trias, O. Lehmkuhl, A self-adaptive strategy for the time integration of Navier-Stokes equations, Numerical Heat Transfer, Part B: Fundamentals 60 (2011) 116–134.

[45] S. Gerschgorin, Über die abgrenzung der eigenwerte einer matrix, Fiziko-Matematicheskaya Nauka 7 (1931) 749–754.

[46] F. Favre, O. Antepara, O. Lehmkuhl, R. Borrell, On the fast transient spoiler deployment in a naca0012 profile using les techniques combined with amr and imb methods, in: 11th World Congress on Computational Mechanics (WCCM XI); 5th European Conference on Computational Mechanics (ECCM V); 6th European Conference on Computational Fluid Dynamics (ECFD VI), International Association for Computational Mechanics (IACM).

[47] E. Fadlun, R. Verzicco, P. Orlandi, J. Mohd-Yusof, Combined immersed-boundary finite-difference methods for three-dimensional complex flow simulations, Journal of computational physics 161 (2000) 35–60.

2

A Low-Dissipation Convection Scheme for the Stable Discretization of Turbulent Interfacial Flow

Main contents of this chapter have been published in:

E.Schillaci, L.Jofre, N. Balcázar, O. Antepara, and A. Oliva. A Low-Dissipation Convection Scheme for the Stable Discretization of Turbulent Interfacial Flow. *Computers & Fluids*, 153:102–117, 2017.

Abstract. This paper analyzes a low-dissipation discretization for the resolution of immiscible, incompressible multiphase flow by means of interface-capturing schemes. The discretization is built on a three-dimensional, unstructured finite-volume framework and aims at minimizing the differences in kinetic energy preservation with respect to the continuous governing equations. This property plays a fundamental role in the case of flows presenting significant levels of turbulence. At the same time, the hybrid form of the convective operator proposed in this work incorporates localized low-dispersion characteristics to limit the growth of spurious flow solutions. The low-dissipation discrete framework is presented in detail and, in order to expose the advantages with respect to commonly used methodologies, its conservation properties and accuracy are extensively studied, both theoretically and numerically. Numerical tests are performed by considering a three-dimensional vortex, an exact sinusoidal function, and a spherical drop subjected to surface tension forces in equilibrium and immersed in a swirling velocity field. Finally, the turbulent atomization of a liquid-gas jet is numerically analyzed to further assess the capabilities of the method.

Additional content have been published in:

E.Schillaci, O.Lehmkuhl, O.Antepara, and A.Oliva. Direct numerical simulation of multiphase flows with unstable interfaces. *Journal of Physics: Conference Series*, (Vol. 745, No. 3, p. 032114). IOP Publishing.

2.1 Introduction

The necessity of introducing a particular form for the discrete convective operator in Navier-Stokes equations governing two-phase flows, rises from two main numerical issues: to limit the rise of spurious currents at the interface, and to assure the conservation properties of secondary operators. These subjects are detailed in the following paragraphs. Next, the current proposal to solve these issues is presented.

Spurious currents As introduced in Chapter 1, the full-domain modelization chosen in this work to represent the movement of the interface embeds the different phases within a single static mesh. This procedure may result, especially in problems presenting large density ratios, in the appearance of parasitic flows (spurious currents) close to the interfaces. These unphysical flows are produced by imbalances between the discrete representation of pressure gradients and capillary forces in the variable density zone. As a consequence, fluids may be artificially accelerated at the interface resulting in poor mass conservation, and consequently failure to properly represent the interface topology. As concluded by Lafaurie et al. [1] and by Renardy and Renardy [2], the magnitude of parasitic flows scales with the inverse of the capillary number, and it may not decrease with mesh refinement. Zahedi et al. [3] comprehensively analyzed the effect of several factors on spurious currents, concluding that, when using a regularized force method for the discretization of capillary forces, the most influential parameter is the numerical evaluation of interface curvature. Other authors managed to reduce the presence of interfacial spurious currents by studying in detail the causes that originate them [4], and by proposing improved discretizations of the pressure gradient and surface tension force [5, 6].
The appearance of spurious currents in the discrete solution of interfacial flows presenting large density ratios is also related to the complexity of ensuring mass conservation at the interface region. For instance, in the case of solving the velocity-pressure coupling of the momentum equations by means of a projection method, e.g., fractional-step method [7], a variable-coefficient Poisson's pressure linear system must be solved at each time step. The ill-posedness of the resulting linear system due to the discontinuity in density across the interface complicates its resolution with high accuracy. As a result, the projection of the predicted velocity field onto a divergence-free space, i.e., $\nabla \cdot \mathbf{u}$, by means of the pressure gradient is difficult to achieve to machine precision with a relatively low computational cost. This turns out in the appearance of spurious velocities that propagate from the high- to the low-density

phase. A solution often considered is to deactivate the light phase and impose a specific pressure at the free surface. This methodology is known as single-phase model [8, 9, 10], and leads to stabler behaviors since the spurious currents can be eliminated by construction. However, although practical for a wide range of free-surface flows —e.g., sea waves or water impact problems, as we will see in Chapter 5—, this simplification is not a general solution for interfacial flow.

Conservation properties Consideration of secondary discrete conservation properties, such as kinetic energy or vorticity, for the development of numerical schemes has barely been a priority in the multiphase literature, and pure dissipative models have been widely used in many reference works [11, 12, 13]. This is in contrast with the path taken by the single-phase turbulent community [14, 15, 16], which has evolved to discretely preserve mass, momentum and, specifically, kinetic energy by using skew-symmetric formulations at expenses of increasing the local truncation error. To the best of the authors' knowledge, only the recent work by Fuster [17] explicitly proposes the use of kinetic-energy-preserving schemes for the discretization of interfacial phenomena on 3-D Cartesian grids.
The absence of artificial numerical dissipation enhances the correct resolution of turbulent flows by mimicking the conservation properties of the continuous governing equations, where dissipation is restricted to the enstrophy term. However, as demonstrated in Sec. 2.4, potential non-physical flows originated during the discrete advancement of the conservation equations may grow unlimited due to the incapacity of the numerical framework to counteract them. This is of paramount importance in the case of interfacial flows presenting large density ratios between phases, in which full-domain modelizations usually propitiate the appearance of spurious currents at the interfaces.

Current proposal The current work aims at developing a low-dissipation convective scheme for interfacial turbulent flow that prioritizes the conservation of kinetic energy, while at the same time presents low-dispersion characteristics at the interface regions. The numerical framework analyzed is suitable for both unstructured and Cartesian 3-D meshes, with the enhanced feature that the interface resolution of the latter can be improved with dynamic refinement strategies.
Particular attention is given to the convection term in the Navier-Stokes equations due to its role in the transfer of energy between turbulent scales. In detail, the work proposes the utilization of a hybrid convection scheme: conservative in the bulk of the phases, whereas stabilizing (and dispersive) at the interface regions. The conservative convection scheme chosen is the symmetry-preserving [14], characterized by the conservative transport of kinetic energy between turbulent scales — this property is fundamental for the correct resolution of turbulence [15]. On the other hand, the dispersive convection scheme selected is the one presented by Veldman and Lam [18], which guarantees that the resulting discrete convective matrix operator is positive-definite, i.e., extracts energy out of the system.

Alike strategies have been proposed for other types of physics. For example, it is commonly used for capturing shock waves in compressible flows. In that context, different authors have proposed hybridization of conservative and discontinuity-capturing convection schemes that reduce numerical dissipation while maintain the ability to capture shocks — a general overview of such methods is proposed by Pirozzoli [19]. A common feature of all these hybrid frameworks is the role played by the position sensors. In compressible flow, their purpose is to limit the activation of the low-dispersion scheme just to the shocked regions, without affecting the rest of the flow field. Similarly, the position sensors in this work will be utilized to stabilize only the interface regions.
Therefore, this Chapter presents and analyzes a low-dissipation and low-dispersion discrete framework for the numerical simulation of interfacial turbulent flow on 3-D unstructured meshes and it is organized as follows. In Sec. 2.2 an analysis of the discrete conservation properties of the governing equations presented in Chapter 1 is given. Sec. 2.3 presents and analyzes the hybrid convection scheme proposed. Finally, numerical tests are performed in Sec. 2.4 and conclusions are drawn in Sec. 2.5.

2.2 Conservation properties

The continuity and Navier-Stokes equations are derived specifically for the conservation of mass and momentum. Thus, finite-volume based discretizations inherently preserve these properties. On the contrary, conservation of secondary derived quantities, such as kinetic energy, entropy or vorticity — which cannot be directly imposed during the construction of the numerical methods — is not always considered.
In this section, discrete conservation properties of the collocated scheme for two-phase flow without surface tension (introduced by Jofre et al. [20]) are theoretically analyzed. Discussion of kinetic energy preservation, partitioned between this section and Sec. 2.3, is presented for a generic treatment of the convective operator. For this purpose, it is useful to introduce the matrix-vector notation of the governing equations, Eqs. 1.1 and 1.2, written as

$$\mathbf{M}\mathbf{u} = \mathbf{0}, \tag{2.1}$$

$$\Omega\frac{d(\rho\mathbf{u})}{dt} + \mathbf{C}(\rho\mathbf{u})\mathbf{u} + \mathbf{G}\mathbf{p} + \mathbf{D}(\mu)\mathbf{u} + \Omega\mathbf{S} = \mathbf{0}, \tag{2.2}$$

where $\mathbf{u}$, $\mathbf{p}$ and $\mathbf{S}$ are the vectors of velocities, pressures and source terms. The diagonal matrix Ω describes the volume of cells, matrices $\mathbf{C}(\rho\mathbf{u})$ and $\mathbf{D}(\mu)$ are the convective and diffusive operators, and matrices $\mathbf{G}$ and $\mathbf{M}$ represent the gradient and divergence operators, respectively.
As proposed by Verstappen and Veldman [14], discrete conservation properties are easily analyzed by considering the symmetries of these matrices. On the one hand, kinetic energy is conserved if and only if the discrete convective operator is skew-symmetric, i.e., the transpose

of the matrix is also its negative, $\mathbf{C}(\rho\mathbf{u}) = -\mathbf{C}(\rho\mathbf{u})^*$, and if the negative conjugate transpose of the discrete gradient operator is equal to the divergence operator, i.e., $\mathbf{M} = -\mathbf{G}^*$. On the other hand, the diffusive operator must be symmetric and positive-definite in order to be dissipative, i.e., the matrix is equal to its transpose $\mathbf{D}(\mu) = \mathbf{D}(\mu)^*$, and $\mathbf{z}^*\mathbf{D}(\mu)\mathbf{z} > \mathbf{0}$ for all nonzero vector $\mathbf{z}$.

2.2.1 Mass conservation

Global mass conservation invokes the integral of Eq. 1.1 over the whole domain, Ω. Thus, if the entire integral is transformed to a summation of integrals for each control volume that form the domain, $c \in \Omega$, the following expression is obtained

$$\int_\Omega \nabla\cdot\mathbf{u}\, dV = \sum_{c\in\Omega}\int_{\Omega_c} \nabla\cdot\mathbf{u}\, dV = \sum_{c\in\Omega}\sum_{f\in F(c)} \hat{U}_f A_f. \tag{2.3}$$

Defining the normal face velocity U_f, as the mass flux at a face M_f, divided by face density ρ_f, and area A_f, rewrites Eq. 2.3 as

$$\int_\Omega \nabla\cdot\mathbf{u}\, dV = \sum_{c\in\Omega}\sum_{f\in F(c)} \hat{U}_f A_f = \sum_{c\in\Omega}\sum_{f\in F(c)} \frac{\hat{M}_f}{\rho_f}. \tag{2.4}$$

For the collocated scheme, a special definition for mass fluxes at faces, Eq. 1.27, has been developed in order to exactly conserve mass on each cell c. Thus, the local conservation of mass for the collocated scheme is demonstrated by dividing Eq. 1.24 by face density, rearranging terms and making use of Eq. 1.18, giving

$$\sum_{f\in F(c)} \frac{\hat{M}_f^{n+1}}{\rho_f^{n+1}} = \sum_{f\in F(c)} \left[\frac{\hat{M}_f^{p}}{\rho_f^{n+1}} - \frac{\Delta t}{\rho_f^{n+1}}(p_{nb}^{n+1} - p_c^{n+1}) \frac{A_f}{\delta d_f} \right] = 0. \tag{2.5}$$

Therefore, total mass preservation results directly from local conservation at each cell, which is expressed as

$$\int_\Omega \nabla\cdot\mathbf{u}\, dV = \sum_{c\in\Omega}\int_{\Omega_c} \nabla\cdot\mathbf{u}\, dV = \sum_{c\in\Omega}\sum_{f\in F(c)} \hat{U}_f A_f = \sum_{c\in\Omega}\sum_{f\in F(c)} \frac{\hat{M}_f}{\rho_f} = 0. \tag{2.6}$$

2.2.2 Momentum conservation

Conservation of momentum is intrinsically guaranteed by writing the equations in divergence form. It is obtained by integrating Eq. 1.2 over the entire domain, which is transformed to a

summation of integrals for each control volume that form the domain and converted to surface integrals by applying the divergence theorem, resulting in

$$\sum_{c\in\Omega}\frac{d(\rho_c\mathbf{u}_c)}{dt}V_c+\sum_{c\in\Omega}\sum_{f\in F(c)}\phi_f\hat{M}_f=-\sum_{c\in\Omega}\sum_{f\in F(c)}p_f\hat{\mathbf{n}}_fA_f \tag{2.7}$$
$$+\sum_{c\in\Omega}\sum_{f\in F(c)}\mu_f\left[(\mathbf{u}_{nb}-\mathbf{u}_c)\frac{A_f}{\delta d_f}+\nabla^{\intercal}\mathbf{u}_f\cdot\hat{\mathbf{n}}_fA_f\right]+\sum_{c\in\Omega}\mathbf{S}_cV_c.$$

Notice that $\hat{M}_f$, $\hat{\mathbf{n}}_f$ and $(\mathbf{u}_{nb}-\mathbf{u}_c)$ are quantities that present equal values but with different sign when evaluating them at a face f from two adjacent interior cells. In this way, interior fluxes cancel out and Eq. 2.7 is evaluated as the summation over boundary faces $f\in F(\partial\Omega)$ written as

$$\sum_{c\in\Omega}\frac{d(\rho_c\mathbf{u}_c)}{dt}V_c+\sum_{f\in F(\partial\Omega)}\phi_f\hat{M}_f=-\sum_{f\in F(\partial\Omega)}p_f\hat{\mathbf{n}}_fA_f \tag{2.8}$$
$$+\sum_{f\in F(\partial\Omega)}\mu_f\left[(\mathbf{u}_f-\mathbf{u}_a)\frac{A_f}{\delta d_f}+\nabla^{\intercal}\mathbf{u}_f\cdot\hat{\mathbf{n}}_fA_f\right]+\sum_{c\in\Omega}\mathbf{S}_cV_c,$$

where $\mathbf{u}_a$ is the boundary-neighbor cell velocity. This equation states that the change in momentum is due to the fluxes through the boundary of the domain and the source terms.

2.2.3 Kinetic energy conservation

The transport equation for kinetic energy, $\frac{1}{2}\rho\mathbf{u}\cdot\mathbf{u}$, is derived from the momentum equation, Eq. 1.2, by taking the velocity dot product and assuming incompressible fluid. Its mathematical expression takes the form

$$\frac{\partial(\frac{1}{2}\rho\mathbf{u}\cdot\mathbf{u})}{\partial t}+\nabla\cdot\left[\mathbf{u}(\frac{1}{2}\rho\mathbf{u}\cdot\mathbf{u})\right]=-\nabla\cdot(p\mathbf{u}) \tag{2.9}$$
$$+\nabla\cdot[\mu(\nabla\mathbf{u}+\nabla^{\intercal}\mathbf{u})]\cdot\mathbf{u}+\mathbf{S}\cdot\mathbf{u},$$

where, from left to right, quantities correspond to time derivative, convection, pressure, diffusion and source terms, respectively. In order to investigate the conservation of kinetic energy for the collocated scheme, Eq. 2.9 is discretized over the whole domain and transformed to a summation of surface integrals for each cell c as

$$\sum_{c\in\Omega}\mathbf{u}_c\cdot\frac{d(\rho_c\mathbf{u}_c)}{dt}V_c+\sum_{c\in\Omega}\mathbf{u}_c\cdot\sum_{f\in F(c)}\phi_f\hat{M}_f=-\sum_{c\in\Omega}\mathbf{u}_c\cdot\sum_{f\in F(c)}p_f\hat{\mathbf{n}}_fA_f \tag{2.10}$$
$$+\sum_{c\in\Omega}\mathbf{u}_c\cdot\sum_{f\in F(c)}\mu_f\left[(\mathbf{u}_{nb}-\mathbf{u}_c)\frac{A_f}{\delta d_f}+\nabla^{\intercal}\mathbf{u}_f\cdot\hat{\mathbf{n}}_fA_f\right]+\sum_{c\in\Omega}\mathbf{u}_c\cdot\mathbf{S}_cV_c.$$

The detailed analysis of the pressure term in Eq. 2.10 is simplified by introducing an identity involving combinations of interpolation and differentiation operators. The relation, first presented by Morinishi et al. [21] and restated in finite-volume form by Felten and Lund [22], reads

$$\varphi_c \sum_{f\in F(c)} \bar{\psi}_f Q_f + \psi_c \sum_{f\in F(c)} \bar{\varphi}_f Q_f = \sum_{f\in F(c)} \widehat{\varphi\psi} Q_f + (\varphi_c \psi_c) \sum_{f\in F(c)} Q_f, \tag{2.11}$$

where φ and ψ are two general variables, Q_f is a general quantity known on the cell face, i.e., no interpolation is needed, the overbars refer to interpolated values, and $\widehat{\varphi\psi} = \frac{1}{2}(\varphi_c \psi_{nb} + \varphi_{nb}\psi_c)$ is a special interpolator operator for products.
Specifying the above identity to the pressure term by taking $\varphi = \mathbf{u}$, $\psi = p$ and $Q_f = \hat{\mathbf{n}}_f A_f$, and using Eq. 1.27 to simplify the expression, results in the following relation

$$\begin{aligned}\sum_{c\in\Omega} \mathbf{u}_c \cdot \sum_{f\in F(c)} p_f \hat{\mathbf{n}}_f A_f &= \sum_{c\in\Omega} \sum_{f\in F(c)} \widehat{\mathbf{u}p} \cdot \hat{\mathbf{n}}_f A_f - \sum_{c\in\Omega} p_c \sum_{f\in F(c)} \frac{\Delta t}{\rho_f} \left[(p_{nb} - p_c) \frac{A_f}{\delta d_f} \right] \\ &+ \sum_{c\in\Omega} p_c \sum_{f\in F(c)} \frac{\Delta t}{2} \left[\frac{1}{\rho_c V_c} \sum_{f\in F(c)} p_f \hat{\mathbf{n}}_f A_f + \frac{1}{\rho_{nb} V_{nb}} \sum_{f\in F(nb)} p_f \hat{\mathbf{n}}_f A_f \right] \cdot \hat{\mathbf{n}}_f A_f. \end{aligned} \tag{2.12}$$

Finally, noticing that interior fluxes in Eq. 2.12 cancel out, Eq. 2.10 can be rewritten as

$$\begin{aligned}&\sum_{c\in\Omega} \frac{d(\frac{1}{2}\rho_c \mathbf{u}_c \cdot \mathbf{u}_c)}{dt} V_c + \sum_{c\in\Omega} \mathbf{u}_c \cdot \sum_{f\in F(c)} \phi_f \hat{M}_f = \\ &- \sum_{f\in F(\partial\Omega)} \frac{1}{2} \left(\mathbf{u}_a p_f + \mathbf{u}_f p_a \right) \cdot \hat{\mathbf{n}}_f A_f + \sum_{c\in\Omega} p_c \sum_{f\in F(c)} \frac{\Delta t}{\rho_f} \left[(p_{nb} - p_c) \frac{A_f}{\delta d_f} \right] \\ &- \sum_{c\in\Omega} p_c \sum_{f\in F(c)} \frac{\Delta t}{2} \left[\frac{1}{\rho_c V_c} \sum_{f\in F(c)} p_f \hat{\mathbf{n}}_f A_f + \frac{1}{\rho_{nb} V_{nb}} \sum_{f\in F(nb)} p_f \hat{\mathbf{n}}_f A_f \right] \cdot \hat{\mathbf{n}}_f A_f \\ &+ \sum_{c\in\Omega} \mathbf{u}_c \cdot \sum_{f\in F(c)} \mu_f \left[(\mathbf{u}_{nb} - \mathbf{u}_c) \frac{A_f}{\delta d_f} + \nabla^{\mathsf{T}} \mathbf{u}_f \cdot \hat{\mathbf{n}}_f A_f \right] + \sum_{c\in\Omega} \mathbf{u}_c \cdot \mathbf{S}_c V_c, \end{aligned} \tag{2.13}$$

which states that in the absence of viscosity ($\mu = 0$) and source terms, the change in kinetic energy is due to the fluxes through the boundary of the domain plus a kinetic energy error related to the pressure term. This error is intrinsic to the collocated formulation, and results from the different pressure gradient evaluations in Eqs. 1.21 and 1.24 necessary to evaluate velocities at centers of cells and mass fluxes at time $n+1$, respectively. This result is related to the symmetries of discrete operators by noticing that the different pressure gradient evaluations do not respect the relation $\mathbf{M} = -\mathbf{G}^*$. Moreover, as further discussed in Sec. 2.3, an additional error appears if the convection scheme ϕ_f is not skew-symmetric.
In order to complete the analysis, it is important to evaluate the scaling order of the kinetic energy pressure error, since it can not be eliminated. In this regard, the error is easily analyzed

when simplifying it for each individual face f as

$$\Delta t A_f \left[\frac{(p_{nb} - p_c)}{\rho_f \delta d_f} - \frac{1}{2} \left(\sum_{f \in F(c)} \frac{p_f \hat{\mathbf{n}}_f A_f}{\rho_c V_c} + \sum_{f \in F(nb)} \frac{p_f \hat{\mathbf{n}}_f A_f}{\rho_{nb} V_{nb}} \right) \cdot \hat{\mathbf{n}}_f \right], \tag{2.14}$$

showing that the total term depends on the density ratio between the two cells adjacent to the face, ρ_c/ρ_{nb}, and is multiplied by time step Δt, and face surface A_f. Hence, the pressure error is proportional to $\Delta\rho$, while spatially scaled as $\mathscr{O}(\Delta h^2)$ and temporally scaled as $\mathscr{O}(\Delta t)$, although it can be reduced through the use of different temporal integration schemes, $\mathscr{O}(\Delta t^m)$, as proposed by Felten and Lund [22] and studied by Fishpool and Leschziner [23].

2.3 Low-dissipation convection scheme

The finite-volume discretization of the convective operator is carried out by isolating the convection term in Eq. 1.2 and integrating it over the volume of a cell c, Ω_c. Next, divergence theorem is applied to the bordering faces of the cell $f \in F(c)$, and the expression is reduced by identifying the part corresponding to the mass flux as

$$\int_{\Omega_c} \nabla \cdot (\rho \mathbf{u}\mathbf{u})\, dV = \sum_{f \in F(c)} \rho_f \mathbf{u}_f \phi_f \cdot \hat{\mathbf{n}}_f A_f = \sum_{f \in F(c)} \phi_f \hat{M}_f, \tag{2.15}$$

where $\hat{\mathbf{n}}_f$, A_f and $\hat{M}_f$ are the normal outward unit vector, the surface and the mass flow corresponding to face f, respectively, whereas ϕ_f is the value of $\mathbf{u}$ at face f evaluated by a convective numerical scheme. A graphical representation of these parameters is shown in Fig. 2.1.

Many different strategies are available in the literature for the evaluation of ϕ_f. Among them, the symmetry-preserving scheme presents discrete conservation of kinetic energy, although it may result unstable in variable-density regions. Alternatively, the upwind scheme improves numerical stability, however, at expenses of adding artificial dissipation into the discrete system. The solution proposed in this work consists in the hybridization of these two approaches to construct a low-dissipation and low-dispersion convection scheme suitable for turbulent interfacial flow.

In this section, the description of the hybrid convection scheme is detailed in three steps. First, the symmetry-preserving and upwind schemes are presented. Second, the hybridization process is formulated. Finally, the discrete kinetic energy conservation properties of the scheme are theoretically analyzed.

2.3.1 Symmetry-preserving

The symmetry-preserving scheme [14] discretizes the convection term by means of a skew-symmetric discrete operator; i.e., the discrete convective operator satisfies $\mathbf{C}(\rho\mathbf{u}) = -\mathbf{C}(\rho\mathbf{u})^*$.

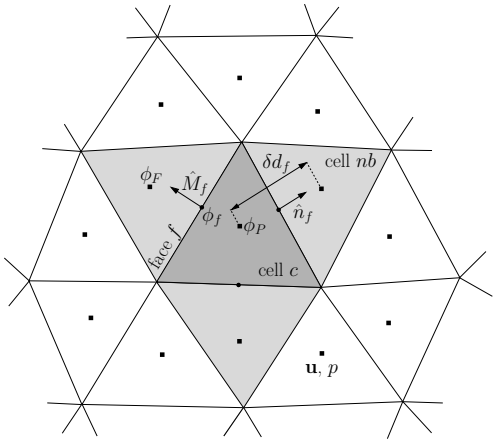

Figure 2.1: Arrangement of variables and notation for the collocated framework and convection scheme on a 2-D unstructured mesh. The schematic representation shows the collocated position of velocity $\mathbf{u}$ and pressure p. The cell c where the discretization is analyzed is shown in dark gray, while the face-neighboring cells nb are depicted in light gray, with an example of normal outward unit vector $\hat{\mathbf{n}}_f$ and distance δd_f between centroids. An example of a face f where the ϕ_f is evaluated, together with the corresponding $\hat{M}_f$, ϕ_P and ϕ_F values, is illustrated.

This particular construction of the convective operator ensures that no artificial dissipation is introduced into the discrete system of equations by the convection term. This property is fundamental if turbulence dominates the physics of the problems under consideration. Indeed, in the absence of source terms, kinetic energy should only be dissipated by viscous forces. Therefore, discretization strategies with excessive numerical dissipation can significantly alter the physics of the flow.
In order to construct a discrete skew-symmetric convective operator, ϕ_f must be evaluated as

$$\phi_f = \frac{\phi_P + \phi_F}{2}, \tag{2.16}$$

where ϕ_P and ϕ_F correspond to the values of $\mathbf{u}$ at the neighboring cells of face f; see Fig. 2.1. As demonstrated in Sec. 2.4.2, this convection scheme is first-order accurate on 3-D unstructured meshes, while it increases its accuracy to second-order on Cartesian grids. Higher-order versions of this scheme are available [14]. However, for the ease of exposition, the hybrid scheme will be presented in terms of the first-order version.

2.3.2 Upwind

The upwind scheme [18] approximates the convection term by a diagonally-dominant positive real discrete operator; i.e., the entries in the i'th row and j'th column, c_{ij}, of matrix $\mathbf{C}(\rho\mathbf{u})$ are $|c_{ii}| \geq \sum_{j\neq i}|c_{ij}|$ for all i, and $\mathbf{z}^{\mathsf{T}}\mathbf{C}(\rho\mathbf{u})\mathbf{z} > \mathbf{0}$ for all nonzero real vector $\mathbf{z}$. This type of convective operator has a slowing-down effect on the discrete flow solutions by adding artificial dissipation, irrespective of grid irregularity, into the problems. This property is not desirable for the correct resolution of turbulence, but may be of key importance to mitigate the growth of spurious currents near interfaces, and therefore stabilize the calculation.
In particular, the upwind scheme considered is constructed by adding a dissipative term into the previous symmetry-preserving expression. This is mathematically formulated as

$$\phi_f = \frac{\phi_P + \phi_F}{2} - \frac{|\hat{M}_f|}{\hat{M}_f}\frac{\phi_F - \phi_P}{2}, \tag{2.17}$$

where $\hat{M}_f$ is the outward-oriented mass flow at face f; see Fig. 2.1. The accuracy of this upwind scheme is also first-order on 3-D unstructured meshes and second-order on Cartesian grids.

2.3.3 Hybridization

The final step is the formulation of the schemes hybridization. Briefly, ϕ_f is evaluated according to the symmetry-preserving scheme, Eq. 2.16, for all the faces of the mesh, except for those adjoining at least one cell containing an interface, where the stabilizing scheme, Eq. 2.17, is activated. This hybrid operator can be expressed in a single equation as

$$\phi_f = \frac{\phi_P + \phi_F}{2} - \alpha_f\frac{|\hat{M}_f|}{\hat{M}_f}\frac{\phi_F - \phi_P}{2}, \tag{2.18}$$

where α_f is a coefficient that takes value 1 for the set of faces belonging at least to one cell containing an interface, and takes value 0 otherwise; see Fig. 2.2.
At this point is where the interface-capturing method is utilized since it is a natural interface sensor. Remember that Eq. 1.6 locates the transient position of the interface by means of scalar values corresponding to the phase k volume fraction within each cell. Therefore, the C_k scalar field itself can be directly used to identify the faces that belong to cells containing an interface. In a mathematical form, this is expressed as

$$\alpha_{f\in F(c)} = \begin{cases} 1 & \text{if } 0 < C_k[c,t] < 1, \\ 0 & \text{otherwise,} \end{cases} \tag{2.19}$$

where $\alpha_{f\in F(c)}$ corresponds to the values of α_f for the faces of cell c, and $C_k[c,t]$ is the volume-fraction value of phase k within cell c at time instant t. Depending on the interface-capturing method chosen, the hybridization will be activated on a smaller or larger band. For

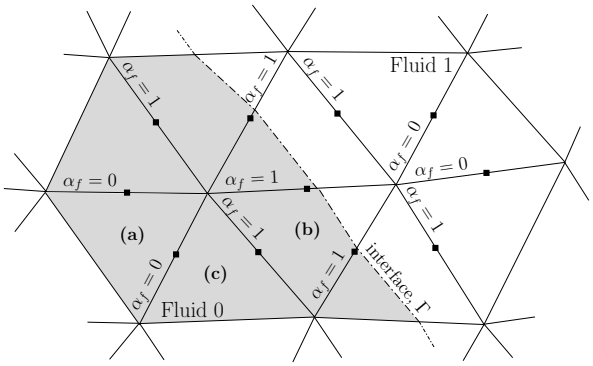

Figure 2.2: Example of the values taken by α_f at different faces according to the interface position when using the VOF method as interface capturer.

instance, if using the VOF method, only the faces of the cells containing an interface will assume $\alpha_f = 1$, as in the example shown in Fig. 2.2. Differently, when using the LS method, the hybridized region will be wider, coinciding with the variable-density zone around Γ with thickness controlled by parameter ε in Eq. 1.9.

2.3.4 Convective kinetic energy conservation

The diagonal elements of the discrete convective matrix, $\mathbf{C}(\rho\mathbf{u})$ of dimension $m \times m$, corresponding to the hybrid symmetry-preserving upwind scheme are

$$c_{ii} = \sum_{f \in F(i)} \frac{1}{2}\left(\hat{M}_f + \alpha_f |\hat{M}_f|\right) \qquad \forall i = 1, ..., m, \tag{2.20}$$

whereas the off-diagonal elements equal

$$c_{ij} = \frac{1}{2}\left(\hat{M}_{ij} - \alpha_{ij} |\hat{M}_{ij}|\right), \tag{2.21}$$

in the case of existing face-connectivity between cells i and j, while are null otherwise. The distribution of the matrix $\mathbf{C}(\rho\mathbf{u})$ eigenvalues on the real-imaginary plot is based on the following proposition.

Proposition 1. *The eigenvalues of a symmetric positive matrix (with real entries) are positive real, and the eigenvalues of a skew-symmetric matrix are pure imaginary.*

As exemplified in Fig. 2.3, three different situations may be encountered, corresponding to the cells labeled as **a**, **b** and **c** in Fig. 2.2. First, in the case of a cell i located far from

an interface, e.g., cell **a**, α_f equals 0 for all its faces and ρ is constant. Consequently, the following result is obtained from the finite-volume discretization of the continuity equation on the cell

$$\int_{\Omega_i} \nabla\cdot\mathbf{u}\, dV = \sum_{f\in F(i)} \mathbf{u}_f\cdot\hat{\mathbf{n}}_f A_f = \frac{1}{\rho}\sum_{f\in F(i)} \rho\mathbf{u}_f\cdot\hat{\mathbf{n}}_f A_f = \frac{1}{\rho}\sum_{f\in F(i)} \hat{M}_f = 0. \tag{2.22}$$

Therefore, Eqs. 2.20 and 2.21 reduce to

$$c_{ii} = 0 \quad \text{and} \quad c_{ij} = \frac{1}{2}\hat{M}_{ij}. \tag{2.23}$$

The resulting submatrix is skew-symmetric, in consequence, it follows from Prop. 1 that its eigenvalue lies on the imaginary axis: $\lambda_i^C \in \mathbb{I}$. Second, considering the case of a cell i containing an interface, e.g., cell **b**, it is straightforward from Fig. 2.2 that α_f is 1 for all its faces, and consequently Eqs. 2.20 and 2.21 are rewritten as

$$c_{ii} = \sum_{f\in F(i)} \frac{1}{2}\left(\hat{M}_f + |\hat{M}_f|\right) \quad \text{and} \quad c_{ij} = \frac{1}{2}\left(\hat{M}_{ij} - |\hat{M}_{ij}|\right), \tag{2.24}$$

which is a diagonally-dominant positive submatrix. Thus, under the hypothesis of Prop. 1, the eigenvalue of the submatrix is positive real: $\lambda_i^C \in \mathbb{R}^+$. Third, in a situation where the faces of a cell i take different values of α_f, e.g., cell **c**, it is direct from the two previous cases that the eigenvalue of the corresponding submatrix lives on the positive real part of the complex numbers: $\lambda_i^C \in \mathbb{C} \mid \Re(\lambda_i^C) \in \mathbb{R}^+$.

The location of the eigenvalues on the real-imaginary diagram has direct relation with the discrete conservation of kinetic energy. In particular, the transport equation for kinetic energy, $\frac{1}{2}\rho\mathbf{u}\cdot\mathbf{u}$, is derived from the momentum equation, Eq. 1.2, by taking the velocity dot product. Hence, multiplying the convection term, expressed in discrete matrix operators, by the velocity vector $\mathbf{u}$ and taking into account the definition of eigenvalue, i.e., $\mathbf{C}(\rho\mathbf{u})\mathbf{u} = \lambda^C\mathbf{u}$, results in

$$[\mathbf{C}(\rho\mathbf{u})\mathbf{u}]\cdot\mathbf{u} = \left[\lambda_i^C\mathbf{u}_i\right]\cdot\mathbf{u}_i \qquad \forall i = 1,...,m. \tag{2.25}$$

Then, depending on the value taken by λ_i^C, the vector $\lambda_i^C\mathbf{u}_i$ is: (1) if $\lambda_i^C \in \mathbb{I}$, just a rotation of vector $\mathbf{u}_i$ around its axis; (2) if $\lambda_i^C \in \mathbb{R}^+$, a deformation of vector $\mathbf{u}_i$ without direction change; or (3) if $\lambda_i^C \in \mathbb{C} \mid \Re(\lambda_i^C) \in \mathbb{R}^+$, a combination of the two previous cases. Consequently, the variation of kinetic energy due to the convection term, written as

$$\mathbf{u}_i\cdot\mathbf{u}_i - \left[\lambda_i^C\mathbf{u}_i\right]\cdot\mathbf{u}_i, \tag{2.26}$$

is zero for case (1), nonzero for case (2) and between zero and a nonzero value for case (3). Therefore, there is no dissipation of kinetic energy by the convection term if an eigenvalue lies on the imaginary axis, while, if it lives on the positive real part of the complex numbers and

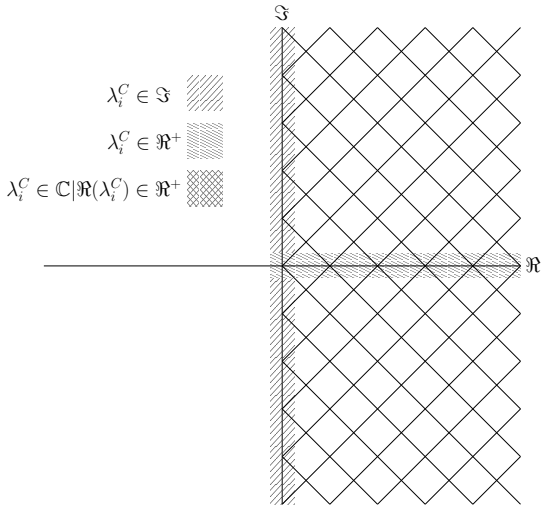

Figure 2.3: Distribution on the real-imaginary diagram of the eigenvalues corresponding to the discrete convective matrix. Three different cases are depicted depending on the values taken by α_f.

$\lambda_i^C < 1$, the convection term adds dissipation into the discrete system and, more important, is of positive sign, i.e., acts as a kinetic energy reliever. In conclusion, the use of the hybrid scheme confines kinetic energy dissipation to the subgroup of cells close to the interfaces. It is worth stressing that this dissipation depends on the interface-capturing method chosen. For instance, given the wider extension of the interface region, the LS method presents larger dissipation than the VOF approach.

2.4 Numerical tests

Four different tests are considered for analyzing the properties of the low-dissipation and low-dispersion method proposed. First, kinetic energy conservation properties are assessed by numerically resolving the evolution of a 3-D vortex. Second, an accuracy assessment is presented using an exact sinusoidal function. Next, the scheme is tested for cases in which the interface-capturing method is coupled to the equations of fluid motion. Initially, a spherical drop first in equilibrium and later submerged in a swirling velocity field is considered as a case to test the capacity of the model to diminish spurious velocities. Finally, its robustness and accuracy are demonstrated by numerically calculating a two-phase turbulent coaxial jet.

2.4.1 Three-dimensional vortex

The conservation of kinetic energy related to the convection term is analyzed numerically by solving a 3-D vortex with zero net mass flux at the boundaries and no interface advection. The set of 3-D vortices shown in Fig. 2.4 are initially described by

$$\begin{aligned} u &= A cos(kx) sin(ky) sin(kz), \\ v &= -A sin(kx) cos(ky) sin(kz), \\ w &= 0, \end{aligned} \tag{2.27}$$

where $A = 1.0 \times 10^{-3}\ m/s$ is the velocity amplitude and $k = 1$ is the wave number. The vortex is solved in a box of side $2\pi \times 2\pi \times 2\pi$ meshed by means of 6.6×10^4 triangular prisms that correspond to a mesh size of $h = 0.2$. In detail, the 3-D mesh is generated by extruding a 2-D grid — composed of 2.2×10^3 triangles — 30 times with a constant length step. The box is filled with two different fluids. One with density $\rho_1 = 1\ kg/m^3$ occupying the entire cube except for a sphere of diameter $D = \pi$ located in the center of the box. This sphere is filled with a different fluid of density ρ_2. In order to study the properties of the different convection schemes, four different cases are analyzed in which progressively larger density ratios between inner and outer fluids, $\mathbf{r}_\rho = \rho_2/\rho_1$, are considered. In particular, ρ_2 is set to 1, 10, 100 and 1000 kg/m^3. A constant time step of $\Delta t = 1.0 \times 10^{-3}\ s$ is used, and slip-wall conditions are applied to all boundaries.

In the absence of body and interfacial forces, and considering incompressible inviscid flow, i.e., $\nabla \cdot \mathbf{u} = 0$ and $\mu = 0$, the kinetic energy conservation equation, Eq. 2.9, reduces to

$$\frac{\partial(\frac{1}{2}\rho \mathbf{u} \cdot \mathbf{u})}{\partial t} + \nabla \cdot \left[\mathbf{u}(\frac{1}{2}\rho \mathbf{u} \cdot \mathbf{u}) \right] = -\nabla \cdot (p\mathbf{u}). \tag{2.28}$$

It is important to note that this equation is intrinsically conservative, as kinetic energy is just redistributed, not created neither dissipated. Therefore, the rate of change of kinetic energy by the convection term is zero. Similarly, discrete systems will be kinetic energy conservative if the convective and pressure operators are shown to be conservative.

Focusing on the convection term, the test proposed here is appropriate to study its kinetic energy conservation since there is no net mass flux across boundaries. This enables a proper characterization, in terms of rate of change of kinetic energy, of the symmetry-preserving (*sp*), upwind (*uw*) and hybrid symmetry-preserving upwind (*hspu*) convection schemes. In this regard, the norm of the kinetic energy rate of change by the convection term, $|\nabla \cdot \mathbf{u}(\frac{1}{2}\rho \mathbf{u} \cdot \mathbf{u})|$, is calculated at every time step by integrating the convection term in Eq. 2.28 over the entire domain, Ω, transforming it to a summation of integrals for each control volume that form the domain $c \in \Omega$, and using the divergence theorem to simplify the expression as

$$\int_\Omega \nabla \cdot \mathbf{u}(\frac{1}{2}\rho \mathbf{u} \cdot \mathbf{u})\, dV = \frac{1}{2} \sum_{c \in \Omega} \mathbf{u}_c \cdot \sum_{f \in F(c)} \phi_f \hat{M}_f. \tag{2.29}$$

Results are reported in Tab. 2.1 for each scheme, and for increasing values of density ratio between fluids. In all cases, the total rate of change of kinetic energy, $\partial(\frac{1}{2}\rho\mathbf{u}\cdot\mathbf{u})/\partial t$, is determined mainly by the convection term with the pressure contribution, $|\nabla\cdot(p\mathbf{u})|$, negligible. The case of uniform density between fluids shows that the *sp* scheme produces zero variation of kinetic energy. On the contrary, the *uw* scheme introduces dissipation of value $\mathscr{O}(10^{-8})$ into the discrete system, while *hspu* consistently reduces the dissipation to $\mathscr{O}(10^{-9})$ by restricting the stabilization to the interface region. Similar trends are observed when assigning different densities to the fluids. In the case of $\mathbf{r}_\rho = 10$, *sp* results in zero variation (machine precision) of kinetic energy. Conversely, the dissipation introduced is of order $\mathscr{O}(10^{-7})$ for *uw* and $\mathscr{O}(10^{-8})$ for *hspu*, and increases with larger density differences. It is important to notice that, despite its small magnitude, the errors in *sp* slightly increase with the density ratio due to the difficulty of the Poisson solver to reach machine precision.
Results in Tab. 2.1 account for the accumulated variation of kinetic energy by the convection term over the entire domain. However, it is interesting to analyze the particular value for each individual cell. The convection term of the kinetic energy transport equation, Eq. 2.9, can be written in discrete matrix-vector notation by left-multiplying $\mathbf{C}(\rho\mathbf{u})$ by $\mathbf{u}^*$ and summing the resulting expression with its conjugate transpose, resulting in

$$\mathbf{u}^*\left[\mathbf{C}(\rho\mathbf{u})+\mathbf{C}^*(\rho\mathbf{u})\right]\mathbf{u}. \tag{2.30}$$

Next, considering the general expression of the *hspu* convection scheme given by Eqs. 2.20 and 2.21, and accounting for the contribution of each cell c —diagonal elements of the $\mathbf{C}(\rho\mathbf{u})+\mathbf{C}^*(\rho\mathbf{u})$ matrix—, the above equation can be reduced to

$$\mathbf{u}_c\cdot\sum_{f\in F(c)}\left(\hat{M}_f+\alpha_f|\hat{M}_f|\right)\mathbf{u}_c. \tag{2.31}$$

Notice that if α_f is 0 the expression collapses to the *sp* convection scheme, whereas $\alpha_f = 1$ corresponds to the *uw* case.
The mathematical expression introduced is evaluated for the three schemes, and the results are presented in terms of relative error with respect to the values obtained with *sp* as

$$\varepsilon_{\text{conv},x} = \frac{|\left[\partial(\frac{1}{2}\rho\mathbf{u}\cdot\mathbf{u})/\partial t\right]_x - \left[\partial(\frac{1}{2}\rho\mathbf{u}\cdot\mathbf{u})/\partial t\right]_{sp}|}{|\left[\partial(\frac{1}{2}\rho\mathbf{u}\cdot\mathbf{u})/\partial t\right]_{sp}|}, \tag{2.32}$$

with x representing the *uw* or *hspu* convection schemes. Results for $\mathbf{r}_\rho = 100$ are plotted in Fig. 2.5 for the cells laying along a radial direction of the sphere with dimensionless coordinate $\hat{r} = r/R$. The figure corroborate that the *uw* scheme dissipates kinetic energy for all cells with a peak in the variable density region, whereas the *hspu* scheme is conservative, i.e., $\varepsilon_{\text{conv},hspu} = 0$, except for the cells close to the interface ($\hat{r} = 1$) where α_f is activated to 1, and therefore the *uw*-dissipation is introduced. In this region, $\varepsilon_{\text{conv},hspu}$ tends to the $\varepsilon_{\text{conv},uw}$ value.

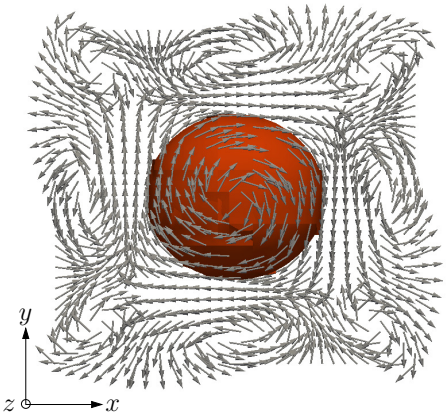

Figure 2.4: 3-D vortex: frontal (*xy*-plane) view of the flow field and interface location. Velocity vectors are displayed in gray while the high-density sphere is shown in orange.

$\mathbf{r}_\rho$	*sp* $\mathscr{O}$(-)	*uw* $\mathscr{O}$(-)	*hspu* $\mathscr{O}$(-)
1	10^{-14}	10^{-8}	10^{-9}
10	10^{-13}	10^{-7}	10^{-8}
100	10^{-12}	10^{-6}	10^{-7}
1000	10^{-11}	10^{-5}	10^{-6}

Table 2.1: 3-D vortex: order of magnitude of kinetic energy variation by the convection term, $|\nabla\cdot\mathbf{u}(\frac{1}{2}\rho\mathbf{u}\cdot\mathbf{u})|$ obtained by using the *sp*, *uw* and *hspu* schemes. The quantity is evaluated for increasingly larger density ratios.

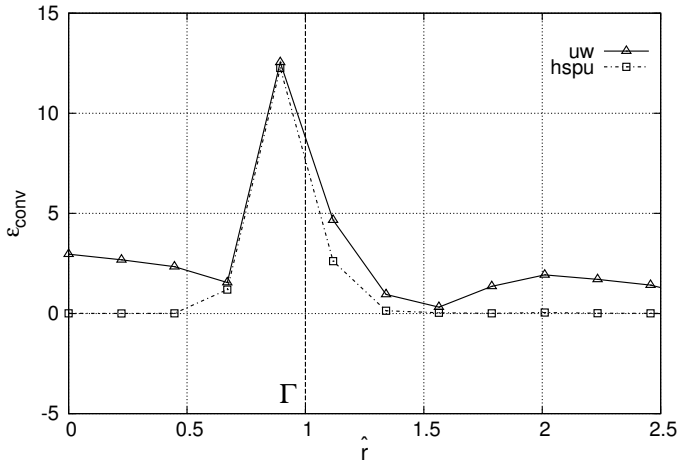

Figure 2.5: 3-D vortex: relative error of convection kinetic energy variation $\varepsilon_{\text{conv}}$ along the cells that lay on the line from the sphere's center to a corner of the domain as a function of dimensionless radius $\hat{r}$. The interface location is indicated by Γ.

2.4.2 Exact sinusoidal function

The spatial accuracy of the hybrid symmetry-preserving upwind (*hspu*) scheme, together with the ones of the symmetry-preserving (*sp*) and upwind (*uw*) schemes, is studied by means of comparing numerical results to the analytical solution of an exact sinusoidal function. On the one hand, for each convection scheme, the numerical values of the convection term on each cell are calculated from the right-hand side of Eq. 2.15, with the corresponding ϕ_f definition, Eqs. 2.16-2.18, by assigning a sinusoidal function to the input variables: (1) velocities at centers of cells $\mathbf{u}_c$, and (2) face mass fluxes at faces $\hat{M}_f$. On the other hand, analytical values are obtained by directly evaluating the left-hand side of Eq. 2.15. Finally, analytical and numerical results are compared by means of the root-square-mean error (rms) x_{rms}, given by

$$x_{rms} = \sqrt{\frac{1}{n}({x_1}^2 + \cdots + {x_n}^2)}, \tag{2.33}$$

where x_i corresponds to each of the n individual errors.
A stream function, determined by $\psi = \frac{1}{2\pi N} sin(2\pi Nx) cos(2\pi Ny)\mathbf{k}$ is utilized in order to ensure that the resulting analytical velocity field is divergence-free. In this way, the derivation

Scheme	Cartesian	Unstructured
sp, *hspu*	2.69	1.53
uw	1.88	1.43

Table 2.2: Order of accuracy of the different convection schemes (*sp*, *uw* and *hspu*) on both mesh types (Cartesian and unstructured).

of ψ, defined as $\mathbf{u} = \nabla \times \psi$, gives the following periodic velocity field

$$\begin{aligned} u &= -sin(2\pi Nx)sin(2\pi Ny), \\ v &= -cos(2\pi Nx)cos(2\pi Ny), \\ w &= 0, \end{aligned} \tag{2.34}$$

which is solved in the three spatial directions and presents a maximum velocity magnitude of one. The test is performed on a cube of side $1.0\times1.0\times1.0$ meshed by means of 9.2×10^3 hexahedral cells (Cartesian mesh) or 9.7×10^3 tetrahedral cells (unstructured mesh). Similarly to the previous test, Sec. 2.4.1, fluid with density $\rho_1 = 1\ kg/m^3$ occupies the entire cube except for a sphere of radius $R = 0.15$, which is fixed in the center of the domain and filled with a fluid of density $\rho_2 = 1000\ kg/m^3$.
In addition, instead of using meshes with different resolutions, the convergence study is performed by enlarging or reducing the wavelength of the input sine functions, and consequently the radius of the centered sphere. In this way, the average mesh volume for both Cartesian and unstructured grids is calculated as $V_{avg} = \frac{1}{c}\sum_c V_c$, giving an average mesh spacing equal to $\Delta X_{avg} = \sqrt[3]{3V_{avg}} = 0.068$, whereas the effective length of the domain is defined as $L_{eff} = 1/N$, being N a variable integer value that is increased or decreased in order to enlarge or refine the effective mesh, respectively. In consequence, the relative mesh size is defined as $h = \Delta X_{avg}/L_{eff} = 0.068N$.
Convection accuracy errors are obtained for relative mesh sizes ranging from ≈ 0.1 to ≈ 0.5 and depicted in Fig. 2.6 — notice that results for the *sp* and *hspu* convection schemes are plotted with a single line since they are practically identical. The figure shows that, first, given a particular type of grid, *uw* errors are larger than *sp* and *hspu* ones for all relative mesh sizes, and second, for each convection scheme, errors are smaller on the Cartesian grid than on the unstructured one. Moreover, the order of accuracy of the different convection schemes have been calculated and collected in Tab. 2.2. These show that the three schemes are second-order accurate on Cartesian grids, while first- to second-order on unstructured meshes.

2.4.3 Spurious velocities around a spherical drop

In order to analyze the capability of the numerical framework to prevent, or diminish, spurious velocities, the test case of a drop first in equilibrium and later submerged in a swirling

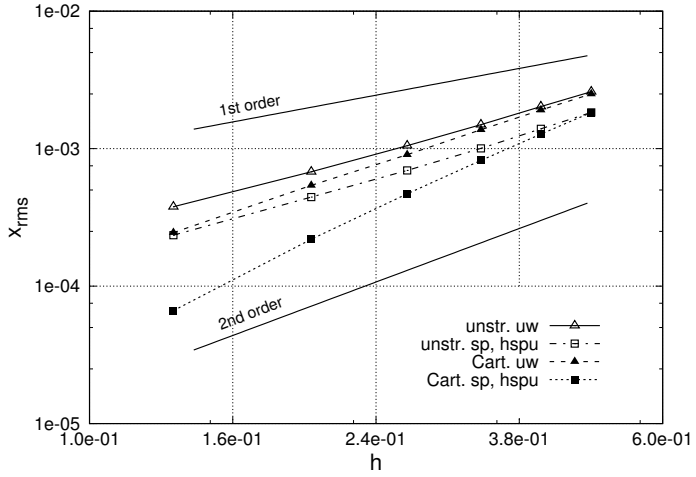

Figure 2.6: Exact sinusoidal function: convection scheme error x_{rms} versus relative mesh size h for the different convection schemes (*sp*, *uw* and *hspu*) and mesh types (Cartesian and unstructured). First- and second-order slopes are also indicated.

velocity field is considered. The drop is subjected to surface tension forces while gravity effects are neglected.

The set-up of the test is similar to the one proposed in Sec. 2.4.1. However, in this case the interface separating the two fluids is set free by coupling the VOF solver [24, 25] to the Navier-Stokes equations. In particular, a spherical drop of diameter $D = \pi$ is fixed in the center of a cubic domain of side 2π. Four different cases are analyzed corresponding to increasingly larger density ratio values $\mathbf{r}_\rho$. The surrounding fluid is of constant density $\rho_1 = 1\ kg/m^3$, while the density of the drop ρ_2 is set to 1, 10, 100 and 1000 kg/m^3. Dynamic viscosity μ and gravity $\mathbf{g}$ are set to zero. Contrarily, the surface tension force, as introduced in Eq. 1.3, is characterized by a surface tension coefficient $\sigma = 7.3\ N/m$, and by a curvature κ equal to $2/R$ in the case of a 3-D sphere. For the discretization of surface tension, a model based on the continuum surface force approach [26] is chosen. Therefore, for each cell c located at the interface, the surface tension is approximated as

$$\mathbf{T}_\sigma^c = \sigma\kappa \left(\frac{\nabla C_k}{\|\nabla C_k\|} \right)_c V_c, \tag{2.35}$$

where $\nabla C_k / \|\nabla C_k\|$ is the normalized gradient of the volume fraction scalar field C_k — in this case of the scalar field defining the surrounding fluid —, and V_c is the volume of the cell. A detailed description of the discretization of this force on 3-D unstructured meshes can be found in [27, 28, 29].

The domain is meshed exactly as in the 3-D vortex case: 6.6×10^4 triangular prisms, generated by extruding 30 times a 2-D grid discretized in 2.2×10^3 triangles. Once more, the time step is chosen to be $\Delta t = 1.0 \times 10^{-3}$ s and velocity free-slip conditions are imposed at X, Y and Z boundaries.

The test is initialized with a zero velocity field for each of the three convection schemes analyzed: symmetry-preserving (*sp*), upwind (*uw*) and hybrid symmetry-preserving upwind (*hspu*). Under these conditions, the velocity field along time should remain undisturbed, i.e., $\mathbf{u} = 0$. However, due to the appearance of spurious velocities at the cells located close to the interface, this is not the numerical solution obtained. Therefore, in order to measure the error in velocity, the following L_1 error norm is utilized

$$L_1(\mathbf{u}) = \frac{1}{n}\left(\|\hat{\mathbf{u}}_1\| + \cdots + \|\hat{\mathbf{u}}_n\|\right), \tag{2.36}$$

where $\hat{\mathbf{u}}_i$ corresponds to each of the n cell dimensionless velocities, evaluated as $\hat{\mathbf{u}}_i = \mathbf{u}_i\sqrt{\rho_2 D/\sigma}$. The velocity L_1 errors for each convection scheme and density ratio are plotted in Fig. 2.7 versus dimensionless time $\hat{t} = t\sqrt{\sigma/(\rho_2 D^3)}$. As expected, for all cases, spurious velocities originate at cells located at the interface between fluids, and continuously propagate to the neighboring elements as time advances. Independently of the magnitudes, errors start at a zero value and increase with time for the three convection schemes. However, there is a clear difference between *sp* and *uw* and *hspu* errors. In the case of uniform density, $\mathbf{r}_\rho = 1$, the error for *sp* rapidly increases for $\hat{t} < 0.4$ first, and then continues smoothly increasing since no dissipation is introduced into the discrete solution to limit the spurious velocities. On the contrary, for the *uw* and *hspu* schemes, the magnitude of the spurious currents stalls at $\hat{t} \simeq 0.2$ due to their low-dispersion characteristics. The contrast in behavior among the convection schemes significantly differs as the density ratio between fluids is increased. For example, for $\mathbf{r}_\rho = 1000$, the error magnitude for *uw* and *hspu* schemes is $\mathscr{O}(10^{-4})$, while it diverges for *sp*.

In order to assess the stabilization in a more realistic scenario, the spherical drop is introduced into the 3-D vortex velocity field described in Sec. 2.4.1. To impose a fast shape deformation, ρ_2 and A are set to 100 kg/m^3 and 1.0×10^{-1} m/s, respectively. In addition, the grid is refined to size $h = 0.1$. Results for the three convective schemes are shown in Fig. 2.8, and correspond to the evolution of the initial drop as dimensionless time $\hat{t} = tA/D$ advances. The figure clearly demonstrates the inability of the *sp* scheme to retain the shape of the deforming sphere due to the appearance of large spurious velocities at the surface. Differently, the solutions obtained with the *uw* and *hspu* are stable and qualitatively very similar —therefore, the transient evolution of the drop is shown by a unique sequence of snapshots. This result highlights the capability of the hybrid scheme to diminish spurious velocities around the interface, and therefore properly advect the surface separating the fluids. Particularly for this test, given the absence of turbulent motions, the two schemes provide a similar solution.

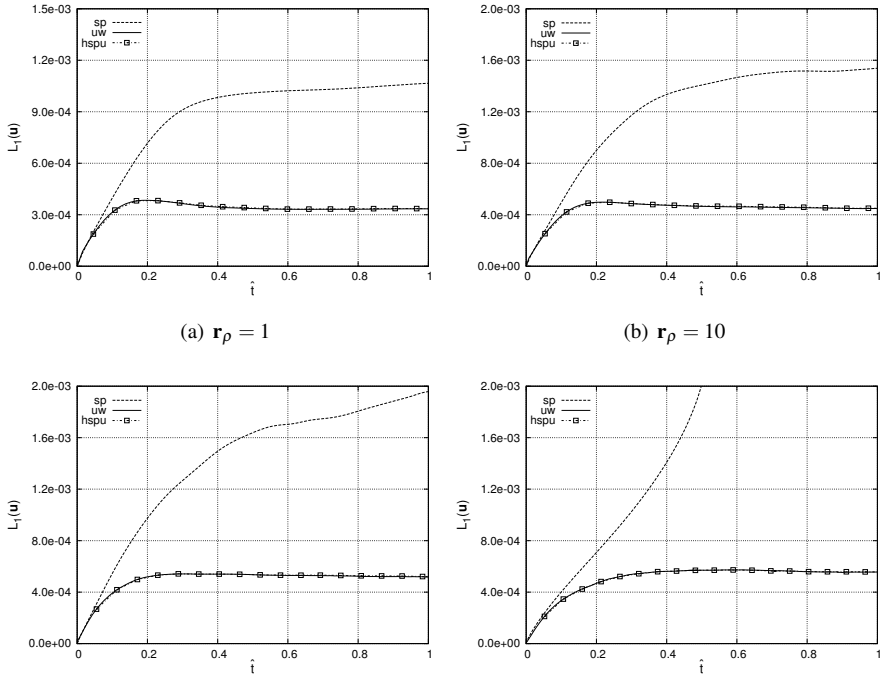

(a) $\mathbf{r}_\rho = 1$ (b) $\mathbf{r}_\rho = 10$

(c) $\mathbf{r}_\rho = 100$ (d) $\mathbf{r}_\rho = 1000$

Figure 2.7: Spherical drop in equilibrium: velocity errors L_1 versus dimensionless time $\hat{t}$ for the three convection schemes analyzed (*sp*, *uw* and *hspu*) and for increasingly larger density ratios $\mathbf{r}_\rho$.

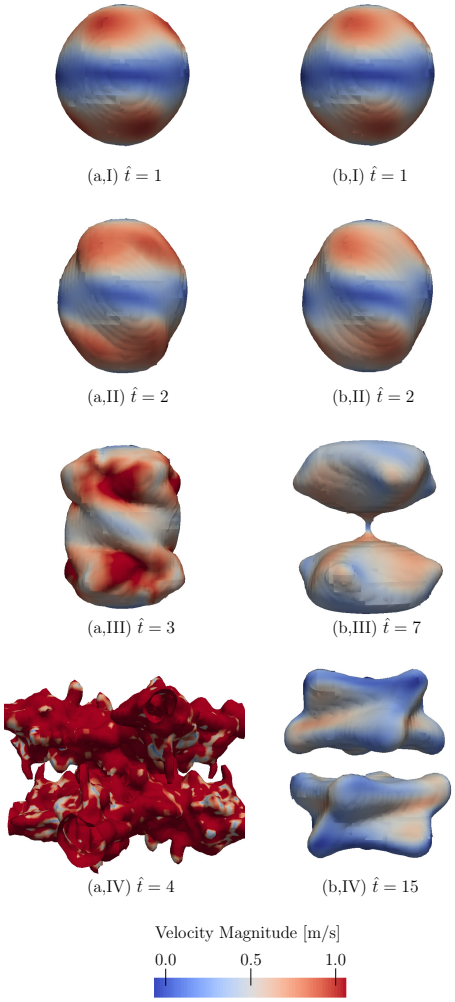

Figure 2.8: Spherical drop under swirling action: time evolution (top to bottom) of the sphere for the *sp* (left), *uw* and *hspu* (right) convection schemes. The interface is colored according to the velocity magnitude.

	U_i[m/s]	ρ_i[kg/m^3]	μ_i [Pa·m]	σ [N/m]	Re$_i$	We$_i$
liquid	20	1000	5×10^{-4}	0.03	16000	5332
gas	100	100	1.7×10^{-5}		235000	13000

Table 2.3: Atomization of a two-phase jet: liquid and gas physical properties and dimensionless parameters.

2.4.4 Atomization of a turbulent two-phase jet

In order to assess the capability of the *hspu* scheme to numerically simulate interfacial turbulent flow, the atomization of a two-phase jet is studied. The computational set-up is validated first by comparing against results reported by Fuster et al. [13]. Next, the advantages led by the adoption of the *hspu* scheme over the *uw* and *sp* are discussed.

Description of the case

The problem consists in the injection of two parallel high-speed streams of liquid l and gas g into an initially quiescent domain. A schematic representation of the jet evolution and geometrical dimensions are depicted in Fig. 2.9. Two dimensionless parameters characterize the problem. The Weber (We) number quantifies the ratio between fluid inertia and surface tension forces, while the Reynolds (Re) number accounts for the ratio of fluid inertia over viscous forces. For each fluid i, these are defined as

$$\text{We}_i = \frac{\rho_i U_i^2 D}{\sigma} \qquad \text{Re}_i = \frac{\rho_i U_i D}{\mu_i}, \tag{2.37}$$

where U_i is the inlet streamwise velocity, D is the liquid jet diameter, and σ is the surface tension coefficient. The physical properties of the fluids, namely ρ_i, μ_i and σ, as well as the resulting dimensionless parameters are reported in Tab. 2.3. Both fluids are injected with constant streamwise velocities starting from the left domain boundary. In addition, triggering of the instabilities responsible for transitioning from laminar to turbulent regime is forced by assigning a random cross-stream velocity to the liquid phase at the inlet, with magnitude $V_l = [-0.1U_l : 0.1U_l]$. Finally, pressure is imposed at outlet such that appropriate outflow boundary conditions are obtained.

The first stages of the jet atomization are shown in Fig. 2.10 as function of dimensionless time tU_l/D. Zoomed figures (a) and (b) show the initial injection stages of the liquid jet. Figures (c) and (d) exhibit the appearance of interface instabilities that cause the formation and rupture of ligaments and the early spreading of droplets. Finally, jet swirling oscillation behavior is depicted in figures (e) and (f). These concatenated phenomena are comprehensively analyzed in the following subsections.

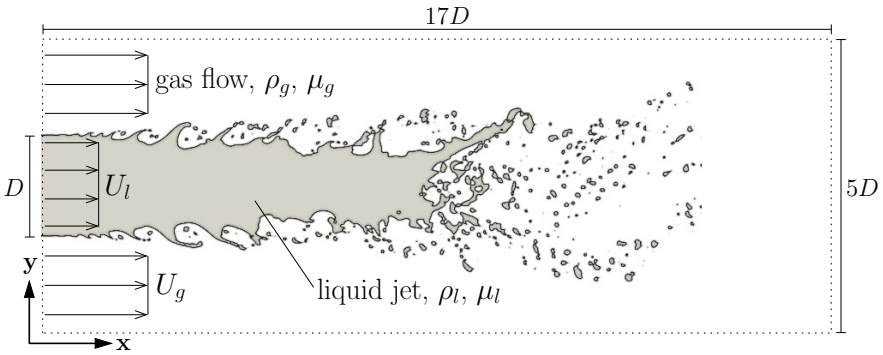

Figure 2.9: Atomization of a two-phase jet: schematic representation of the liquid jet test indicating the flow configuration and geometrical parameters.

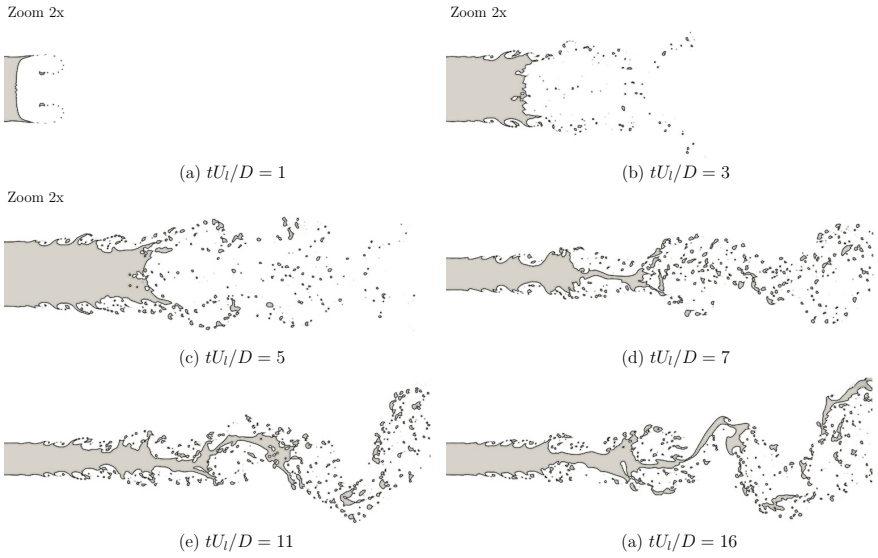

Figure 2.10: Atomization of a two-phase jet: initial stages of the liquid atomization process.

Numerical method

As indicated in the introduction, the low-dissipation convective scheme presented can be coupled to different interface-capturing methods. In order to demonstrate this capability, and motivated by a significant reduction in computational cost, the interface motion in this test is solved by means of the LS method. Additionally, in order to reduce the computational requirements, the adaptive mesh refinement (AMR) strategy presented in Chapter 3 is employed. As shown in Fig. 2.12 (Zoom B), the strategy consists in a dynamic refinement of the baseline mesh at the interfacial region. This refinement is essential for capturing physical phenomena occurring at scales smaller than the initial mesh size, such as thin filaments or small drops. The base mesh is a uniform Cartesian grid with $\approx 5.0 \times 10^4$ cells. For this test, two levels of mesh refinement are utilized, i.e., the parent cell is divided at most into 16 sub-cells. Thus, at statistical steady-state conditions, the mesh reaches an average size of $\approx 2.3 \times 10^5$ elements, instead of the $\approx 8.2 \times 10^5$ elements that would be needed on a static mesh to obtain the same resolution. The refinement level is chosen after carrying out preliminary tests to determine the minimum mesh size necessary to obtain an acceptable convergence of the solution to the benchmark. Further details on the application of the AMR strategy to the jet atomization problem can be found in previous works [30, 31].

Validation and results

The case is discretely solved by utilizing the three convection schemes considered in this work: *sp*, *uw* and *hspu*. The first important outcome is that the *sp* scheme is not able to complete the calculation. Indeed, as previously demonstrated in Sec. 2.4.3, the inability of the scheme to contain spurious currents originated at the interface, results in the divergence of the numerical simulation in few time steps. On the other hand, calculations performed with the *uw* and *hspu* schemes are stable and their results are discussed below.

First, the use of the *hspu* convection scheme is validated by comparing the discrete results to the numerical data reported in [13]. For instance, Fig. 2.11 shows the comparison of the time-averaged energy of the cross-stream normal velocity fluctuations $E_{v'} = (v')^2$ normalized by its inlet value $E_0 = (U_l)^2$. In particular, the figure shows the $E_{v'}/E_0$ profiles for three different inlet distances x/D. Due to the symmetry in geometry, only the profiles corresponding to the top-half part of the domain are represented. The results are compared to the same magnitudes measured in [13]. Regarding the first two distances, $x/D = 1.25$ and $x/D = 1.9$, present solution and benchmark match closely, thus, demonstrating a similar mechanism in the early growth of perturbations. At $x/D = 3.1$, where the process of disruption of the interface has taken place, despite showing an overall good agreement, the solutions result more distant. This is probably due to the different local definition of the mesh used in the representation of interface phenomena, that leads to a slightly different phenomenology of the unstable structure appearing after the core break-up.

The appearance of Kelvin-Helmholtz (KH) instabilities at the interface is due to the competi-

tion between shear forces, caused by the velocity difference of the two streams, and capillary stresses. This is in agreement with the reference work [13] and other studies regarding two-phase coaxial jets [32, 33, 34]. The KH instabilities are responsible for triggering the jet transition from laminar to turbulent regime. This phenomenon is captured by the intact jet profiles, $x/D = 1.25$ and 1.9, shown in Fig. 2.11, since E_i progressively rises in the interface proximity. In this zone, the fluctuations cause the appearance of waves at the interface that quickly grow, amplify and roll-up, breaking the interface and spreading droplets downstream, as shown in Fig. 2.12 (Zoom A). The increase of the instability continues downstream, as the fluctuations are gradually transferred to the bulk of the fluids. Finally, perturbations cause the complete break-up of the liquid core, that fragments into droplets of several different sizes. The evolution of these physical mechanisms is depicted in Fig. 2.12.
The results obtained with the *uw* convection scheme are depicted in Fig. 2.13 where they are compared to *hspu* data. In detail, the figures compare the cross-stream kinetic energy of velocity fluctuations at entrance lengths $x/D = 1.25$ and 1.9. $E_{v'}$ evaluated with *uw* is slightly lower than *hspu*, due to the dissipative nature of the method, which causes a partial attenuation of kinetic energy also in the core of the liquid phase. However, results are comprehensibly similar, demonstrating an equivalent representation of the KH instability mechanism for the two schemes. As it will be demonstrated in the next subsection, Sec 2.4.4, this similarity in behavior is not encountered for the energy spectra of the downstream turbulent region.

Energy spectra

Following the complete breakdown of the liquid-phase core, a downstream turbulent dispersion of droplets is observed. After ≈ 60 dimensionless time units tU_l/D, the two-phase dispersed system reaches a statistical steady state regime with the overall wake fluctuating under a constant vortex shedding frequency f_{VS}. In this context, the analysis of the flow energy spectrum allows a more complete knowledge of its turbulent behavior and a further verification of the *hspu* scheme. The spectra have been calculated from the time series of the vertical velocity v over a large exhibition period of ≈ 25 shedding cycles.
The velocity probes are located at different inlet distances x/D, and at a vertical position equal to the inlet interface y-axis value y_{int}. This vertical position of the probes ensures a better capturing of the interface fluctuations. A satisfactory description of the jet turbulent behavior can be drawn from the analysis of the results obtained on two probes. The first, S1, is placed in the zone of the earliest interface instabilities ($x/D = 2$), where the disturbances have not yet broken the liquid core, whereas the second, S2, is located at $x/D = 6$, where the core is partially broken and the vortex shedding has begun to drag the structures downstream — see position of the probes in Fig. 2.12.
Segments of the velocity signals collected by the probes at statistical steady state conditions are plotted in Fig. 2.14. The *hspu* velocity signal of probe S1, reported in Fig. 2.14(a), shows much more regular oscillations than the *uw* signal, and a notably higher value of root-mean-square velocity. In the case of probe S2 — see Fig. 2.14(b) —, the *uw* signal fluctuates more

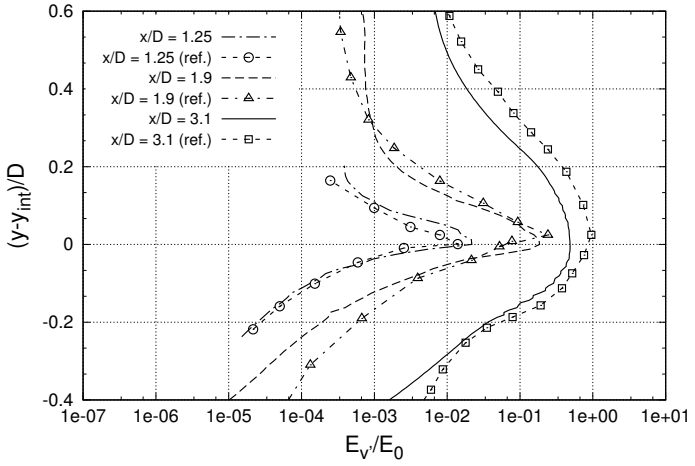

Figure 2.11: Atomization of a two-phase jet: energy of the cross-stream normal velocity fluctuations $E_{v'} = (v')^2$ normalized by its inlet value E_0 and evaluated at different distances from the inlet x/D. Present results are compared to reference data reported in [13]. The *hspu* convection scheme is used to discretize the convection term. Parameter y_{int} corresponds to the value of the interface vertical position at inlet.

strongly, but oscillations are still less regular and energetic than the *hspu* ones.
The described velocity signals are post-processed by using the Lomb periodogram technique [35] to yield the turbulent energy spectra, reported in Fig. 2.15. The plots depict the dimensionless energy of cross-stream velocity fluctuations, $E_{v'}/E_0$, as function of fD/U_l. All the curves are compared to the (-3)-slope, characteristic of the direct energy cascade in 2-D turbulence [36]. Regarding the *hspu* scheme, the spectra show the same dominant peak for both S1 and S2 probes, Figs. 2.15(a) and 2.15(c), corresponding to the vortex shedding Strouhal number $\mathrm{St_{VS}} = f_{\mathrm{VS}}D/U_l = 0.27$. The existence of a strong dominant frequency is confirmed by the appearance of harmonic peaks — up to the third in probe S1, and up to the fourth in probe S2. In probe S1, a peak associated to the KH instability is visible at $f_{\mathrm{KH}}D/U_l \approx 1.0$. Despite being responsible for the laminar to turbulent transition, KH remains embedded in the vortex shedding frequency, and becomes barely distinguishable. The slope of the energy cascade is well represented in both probes.
On the other hand, referring to the *uw* scheme, two energy peaks are detected by both probes, at $\mathrm{St_{VS1}} = 0.24$ and $\mathrm{St_{VS2}} = 0.31$, as shown in Figs. 2.15(b) and 2.15(d). These are responsible for an irregular fluid shedding, previously suggested by the uneven velocity signal shown in Fig. 2.14. Indeed, the dissipative nature of the scheme makes the wake more fragmented and driven by different fluctuation frequencies. Conversely, the foot print of KH instabilities at the interface is well captured by probe S1, at $\mathrm{f}_{KH}D/U_l \approx 0.9$, due to the absence of a strong

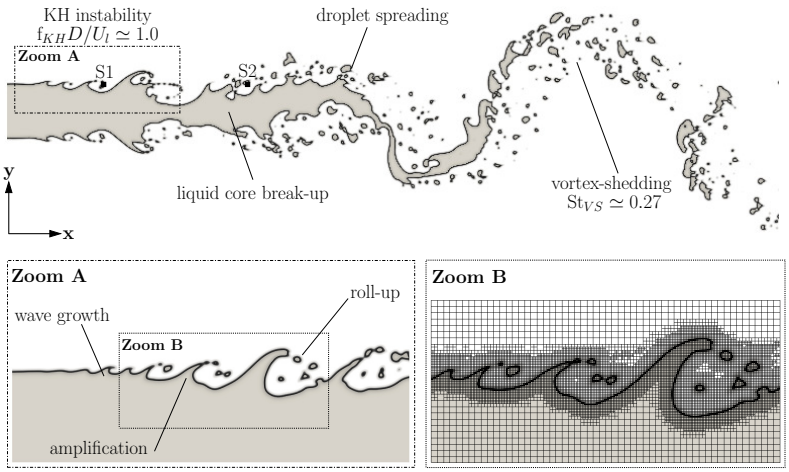

Figure 2.12: Atomization of a two-phase jet: visualization of the primary and secondary stages of the atomization process obtained from the numerical simulation. The position of velocity probes $(S1, S2)$ is indicated. In Zoom A, a detail of the waves evolution at the interface is shown. Zoom B is an example of the refined mesh achieved with the AMR strategy at the interface.

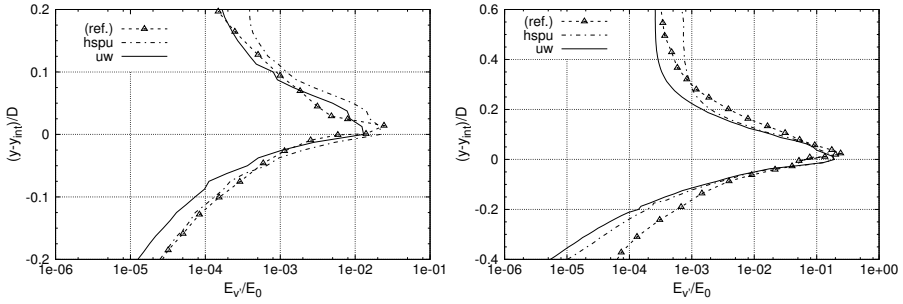

(a) x/D=1.25 (b) x/D=1.9

Figure 2.13: Atomization of a two-phase jet: energy of the cross-stream normal velocity fluctuations $E_{v'}/E_0$ measured at different distances from the inlet x/D using the *uw* and *hspu* convection schemes. Results are compared to numerical data reported in reference [13].

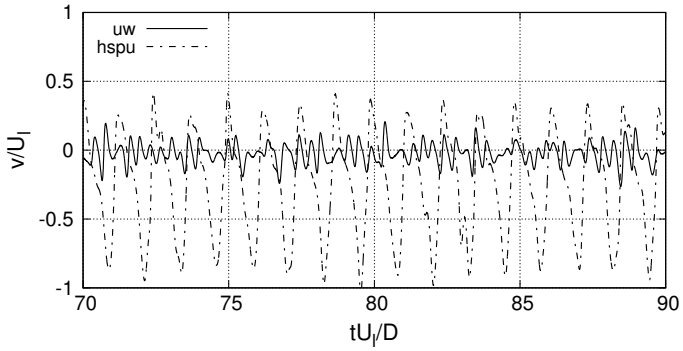

(a) Probe S1

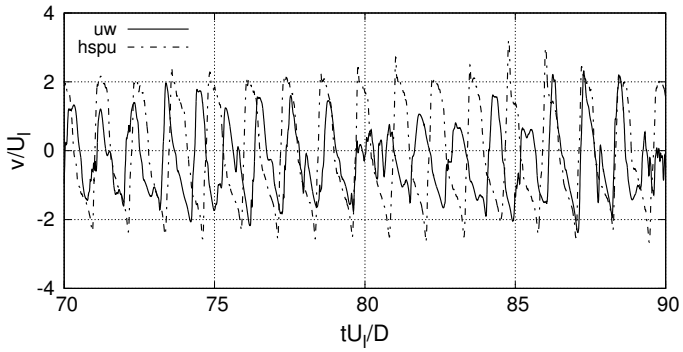

(b) Probe S2

Figure 2.14: Atomization of a two-phase jet: dimensionless vertical velocity v/U_l measured at probes S1 and S2 using the *uw* and *hspu* schemes.

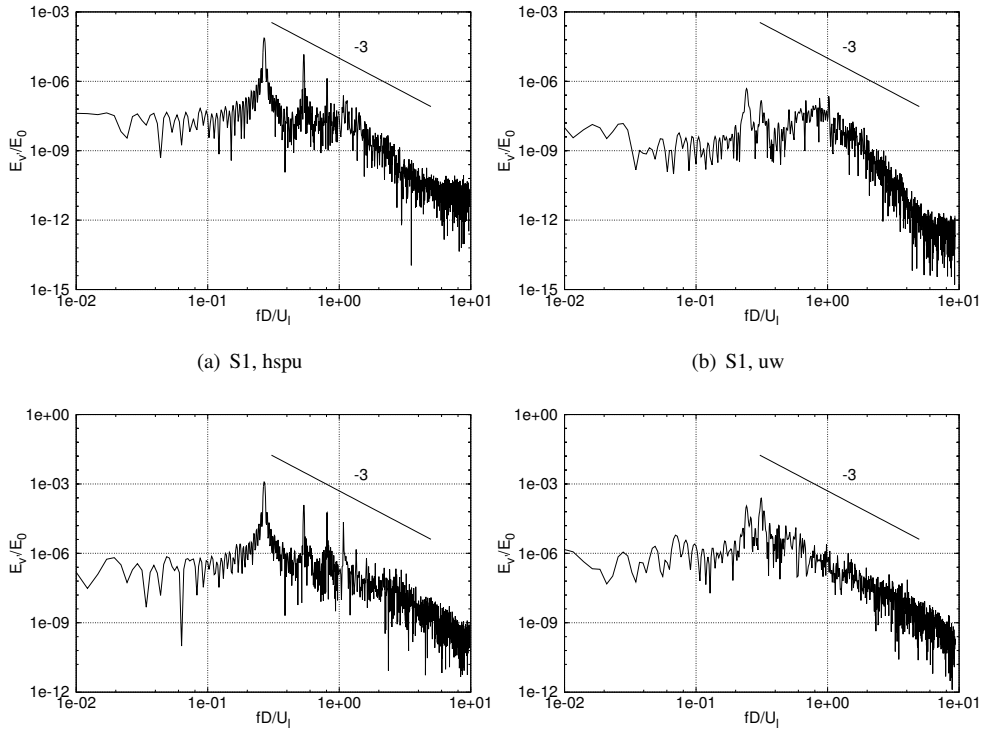

(a) S1, hspu

(b) S1, uw

(c) S2, hspu

(d) S2, uw

Figure 2.15: Atomization of a two-phase jet: energy spectra $E_{v'}/E_0$ measured at probes S1 and S2 using the *uw* and *hspu* convection schemes.

dominant shedding frequency.

In conclusion, the *hspu* scheme proves to be effective in the simulation of turbulent jet atomization, as it is able to properly resolve the energy cascade and to reproduce the vortex shedding effect. Moreover, its adoption has many advantages in comparison to other existing schemes. For instance, *hspu* solves the poor numerical stability shown by *sp* at liquid-gas interfaces. On the other hand, it provides a proper transport of kinetic energy in the vortex shedding mechanism, thus, overcoming the inability of *uw* to accurately solve turbulent flows. Indeed, the utilization of the *sp* scheme for the cells located in the bulk of the fluids guarantees the discrete convective operator to be locally skew-symmetric and, therefore, the correct conservation of mass, momentum and kinetic energy [15].

2.5 Conclusions

In this work, a low-dissipation and low-dispersion discretization for the numerical simulation of turbulent interfacial flow is analyzed. The scheme is designed to minimize the amount of artificial dissipation introduced into the discrete system, while manages to limit the growth of spurious currents. In addition, as demonstrated in the series of tests performed, the hybrid convection scheme proposed can be coupled to different interface-capturing methods.

The theoretical analysis presented in Secs. 2.2 and 2.3 demonstrates that the scheme is conservative except for the subgroup of cells found in the vicinity of the interface, where a controlled amount of dissipation is introduced to diminish spurious flows. This feature is confirmed by the numerical results of a 3-D vortex presented in Sec. 2.4.1. The same test shows that the overall kinetic-energy dissipation is kept to a level well lower than classic dissipative schemes. The spatial accuracy of the method is numerically analyzed in Sec. 2.4.2, where it is shown to be second-order accurate on Cartesian grids and first-order on unstructured 3-D meshes.

The localized injection of dissipation allows an effective control of the spurious currents growth, which provides enhanced stability to the numerical method. Indeed, as demonstrated in the spherical drop test in Sec. 2.4.3, spurious flows grow unbounded when using purely conservative discretizations, whereas remain contained to small values in the case of utilizing the hybrid convection scheme. This behavior is further corroborated by obtaining a proper interface advection when the sphere is placed in a swirling velocity field.

The performance of the numerical framework in a complete multiphase turbulent scenario has been tested by solving a liquid-gas atomizing jet. On the one hand, the test demonstrates that the controlled dissipation added to the interfacial region is sufficient to stabilize the numerical simulation. On the other hand, the results expose that, unlike pure dissipative schemes, the hybrid convection approach presented in this work is able to properly represent the underlying physics of turbulent flow. Consequently, the inability of a pure dissipative method to properly transport swirling structures is overcome.

Bibliography

[1] B. Lafaurie, C. Nardone, R. Scardovelli, S. Zaleski, G. Zanetti, Modelling merging and fragmentation in multiphase flows with SURFER, Journal of Computational Physics 113 (1994) 134–147.

[2] Y. Renardy, M. Renardy, PROST: a parabolic reconstruction of surface tension for the volume-of-fluid method, Journal of Computational Physics 183 (2002) 400–421.

[3] S. Zahedi, M. Kronbichler, G. Kreiss, Spurious currents in finite element based level set methods for two-phase flow, International Journal for Numerical Methods in Fluids 69 (2012) 1433–1456.

[4] F. Denner, B. G. van Wachem, On the convolution of fluid properties and surface force for interface capturing methods, International Journal of Multiphase Flow 54 (2013) 61–64.

[5] M. M. François, S. J. Cummins, E. D. Dendy, D. B. Kothe, J. M. Sicilian, M. W. Williams, A balanced-force algorithm for continuous and sharp interfacial surface tension models within a volume tracking framework, Journal of Computational Physics 213 (2006) 141–173.

[6] A. Y. Tong, Z. Wang, A numerical method for capillarity-dominant free surface flows, Journal of Computational Physics 221 (2007) 506–523.

[7] A. Chorin, A numerical method for solving incompressible viscous flow problems, Journal of Computational Physics 2 (1967) 12–26.

[8] A. Di Mascio, R. Broglia, R. Muscari, On the application of the single-phase level set method to naval hydrodynamic flows, Computers & Fluids 36 (2007) 868–886.

[9] X. Lv, Q. Zou, Y. Zhao, D. Reeve, A novel coupled level set and volume of fluid method for sharp interface capturing on 3D tetrahedral grids, Journal of Computational Physics 229 (2010) 2573–2604.

[10] E. Schillaci, L. Jofre, N. Balcázar, O. Lehmkuhl, A. Oliva, A level-set aided single-phase model for the numerical simulation of free-surface flows on unstructured meshes, Computers & Fluids 140 (2016) 97–110.

[11] S. Popinet, An accurate adaptive solver for surface-tension-driven interfacial flows, Journal of Computational Physics 228 (2009) 5838–5866.

[12] R. Löhner, C. Yang, E. Onate, Simulation of flows with violent free surface motion and moving objects using unstructured grids, International Journal for Numerical Methods in Fluids 53 (2007) 1315–1338.

[13] D. Fuster, A. Bagué, T. Boeck, L. Le Moyne, A. Leboissetier, S. Popinet, P. Ray, R. Scardovelli, S. Zaleski, Simulation of primary atomization with an octree adaptive mesh refinement and vof method, International Journal of Multiphase Flow 35 (2009) 550–565.

[14] R. Verstappen, A. Veldman, Symmetry-preserving discretization of turbulent flow, Journal of Computational Physics 187 (2003) 343–368.

[15] L. Jofre, O. Lehmkuhl, J. Ventosa, F. X. Trias, A. Oliva, Conservation properties of unstructured finite-volume mesh schemes for the Navier-Stokes equations, Numerical Heat Transfer, Part B: Fundamentals 65 (2014) 53–79.

[16] X. Trias, O. Lehmkuhl, A. Oliva, C. Pérez-Segarra, R. Verstappen, Symmetry-preserving discretization of navier-stokes equations on collocated unstructured grids, Journal of Computational Physics 258 (2014) 246–267.

[17] D. Fuster, An energy preserving formulation for the simulation of multiphase turbulent flows, Journal of Computational Physics 235 (2013) 114–128.

[18] A. E. Veldman, K.-W. Lam, Symmetry-preserving upwind discretization of convection on non-uniform grids, Applied Numerical Mathematics 58 (2008) 1881–1891.

[19] S. Pirozzoli, Numerical methods for high-speed flows, Annual review of fluid mechanics 43 (2011) 163–194.

[20] L. Jofre, O. Lehmkuhl, N. Balcázar, J. Castro, J. Rigola, A. Oliva, Conservative discretization of multiphase flow with high density ratios, WIT Transactions on Engineering Sciences 82 (2014) 153–164.

[21] Y. Morinishi, T. Lund, O. Vasilyev, P. Moin, Fully conservative higher order finite difference schemes for incompressible flow, Journal of Computational Physics 143 (1998) 90–124.

[22] F. N. Felten, T. S. Lund, Kinetic energy conservation issues associated with the collocated mesh scheme for incompressible flow, Journal of Computational Physics 215 (2006) 465–484.

[23] G. Fishpool, M. Leschziner, Stability bounds for explicit fractional-step schemes for the Navier-Stokes equations at high Reynolds number, Computers & Fluids 38 (2009) 1289–1298.

[24] L. Jofre, O. Lehmkuhl, J. Castro, A. Oliva, A 3-D volume-of-fluid advection method based on cell-vertex velocities for unstructured meshes, Computers & Fluids 94 (2014) 14–29.

[25] L. Jofre, R. Borrell, O. Lehmkuhl, A. Oliva, Parallel load balancing strategy for volume-of-fluid methods on 3-D unstructured meshes, Journal of Computational Physics 282 (2015) 269–288.

[26] J. Brackbill, D. B. Kothe, C. Zemach, A continuum method for modeling surface tension, Journal of Computational Physics 100 (1992) 335–354.

[27] N. Balcázar, L. Jofre, O. Lehmkuhl, J. Castro, J. Rigola, A finite-volume/level-set method for simulating two-phase flows on unstructured grids, International Journal of Multiphase Flow 64 (2014) 55–72.

[28] N. Balcázar, O. Lehmkuhl, L. Jofre, J. Rigola, A. Oliva, A coupled volume-of-fluid/level-set method for simulation of two-phase flows on unstructured meshes, Computers & Fluids 124 (2016) 12 –29.

[29] N. Balcázar, J. Rigola, J. Castro, A. Oliva, A level-set model for thermocapillary motion of deformable fluid particles, International Journal of Heat and Fluid Flow 62 (2016) 324–343.

[30] E. Schillaci, O. Antepara, O. Lehmkuhl, N. Balcázar, A. Oliva, Effectiveness of adaptive mesh refinement strategies in the DNS of multiphase flows, in: Proceedings of International Symposium Turbulent Heat and Mass Transfer VIII, 2015.

[31] E. Schillaci, O. Lehmkuhl, O. Antepara, A. Oliva, Direct numerical simulation of multiphase flows with unstable interfaces, Journal of Physics: Conference Series 745 (2016).

[32] M. Gorokhovski, M. Herrmann, Modeling primary atomization, Annual Review of Fluid Mechanics 40 (2008) 343–366.

[33] J. Lasheras, E. Hopfinger, Liquid jet instability and atomization in a coaxial gas stream, Annual Review of Fluid Mechanics 32 (2000) 275–308.

[34] H. Grosshans, A. Movaghar, L. Cao, M. Oevermann, R.-Z. Szász, L. Fuchs, Sensitivity of VOF simulations of the liquid jet breakup to physical and numerical parameters, Computers & Fluids 136 (2016) 312–323.

[35] N. R. Lomb, Least-squares frequency analysis of unequally spaced data, Astrophysics and space science 39 (1976) 447–462.

[36] R. H. Kraichnan, Inertial ranges in two-dimensional turbulence, Physics of Fluids 10 (1967) 1417–1423.

3

Adoption of AMR for resource optimization in two-phase flow

Main contents of this chapter are currently Under Review in:

E.Schillaci, O. Antepara, N. Balcázar, and A. Oliva. A dynamic mesh refinement strategy for the simulation of break-up phenomena in two-phase jets *International Journal of Heat and Fluid Flow*, Under Review.

Abstract. In this work we adopt an Adaptive Mesh Refinement (AMR) strategy to carry out the direct numerical simulation of complex multiphase flows by means of interface-capturing schemes. The model is globally addressed at improving the representation of interfacial and turbulent scales in the simulation of instability and break-up phenomena, while simultaneously reducing the computational requirements in comparison to static mesh computations. The refinement criteria are designed to ensure the proper representation of the characteristic lengths, by achieving the required mesh definition in each part of the domain. The discretization, built on a finite-volume basis, accounts for a divergence-free treatment of the refined/coarsened cells, that ensures the correct transport of mass, momentum and kinetic energy.
Initially, we demonstrate the accuracy of the method and the benefits brought in contrast with static mesh for general multiphase cases, as vortex flow and rising bubbles. Next, we propose the analysis of various basic instability phenomena, including the capillary break-up of a liquid column, the injection of a liquid jet at different speeds, and the validation of a 2-D coaxial turbulent jet. In the last section, the simulation of a 3-D coaxial jet is presented and the physical features that we observed are validated by comparison to semi-empirical laws.

Additional contents have been published in:

E.Schillaci, O.Lehmkuhl, O.Antepara, and A.Oliva. Direct numerical simulation of multiphase flows with unstable interfaces. *Journal of Physics: Conference Series*, (Vol. 745, No. 3, p. 032114). IOP Publishing.

E.Schillaci, O.Antepara, O.Lehmkuhl, N. Balcázar, and A. Oliva. Effectiveness of adaptive mesh refinement strategies in the DNS of multiphase flows. In: Proceedings of international symposium turbulent heat and mass transfer VIII; 2015 .

3.1 Introduction

In this section we first want to explain the various reasons that make the direct numerical simulation of multiphase flow particularly costly from the computational point of view. Following, we introduce the Adaptive Mesh Refinement technique as a tool to improve the efficiency of simulations. Finally, we present the numerical framework analyzed in this work and the proposed numerical tests.

Mesh limitations in two-phase flow The Direct Numerical Simulation (DNS) of multiphase flow can result particularly challenging and expensive in terms of computational cost in the case of complex interfacial phenomena and high Reynolds numbers —a complete overview is given by Tryggvason et al. [1]. Indeed, in each part of the domain, different characteristic length requirements have to be ensured. In the first place, the mesh must be sufficiently fine to correctly model the Kolmogorov length scales that appear in turbulent flow. Second, the phenomena involving the instability and rupture of the interface must be correctly represented. That include the growth of waves and filaments, as well as the generation of drops of varying size in primary and secondary atomization processes, with the smallest size equal or smaller than Kolmogorov length scales [2]. As a further requirement, the grid spacing at the interface has to be fine enough to properly evaluate interface properties, as gradients and curvature. Due to these conditions, the same concept of DNS may be considered inappropriate for some kinds of turbulent multiphase flow, as the minimum mesh size that properly represent the interface phenomena cannot be defined apriori. In the practice, it is assumed that structures smaller than the minimum mesh size have no practical effect on the global behavior of the flow [3]. The engineering problems that better highlight these complex numerical issues and strong mesh limitations are constituted by atomizing two-phase flow, including injection sprays and coaxial jets, with important applications in the field of combustion injector and pharmaceutical sprays. Another notable example is the case of rising bubbles, where the leading forces are due to surface tension stresses that develop in proximity of the interface. Consequently, fine mesh resolutions are needed in the proximity of the interface to evaluate accurately these forces.

Adoption of dynamic meshes An effective strategy to improve the feasibility of DNS in multiphase flow consists in the adoption of the Adaptive Mesh Refinement (AMR) technique. The tool performs a dynamic refinement of the mesh, depending on the local definition requirement, with a global consistent reduction of the allocated computational resources. The robustness of AMR on 2D structured meshes was firstly demonstrated by Berger and Oliger [4] and by Berger and Colella [5]. More recently, AMR strategies have also appeared in unstructured hexahedral [6] and tetrahedral [7] meshes. The combined utilization of interface-capturing methods and AMR techniques was firstly introduced by Sussman et al. [8]. In Sussman [9], a parallelized algorithm to achieve mesh refinement in a coupled level-set/volume-of-fluid Navier-Stokes solver is described. More recently, Popinet et al. [10] combined the adaptive octree spatial discretization to Volume of Fluid (VOF) interface representation, by focusing on the correct balancing of surface tension forces and pressure gradients at the interface, while Zuzio and Estivalezes [11] coupled Level-Set and AMR, by applying particular procedures at the fine/coarse mesh interfaces to preserve the accuracy. Both authors were focusing on the simulation of laminar phenomena, as rising bubbles and Rayleigh-Taylor instabilities. Fuster et al. [3] also coupled octree AMR and VOF, and applied the method to atomization phenomena. One of the main issues connected to AMR discretizations, when dealing with incompressible problems, consists in the extension of the divergence-free constraint to child cells. One of the most common strategies has been proposed by Balsara [12] and applied to two-phase simulations by [11]. An alternative scheme to deal with the incompressibility constraint can be found in Vanella et al. [13].

Current proposal In this work, we analyze a CLS-AMR framework that allows the simulation of turbulent multiphase flow in a wide range of situations, particularly, focusing on instability and atomization phenomena. In the presented method, the CLS scheme proposed and implemented by Balcàzar et al. [14] for interface-capturing of two-phase flows on 3D unstructured domains is adopted, due to its proven reliability on this class of phenomena —details above the scheme are reviewed in Chapter 1. It is coupled to an adaptive mesh refinement algorithm, whose implementation follows the work of Antepara et al. [15]. The algorithm carries out a quad/octree (2D/3D) hierarchical decomposition of the existing structured mesh. In addition, a simple and low-cost reconstruction scheme for the face fluxes and cell-centered values has been introduced. Unlike similar approaches, this strategy is designed to exactly preserve mass, momentum and kinetic-energy in the sub-cells during the refinement/ coarsening procedures. This treatment allows to maintain the discrete conservation properties of the adopted collocated scheme, demonstrated in [15, 16] for single-phase flows and analyzed in the context of multiphase flow by Schillaci et al. [17], thus, creating the basis for the correct resolution of turbulence. As demonstrated in the following sections, the analyzed scheme permits a considerable reduction of computational costs, both in terms of memory requirement and calculation time in comparison to fixed mesh schemes. At the same time, the method allows to obtain the required mesh size in each area of the domain,

without significantly affecting the stability and the accuracy of the simulation.
This Chapter is organized as follows. In Sec. 3.2, the general features of the AMR methods are explained. Then, in Sec. 3.3, the advantages led by the adoption of this strategy in contrast with static mesh schemes are highlighted by numerical tests. We consider the tests of a vortex flow and different set-up of rising bubbles, including the case of 3D merging bubbles in different configurations. In Sec. 3.4, the capability of the method to correctly simulate basic instability phenomena is shown, including the atomization of a 2-D coaxial jet.

3.2 Adaptive mesh refinement

The adaptive mesh refinement (AMR) strategy consists of a dynamic treatment of the mesh aimed at improving the resolution in the regions in which a particularly small characteristic length is needed. A simple example of a 2D mesh refinement is shown in Fig. 3.1(a). The treatment used in this work is based on the quad/octree algorithm presented by Antepara et al. [15] for single-phase turbulent flow. The refinement is performed over the initial static mesh by dividing progressively a parent cell into four, in the 2D case, or eight, in the 3D one, child cells. The progressive refinement stages are referred to as level 2, 3, 4 and so on, as depicted in Fig. 3.1(b). As an example, Fig. 3.1(c) shows the inner section of a refined domain, referring to the mesh of the coaxial 3-D jet described in Sec. 4.2.2. In this work, the AMR strategy is extended to the multiphase flow case by choosing the appropriate refinement criteria and by applying a particular discretization procedure to treat refined/coarsened face and cells. This procedure is aimed at conserving discrete magnitudes —mass, momentum and kinetic energy— despite the dynamic transformation of the grid. In some previous works, the method demonstrated to apply efficiently also to general multiphase [18] and unstable two-phase phenomena [19]. In this section, the refinement criteria used in this work and the proposed discretization procedure are presented in detail. Finally, some validation tests are proposed to show the reliability of the AMR on basic multiphase phenomena, and to highlight the computational advantages led by its adoption.

3.2.1 Refinement criteria

The refinement step is carried out when certain refinement criteria are met over a list of cells. These cells are marked with the corresponding level of refinement during a checking process, performed every certain number of iterations. The refinement criteria used in this work or in previous experiences from our group [15, 18, 19] are listed below.

Interface-capturing criterion It follows the behavior of the level-set function to assign the highest level of refinement in the proximity of the interface, Γ. The refining process is triggered when a minimum number of interfacial control volumes approximates the non-refined domain area. Some additional rings of cells are added to the refined zone, so as to

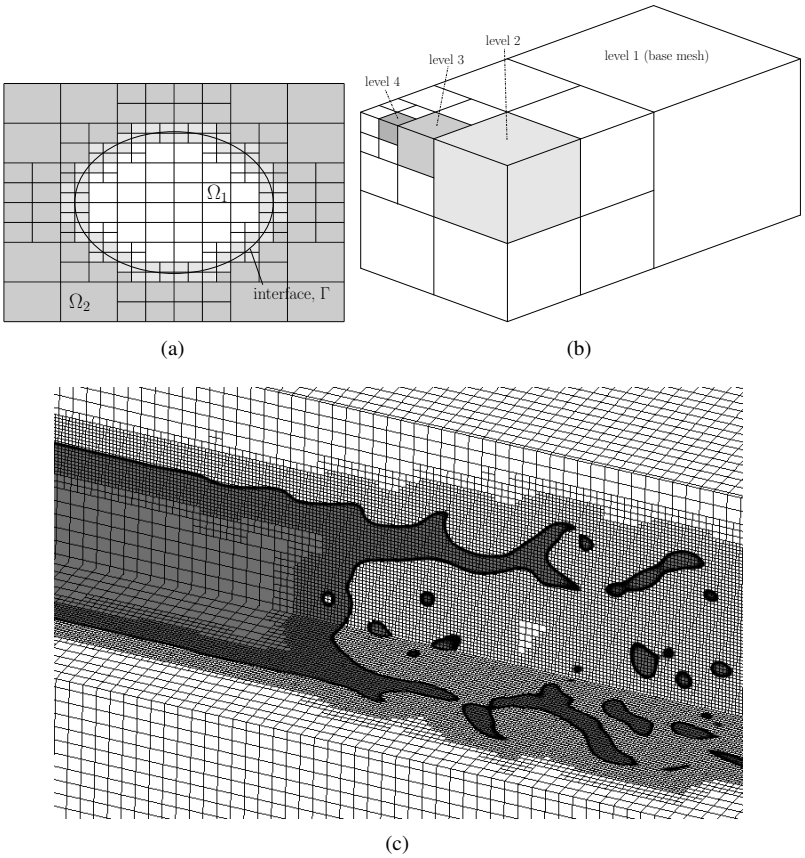

Figure 3.1: (a) Progressive quad refinement of a Cartesian mesh around the surface of a 2D ellipsoidal body. (b) Octree decomposition of a uniform 3D Cartesian mesh. (3) Inner section of a 3-D domain refined with AMR in this work.

forestall the movement of the fluid and avoid the process of mesh renewal at each iteration. The number of additional rings ranges from 1-2 in the case of slowly rising bubbly flows, to 5-6 in the case of rapid movements of the interface —e.g. high velocity injection jets. Finally, departing from Γ, a decreasing level of refinement is assigned, to obtain a smooth transition between highly refined and coarse mesh regions.

Vorticity-based criterion It is intended to refine the mesh in the zones in which a high vorticity is measured, thus, guaranteeing that the smallest scales of the vortices generated by turbulence are well captured. In particular, a specific cell is refined if

$$\frac{\Delta h|\nabla \times \mathbf{u}|}{\max\{\mathbf{u}\}} > \Omega_{\text{lim}} \tag{3.1}$$

where Δh is cubic root of the cell volume, and Ω_{lim} is a threshold parameter between 0.01 and 0.02.

Residual velocity criterion This method, proposed by [15] and further used in [20], is applicable to turbulent flows resolved with LES models, and consists in refining the cells in which a limit value of the residual velocity, $\mathbf{u}' = \mathbf{u} - \overline{\mathbf{u}}$, is exceeded. $\mathbf{u}'$ depends on the filter chosen to obtain the filtered velocity, $\overline{\mathbf{u}}$, in LES simulations. This criterion is alternative to the vorticity-based one; however, differently from the latter, the threshold value for triggering the refinement can be established in a general way to resolve basic turbulent problems.

3.2.2 Refined/Coarsened cells discretization

The proposed quad/octree AMR algorithm works on a hexagonal based mesh and operates in the regions of the domain marked for refinement. The original centered scalar– and face fields owned by the parent mesh are redistributed over the new cells– and faces according to an appropriate scheme. The same happens during the coarsening step, consisting in the recovery of the original parent cell from the child ones. In this work, the aim is that of re-distributing the initial scalar fields as to maintain the conservation of discrete properties —mass, momentum and kinetic energy— unaltered. In Fig. 3.2 the relation between parent/child cells in a 2D case is represented. In the distribution process, the normal mass fluxes, $\hat{M}_f$, are considered uniform along the faces and the normal mass flow through the parent face can be expressed as

$$\hat{M}_{pf} = \sum_{i \in F(pf)}^{i=N} \hat{M}_{cf,i}, \tag{3.2}$$

where pf indicates the parent face, and N is the total number of child faces, cf, in which the original one has been divided ($N = 2$ in the 2D case, $N = 4$ in the 3D one). In a 2D Cartesian

mesh —as the one depicted in Fig.3.2—, the following relation apply

$$\hat{M}_{f,1} = \hat{M}_{f,1a} + \hat{M}_{f,1b}. \tag{3.3}$$

Moreover, in the case of a uniformly refined mesh, where the proportions of the child cells respect the parent's one, the fluxes on child cells are equal to

$$\hat{M}_{f,1a} = \frac{\hat{M}_{f,1}}{2}, \qquad \hat{M}_{f,2a} = \frac{\hat{M}_{f,2}}{2}. \tag{3.4}$$

The normal mass fluxes passing through the new internal faces are evaluated by means of a weighted average of the mass fluxes of the neighbor cells. For instance, the mass fluxes of the new faces in the child cell underlined in the picture, are evaluated as

$$\hat{M}_{f,5} = \frac{\hat{M}_{f,1a} + \hat{M}_{f,3a}}{2} \quad \hat{M}_{f,6} = \frac{\hat{M}_{f,2a} + \hat{M}_{f,4a}}{2} \tag{3.5}$$

During the coarsening step, mass fluxes on parent faces are recovered by summing the children ones, according to Eq. 3.2. Centered velocities, $\mathbf{u}_c$, are reconstructed by interpolating the surrounding face normal velocities, both in refined and coarsened cells. A centered divergence-free velocity field is obtained by extending the scheme proposed in [21] to the variable-density case. Considering a uniform momentum field ($\rho\mathbf{u}$) over the cell volume, the cell centered velocity is evaluated as the weighted average of the surrounding face mass fluxes, expressed as

$$\mathbf{u}_c = \frac{1}{\rho_c V_c} \sum_{f \in F(c)} \hat{M}_f \mathbf{r}_f^c, \tag{3.6}$$

where $\mathbf{r}_f^c$ is the weight of the components, as it expresses the distance between cell circumcenter and face centroids. Finally, scalar field variables, as pressure, p, and volume fraction, ϕ, are simply inherited by refined cells, while in the coarsening step, the parent value is obtained by means of a weighted average (on volume) of the child cells values. For a generic variable ξ in the 2D uniform case, it simply yields

$$\xi_f = \frac{\xi_{c,1} + \xi_{c,2} + \xi_{c,3} + \xi_{c,4}}{4}. \tag{3.7}$$

Besides its simplicity, this process allows the conservation of mass, momentum and kinetic energy in incompressible flows. In Appendix 1, the global mass conservation of the AMR method in demonstrated. Moreover, providing that mass fluxes on refined/coarsened faces are built to respect flux conservation, the considerations made by [16] and [15] —and analyzed in the context of multiphase flows by [17]— over conservation properties of discrete quantities apply. This guarantees the discrete conservation of momentum and kinetic energy in the frame of collocated discretization, which is of key importance for the correct resolution of turbulent phenomena.

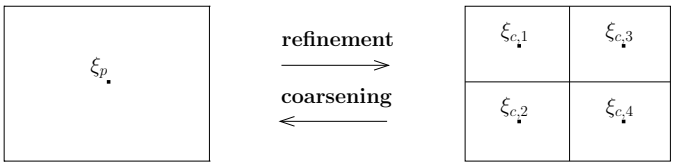

(a) Scalar fields

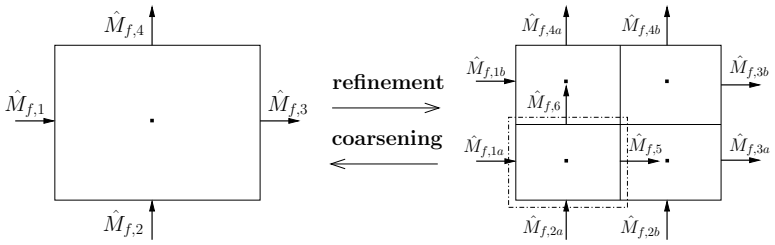

(b) Mass flux

Figure 3.2: The relation between parent (left) and child (right) cells during the refinement/coarsening step, referred to a first level refinement in a 2D Cartesian mesh. In (a) ξ is a generic centered variable whereas in (b) mass fluxes distribution is shown.

3.3 AMR Validation tests

The impact led by the adoption of AMR on simulations can be assessed in a systematic way by comparing the solution obtained with adaptive and static meshes in some selected validation cases. In the vortex flow test we analyze the advection of the level-set function subjected to a given velocity field. Next, in the simulation of 3D rising bubbles, the interface-capturing method is coupled to complete fluid motion equations. Some parameters can be used for the assessment of AMR effectiveness. As defined in Fuster et al. [3], the efficiency of an AMR scheme can be evaluated as

$$\eta_{\text{AMR}} = \frac{t_{\text{static}}}{t_{\text{AMR}}} \frac{\text{CV}_{\text{AMR}}}{\text{CV}_{\text{static}}}, \tag{3.8}$$

where t_{static} and t_{AMR} are the total computational times of static and AMR simulations, respectively, CV_{AMR} is the average number of control volumes in the AMR simulation and $\text{CV}_{\text{static}}$ is the number of control volumes of a static mesh with a characteristic length equal to the smallest one achieved with AMR. Other characteristic values are the time ratio, $\tau_r = 1 - t_{\text{AMR}}/t_{\text{static}}$, and the control volumes reduction ratio, $\eta_{\text{CV}} = 1 - \text{CV}_{\text{AMR}}/\text{CV}_{\text{static}}$. In all the tests proposed in this work, $D/\Delta h$ is the relative definition of the mesh, being D the characteristic dimension of the problem and Δh the grid spacing. In AMR cases Δh is the grid spacing set at the interface.

3.3.1 Vortex flow

In this test, a level-set distribution which initially describes a circle of diameter $D = 0.2$ —as depicted in Fig. 3.3(a)—, is advected under the effect of a given flow field, $\mathbf{u}(\mathbf{x})$, described by the following equations

$$\begin{aligned} u(\mathbf{x}) &= -\sin^2(\pi x) sin(2\pi y), \\ v(\mathbf{x}) &= \sin^2(\pi y) sin(2\pi x). \end{aligned} \tag{3.9}$$

At the inversion time, t_{inv}, the velocities are inverted and the simulation is continued until $t_{\text{end}} = 2t_{inv}$, when the level-set function should recover its initial circular shape. The inversion time, t_{inv}, is fixed at 1.
Two series of simulations are carried out. First, the test is performed on static regular Cartesian meshes with increasing definition (Tests 1 to 4). Next, an increasing AMR level (from 2 to 4) is imposed to Mesh 1, in order to obtain a grid spacing at the interface correspondent to the previous tests (Tests 5 to 7)). A resume is reported in Tab. 3.1. The accuracy of the results is evaluated by calculating the error over mass, $||\varepsilon_M||$, and the error over the norm of the mass center vector position, $||\varepsilon_P||$, defined as

$$||\varepsilon_M|| = \frac{||M(t_0) - M(t_{\text{end}})||}{M(t_0)}, \qquad ||\varepsilon_P|| = \frac{||\mathbf{x}_P(t_0) - \mathbf{x}_P(t_{\text{end}})||}{||\mathbf{x}_P(t_0)||}, \tag{3.10}$$

Test	Mesh	AMR	$(D/\Delta h)$
1	1	no	10
2	2	no	20
3	3	no	40
4	4	no	80
5	1	lv.2	20
6	1	lv.3	40
7	1	lv.4	80

Table 3.1: Vortex flow: list of meshes used for the numerical experiments. $D/\Delta h$ is relative definition of the mesh.

Static test	AMR test	CV_{static}	CV_{AMR}	τ_r	η_{AMR}
2	5	9.8×10^3	3.6×10^3	56%	83%
3	6	3.9×10^4	6.8×10^3	76%	69%
4	7	1.6×10^5	1.5×10^4	85%	61%

Table 3.2: Vortex flow: comparison between static and AMR cases. In the compared tests Δh is equivalent in the interface region.

where $M(t)$ indicates the mass of Ω_1, and $\mathbf{x}_P(t)$ is its vector center position. Both are evaluated at the beginning of the simulation, t_0, and at the end, t_{end}.
As shown in Fig. 3.4(a), $||\varepsilon_M||$ reduces similarly in AMR and static tests, showing an order of convergence between first and second for both cases. $||\varepsilon_P||$ is slightly lower in static cases, however, still showing an order of convergence between first and second. In Fig. 3.4(b), it is possible to appreciate the difference in computational time between AMR and static cases. In particular, this difference increases when reducing Δh, as remarked by the reduction of the time ratio, τ_r, reported in Tab. 3.2. Finally, despite its slight reduction with the decrease of Δh, η_{AMR} keeps a value that exceeds 60%, thus, indicating an overall good effectiveness of the AMR strategy. Some screenshots of flow evolution (referred to test 6) are reported in Fig. 3.3.

3.3.2 Rising bubbles

According to the classification by Clift et al. [22], rising bubbles are characterized by Eötvös, Eo —ratio between buoyant forces and surface tension—, Reynolds, Re —ratio between

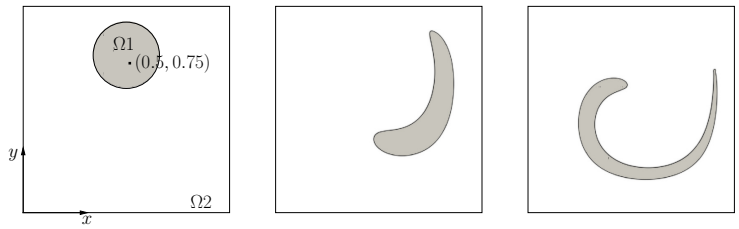

(a) $t = 0$ (b) $t = 0.5t_{inv}$ (c) $t = t_{inv}$

(d) $t = 1.3t_{inv}$ (e) $t = 1.7t_{inv}$ (f) $t = 2.0t_{inv}$

Figure 3.3: Vortex flow: evolution of the level-set function. The pictures refer to test 6 of Tab. 3.1.

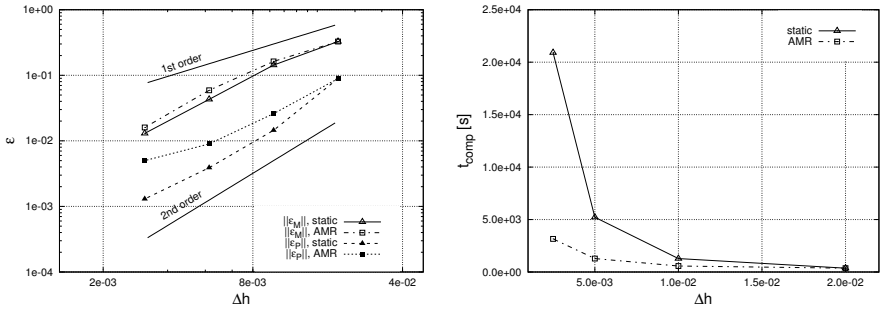

(a) Error (b) Computational time

Figure 3.4: Vortex flow: comparison between static and AMR simulations for (a) error in mass, $||\varepsilon_M||$, error on vector position, $||\varepsilon_P||$ and (b) computational time. Magnitudes are plotted against mesh size, Δh.

Test	$\rho 1$	$\mu 1$	r_ρ	r_μ	σ	g	Eo
small r_ρ	1000	10	10	10	24.5	0.98	10
high r_ρ	1000	10	1000	100	1.96	0.98	125

Table 3.3: Physical parameters used for the single bubble tests.

inertial and viscous forces—, and Morton number, Mo, defined as

$$\text{Eo} = \frac{(\rho_1 - \rho_2) g D^2}{\sigma}, \quad \text{Re} = \frac{\rho_1 v_b D}{\mu_1}, \quad \text{Mo} = \frac{g \mu_1^4 (\rho_1 - \rho_2)}{\rho_1^2 \sigma^3}, \tag{3.11}$$

respectively, where D is the bubble diameter, ρ_1 and μ_1 characterize the surrounding medium, ρ_2 and μ_2 represent the bubble fluid, σ is the surface tension coefficient and v_b is the bubble rising velocity. The Clift's diagram, reported in Fig. 3.8, relates Eo and Mo with Re and the bubble shape. Other characteristic values are the bubble sphericity, S —ratio between surface of the initial bubble and surface at time t— and its dimensionless mass center position, $\mathbf{x}_b' = \mathbf{x}_b / D$. Time is represented in dimensionless form, as $t' = t\sqrt{g/D}$. In the 2D case, the sphericity is substituted by the circularity, C, consisting in the ratio between the perimeter of the initial bubble and the perimeter of the bubble at time t.
Some of the cases proposed in this section, as the **small $\mathbf{r}_\rho$** case (originally introduced by Hysing et al. [23]), the 3D rising bubble case and the merging bubble cases (originally introduced by Van Sint Annaland et al. [24]) were used by Balcàzar et al. [14] to validate the CLS methodology on fixed meshes. In this work, they are reproposed, together with additionals tests, to demonstrate the computational advantages led by the adoption of the current AMR methodology to the proposed physics, as well as its spatial convergence.

2D bubbles

This test case consists in the simulation of the two dimensional movement of a circular bubble of diameter D. The fluids are assigned properties as to reproduce the benchmark results reported by Hysing et al. [23, 25]. The domain, depicted in Fig. 3.5(a), is bounded by solid walls —no-slip boundary conditions— on the $x-$ and $y-$axis and the fluids are initially at rest. Hence, the rise of velocity fields is due to the density difference between the involved phases. Two physical situations are studied, as resumed in Tab. 3.3, where the physical parameters of the fluids and the Eo number are reported. The cases are also defined in terms of density ratio, $r_\rho = \rho_1/\rho_2$, and viscosity ratio, $r_\mu = \mu_1/\mu_2$.

Small $\mathbf{r}_\rho$ Three simulations are carried out, as resumed in Tab. 3.4. In the first two, static meshes are used: a coarse one, characterized by a number of characteristic lengths per bubble diameter, $(D/\Delta h)_{\text{lv.1}} = 25$, and fine one, $(D/\Delta h)_{\text{lv.1}} = 50$. In addition, an AMR simulation is

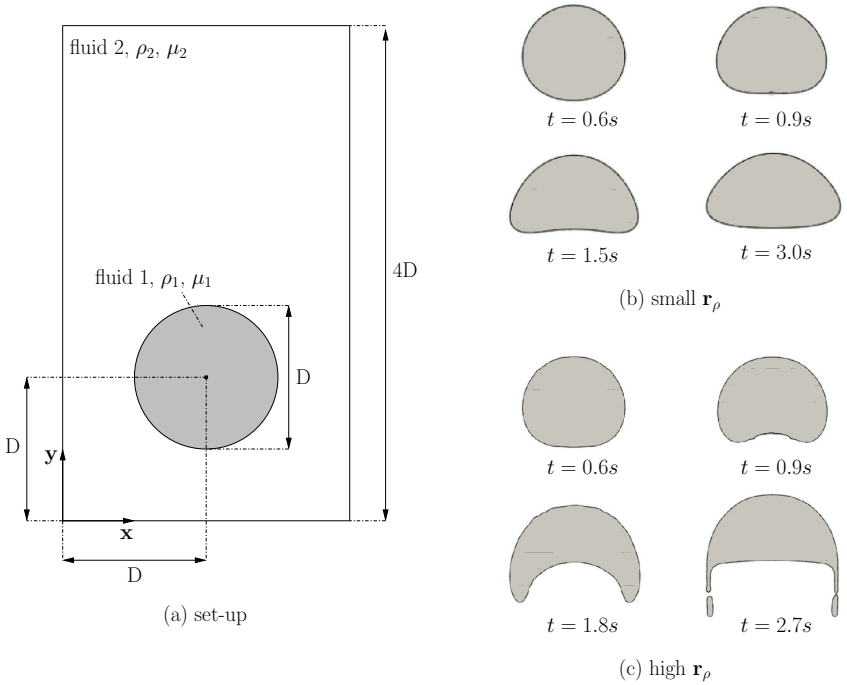

(a) set-up

(b) small $\mathbf{r}_\rho$

(c) high $\mathbf{r}_\rho$

Figure 3.5: 2D bubble: (a) initial set-up; (b) evolution in the small r_ρ case ($r_\rho = 10$); (c) evolution in the high r_ρ case ($r_\rho = 1000$).

Test	clock time [min]	CVs	$D/\Delta h$
coarse	10	5000	25
fine	96	20000	50
coarse + AMR lv.2	13	6300	50

Table 3.4: Mesh data and computational times measured in the 2D bubble low $\mathbf{r}_\rho$ simulations. performed on 4CPUs of the JFF cluster. $D/\Delta h$ is the number of characteristic lengths per bubble diameter (referred to the interface zone in the AMR cases).

performed, with the coarse static mesh as basic grid. A lv.2 refinement is used, thus, achieving the resolution of the fine grid, $(D/\Delta h)_{\text{lv.2}} = 50$.
The advancement in time of y_b (vertical value of $\mathbf{x}_b$), v_b and C for the different cases are shown in Figs. 3.6(a), 3.6(c), 3.6(e), where the experimental data extracted by [25] are also reported. It is possible to notice that the AMR simulation accurately reproduces the results obtained with the fine mesh —while an overall good agreement is found with the experimental data. On the other hand, the data obtained with coarse mesh, do not differ excessively from the experimental data, but the solution is generally worse than the other cases, especially with regard to C. Finally, The computational time of the AMR case is very similar to the coarse mesh one, as reported in Tab. 3.4, leading to a very high performance of the method, as $\eta_{\text{AMR}} = 2.3$, and $\eta_t = 0.86$.
In the simulation, the buoyancy forces produce the rising of the bubble, that quickly reaches a stable rising velocity. At the same time, the bubble is deformed, and, helped by strong surface tension forces, it assumes a stable ellipsoidal shape. In Fig. 3.5(b), some snapshots of the rising bubble evolution are shown, reflecting the same behavior reproduced by other authors as [23], and by Balcàzar et al. [14, 26] when using the CLS method on fixed meshes.

High $\mathbf{r}_\rho$ Also in this case, the simulation is carried out with the fine and the coarse meshes, where the fine mesh has $(D/\Delta h)_{\text{lv.1}} = 100$. Next, the case is simulated with a lv.3 AMR on the coarse mesh, in order to reach the resolution of the fine mesh —resume in Tab. 3.5. The results are contrasted with data reported in [23], where the experiments performed by different authors are compared. However, these solutions do not have the same identical behavior, so the series of data that the more coincide between them are used as benchmarks. Concerning the vertical position of the bubble, y_b, and the rising velocity, v_b, the solution obtained on the coarse mesh is very poor —as shown in the graphs, Figs. 3.6(b), 3.6(d). Both improve considerably when using the fine mesh and get closer to the benchmark values. The AMR test gives good results for both y_b and v_b, approaching the fine mesh results with small variances.
In Fig. 3.5(c), some snapshots of the rising bubble evolution, simulated with AMR, are shown. The predominance of the buoyancy forces and the low surface tension, firstly promote the

Test	clock time [min]	CVs	$D/\Delta h$
coarse	169	5000	25
fine	5877	80000	100
coarse + AMR lv.3	455	∼9500	100

Table 3.5: Mesh data and computational times measured in the 2D bubble high $\mathbf{r}_\rho$ simulations. The computations are performed by using 16 CPUs on JFF cluster.

appearance of a concavity at the bottom of the bubble. Hence, thin filaments develop in the extremities, leading to the detachment of small secondary bubbles around $t_{\text{break}} = 2.1\ s$. The appearance of such secondary structures (filaments, satellite bubbles), and therefore, the breaking of the original bubble structure, make the measurement of the bubble circularity of little significance after t_{break}. C data reported in Fig. 3.6(f), show that the solution continues to be poor on the coarse mesh. On the other hand, the ones obtained on the fine mesh and with AMR, reflect well the behavior of the reference, up to t_{break}. After, both depart from the benchmark, but follow the same path maintaining a stable gap.
In conclusion, the adoption of AMR, despite some low difference in the results —probably due to the different mesh resolution in the bulk of the phases—, approximates well the solution obtained on the fine mesh, with a substantial lower computational time. Performances of AMR strategy are still very good, being $\eta_{\text{AMR}} = 1.52$ and $\eta_t = 0.92$.

3D bubble

In this part, the vertical motion of 3D bubbles in a cylinder tube is analyzed. The domain used for the simulations consists of a cylinder with diameter $D_c = 6D$, large enough not to affect the shape of the bubble, and a variable height, $H_c = [8 : 10]\ D$, that should allow the bubbles to reach the terminal velocity before encountering the top. The basic mesh, depicted in Fig. 3.7(a), has a characteristic length per bubble diameter $(D/\Delta h)_{\text{lv.1}} = 8$. The tests are carried out by using three progressive mesh refinement levels around the interface, thus, achieving the maximum definition of $(D/\Delta h)_{\text{lv.4}} = 64$. No-slip boundary conditions are applied to the top and bottom part of the domain, while slip condition is used on the external walls. First, the analysis of single rising bubbles is performed; next, a further verification is given by the study of the merging process between bubbles.

Single bubbles In this case, the rising of a single bubble inside the domain depicted in Fig. 3.7(b) is analyzed. The validity of the results is assessed by comparing the shape and the terminal rising velocity of the bubble with the experimental benchmark proposed by [22] —see Fig.3.8. The terminal rising velocity is related to the rising Re number of the diagram by means of the Reynolds number.

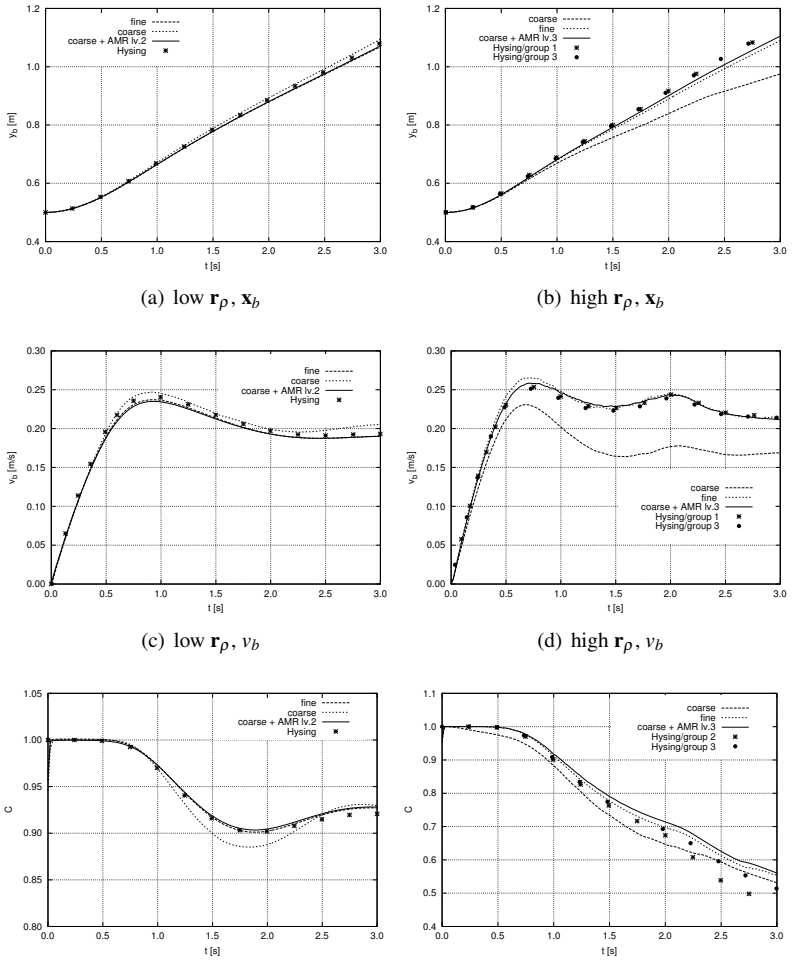

(a) low $\mathbf{r}_\rho$, $\mathbf{x}_b$ (b) high $\mathbf{r}_\rho$, $\mathbf{x}_b$

(c) low $\mathbf{r}_\rho$, v_b (d) high $\mathbf{r}_\rho$, v_b

(e) low $\mathbf{r}_\rho$, C (f) high $\mathbf{r}_\rho$, C

Figure 3.6: Results for y_b, v_b and C obtained in the simulation of the 2D bubble, in both low $\mathbf{r}_\rho$ and high $\mathbf{r}_\rho$ cases. Hysing data refer to [25] in the low $\mathbf{r}_\rho$ case, and to [23] in the high $\mathbf{r}_\rho$ one.

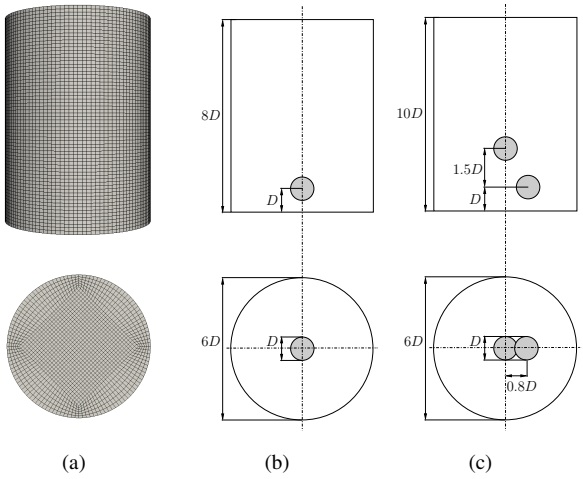

Figure 3.7: (a) Mesh used for the simulation of the 3D bubbles. Set-up used for the various cases: (b) single bubbles, (c) oblique merging bubbles.

The cases listed in Tab. 3.6 are analyzed. The same table reports the Re numbers evaluated at steady state in the AMR simulations, when using the highest level of refinement (lv.4). In the first example (case A), the bubble assumes a spherical shape due to the low Eo number, that means a predominance of the surface tension forces. Once the steady rising velocity is reached, the simulated value of the Reynolds number, $Re_{\text{sim}} = 1.83$, is close to the one reported in the Clift's diagram ($Re_{\text{Clift}} \simeq 2$). In case B, where a higher Eo is set, the bubble undergoes a progressive deformation and assumes an ellipsoidal shape. The final rising velocity is sustained ($Re_{\text{sim}} = 23$, $Re_{\text{Clift}} \simeq 25$). In the last example (case C), characterized by the highest Eo number, the predominance of buoyant forces produces the ellipsoidal/skirted shape of the bubble. However, the final Re number ($Re_{\text{sim}} = 18.5$, $Re_{\text{Clift}} \simeq 20$) is limited by the high Mo number. As shown in the graphical comparison depicted in Fig.3.8, the expected bubble shape is correctly reproduced in all the proposed cases.
A quantification of the benefits led by the adoption of the AMR strategy can be done by comparing the results with the ones obtained by Balcàzar et al. [14], that performed similar simulations on static meshes. The number of control volumes is dramatically reduced in the current work, as reported in Tab. 3.7, where the static CVs [14] and the AMR lv.4 CVs are compared. The obtained results are in good agreement with the numerical reference for the whole evolution of the flow, for both Re and S measurements, as shown in Fig. 3.9. The accuracy of the solution is improved by increasing the AMR level, reaching an acceptable mesh convergence with a lv.3 (case B) or a lv.4 (case A and C) refinement. Concluding, this test demonstrates that despite the strong reduction of mesh requirements, no practical loss of

case	Eo	Mo	Re [22]	reproduced Re	predicted shape
A	1.0	1e-3	2	1.83	spherical
B	10.0	1e-3	25	23	ellipsoidal
C	100.0	1	20	18.5	ellipsoidal/skirted

Table 3.6: 3D bubbles: solitary bubbles reproduced and analyzed in this work.

case	CV_{static}[14]	CV_{AMR}[lv.4]	η_{CV}
A	2.3×10^6	3.2×10^5	86%
B	2.3×10^6	3.4×10^5	85%
C	3.4×10^6	3.5×10^5	90%

Table 3.7: 3D bubbles: number of control volumes needed for dynamic and static mesh simulations [14] in the single bubble case. The percentage reduction of control volumes, η_{CV}, is also indicated.

accuracy is found between AMR and static mesh computations for the analyzed flow regimes.

Merging bubbles In the following test, the merging process of two rising bubbles is reproduced. This test, already proposed by Balcázar at al. [14] to validate the CLS method on fixed meshes, is here reproposed to show the capability of the AMR methodology to yield a convergent solution when studying the complex phenomenon of merging between bubbles. In particular, the coalescence is considered to happen when the interfaces of two bubbles fall inside the same cells, hence, without taking into account any other effect related to surface tension. In this sense, the CLS accuracy is improved by reducing the mesh size in the proximity of the contact zone by means of AMR. The single bubbles are defined by the following dimensionless numbers, $Eo = 16$ and $Mo = 2 \times 10^{-4}$, in order to reproduce the simulation realized by van Sint Annaland et al. [24] on the OBLIQUE configuration.
The initial configuration of the bubbles is depicted in Fig. 3.7(c). A slightly higher computational domain is used in this case, to allow the achievement of a more stable final rising velocity. The two bubbles assume different shapes during the rising. The leading bubble rises without suffering any disturbance and assuming its typical ellipsoidal shape, hence, respecting the Clift's diagram behaviour. On the other side, the second bubble deforms, assuming a slug-like shape, and directing its top towards the wake of the first bubble. This rises more quickly, due to the suction effect caused by the leading bubble. The merging happens at $t' \simeq 6.0\ s$. The resulting bubble has an elliptical shape and rises with $Re_{\text{sim}} \simeq 47.5$, close to the one indicated in the Clift's diagram, $Re_{\text{Clift}} \simeq 52$. It is slightly inclined on one side, probably because the domain is not large enough to allow the achievement of a full rising symmetry. Finally, the bubble reduces its velocity due to the vicinity of the upper boundary.

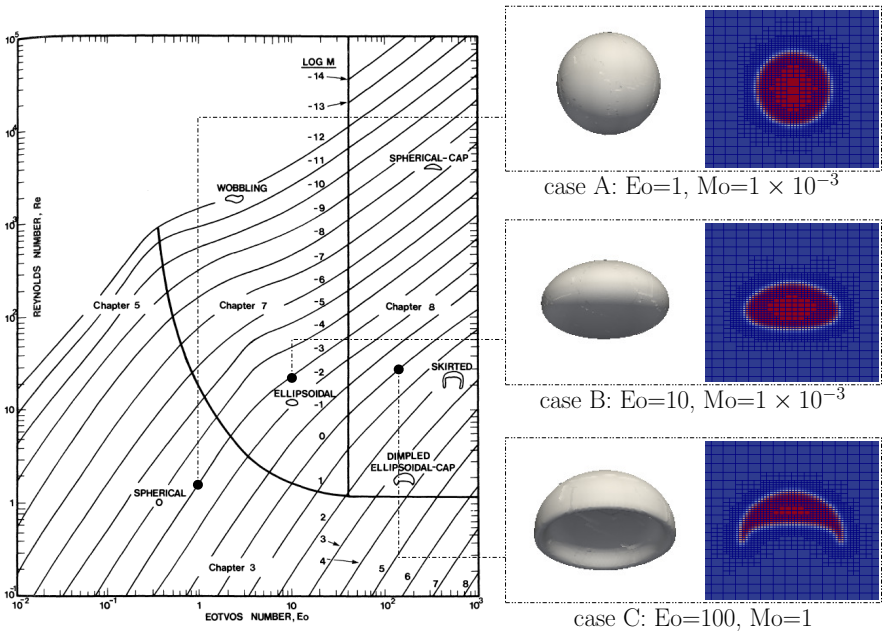

Figure 3.8: 3D bubbles: on the left, bubble regime diagram proposed by [22]. On the right, the single bubbles at steady state simulated in this work are depicted. A zoom over the refined area is also proposed. For clarity of representation, lv.3 refinement pictures are plotted.

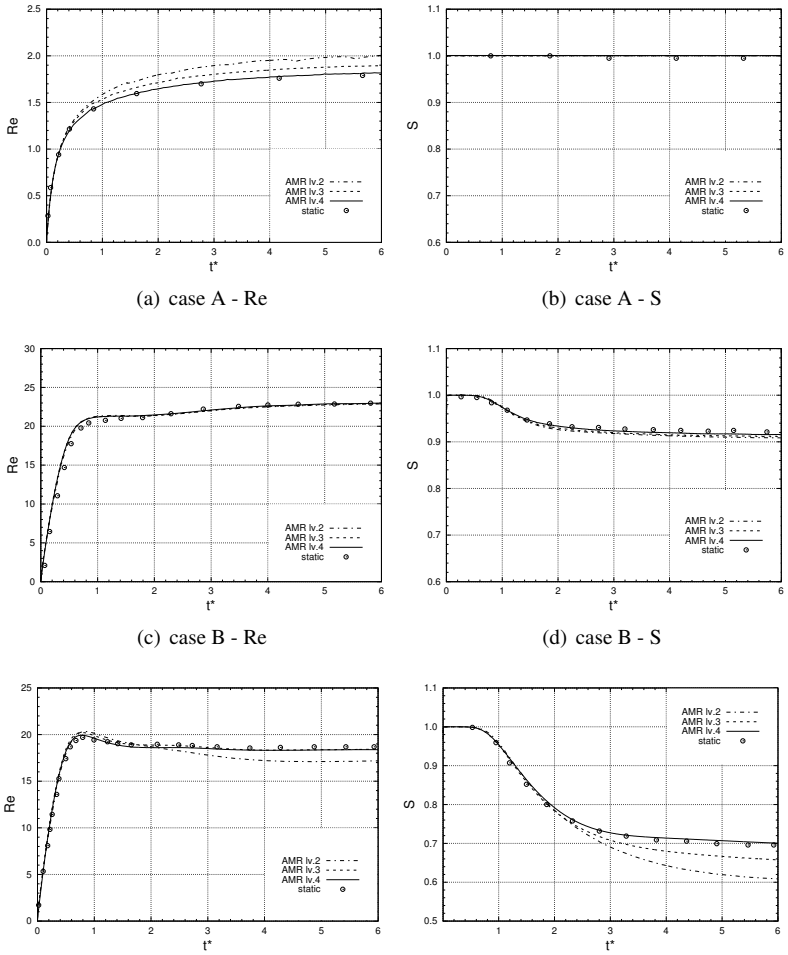

(a) case A - Re (b) case A - S

(c) case B - Re (d) case B - S

(e) case C - Re (f) case C - S

Figure 3.9: 3D bubbles: Re number and sphericity, S, obtained in single bubble simulations with increasing levels of refinement, and comparison with static mesh reference by [14].

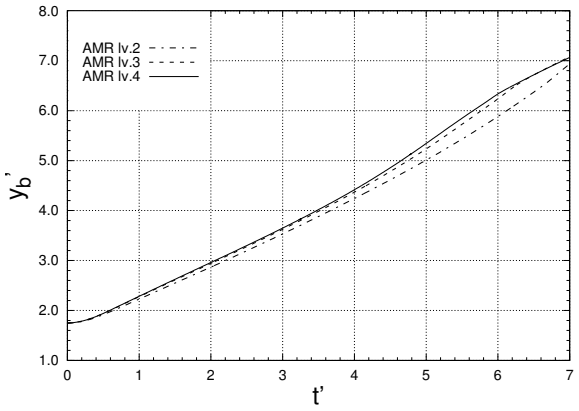

Figure 3.10: Joint centre of mass position evolution in the bubbles merging test calculated for increasing levels of refinement.

Some snapshots of the flow evolution are depicted in Fig. 3.11, where they are compared to the equivalent pictures proposed in [24]. The strong similarity with the reference pictures confirms the reliability of the results. The solution showed to be convergent when increasing the AMR level, as shown in Fig. 3.10, where the behaviour of joint bubbles mass centre position is plotted.

3.4 Instability phenomena

The break-up process of a two-phase jet embraces a wide scale of turbulent and interfacial characteristics lengths. Therefore, if we intend to study a complete atomization process, we must firstly ensure the capability of the numerical scheme to simulate the phenomena that occur at the smaller scales. In this section, we present some basic tests aimed at demonstrating the correct capture of such phenomena. First, we analyze the breakage of a liquid column subjected to capillary instability. Finally, in the turbulent 2-D Jet case, the appearance of Kelvin-Helmoltz instabilities due to the shear stress between two co-flowing high speed fluids is shown and the mesh convergence achieved by means of the AMR strategy is further demonstrated.

3.4.1 Plateau-Rayleigh Instability

A column of liquid stressed by a surface disturbance tends to minimize its surface under the action of capillary forces, and finally degenerates into droplets. This phenomenon is com-

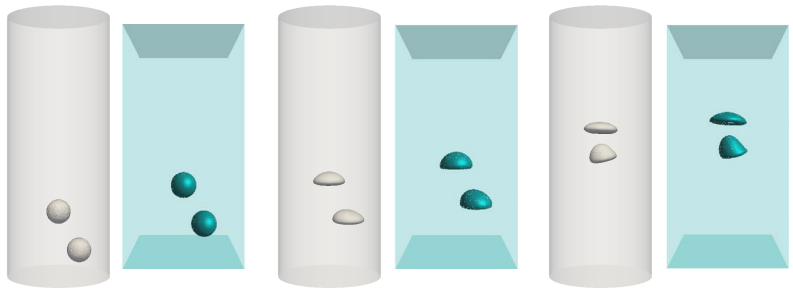

(a) $t' = 0$s (b) $t' = 2.1$s (c) $t' = 5$s

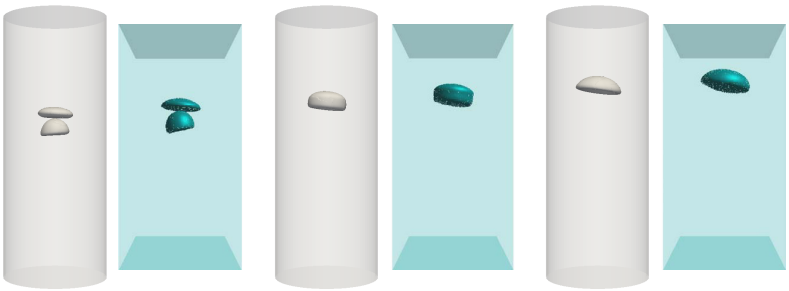

(d) $t'* = 5.8$s (e) $t' = 6.7$s (f) $t' = 7.5$s

Figure 3.11: Screenshots comparison of the flow evolution in the 3D merging bubbles test, OBLIQUE configuration, with the numerical experiments performed by van Sint Annaland et al. [24] —depicted on the right-sides. Compared pictures refer to the same dimensionless time, t'.

monly called Plateau-Rayleigh instability. In this test, the disintegration of a liquid column is studied, and the growth rate of the surface instabilities, ω, measured in numerical experiments, is compared to the linear capillary instability theory of viscous jets, studied by Weber [27]. The domain, a rectangular box of sizes $1.0 \times 0.5 \times 0.5$, is occupied by a water column of diameter $D = 0.2$, surrounded by air at ambient temperature. The surface tension is set to $\sigma = 0.07$, and Oh $\sim \mathcal{O}(10^{-4})$ indicates a low influence of viscous dissipating forces. The surface is perturbed by a sinusoidal instability, described by $y(x) = a\sin(2\pi x/\lambda)$, where $a = 0.02$ is the amplitude and λ is the wavelength. Simulations are performed by using a lv.3 refinement over the basic mesh to achieve a grid spacing at the interface of $(D/\Delta h)_{\text{lv.3}} \simeq 26$ and slip boundary conditions are applied to the boundaries. Several experiments are carried out by varying the input value for λ, and evaluating the maximum growth rate at each time step as

$$\frac{\omega_{\max}}{\omega_0} = \frac{\max\{\ln(y(x,t+1)) - \ln(x,y(t))\}}{\Delta t} \tag{3.12}$$

where $\omega_0 = \sqrt{\rho_l r_0^3/\sigma}$ is the characteristic time scale of break-up and $y(x,t)$ is the liquid column profile at time t. Numerical results for $\omega_{\max}$ are compared to the curve obtained from the solution of the equation reported by Ashgriz [28] for the perturbation spectrum. The relation, valid for sufficiently long waves ($ka << 1$), reads as

$$\omega^2 + \frac{3\mu k^2}{\rho}\omega - \frac{\sigma}{2\rho as}(1 - k^2a^2)k^2a^2 = 0 \tag{3.13}$$

where $k = 2\pi/\lambda$ is the wave number. Fig. 3.12 shows numerical and theoretical results versus dimensionless wave number, ka, demonstrating the validity of our results. The snapshots of Fig. 3.13 describe the evolution of the flow when λ is set to 1, as a function of $t' = t/\omega_0$. In the first stages of the simulation, the filament undergoes a slow deformation, up to approximately $t' = 5.5$, when it tapers quickly near the edges up to point at which breakage occurs, between $t' = 5.5$ and $t' = 5.8$. The large central drop, initially deformed, is subjected to a series of oscillations, until it reaches a fully spherical and stable shape, at $t' \simeq 8.5$. The same behavior was observed by other authors [10, 29].

3.4.2 Turbulent 2-D Coaxial Jet

In this section, we re-propose the test presented in Chapter 2 regarding the atomization of a 2-D multiphase jet. In this case, we want to demonstrate the ability of the AMR method to yield a convergent solution when increasing the refinement level in instability phenomena. The test is validated by comparison to numerical results presented by Fuster et al. [3]. All the details about the set-up and the validation process are given in Sec. 2.4.4.

The original results proposed in the current Chapter are reported in Figs. 3.14(a), 3.14(c) and 3.14(e), where the evolution of the time-averaged energy of velocity fluctuations $E_{v'}/E_0$,

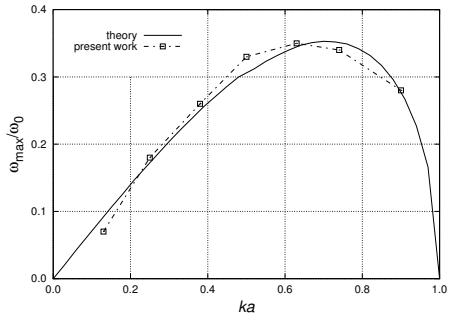

Figure 3.12: Plateau-Rayleigh Instability test: growth rate of instabilities. Comparison between present work and theory by [28].

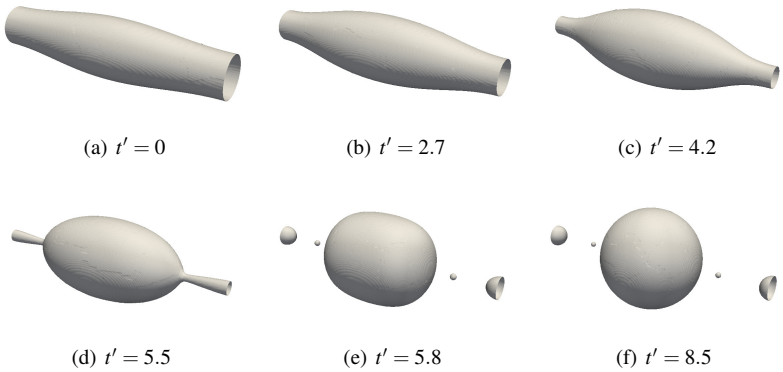

(a) $t' = 0$ (b) $t' = 2.7$ (c) $t' = 4.2$

(d) $t' = 5.5$ (e) $t' = 5.8$ (f) $t' = 8.5$

Figure 3.13: Plateau-Rayleigh Instability test: deformation of a liquid column under the effect of capillary forces. Case of $\lambda = 1$.

along the jet profile is depicted, being $E_{v'} = (v')^2$, and $E_0 = (u_l)^2$. The profiles are taken at three different distances from the inlet, x/D, and due to the symmetry of the geometry, only the sectors corresponding to the top half part of the domain are represented. In parallel, Figs. 3.14(b), 3.14(d) and 3.14(f) report the time-averaged relative horizontal velocity of the fluid, $(u-u_l)/u_l$, for different x/D. The results are compared to the same magnitudes measured by [3], showing an overall good agreement while the solution gets closer to the reference by increasing the degree of AMR. The measurements show that a lv.3 refinement is needed to obtain a sufficient convergence of the solution in all the profiles analyzed.
The presented plots for $E_{v'}$, taken from the intact part of the jet, show how the energy of fluctuations progressively rises in the proximity of the interface. At the same time, $E_{v'}$ grows inside the liquid and air bulks, indicating the transfer of energy to the inside of the jet. Next, the internal stresses cause the complete breakdown of the fluid core, which happens at $L/D \simeq 10$. After a transition phase, the jet reaches a statistical steady-state condition, in which the dispersion of the atomized flow occurs according to a constant frequency of shedding. In [17], we analyze and comment the power energy spectrum of the coaxial 2-D flow, which permits a characterization of its turbulent behavior.

3.5 Conclusions

In this work a CLS-AMR strategy for the finite-volume discretization of multiphase flow, mainly intended for the simulation of break-up and atomization phenomena, is analyzed. As numerically demonstrated in the various tests, the method is able to dramatically reduce the computational resources involved if compared to static mesh methods, without at the same time losing accuracy in the solution. The model accounts for a divergence-free treatment of the refined and coarsened cells, which is analytically demonstrated to ensure the correct transport of mass, momentum and kinetic energy.
In a first series of tests, accounting for a vortex flow and different rising bubble cases, the convergence of the results obtained in two-phase flows is demonstrated. The sharp decline in computational resources required in comparison to static mesh cases is also highlighted.
In the instability phenomena section, we have presented some basic tests aimed at demonstrating the correct capture of instability and break-up phenomena at small scales. First, the Plateau-Rayleigh instability growth ratio was correctly measured on unstable liquid columns. Hence, in the 2-D coaxial jet case the capability of the CLS-AMR method to yield a convergent solution when increasing the refinement level in two-phase phenomena with interface break-up and turbulent fluctuations is demonstrated.

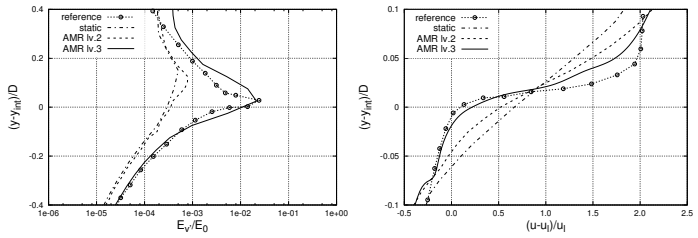

(a) $x/D = 1.25$, $E_{v'}/E_0$ (b) $x/D = 1.25$, $(u-u_l)/u_l$

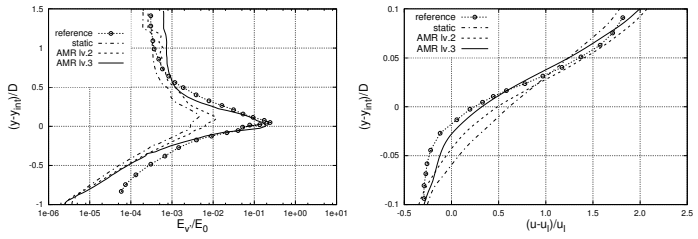

(c) $x/D = 1.9$, $E_{v'}/E_0$ (d) $x/D = 1.9$, $(u-u_l)/u_l$

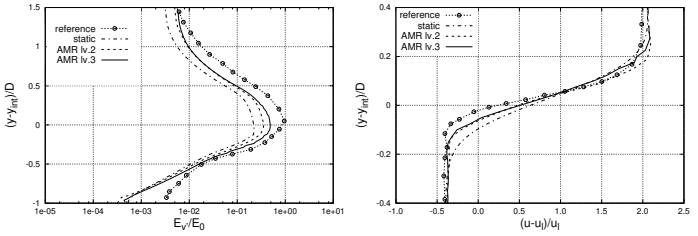

(e) $x/D = 3.1$, $E_{v'}/E_0$ (f) $x/D = 3.1$, $(u-u_l)/u_l$

Figure 3.14: 2-D Turbulent Jet: kinetic energy of velocity fluctuations $E_{v'}/E_0$ and horizontal velocity of the fluid $(u-u_l)/u_l$ measured with different levels of refinement. Comparison to reference data by [3] for different distances from the inlet, x/D.

Bibliography

[1] G. Tryggvason, R. Scardovelli, S. Zaleski, Direct numerical simulations of gas–liquid multiphase flows, Cambridge University Press, 2011.

[2] M. Gorokhovski, M. Herrmann, Modeling primary atomization, Annual Review of Fluid Mechanics 40 (2008) 343–366.

[3] D. Fuster, A. Bagué, T. Boeck, L. Le Moyne, A. Leboissetier, S. Popinet, P. Ray, R. Scardovelli, S. Zaleski, Simulation of primary atomization with an octree adaptive mesh refinement and vof method, International Journal of Multiphase Flow 35 (2009) 550–565.

[4] M. J. Berger, J. Oliger, Adaptive mesh refinement for hyperbolic partial differential equations, Journal of computational Physics 53 (1984) 484–512.

[5] M. J. Berger, P. Colella, Local adaptive mesh refinement for shock hydrodynamics, Journal of computational Physics 82 (1989) 64–84.

[6] J. Wackers, G. Deng, A. Leroyer, P. Queutey, M. Visonneau, Adaptive grid refinement for hydrodynamic flows, Computers & Fluids 55 (2012) 85–100.

[7] X. Zheng, J. Lowengrub, A. Anderson, V. Cristini, Adaptive unstructured volume remeshing–ii: Application to two-and three-dimensional level-set simulations of multiphase flow, Journal of Computational Physics 208 (2005) 626–650.

[8] M. Sussman, A. S. Almgren, J. B. Bell, P. Colella, L. H. Howell, M. L. Welcome, An adaptive level set approach for incompressible two-phase flows, Journal of Computational Physics 148 (1999) 81–124.

[9] M. Sussman, A parallelized, adaptive algorithm for multiphase flows in general geometries, Computers & structures 83 (2005) 435–444.

[10] S. Popinet, An accurate adaptive solver for surface-tension-driven interfacial flows, Journal of Computational Physics 228 (2009) 5838–5866.

[11] D. Zuzio, J. Estivalezes, An efficient block parallel amr method for two phase interfacial flow simulations, Computers & Fluids 44 (2011) 339–357.

[12] D. S. Balsara, Divergence-free adaptive mesh refinement for magnetohydrodynamics, Journal of Computational Physics 174 (2001) 614–648.

[13] M. Vanella, P. Rabenold, E. Balaras, A direct-forcing embedded-boundary method with adaptive mesh refinement for fluid–structure interaction problems, Journal of Computational Physics 229 (2010) 6427–6449.

[14] N. Balcázar, L. Jofre, O. Lehmkuhl, J. Castro, J. Rigola, A finite-volume/level-set method for simulating two-phase flows on unstructured grids, International Journal of Multiphase Flow 64 (2014) 55–72.

[15] O. Antepara, O. Lehmkuhl, R. Borrell, J. Chiva, A. Oliva, Parallel adaptive mesh refinement for large-eddy simulations of turbulent flows, Computers & Fluids 110 (2014) 48–61.

[16] L. Jofre, O. Lehmkuhl, J. Castro, A. Oliva, A 3-D volume-of-fluid advection method based on cell-vertex velocities for unstructured meshes, Computers & Fluids 94 (2014) 14–29.

[17] E. Schillaci, L. Jofre, N. Balcázar, O. Antepara, A. Oliva, A low-dissipation convection scheme for the stable discretization of turbulent interfacial flow, Computers & Fluids 153 (2017) 102–117.

[18] E. Schillaci, O. Antepara, O. Lehmkuhl, N. Balcázar, A. Oliva, Effectiveness of adaptive mesh refinement strategies in the DNS of multiphase flows, in: Proceedings of International Symposium Turbulent Heat and Mass Transfer VIII, 2015.

[19] E. Schillaci, O. Lehmkuhl, O. Antepara, A. Oliva, Direct numerical simulation of multiphase flows with unstable interfaces, Journal of Physics: Conference Series 745 (2016).

[20] O. Antepara, R. Borrell, O. Lehmkuhl, I. Rodriguez, A. Oliva, Parallel adaptive mesh refinement of turbulent flow around simplified car model using an immerse boundary method, in: In ECFD VI: European Conference on Computational Fluid Dynamics, 2014.

[21] B. Perot, Conservation properties of unstructured staggered mesh schemes, Journal of Computational Physics 159 (2000) 58–89.

[22] R. Clift, J. R. Grace, M. E. Weber, Bubbles, drops, and particles, Courier Corporation, 2005.

[23] S.-R. Hysing, S. Turek, D. Kuzmin, N. Parolini, E. Burman, S. Ganesan, L. Tobiska, Quantitative benchmark computations of two-dimensional bubble dynamics, International Journal for Numerical Methods in Fluids 60 (2009) 1259–1288.

[24] M. van Sint Annaland, N. Deen, J. Kuipers, Numerical simulation of gas bubbles behaviour using a three-dimensional volume of fluid method, Chemical Engineering Science 60 (2005) 2999–3011.

[25] S. Hysing, Mixed element fem level set method for numerical simulation of immiscible fluids, Journal of Computational Physics 231 (2012) 2449–2465.

[26] N. Balcázar, O. Lehmkuhl, L. Jofre, J. Rigola, A. Oliva, A coupled volume-of-fluid/level-set method for simulation of two-phase flows on unstructured meshes, Computers & Fluids 124 (2016) 12 –29.

[27] C. Weber, Zum zerfall eines flüssigkeitsstrahles, ZAMM-Journal of Applied Mathematics and Mechanics/Zeitschrift für Angewandte Mathematik und Mechanik 11 (1931) 136–154.

[28] N. Ashgriz, Handbook of atomization and sprays: theory and applications, Springer Science & Business Media, 2011.

[29] M. Herrmann, A sub-grid surface dynamics model for sub-filter surface tension induced interface dynamics, Computers & Fluids 87 (2013) 92–101.

4

Numerical simulation of two-phase 3-D jets

Part of the contents of this chapter are currently Under Review in:

E.Schillaci, O. Antepara, N. Balcázar, and A. Oliva. A dynamic mesh refinement strategy for the simulation of break-up phenomena in two-phase jets *International Journal of Heat and Fluid Flow*, Under Review.

4.1 Introduction

The study of the liquid atomization process is currently a problem not totally understood in the engineering field, due to the high complexity of the phenomena that lead to the generation and amplification of instabilities at the interface, and, next, to the complete pulverization of the liquid core —an introduction to the physical processes involved is available in Tryggvason at al. [1]. A correct numerical representation of such processes would bring great advances in the simulation of important applications, such as automotive engines and propulsion systems. In this Section, we will present the numerical methods recently used in the scientific community to study atomization processes. Hence, we introduce the numerical simulations of atomization phenomena carried out in the mark of this thesis, and described in detail in the following of this Chapter. Finally, the dimensionless numbers used to characterize this kind of flows are presented.

Simulation of two-phase jets in literature In the last decades, several numerical methods have been proposed to solve atomization problems, spacing between the three main classes of computational fluid dynamics (CFD) models: in Reynolds-averaged Navier-Stokes equations (RANS) [2], the approach is based on a homogeneous formulation of the two-phase medium, and the transport of mean interface density is modeled by diffusion-like hypothesis,

therefore neglecting the effect of the interaction between liquid structures [3]; on the other side, large eddy simulations (LES) approaches [4] still suffer the complexity of coupling turbulence modeling and interface-capturing methods. In particular, many LES models are not able to take into account surface tension forces, that play a key role in atomization processes [5]. Finally, direct numerical simulation (DNS) approaches involve strict requirements in terms of computational resources, because of the numerous length scales involved in the phenomenon. That include the correct representation of surface phenomena, such as the growth of waves and filaments, as well as the generation of drops of varying size in primary and secondary atomization processes. Indeed, as demonstrated by Shinjo and Umemura [6], the use of huge computational resources is needed to carry out the DNS of complete atomization phenomena. Nevertheless, the quality of the results is excellent, as also demonstrated by other authors. While an early overview above authors that worked on the DNS of atomizing flow is given by Gorokhovski and Herrmann [3], some of the latest works in this field are listed below. Between the others, Desjardins et al. [7] proposed a robust and mass conservative numerical method for the study of the turbulent atomization of a liquid Diesel jet, consisting in the injection of a high-velocity liquid into a still air chamber. In Desjardins et al. [8] the same method is used to perform further simulations of Diesel injectors. Moreover, they applied it to the simulation of coaxial jets —where the atomization of the liquid is assisted by the coaxial injection of a high-speed gas— obtaining a good agreement between experimental and numerical data in a wide range of situations. An example of the flow evolution, which is analyzed also in this work, is proposed in Fig. 4.1, where both experimental and numerical results are shown. Mènard et al. [9] and Lebas et al. [10] contributed to the understanding of primary break-up in Diesel spray by means of simulations, e.g. correctly representing the influence of gas temperature. Fuster et al. [11] studied the influence of the injector and the effect of vortices generation and swirling in high Reynolds number simulations of coaxial jets. Again, Shinjo and Umemura [6] performed detailed simulations of liquid injection in still air, obtaining detailed insights on the formation of ligaments and drops during the primary atomization process. Delteil et al. [12] analyzed in detail the break-up of a water jet in the wind-induced regime. More recently, Salvador et al. [13] studied the influence of mesh size in Diesel spray simulations. Grosshans et al. [14] analyzed the influence of various parameters as nozzle turbulence, cavitation bubbles, density and viscosity liquid-gas ratio in the final size of droplets. Finally, Shao et al. [15] performed detailed simulations of the swirling liquid primary atomization process. In most of the cited works, up to several hundreds millions control volumes are used to carry out detailed simulations of the jet behavior, demonstrating that the accurate DNS of complete atomization phenomena can lead to quality results. However, the huge computational cost of such simulations makes them unfeasible for common resources, as indicated by the huge numbers reported in Tab. 4.1. As explained in Chapter. 3, our strategy to improve the feasibility of multiphase flow simulations, in particular, regarding atomization phenomena, consists in the adoption of the Adaptive Mesh Refinement (AMR) technique.

Author	type of simulations	Re_l	CVs
Desjardins et al. [8]	coaxial jet	1336	3.4×10^7
Desjardins et al. [8]	diesel injection	5000	up to 4×10^8
Shinjo and Umemura [6]	liquid injection	1470	6×10^9

Table 4.1: Size of computational domains reached by some authors when performing detailed numerical simulations of high-speed liquid injection phenomena.

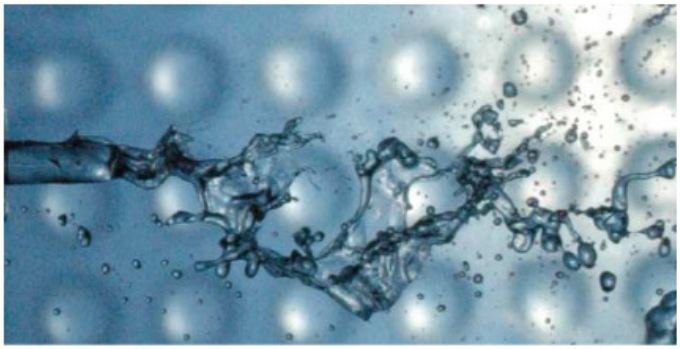

(a)

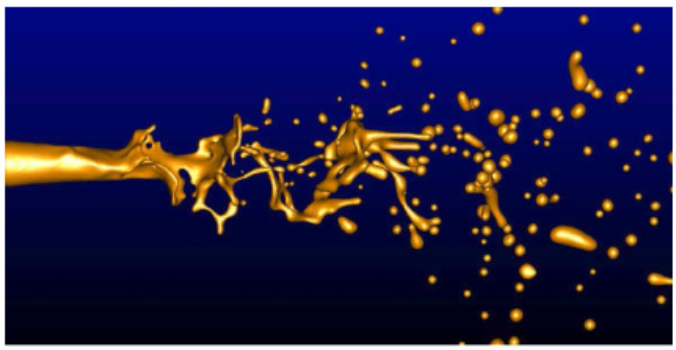

(b)

Figure 4.1: Comparison of flow evolution obtained in coaxial jet experiments by Desjardins et al. [8], $Re_l = 1336$, $We_g = 321$.

Present work In this Chapter, we report the numerical results which were obtained in the analysis of various break-up and atomization phenomena. In particular, in Sec. 4.2, we demonstrate the capability of the numerical framework described in Chapters 1 to 3 to correctly achieve the complete simulation of coaxial jets, from the initial instability to the complete rupture of the liquid core. The proposed contents have been included in [16] and in [17]. In the analyzed cases the Reynolds number of the liquid jet varies between 600 and $\sim 1 \times 10^4$, while the Weber number, which indicates the aerodynamic pressure exerted by the gas on the liquid, ranges between $\sim 2 \times 10^2$ and $\sim 5 \times 10^3$. The numerical results are compared with the empirical relation obtained in experimental works by [18] and by [19] in the context of round-water jet break-up.
In Sec. 4.3, the injection of a liquid flux in a quiescent air environment is studied. The basic set-up is simulated for a wide range of physical parameters as the inlet velocity of the liquid, the density of the gas, and the surface tension coefficient. Our aim is to propose some additional insights to the atomization literature, by studying numerically the atomization regime as function of these input parameters. Hence, the various tests are placed on break-up regime maps as function of dimensionless parameters, as Re_l, We_g and Oh, to be compared with the correlations found in literature.

Dimensionless numbers in two phase jets The nature of break-up instability of liquid-gas systems depends on the dimensionless parameters of the fluids, i.e. the Weber number, We —fluid inertia over surface tension ratio—, the Reynolds number, Re —fluid inertia over viscous forces ratio—, and the momentum flux ratio, M, defined as

$$\mathrm{We}_i = \frac{\rho_i u_i^2 D}{\sigma}, \quad \mathrm{Re}_i = \frac{\rho_i u_i D}{\mu_i}, \quad M = \frac{\rho_g u_g^2}{\rho_l u_l^2}, \tag{4.1}$$

where i refers to liquid, l, or gas, g, respectively, and D is the characteristic diameter of the liquid. In the case of liquid flows dispersed into quiescent non-dense environments, an important parameter is the Ohnesorge number

$$\mathrm{Oh} = \frac{\mu_l}{\sqrt{\rho_l \sigma D}}, \tag{4.2}$$

defined as the ratio between viscous forces, that tend to keep the flow stable, and the product of inertia and surface tension that tend to break the liquid surface.

4.2 Coaxial Jet

The 3-D coaxial jet physics, consisting in the coaxial injection of two liquid and gas streams, embraces a large range of industrial operations. Some examples are the generation of pharmaceutical sprays or the atomization of liquid propellants in combustion engines. The DNS

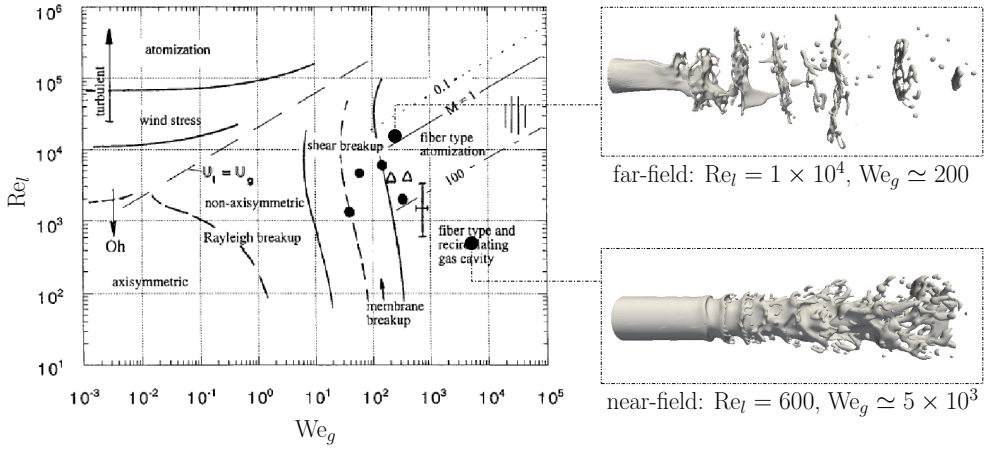

Figure 4.2: Break-up regime diagram of coaxial jets extracted from [18], function of Re_l and We_g parameters. M$= \rho_g u_g^2 / \rho_l u_l^2$ is the momentum flux ratio. On the right, a graphical resume of the cases analyzed in this work is depicted.

of such phenomena would allow a precise knowledge of the liquid dispersed structures, as well as the diameter of droplets resulting from the atomization process. In this section, we first present a review of the information available from experimental literature above coaxial jets. Hence, we show the results obtained in two different numerical simulations and their comparison with semi-empirical relations. In the first case, the objective is pointed on the analysis of the initial destabilization of the jet and its primary break-up. In the second test, the secondary atomization process is analyzed more in detail, focusing on the measurement of the final droplet diameter. Simulations are verified by comparing the characteristic amplitudes with reference value found in literature, i.e. the wavelength of the KH instability, λ_{KH}, the Rayleigh-Taylor wavelength, λ_{RT}, and the Sauter mean diameter of droplets, d_{32}. As for the other instability phenomena presented in Sec. 3.4, this kind of flow is characterized by the parameters presented in Eq. 4.1, while dimensionless time is $t' = t u_l / D$.

4.2.1 A review of the experimental literature.

The atomization of a liquid jet by means of a fast parallel gas stream has been analyzed experimentally by several authors. Their works provide semi-empirical relations for the calculation of characteristic amplitudes, as the wavelength of the KH instability, λ_{KH}, the Rayleigh-Taylor wavelength, λ_{RT}, and the intact jet length, L/D. Each relation presented in this paragraph has to be applied to a specific range of physical conditions and set-up features

of the coaxial jet. In the case of an axial liquid injection, perturbed by a thin parallel laminar gas flow ($D > h$), λ_{KH} can be evaluated by using the formulation proposed by Marmottant and Villermaux [19]. They state that, in case of high We number, the wavelength is proportional to the vorticity layer thickness, δ, and it may be evaluated as

$$\lambda_{\mathrm{KH,mar}} \simeq C\sqrt{\frac{\rho_l}{\rho_g}}\delta, \tag{4.3}$$

with constant $C \simeq 1.2$ for the coaxial axisymmetric configuration. In the case of laminar flow inlet, the vorticity layer thickness can be evaluated as $\delta = 5.6h/\mathrm{Re}_g$ where h is the air-gap inlet length. Similarly, the situation of a small-diameter liquid jet exposed to a large diameter high-speed gas (h≫D) is analyzed by Varga et al. [20]. In this case, the liquid atomization is completed within a few liquid-jet diameters of the nozzle exit. Again, the wavelength is proportional to the vorticity layer thickness, $\delta \propto (\mu_g/(u_g\rho_g))^{0.5}$, and it reads as

$$\lambda_{\mathrm{KH,var}} \simeq 0.055\sqrt{\frac{\rho_l}{\rho_g}}\sqrt{\frac{\mu_g}{\rho_g u_g}}. \tag{4.4}$$

Following the primary destabilization, ligaments appear on wave crests. [19] proposes a relation for the evaluation of λ_{RT}, expressed as as

$$\lambda_{\mathrm{RT,mar}} \simeq 2.8\delta\mathrm{We}_\delta^{-1/3}\left(\frac{\rho_g}{\rho_l}\right)^{-1/3}, \tag{4.5}$$

where We_δ is the Weber number of the vorticity layer, evaluated as $\mathrm{We}_\delta = \rho_g u_g^2\delta/\sigma$. In the case analyzed by [20], λ_{RT} is evaluated as

$$\lambda_{\mathrm{RT,var}} \simeq \frac{\kappa\xi}{\left[u_g\left(1+\sqrt{\frac{\rho_g}{\rho_l}}\right)-u_l\right]u_g^{1/4}}, \tag{4.6}$$

where κ and ξ are a constant factor and a fluid properties factor, respectively, specified in the reference. Once ligaments are generated by the transverse instability, they quickly degenerate into droplets and their size is demonstrated to be proportional to the wavelength of the transverse instability [19, 20, 21]. The latter is much smaller than the axisymmetric (Kelvin-Helmholtz) wavelength. Hence, some proportionality relation between the mean droplet size in the atomized region and λ_{RT} are found in literature, e.g. [19] states that the Droplet Mean Diameter, d_{32}, can be found as

$$d_{32,\mathrm{mar}} \simeq 0.28\lambda_{\mathrm{RT,mar}}. \tag{4.7}$$

Instead, the relation proposed by [20] is

$$d_{32,\mathrm{var}} \simeq 0.68\sqrt{\frac{\sigma\lambda_{\mathrm{KH,var}}}{\rho_g(u_g-u_l)^2}}. \tag{4.8}$$

	Re_l	We_l	Re_g	We_g	CVs
near-field	600	800	1400	4667	2.5×10^6
far-field	9980	137	23400	203	6.6×10^6

Table 4.2: 3D Coaxial Jet: dimensionless numbers and CVs at steady state.

Test	SPC	CPUs	CVs	time [h×CPU]
near-field	JFF	128	∼2.5M	∼720
far-field	Finisterrae	512	∼6.5M	∼500

Table 4.3: Coaxial Jets: computational details of the simulations. SPC is the employed supercomputer, with the related number of CPUs; CVs is the averaged number of dynamic cells involved in the simulations while the time indicates the number of hour (per CPU) for which the case was run. More details above SPC resources are reported in Sec. 1.1.1.

Following the generation of ligaments and droplets, and the increasing destabilization of the liquid structure, a complete break-up of the liquid core occurs at some liquid-jet diameters from the injection. Some authors have analyzed the mean liquid-core intact length, L/D, e.g. Lasheras and Hopfinger [18] provide a general expression that reads as

$$\frac{L}{D} \simeq \frac{6}{\sqrt{M}} \left(1 - \frac{u_l}{u_g}\right)^{-1}. \tag{4.9}$$

4.2.2 Near-field analysis

In this paragraph, we propose the simulation of a coaxial jet with $\mathrm{Re}_l = 600$ and $\mathrm{We}_g \simeq 5 \times 10^3$. These properties are appropriate to show in detail the phases of the destabilization process that lead to primary break-up. The numerical set-up, depicted in Fig. 4.3, consists of a rectangular box, in which a high-speed round liquid jet, with diameter D, is injected at constant horizontal velocity. The coaxial gas flux flows from the outer gap of amplitude h. Dimensionless numbers are reported in Tab. 4.4 (near-field case). At the other boundaries an outflow pressure based condition is applied. A lv.3 AMR is used on a basic mesh of $\sim 3.5 \times 10^5$ cells. At statistical steady state, the mesh counts $\sim 2.5 \times 10^6$ elements, and $(\mathrm{D}/\Delta h)_{\mathrm{lv.3}} = 60$. Alternatively, the achievement of the same resolution on a static Cartesian mesh would require the employment of $\sim 2.1 \times 10^7$ elements. More details above computational data are given in Tab. 4.3.
According to the break-up regime diagram proposed by [18], and reproduced in Fig. 4.2, the flow properties indicate a fiber type atomization regime. In Fig. 4.3, a screenshot of the completely developed coaxial jet is also reported. In the zoom one can observe in detail

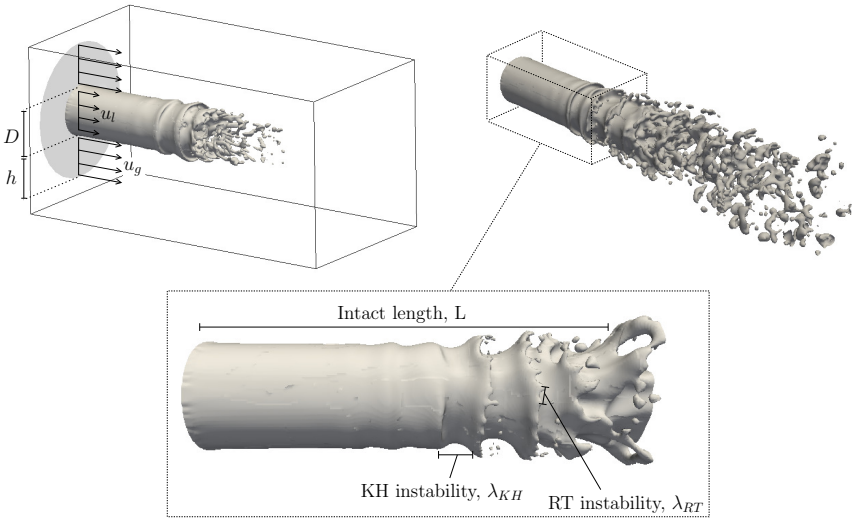

Figure 4.3: 3-D Coaxial Jet: near-field analysis of the jet ($\mathrm{Re}_l = 600$, $\mathrm{We}_g \simeq 5 \times 10^3$). On the top-left, the numerical set-up is depicted. In the top-right screenshot ($t' = 6.3$), the jet surface is first unstabilized by waves, that successively roll-up causing primary atomization. In the zoom, the instability wavelengths λ_{KH}/D and λ_{RT}/D and the intact length of the jet, L/D, are indicated.

the Kelvin-Helmholtz mechanism —characterized by the Kelvin-Helmholtz instability wavelength, λ_{KH}— already described in the case of the 2D jet, which leads to destabilization of the surface with the consequent breakage of the liquid core. Numerical values for λ_{KH}/D, are evaluated from a graphical analysis of the jet pictures and compared to the semi-empirical relationships, being $(\lambda_{\mathrm{KH}}/D)_{\mathrm{num}} \simeq 0.37$. Good agreement is found with the reference value, $(\lambda_{\mathrm{KH}}/D)_{\mathrm{ref}} \simeq 0.43$, evaluated according to Eq. 4.3 [19]. Results are reported in Tab. 4.4. The acceleration of the liquid surface due to the KH instability is the triggering for the further destabilization of the flow. Indeed, the accelerated crest of the waves generated by the first instability, developing on a direction perpendicular to the main flow, are subjected to a Rayleigh-Taylor (transverse) type instability. This consists in the action of the light phase pushing on the heavier one, causing the appearance of ligaments on the top of the wave crests. This phenomenon, characterized by λ_{RT} wavelength, is also highlighted in the zoom of Fig. 4.3. Again, good agreement is found between the numerical value, $(\lambda_{\mathrm{RT}}/D)_{\mathrm{num}} \simeq 0.14$, and the experimental one, $(\lambda_{\mathrm{RT}}/D)_{\mathrm{ref}} \simeq 0.11$, evaluated from Eq. 4.5 [19].

	λ_{KH}/D		λ_{RT}/D		L/D		$d_{32}[\mu m]$	
	num.	ref.	num.	ref.	num.	ref.	num.	ref.
near-field	0.37	0.43 [19] 0.04 [20]	0.14	0.11 [19] 0.014 [20]	4.66	4.75 [18]	-	- -
far-field	-	1.26 [19] 0.1 [20]	-	0.49 [19] 0.077 [20]	4	5 [18]	1180	1377 [19] 157 [20]

Table 4.4: 3D Coaxial Jet: characteristic lengths measured in simulations (num.) and comparison to experimental data (exp.) by [19], [20] and [18].

Altogether, the two instability mechanisms described form the primary break-up process. Following, the amplification of the disturbances downstream leads to the fragmentation of the liquid core and the spreading of droplets downstream. The numerical value for the intact-length of the jet, L/D, is well captured, as $(L/D)_{num} \simeq 4.66$ acceptably matches the experimental data, $(L/D)_{ref} \simeq 4.75$, expressed by Eq. 4.9 [18]. The droplet size is not analyzed in this case as the test was focused on the near-field of the jet and the path traveled by particles is not long enough to show a complete spray atomization. Generally, as shown in Tab. 4.4, the relationships presented by [19] (case of an axial liquid injection perturbed by a thin parallel laminar gas flow), agree with present set-up. On the other side, the data obtained from [20] expressions (case of a small-diameter liquid jet exposed to a large diameter high-speed gas) are different, highlighting a poor compatibility between the models.

4.2.3 Far-field analysis

In the second test, a longer domain is adopted. It allows the analysis of the far-field, where the liquid core is totally broken and the structures resulting from primary break-up have mostly degraded into droplets. The numerical set-up reflects the one used in the near-field analysis, while the new properties are highlighted by dimensionless numbers in Tab. 4.2. $Re_l \simeq 1 \times 10^4$ and $We_g \simeq 200$, indicate a fiber type atomization regime closer to the turbulent zone. At statistical steady state, the mesh is characterized by a dynamic definition of $(D/\Delta h)_{lv.3} = 72$. The minimum definition is set as a result of preliminary tests and it is aimed at guaranteeing the maximum reduction of numerical coalescence between the particles generated by the primary break-up. Further details above computational resources are given in Tab. 4.3.
An overview of the flow evolution is presented in Fig. 4.4. The increase of turbulence with respect to the previous case makes it difficult the graphical identification of the initial instabilities that lead to the core breakdown, λ_{KH} and λ_{RT}. Indeed, the instabilities present a large temporal variability and appear partially overlapped. Furthermore, the low Weber number, We_g, indicates a decrease in the efficiency of the aerodynamic forces in the generation of surface waves. Due to the fact that the instabilities are not clearly distinguished (as in the near-field analysis), their wavelengths are not measured in this case. On the other side, the liquid core intact-length, $(L/D)_{num} \simeq 4$, despite being slightly sub-estimated, is in good

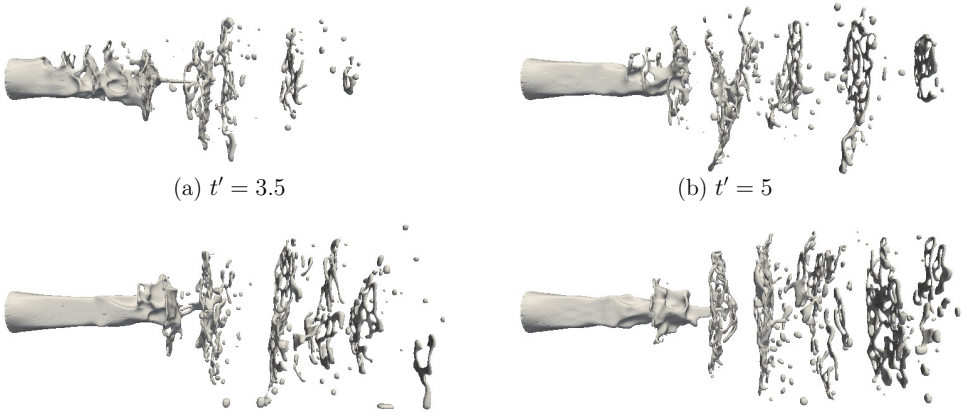

(a) $t' = 3.5$ (b) $t' = 5$

(c) $t' = 6.5$ (d) $t' = 8$

Figure 4.4: 3-D Coaxial Jet: snapshots of the jet simulated in the far-field analysis ($\mathrm{Re}_l \simeq 1 \times 10^4$, $\mathrm{We}_g \simeq 200$).

agreement with the reference value by [18], $(L/D)_{\mathrm{ref}} \simeq 5$, expressed by Eq. 4.9.
After the core break-up, the release of secondary structure occurs by following a constant pulsation. The characteristics of the droplets cloud is studied by analyzing the zone of the domain where, after a few diameter lengths, x/D, the presence of droplets is stable. The analysis is carried out by means of an image treatment that allows the recognition of the diameter of the droplets that pass through a given section —see example in Fig. 4.5(a). The distribution of the drops presents a fairly regular normal distribution after a certain distance from the origin, $x/D \simeq 6$. An example is shown in Fig. 4.5(b). A statistical analysis allows the identification of the Sauter Mean Diameter, d_{32}, to be compared with reference data. The measured value for $(d_{32})_{\mathrm{num}} \simeq 1180$ μm agrees well with reference value, $(d_{32})_{\mathrm{num}} \simeq 1377$ μm, evaluated with Eq. 4.7 [19]. The number of cells per average droplet diameter, $(d_{32}/\Delta h)_{\mathrm{lv.3}} \simeq 8.5$, results appropriate to represent correctly the small interfacial scales.
Also in this case, the relations proposed by [19] prove to be better suited to the representation of the set-up compared to those of [20].

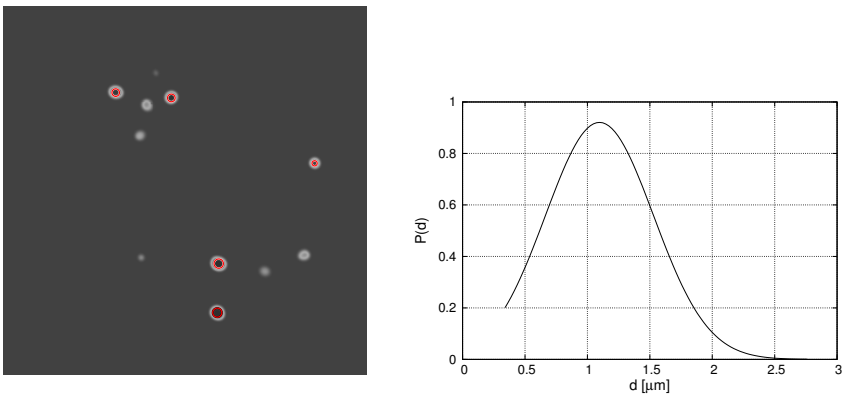

(a) (b)

Figure 4.5: Coaxial Jet: (a) example of a section in which the droplets are marked and their diameter is collected for statistical analysis. (b) Normal distribution of droplet size in the 3-D Jet evaluated at $x/D = 7$ for the far-field analysis.

4.3 Liquid injection

The injection of a liquid flux in a quiescent air environment is a recurrent set-up in industrial applications. Some remarkable examples are the fuel injectors in Diesel engines or some kinds of pharmaceutical sprays. In this section we firstly propose an overview of the physical behavior of this kind of flow, mainly proceeding from theoretical and experimental works. Hence, we will perform a series of simulations aimed at studying the variability of the jet characteristics as function of selected input parameters. In particular, the analyzed variables are Re_l, Oh and We_g. We will compare the pattern obtained in simulations with the one expected from bibliographic study, situating each case on a break-up regime map. All the simulations were carried out on Mare Nostrum IV supercomputer (more details are given in Sec. 1.1.1), by employing up to 288 CPUs during 10–15 days of simulation to reach a statistical steady-state.

4.3.1 Atomization Regimes

As reported by various authors [22, 23, 24], the dispersion pattern of a liquid jet mainly depends on Re_l and Oh parameters. By maintaining the fluids properties fixed, the most universally recognized regimes can be obtained by progressively increasing the fluid intake rate, as described below. In the *dripping regime*, the liquid drops are directly emitted at the nozzle exit. This regime is characterized by a very low value of u_l. When a laminar liquid is injected

at low velocity (*Rayleigh regime*), it forms a ligament that degenerates into droplets. The break-up length, or intact-length of the jet, L, is defined as the length at which the rupture of the ligament occurs, or, alternatively, as the length of the intact jet attached to the nozzle. These drops have a characteristic diameter, d_{drop}, in the order of magnitude of the inlet jet diameter, D. This phenomenon, similar to the dripping of water from a tap, is due to the axisymmetric propagation of Rayleigh waves and is it driven by surface tension forces. For higher Reynolds number (wind-Induced regime), the inertial forces assume greater importance. The jet develops asymmetric instabilities, and releases small droplets, $d_{\text{drop}} < D$. The intact length of the jet initially increases with the velocity, but it starts to recede once a limit Re number has been reached [25]. Some authors as Dumouchel [24] distinguish between *first* and *second wind-induced regime*. In the first wind-induced regime there is a dominant perturbation evolving on the jet interface, which, although showing axisymmetric characteristics, does not produce organized drops as in the Rayleigh regime. The drop-size distribution may become wider, but the diameters are still in the order of magnitude of the jet diameter. On the other side, in the second wind-induced regime the jet column shows a more disturbed shape and different length scales of the growing perturbations. Droplets are generated firstly by a peeling-off of the interface, and, secondly, from the rupture of the liquid core. The large structure that may results from the core break-up may still undergo secondary atomization. For stronger flow rates (Atomization regime), the aerodynamic effects become dominant and the jet undergoes a total atomization close to the inlet. The final size of the droplets —generated by both primary and secondary break-up processes—, span over a wide range of scales, and is defined by means of a statistical value ($d_{\text{SMD,drop}} << D$).

A common way used to characterize the disintegration mechanism consists in the study of the break-up length as function of the inlet velocity. A typical L versus u_l plot is shown in Fig. 4.6(a), extracted from Reitz and Bracco [26]. This plot shows how —as explained before—, L initially increases with the velocity, but it reaches a peak and starts to diminish when aerodynamic forces increase their importance. When entering in the second wind-induced regime, there still remain some confusion over the true shape of the curve: some authors state that the break length remains constant [23], while others as [24, 27] suggest that it may initially increase again. It should be noted that the definition and measurement of the intact length in the most chaotic regimes become more difficult. For these cases, it is helpful to define two different break-up length: the intact-surface length, L_s, indicates the minimum distance at which particles begin to be disrupted from the jet surface; the intact-core length, L or L_c, indicates the length for the complete disintegration of the liquid core. The two lengths coincide in Rayleigh and first wind-induced regime, but become different in the second wind-induced, as the disruption of the jet-surface starts to generate primary droplets. According to [26], the atomization regime is characterized by the fact the L_s is always zero, while being L_c still different to zero.

Several authors have tried to delimit the various regions by means of dimensionless value correlations, usually involving We_l, We_g, Re_l and Oh numbers. For this class of phenomena,

characterized by $u_g = 0$, We_g is defined differently than Eq. 4.1, as

$$\mathrm{We}_g = \frac{\rho_g u_l^2 D}{\sigma}. \tag{4.10}$$

The most commonly used relations to delimit the various regimes are following listed.

- From dripping to Rayleigh regime: as stated by Ranz [28], the dripping from the nozzle no longer occurs if the liquid inertia overcomes surface tension constraining forces. This happens when
$$\mathrm{We}_l > 8 \tag{4.11}$$
- From Rayleigh to first wind-induced regime: the limit comes from linear stability theorem considerations, and, as expressed by Sterling and Sleicher [29], it can be written as
$$\mathrm{We}_g > 1.2 + 3.41\mathrm{Oh}^{0.9} \tag{4.12}$$
- From first to second wind-induced regime: the same Ranz [28] argued that this transition occurs when gas inertia forces reach the magnitude of surface tension forces. This is expressed by
$$\mathrm{We}_g > 13 \tag{4.13}$$
- From wind-induced to atomization regime: the criterion, provided by Miesse [30], comes from empirical considerations, stating that transition occurs when
$$\mathrm{We}_g > 40.3 \tag{4.14}$$

The relation expressed are plotted on the spray break-up regimes (function of We_g and Oh) provided by Faeth [22], and shown in Fig. 4.6(b). However, these relations are not taking into account the role of liquid viscosity. In Reitz and Bracco [26], the jet break-up regimes are represented as function of Re_l and Oh parameters, but, as pointed out by the same authors, the plot does not take into account the effect of gas density or the initial turbulence of the jet. This demonstrates that satisfactory correlations for the regime boundaries are not still available, and that more results from experimental, and, maybe, numerical works are needed to obtain a complete knowledge of the considered phenomena.

4.3.2 Study of inlet velocity variation

In this work we performed simulations of jets with increasing inlet velocity, u_l. The first tests are intended to reproduce some of the laboratory experiments carried out by [23]. However, further simulations were carried out to further investigate the physics of the jet. In the tests described in this section. the physical properties of the fluids correspond to the ones of water

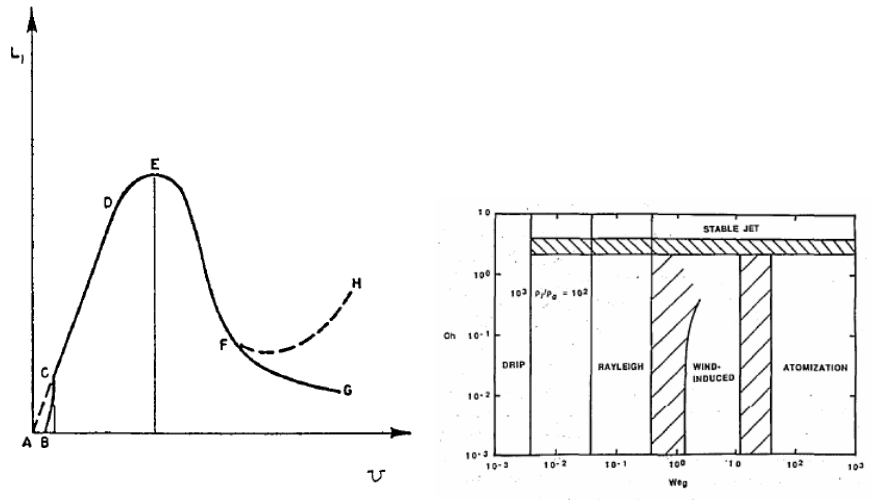

(a) (b)

Figure 4.6: (a) Jet break-up length as function of the inlet liquid velocity, extracted from Reitz and Bracco [26]. (b) Break-up regime map as function of We_g and Oh dimensionless numbers, extracted from Faeth [22].

dispersed into carbon dioxide at 308 K and 6 MPa, hence, the Oh number is kept constant in the experiments, while constantly increasing Re_l and We_g. A summary of the dimensionless numbers used in the simulations is reported in Tab. 4.5. The domain consists of a rectangular box, of sides $42D \times 9D \times 9D$, in which a round liquid jet is injected at constant horizontal velocity, while a pressure based condition is applied at the outflow boundaries. The mesh definition at the interface is dynamically achieved by means of a lv.3 refinement and reaches $(D/\Delta h)_{\mathrm{lv.3}} \simeq 30$. The approximate number of cells at steady-state is indicated in Tab. 4.5. Figs. 4.7 to 4.13 are intended to show the behavior of the different jets during the initial transition phase and at steady-state. The single tests are following described.

- In Fig. 4.7 some screenshots of the flow simulated in Test 1 —characterized by Re_l=227— are reported, as function of dimensionless time $t' = tu_l/D$. As a characteristic feature of the Rayleigh regime, the jet releases droplets with the order of magnitude of its diameter. The average break-up length, that varies in the range of $L/D = 15 \pm 2$, is similar to that reported by [23]. Following, some droplets merge downstream, creating bigger leading drops.

- In Test 2, in which the input speed of the liquid is higher (Re_l=321), L/D is longer than in the previous case, ranging between $L/D = 21 \pm 3$. This is consistent with the behavior of jets in the Rayleigh regime [22], whose pinch-off length become longer with the increase of jet velocity. We also noticed a smaller diameter of the released droplets, and a less relevant downstream merging process, as shown in Fig. 4.8.

- In Test 3, characterized by Re_l=852, one can observe how the growth of instability is no longer axisymmetrical, highlighting an increasing influence of shear stresses as responsible for the jet break-up. This indicates the passage of the jet to the Wind-Induced regime mentioned above. Also the release of droplets from the tip of the jet becomes irregular, as shown in the screenshots of Fig. 4.9. The intact length of the jet results increased also in this case, $L/D \simeq 40$.

- In Test 4 (Fig. 4.10), we can observe a path similar to the one shown in Test 3, characterized by the growth of non-symmetrical instabilities and the irregular rupture of the ligament, which occurs at $L/D \simeq 54$, very far from the inlet. We can observe a higher peeling off of droplets from the jet surface, in comparison to Test 3, characteristics of the second wind-induced regime.

- In Test 5, the scenario changes again, as demonstrated by screenshots of Fig. 4.11. The liquid column is quickly made unstable by asymmetrical perturbations, that lead to the rapid and violent breakage of the core. The liquid then disperses in a myriad of small particles, whose diameter distribution can be studied through a statistical study and expressed as a function of a mean diameter and a variance. The intact length is subjected to a strong retreat, as it fluctuates around $L/D \simeq 26$. The same pattern is observed in Tests 6 and 7 (Figs. 4.12 and 4.13), where the intact length results stabilized around

	Re_l	We_g	Oh	L/D	CVs
Test 1 (T1)	227	0.8	0.01	~ 15	3.6×10^6
Test 2 (T2)	321	1.7	0.01	~ 21	4.0×10^6
Test 3 (T3)	852	12	0.01	~ 40	4.3×10^6
Test 4 (T4)	1700	47	0.01	~ 54	4.5×10^6
Test 5 (T5)	2500	102	0.01	~ 27	7.2×10^6
Test 6 (T6)	3400	189	0.01	~ 21	1.1×10^7
Test 7 (T7)	5100	426	0.01	~ 24	1.5×10^7

Table 4.5: Water Jet: dimensionless numbers of the injected liquid and intact length of the jet. The approximate number of CVs is also indicated.

	Re_l	$\mathrm{d_{mean}/D}$
Test 5	2500	0.125
Test 6	3400	0.12
Test 7	5100	0.11

Table 4.6: Water Jet: mean size of the particles measured in the cases identifiable as belonging to the Atomization regime.

$L/D \simeq 21 : 24$. In these cases, clearly identifiable as belonging to the Atomization regime, we measured the size of the small droplets resulting from the disruption of the core using the method proposed in Sec. 4.2.3. As expected, their size decreases with the increase in the number of Reynolds, reaching the lowest value of $\mathrm{d_{mean}}/D = 0.11$ in Test 7. Tab. 4.6 shows the mean particle size measured in sections $x/D = 27 : 29$, immediately after the core break-up zone in all the analyzed cases.

As explained in the previous section, the analysis of the variation of the break-up length with the inlet liquid speed, constitutes a qualitative verification of the jet study. As shown in Fig. 4.14, which represents the trend of the dimensionless value of L as a function of Re_l, L/D increments initially, passing from the Rayleigh regime to the first-wind induced one. Subsequently, it undergoes a reduction in the transition from wind-induced to atomization; then, it stabilizes to a nearly constant value. The graph shows the trend of the same magnitude measured in the experimental work of Badens et al. [23]. We can observe that, despite following the same pattern, this function has a significantly lower scale. We are not sure of the explanation of this fact, but probably, the *real* jet of Badens presents an inlet turbulence coming from the injection mechanism —not present in our inlet numerical model—, which may accelerate the transition between the different regimes.

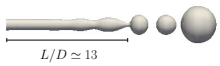

(a) $t' = 24$

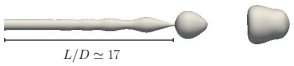

(b) $t' = 32$

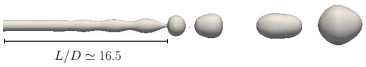

(c) $t' = 42$

(d) $t' = 60$

Figure 4.7: Water Jet (test 1): screenshots of the flow characterized by $\mathrm{Re}_l = 227$. Dripping/Rayleigh Regime.

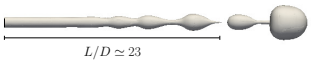

(a) $t' = 27$

(b) $t' = 38$

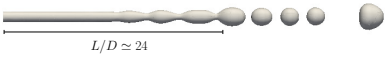

(c) $t' = 44$

(d) $t' = 53$

Figure 4.8: Water Jet (test 2): screenshots of the flow characterized by $\mathrm{Re}_l = 321$. Rayleigh Regime.

(a) $t' = 45$

(b) $t' = 63$

Figure 4.9: Water Jet (test 3): screenshots of the flow characterized by $\mathrm{Re}_l = 852$. First Wind-Induced Regime.

(a) $t' = 41$

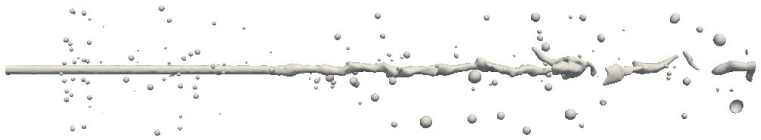

(b) $t' = 63$

Figure 4.10: Water Jet (test 4): screenshots of the flow characterized by $\mathrm{Re}_l = 1700$. Second Wind-Induced Regime.

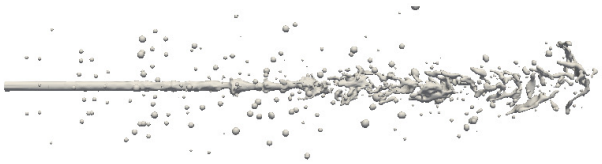

(a) $t' = 45$

(b) $t' = 70$

Figure 4.11: Water Jet (test 5): screenshots of the flow characterized by $\mathrm{Re}_l = 2500$. Atomization Regime.

(a) $t' = 45$

(b) $t' = 70$

Figure 4.12: Water Jet (test 6): screenshots of the flow characterized by $\mathrm{Re}_l = 3400$. Atomization Regime.

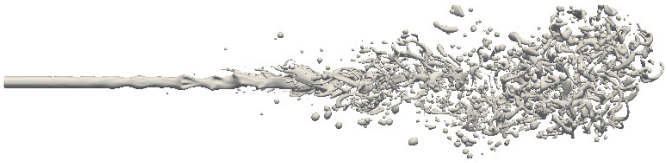

(a) $t' = 81$

(b) $t' = 122$

Figure 4.13: Water Jet (test 7): screenshots of the flow characterized by $\mathrm{Re}_l = 5100$. Atomization Regime.

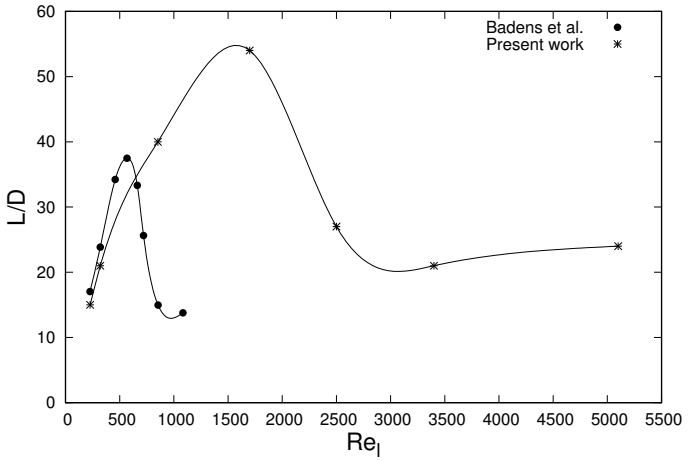

Figure 4.14: Variation of the dimensionless break-up length of the jet as a function of the inlet Reynolds number, Re_l. The behavior obtained in our simulations is plotted together with the one obtained by Badens et al. [23] in their experimental work.

4.3.3 Other parametric studies

The study of the coaxial jet physics is extended by analyzing the effect of physical parameters as the gas density/pressure and the surface tension.

Effect of gas density

In this section we comment the observations obtained from the study the effect of the increase of the gas pressure on the jet dynamics. Some of the cases listed in the past section (Tests 3, 4 and 6) have been repeated by increasing the density of the gas and, consequently, its pressure. This is reflected in the increase of We_g, indicating the action of the aerodynamic forces on the liquid jet. The cases analyzed are resumed in Tab. 4.7 and following commented.

- In Test 3–b, we can notice a higher frequency of the perturbations, leading to an earlier ligament rupture than in Test 3 —as depicted in Fig. 4.15—, namely, a reduction of the break-up length. However, the structures released from the break-up have similar dimensions and no particular regime change is observed.
- Similarly, in Test 4–b, a breakthrough in the core break-up length is observed, due to the increased frequency of excitation. However, despite a noticeable increment in the fragmentation of structures, we can not observe a closer proximity to the atomization regime —see comparison reported in Fig. 4.16.

	Re_l	p[MPa]	We_g	Oh	L/D	d_{mean}/D	CVs
Test 3	852	60	12	0.01	~ 40	–	4.3×10^6
Test 3–b (T3–b)	852	80	42	0.01	~ 25	–	3.8×10^6
Test 4	1700	60	47	0.01	~ 54	–	4.5×10^6
Test 4–b (T4–b)	1700	80	166	0.01	~ 26	–	6.5×10^6
Test 6	3400	60	189	0.01	~ 21	0.12	1.1×10^7
Test 6–b (T6–b)	3400	80	667	0.01	~ 20	0.13	1.2×10^7

Table 4.7: Water Jet: parameters of the simulations in the series of variable We_g number.

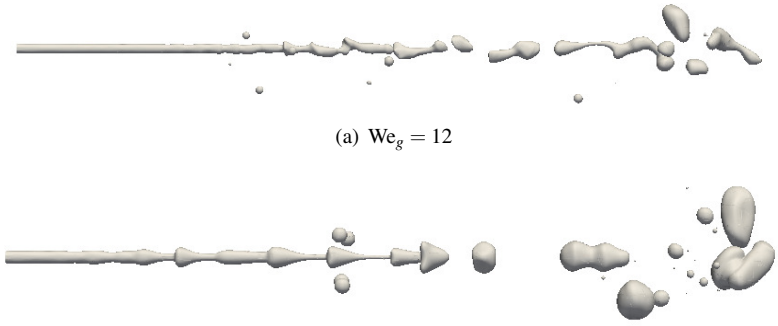

(a) $We_g = 12$

(b) $We_g = 42$

Figure 4.15: Water Jet: $Re_l = 852$, effect of the gas density increase (Test 3 and Test 3–b). The pictures refer to the same t^*, approximately.

- In graphical comparison between Test 6–b and Test 6 —Fig. 4.17—, we can notice again an increased frequency of excitation of the perturbations. However, the final size of particles does not result smaller than Test 6, being both close to $d_{mean}/D \sim 0.12$ after the rupture of the liquid core. A particular feature of the lower pressure case, is the presence of a fine droplet cloud which surrounds the jet in the proximity of the break-up length zone.
- In general, in the high pressure cases, the generation of droplets seems more connected to the stripping of long ligaments than to the instantaneous peeling-off from the jet structures.

Effect of surface tension coefficient

Some of the cases previously analyzed (Tests 2, 3 and 4) are repeated using a lower surface tension value. This effect causes an increase in the Ohnesorge number (and in We_g), and, con-

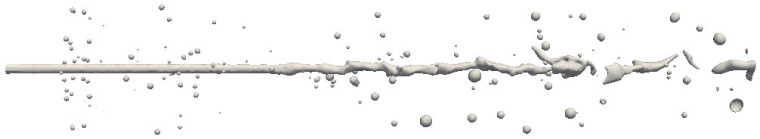

(a) $\mathrm{We}_g = 47$

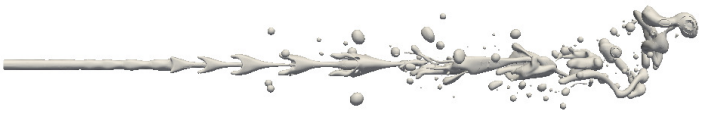

(b) $\mathrm{We}_g = 166$

Figure 4.16: Water Jet: $\mathrm{Re}_l = 1700$, effect of the gas density increase (Test 4 and Test 4–b). The pictures refer to the same t^*, approximately.

(a) $\mathrm{We}_g = 189$

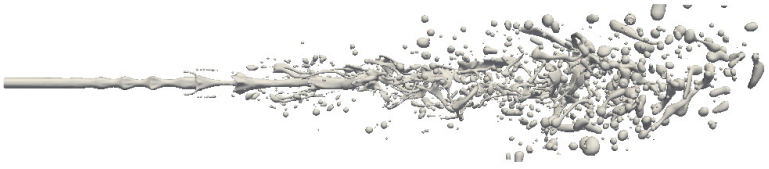

(b) $\mathrm{We}_g = 667$

Figure 4.17: Water Jet: $\mathrm{Re}_l = 3400$, effect of the gas density increase (Test 6 and Test 6–b). The pictures refer to the same t^*, approximately.

	Re_l	We_g	Oh	L/D	CVs
Test 2	321	1.7	0.01	~ 21	4.0×10^6
Test 2–c (T2–c)	321	5.2	0.017	~ 54	4.0×10^6
Test 3	852	12	0.01	~ 40	4.3×10^6
Test 3–c (T3–c)	852	36	0.017	~ 70	4.0×10^6
Test 4	1700	47	0.01	~ 54	4.5×10^6
Test 4–c (T4–c)	1700	146	0.017	~ 39	8.6×10^6

Table 4.8: Water Jet: parameters of the simulations in the series of variable Oh number.

(a) Oh= 0.01

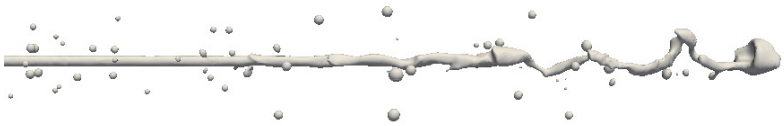

(b) Oh= 0.017

Figure 4.18: Water Jet: $\mathrm{Re}_l = 321$, effect of the surface tension increase (Test 2 and Test 2–c). The pictures refer to the same t^*, approximately.

sequently, a stronger tendency of the structure to break under the effect of perturbations. The cases analyzed are resumed in Tab. 4.8. Respectively, we can notice the following transitions.

- In Test 2–c, the regime has passed from a Rayleigh to a wind-induced one (between first and second), as indicated by the rise of non-symmetrical instabilities (Fig. 4.18) and the longer break-up length.
- In Test 3–c, depicted in Fig. 4.19, we can see a stronger peeling-off of droplets, indicating the passage from first to second wind-induced regime.
- In Test 4–c, the regime has clearly passed from wind-induced to atomization, as shown in Fig. 4.20. The break-up length is substantially reduced.

4.3.4 Atomization Map

In this paragraph, all the simulations performed in this work are collected and classified as function of dimensionless parameters; in particular, Re_l versus Oh, and We_g versus Oh. The

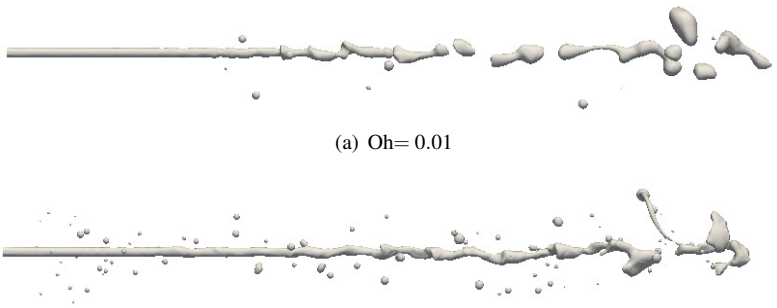

(a) Oh= 0.01

(b) Oh= 0.017

Figure 4.19: Water Jet: $\mathrm{Re}_l = 852$, effect of the surface tension increase (Test 3 and Test 3–c). The pictures refer to the same t^*, approximately.

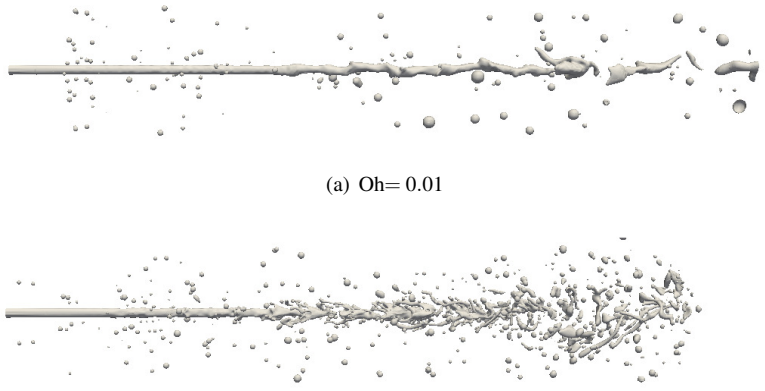

(a) Oh= 0.01

(b) Oh= 0.017

Figure 4.20: Water Jet: $\mathrm{Re}_l = 1700$, effect of the surface tension increase (Test 4 and Test 4–c). The pictures refer to the same t^*, approximately.

scope is to compare the pattern found in numerical experiments with the one dictated by the empirical relationships found in literature for the identification of the disintegration regimes. As explained in Sec. 4.3.1, the limit between the regimes is usually described as a function of the Weber number. Given the characteristics of the fluids used in our simulations, we can however plot the lines on a Re_l vs. Oh chart, as shown in Fig. 4.21. In the analysis of the tests proposed in Sec. 4.3.2, we can observe the following features: Test 1 lies in its proper range, being a pure Rayleigh break-up case. Instead, Test 2, while also being a Rayleigh case, lies slightly inside the first wind-induced. Test 3 is at the limit between 1°W.I. and 2°W.I., while Test 4, which we identified as belonging to 2°W.I., lies slightly inside the atomization regime region. Tests 5 and 6 are clearly within the atomization regime, as previously observed. The tests resumed in the variable surface tension series proposed in Sec. 4.3.3 can be plotted on the same chart as well. Test 2–c lies correctly in 1°W.I., while Test 3–c lies at the limit between 2°W.I. and Atomization, despite being closer to the wind-induced regime. Finally, Test 4–c fully falls inside the Atomization range. In Fig. 4.21 we have plotted, together with the black lines indicating the correlations taken from literature, two red lines representing the approximate transition zones observed in our simulations. The two lines represent the transition between Rayleigh to 1°W.I., and from 2°W.I. to Atomization, approximately. We have not plotted the transition line between 1°W.I. and 2°W.I., because we believe that the information available is not complete enough to allow for a clear distinction between these two regimes. As you can see, the red lines lie slightly to the right of the black ones. Such delay in transitions may be due to the fact that we does not consider the effect of the initial jet turbulence in numerical simulations, which would favor a higher jet instability for lower inlet velocities. The same correlations, e.g. that of Miesse [30] —limit between 2°W.I. and Atomization regimes—, come from empirical considerations that may take into account the initial turbulence of the jet.

As indicated before, the effect of the gas density–pressure is not considered in the Re_l vs. Oh chart (for this reason, Tests 3–b, 4–b and 6–b does not appear in this plot). Hence, to depict this effect on a graphical way, we also propose a We_g vs. Oh plot —see Fig. 4.22— , reporting the regime limits extracted from literature and obtained from our experiments. By placing the points corresponding to our simulations on the chart, we can get the same information extracted from the previous analysis (Re_l vs. Oh). Additional considerations can be made on tests proposed in the variable density series proposed in Sec. 4.3.3. Test 3–b lies at the limit between 2°W.I. and Atomization, although it is still a pure W.I.. Test 4–b, lies incorrectly inside atomization, not having the characteristics, while T6–b is within its proper range. Our conclusions is that the effect of gas density is not correctly caught on this plot.

4.4 Conclusions

In the first part of this chapter, we describe the results obtained when performing the complete simulation of 3-D coaxial jets at Re_l=600 and $Re_l \simeq 1.0 \times 10^4$, respectively. The simulations

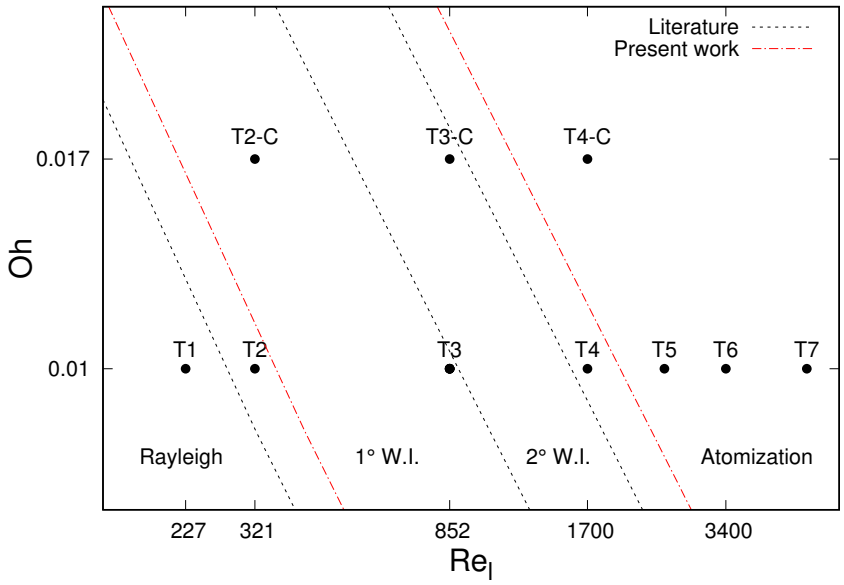

Figure 4.21: Atomization regime map as a funtion of Re_l and Oh. Black points represent the cases analyzed by means of numerical simulations in the present work. Black lines are the regime transition lines obtained from literature and exposed in Sec. 4.3.1. Red lines represent the approximate transition zones observed in our simulations.

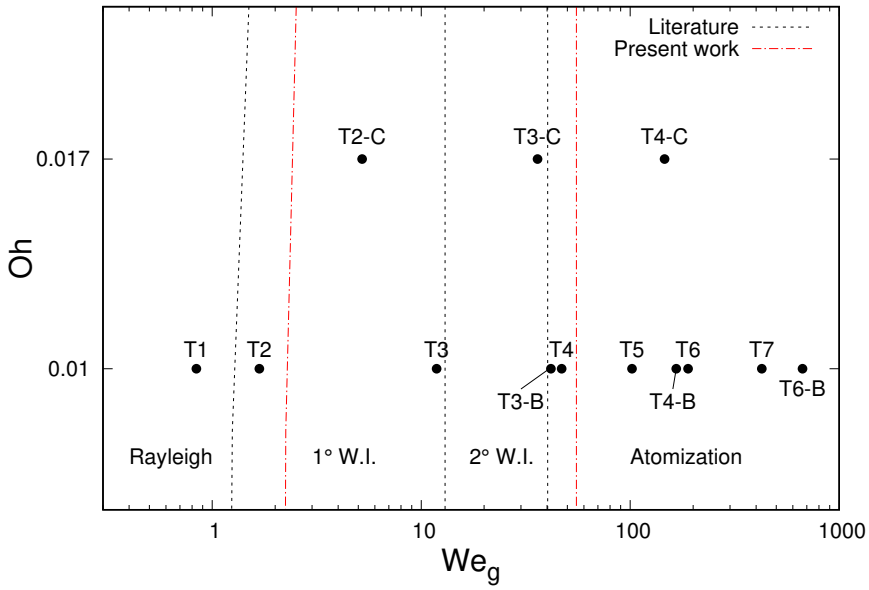

Figure 4.22: Atomization regime map as a funtion of We$_g$ and Oh. Black points represent the cases analyzed by means of numerical simulations in the present work. Black lines are the regime transition lines obtained from literature and exposed in Sec. 4.3.1. Red lines represent the approximate transition zones observed in our simulations.

are validated by observing the physical features of the flow, and comparing them with experimental sources. In particular, in the near-field test, where the primary instabilities lead to the core break-up, we have measured the wavelengths connected to both Kelvin-Helmholtz and Rayleigh-Taylor instabilities, finding good agreement with the semi-empirical relations proposed by Marmottant and Villermaux [19]. Hence, in a second test, we focused on the study of the far-field region, where the secondary structures have mostly degraded into droplets. Here we have evaluated the statistical distribution of droplets, obtaining a Sauter Mean Diameter close to that indicated by [19].
In the second part, after introducing some theoretical and experimental studies concerning the physics of liquid sprays, we conducted a series of simulations to analyze their physical behavior as function of different input parameters. The set-up in question has the same characteristics as that proposed by Badens et al. [23], and some of the tests performed are equivalent. In a first study (Tests 1–7) we analyzed the variation of the break-up regime according to the input speed, and therefore the Reynolds number ($\mathrm{Re}_l = 227 : 5400$). The characteristics of the various regimes encountered when increasing Re_l are consistent with the observations made in various studies [22, 24, 26], allowing to qualitatively recognize the four stages of instability of a jet: Rayleigh, 1°and 2°Wind-Induced and Atomization. The intervals in which these transitions occur are not in line with those observed by Badens et al. in their experiments, probably because our simulations do not take into account the initial state of the jet. This is laminar in current numerical simulations and probably already turbulent due to the effect of the injector in laboratory experiments. Further simulations were performed by varying the magnitude of other parameters such as gas density (Tests 3–b, 4–b and 6–b) and surface tension (Tests 2–c, 3–c, 4–c), allowing additional observations. The various simulations have been placed inside the regime maps, such as Re_l vs. Oh, and We_g vs. Oh. We noted that, despite finding a good agreement in most of the analyzed cases, the transition zones observed in the simulations are slightly shifted to the right compared to those found in the literature. Once again, the interpretation we give to this effect is the absence of an initial jet turbulence in the numerical set-up. Finally, we observed that the effect of increasing gas density, which can be viewed on the We_g vs. Oh chart, is not properly represented in the simulations. We ignore the reasons for such mismatch.

Bibliography

[1] G. Tryggvason, R. Scardovelli, S. Zaleski, Direct numerical simulations of gas–liquid multiphase flows, Cambridge University Press, 2011.

[2] A. Vallet, A. Burluka, R. Borghi, Development of a eulerian model for the atomization of a liquid jet, Atomization and Sprays 11 (2001) 619–642.

[3] M. Gorokhovski, M. Herrmann, Modeling primary atomization, Annual Review of Fluid Mechanics 40 (2008) 343–366.

[4] E. Labourasse, D. Lacanette, A. Toutant, P. Lubin, S. Vincent, O. Lebaigue, J.-P. Caltagirone, P. Sagaut, Towards large eddy simulation of isothermal two-phase flows: Governing equations and a priori tests, International Journal of Multiphase Flow 33 (2007) 1–39.

[5] M. Herrmann, A sub-grid surface dynamics model for sub-filter surface tension induced interface dynamics, Computers & Fluids 87 (2013) 92–101.

[6] J. Shinjo, A. Umemura, Simulation of liquid jet primary breakup: Dynamics of ligament and droplet formation, International Journal of Multiphase Flow 36 (2010) 513–532.

[7] O. Desjardins, V. Moureau, H. Pitsch, An accurate conservative level set/ghost fluid method for simulating turbulent atomization, Journal of Computational Physics 227 (2008) 8395–8416.

[8] O. Desjardins, J. McCaslin, M. Owkes, P. Brady, Direct numerical and large-eddy simulation of primary atomization in complex geometries, Atomization and Sprays 23 (2013).

[9] T. Ménard, S. Tanguy, A. Berlemont, Coupling level set/vof/ghost fluid methods: Validation and application to 3d simulation of the primary break-up of a liquid jet, International Journal of Multiphase Flow 33 (2007) 510–524.

[10] R. Lebas, T. Menard, P.-A. Beau, A. Berlemont, F.-X. Demoulin, Numerical simulation of primary break-up and atomization: Dns and modelling study, International Journal of Multiphase Flow 35 (2009) 247–260.

[11] D. Fuster, A. Bagué, T. Boeck, L. Le Moyne, A. Leboissetier, S. Popinet, P. Ray, R. Scardovelli, S. Zaleski, Simulation of primary atomization with an octree adaptive mesh refinement and vof method, International Journal of Multiphase Flow 35 (2009) 550–565.

[12] J. Delteil, S. Vincent, A. Erriguible, P. Subra-Paternault, Numerical investigations in rayleigh breakup of round liquid jets with vof methods, Computers & Fluids 50 (2011) 10–23.

[13] F. Salvador, J. Romero, M. Roselló, D. Jaramillo, Numerical simulation of primary atomization in diesel spray at low injection pressure, Journal of Computational and Applied Mathematics 291 (2016) 94–102.

[14] H. Grosshans, A. Movaghar, L. Cao, M. Oevermann, R.-Z. Szász, L. Fuchs, Sensitivity of VOF simulations of the liquid jet breakup to physical and numerical parameters, Computers & Fluids 136 (2016) 312–323.

[15] C. Shao, K. Luo, Y. Yang, J. Fan, Detailed numerical simulation of swirling primary atomization using a mass conservative level set method, International Journal of Multiphase Flow 89 (2017) 57–68.

[16] E. Schillaci, O. Lehmkuhl, O. Antepara, A. Oliva, Direct numerical simulation of multiphase flows with unstable interfaces, Journal of Physics: Conference Series 745 (2016).

[17] E. Schillaci, O. Antepara, N. Balcázar, A. Oliva, A dynamic mesh refinement strategy for the simulation of break-up phenomena in two-phase jets, Under Review (????).

[18] J. Lasheras, E. Hopfinger, Liquid jet instability and atomization in a coaxial gas stream, Annual Review of Fluid Mechanics 32 (2000) 275–308.

[19] P. Marmottant, E. Villermaux, On spray formation, Journal of Fluid Mechanics 498 (2004) 73–111.

[20] C. Varga, J. Lasheras, E. Hopfinger, Initial breakup of a small-diameter liquid jet by a high-speed gas stream, Journal of Fluid Mechanics 497 (2003) 405–434.

[21] F. Rayana, A. Cartellier, E. Hopfinger, Assisted atomization of a liquid layer: investigation of the parameters affecting the mean drop size prediction, in: Proceedings of the International Conference on Liquid Atomization and Spray Systems (ICLASS), Kyoto, Japan.

[22] G. Faeth, Structure and atomization properties of dense turbulent sprays, in: Symposium (International) on Combustion, volume 23, Elsevier, pp. 1345–1352.

[23] E. Badens, O. Boutin, G. Charbit, Laminar jet dispersion and jet atomization in pressurized carbon dioxide, The Journal of supercritical fluids 36 (2005) 81–90.

[24] C. Dumouchel, On the experimental investigation on primary atomization of liquid streams, Experiments in fluids 45 (2008) 371–422.

[25] J. Eggers, E. Villermaux, Physics of liquid jets, Reports on progress in physics 71 (2008) 036601.

[26] R. Reitz, F. Bracco, Mechanism of atomization of a liquid jet, The Physics of Fluids 25 (1982) 1730–1742.

[27] M. McCarthy, N. Molloy, Review of stability of liquid jets and the influence of nozzle design, The Chemical Engineering Journal 7 (1974) 1–20.

[28] W. Ranz, On sprays and spraying, Dep. Eng. Res., Penn State Univ. Bull 65, 1956.

[29] A. M. Sterling, C. Sleicher, The instability of capillary jets, Journal of Fluid Mechanics 68 (1975) 477–495.

[30] C. Miesse, Correlation of experimental data on the disintegration of liquid jets, Industrial & Engineering Chemistry 47 (1955) 1690–1701.

5

A single-phase model for the numerical simulation of free-surface flow

Main contents of this chapter have been published in:

E.Schillaci, L.Jofre, N.Balcázar, O.Lehmkuhl and A. Oliva. A level-set aided single-phase model for the numerical simulation of free-surface flow on unstructured meshes. *Computers & Fluids*, 140:97–110, 2016.

Abstract. A new single-phase scheme for the numerical simulation of free-surface problems on 3-D unstructured meshes is presented. The flow field is obtained from the discrete solution of the incompressible Navier-Stokes equations, whereas a conservative level-set method is employed to capture fluid interfaces on an Eulerian approach. The scheme is based on a novel treatment of the interface for the deactivation of the light phase, allowing an optimization of the classic two-phase model for the cases in which the influence of the lighter phase is negligible. The deactivation is performed by directly imposing the appropriate pressure at the surface boundary, and, unlike similar approaches, without the need to treat near-interface velocities. The method is validated against various analytical and experimental references, demonstrating its potential on both hexahedral and unstructured meshes. Moreover, it shows higher numerical stability in comparison to two-phase solvers, as well as significant advantages in terms of computational performance.

Additional content has been published in: E.Schillaci, F.Favre, O.Antepara, N.Balcázar and A. Oliva. Numerical study of an impulse wave generated by a sliding mass. *International Journal of Computational Methods and Experimental Measurements*, 6:98–109, 2018.

5.1 Introduction

In this Chapter we will introduce the possibility of specifying the multiphase solver for the cases that involve a free-surface flow. In the next paragraphs, we will explain in detail what is meant for free-surface flow, and which are the necessary conditions for adopting such simplification. Hence, after listing the works dealing with this subject in literature, we will provide our proposal for solving the problem.

Single-phase approximation In the past sections of this Thesis, the interface-capturing strategies are coupled to the discrete solution of the Navier-Stokes equations to provide a numerical framework for the simulation of all the phases involved in a multiphase flow. In this Chapter, we will refer to this scheme as full-domain model. However, in some engineering applications involving the interaction of two fluids, usually a liquid and a gas, the classic two-phase simulation can be simplified by limiting the calculations to the single liquid phase. This occurs when the interface between the two phases behaves as a free-surface, i.e. it is subjected to constant perpendicular normal stress and it is free from parallel shear solicitations. In such cases, the pressure at the free-surface can be approximated to the free-stream value, e.g. atmospheric pressure. This simplification applies only to the cases in which the gaseous phase has no effect on the physics of the problem. Hence, it should not be expected the formation of gaseous bubbles, nor the presence of stresses in the liquid phase generated by the gas, due for example to its pressurization in a section of the domain. These assumptions are usually fulfilled in ocean engineering problems, such as the simulation of wave motion and its interaction with submerged or semi-submerged obstacles. The adoption of this strategy, to which we will refer to as single-phase model, can lead to consistent savings in computational time as a result of the deactivation of the light phase. Moreover, the transition from a full-domain model to a single-phase one simplifies the problem, resulting in more stable numerical schemes due to the disappearance of high density ratios along the interface. In the deactivation process, the additional resources spent for the individuation of the transition region, as well as for the enforcement of pressure and velocity conditions at the interface, are counterbalanced by the computational memory saved to update numerical operators in the light phase. Therefore, as demonstrated in this work, the single-phase scheme reduces significantly the time-to-solution and memory requirements with respect to the full-domain approach, while not appreciably affecting the physics of the problem.

State-of-the-art In the past years, researchers have developed various types of single-phase models, mainly differing in the way in which the process of deactivating the light phase is carried out. To mention some, in Löhner et al. [1], VOF and LS techniques are used to advect the interface, and the scalar fields are deactivated for the light phase. Then, in order to ensure the correct advection of the volume fractions, pressure and velocity are evaluated at the interface by extrapolation from the values of the points inside the liquid region. Lv et al. [2] employed a similar scheme for the pressure-velocity extension, but the interface capturing was accomplished by means of a hybrid LS/VOF strategy. Kleefsman et al. [3] utilized a VOF method and interpolated both pressure and velocities at the interface. Carrica et al. [4] and Di Mascio et al. [5] used Standard Level-Set approaches, imposed the pressure value at the free-surface to enforce the jump conditions by directly intervening on the pressure equation, and extended the velocity field in order to correctly transport the level-set function. Finally, Enright et al. [6] applied hybrid particle/Level-Set methodologies to impose internal pressure boundary conditions, and extrapolated velocity across the interface.

Current proposal In this Chapter, which reflects the work published in Schillaci et al. [7], we propose a novel strategy to solve the liquid phase on an Eulerian grid by explicitly imposing the pressure at the free-surface and deactivating the light phase. The interface is transported by means of the CLS method proposed and implemented by Balcázar et al. [8, 9] and reviewed in Sec.1. At the same time, the CLS method facilitates the deactivation process, as the same level-set function provides a convenient tool to identify the interface. The resolution of the Navier-Stokes equations on the interfacial region avoids the requirement to extrapolate the velocity field. Consequently, the costly process of evaluating interpolation stencils at every iteration is spared, thus, making the algorithm easier to implement and resulting in faster computations. In order to check the convergence of the numerical method, the verification process begins with the analysis of the spurious currents on the interface of a static liquid column. Next, the method is tested on a series of problems in which the assumptions of free-surface and the physical independence from the light phase —no bubble formation, no gas pressurization— are fulfilled. These correspond to the sloshing of a linear wave inside a fixed basin, the viscous damping of a solitary wave in shallow water, and the dam-breaking problem; first for the classic 2-D case, and second, in a more complex 3-D configuration. The results are compared to the ones obtained by means of the full-domain model and to the available experimental data, focusing on the discrepancy between the results and the savings in computational time. A possible industrial application of the free-surface model, partially presented in Schillaci et al. [10], is discussed in Appendix A, where we study numerically the hydrodynamic behavior of an Oscillating Water Column (OWC) device for the extraction of mechanical energy from ocean waves. A similar set-up was analyzed in [9].
In addition to the content that reflect the work presented in [7, 10], we propose an extension of the free-surface model, including the possibility of considering the interaction with a moving object by means of the Immersed Boundary Method —details on the numerical model are

given in Sec. 1.3.5. The model is firstly validated by analyzing the case of the cylinder entry in water. Hence, a possible practical application is presented, consisting in the study of impulse waves generated by a sliding mass. This problem, presented in Schillaci et al. [11], include several numerical complexities and a further validation of the numerical framework by comparison to experimental data.
This Chapter is organized as follows. The advantages of the single-phase approach in comparison to the full-model are comprehensively discussed in Sec. 5.2, together with the light phase deactivation process. In Sec. 5.3 the results obtained from the test simulations, and their comparison to the benchmark solutions are discussed. In Sec. 5.4, validation and results of the free-surface model with solid interaction are presented. The final conclusions of the chapter are given in Sec. 5.5.

5.2 Single-phase discretization

As introduced in Sec. 5.1, when the solution of the light phase does not affect the global behavior of the flow, and its analysis can be considered not essential for the scope of the simulation, it may be convenient to specialize the full-domain solver in order to improve its performance. For this purpose, the adoption of a single-phase model is presented.
In this model, the interface is still advected, but it is treated as a moving internal boundary with the scalar and vector fields of the light density phase deactivated. This method can lead to several advantages. For instance, in multiphase flows with high density ratios —as in the air-water case—, spurious currents may appear at the interface. They are due to the improper propagation of pressure gradients from the high-density phase to the low-density one, excessively accelerating it and, consequently, making it lose its divergence [2]. Conversely, single-phase solvers usually show more stable behaviors, due to the light-phase deactivation, and consequent reduction of density jumps. Additionally, the consideration of just one phase facilitates the iterative solution of the Poisson linear system, Eq. (1.19), leading to a reduction in computational costs.
Another advantage is related to the evaluation of the time step. In air-water flows, the time step is mainly limited by the maximum velocity of the air, which can be orders of magnitude larger than the velocity of the water. This is usually consequence of spurious currents advected from the water phase, or excessive acceleration due to geometrical or physical features of the problem configuration. Consequently, deactivating the light phase leads to an overall decrease of the maximum velocity, and to a consequent increase of the time step.
The deactivation is carried out modifying the Poisson linear system, Eq. (1.19), and the face normal mass flux expression, Eq. (1.27), i.e. steps 2 and 3 of the solution algorithm proposed in Sec. 1.3.4. The level-set function, $\phi(\mathbf{x},t)$, is used as a tool to identify the interface region, since it directly indicates the volume fraction of one of the phases —in this work, the heavy phase one. The process starts by choosing a value of ϕ between 0 and 1 (e.g. $\phi_{\text{lim}} = 0.5$) that identifies the limit at which the solution of the two-phase flow has to be cut. Hence, as

shown in the example of Fig. 5.1, the cells located in the interface region are individuated and tagged as state cells (SC) according to the following scheme:

- SC1: cells in heavy phase located just below the interface. They are identified as the cells with $\phi > \phi_{\text{lim}}$, presenting at least one neighbor cell with $\phi <= \phi_{\text{lim}}$.
- SC2: after completely defining SC1 cells, SC2 cells correspond to the ones with $\phi <= \phi_{\text{lim}}$ and at least a SC1 neighbor cell.

The Poisson linear system, is modified according to the jump condition proposed by Kang [12], written as

$$[p] - 2[\mu](\nabla \mathbf{u} \cdot \mathbf{n}) \cdot \mathbf{n} = \sigma \kappa, \tag{5.1}$$

where the $[\cdot]$ notation defines the jump of that quantity across the interface. In the case of smeared out viscosity —guaranteed by the smooth distribution of properties at the interface—, the pressure difference reduces to $[p] = \sigma\kappa$. Further setting the air pressure to the atmospheric value, p_{atm}, results in the following expression for free-surface pressure

$$p_{fs} = p_{\text{atm}} + \sigma\kappa. \tag{5.2}$$

Thus, the imposition of a given pressure at the free-surface is achieved modifying the coefficients of Eq. (1.19) for the SC2 cells; the neighbor coefficients, a_{nb}, are set to 0, the central coefficient, a_c, is changed to 1, while the source term, b, is modified such that it is equal to the free-surface pressure value. In the same way, the pressure is set to p_{atm} everywhere in the light phase. The strategy is summarized as

$$\begin{aligned}
a_c &= \begin{cases} \sum_{f \in F(c)} a_{nb} & \text{if} \quad \phi > \phi_{\text{lim}}, \\ 1 & \text{if} \quad \phi <= \phi_{\text{lim}}, \end{cases} \\
a_{nb} &= \begin{cases} \Delta t \frac{A_f}{W_f \rho_f^{n+1}} & \text{if} \quad \phi > \phi_{\text{lim}}, \\ 0 & \text{if} \quad \phi <= \phi_{\text{lim}}, \end{cases} \\
b &= \begin{cases} -\sum_{f \in F(c)} \frac{\hat{M}_f^p}{\rho_f^{n+1}} & \text{if} \quad \phi > \phi_{\text{lim}}, \\ p_{\text{atm}} + \sigma\kappa & \text{if} \quad \phi = \phi_{\text{lim}} \text{ (SC2 cells)}, \\ p_{\text{atm}} & \text{if} \quad \phi < \phi_{\text{lim}}. \end{cases}
\end{aligned} \tag{5.3}$$

Furthermore, assuming the surface tension negligible for the class of problems considered —mainly marine applications—, the free-surface pressure can be directly set to p_{atm}.
The next step is to consider all the cell pairs, a and b, that lie on the two sides of a face f. Then, the face normal mass flux is evaluated according to Eq. (1.27) in the heavy phase,

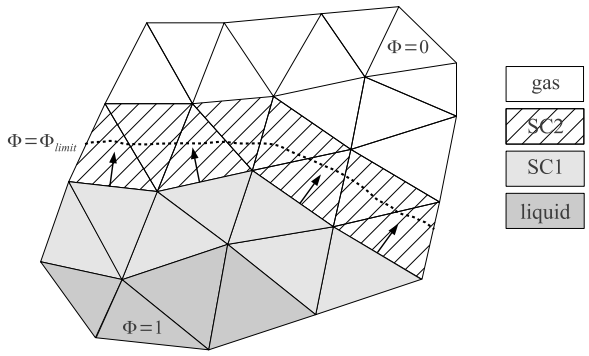

Figure 5.1: Example of the cells tagging required for the deactivation of the light phase as function of the interface position. The interface is indicated by the fine dashed line.

whereas it is deactivated in the light one, as described below

$$M_f^{n+1} = \begin{cases} 0 & \text{if} \quad \phi(a) <= \phi_{\text{lim}} \text{ and } \phi(b) <= \phi_{\text{lim}} \\ M_f^p - \Delta t (p_b^{n+1} - p_a^{n+1}) \frac{A_f}{(W_a + W_b)} & \text{otherwise} \end{cases} . \tag{5.4}$$

Thus, cell center velocities assume non-zero values only for the heavy phase.

Interface advection

In terms of the level-set advection and re-initialization equations, Eqs. 1.6 and 1.9, no particular intervention is required. However, the volume fraction value of the heavy phase that identifies the deactivation limit, ϕ_{lim}, plays an important role in the correct advection of the fluid interface. As explained in Sec. 1.2.1, the level-set function is used to evaluate the transport properties on the entire domain, even in the interfacial region. Therefore, recalling that $\phi(\mathbf{x},t) = 1$ in the heavy phase region, and evaluating Eq. (1.4) for $\phi(\mathbf{x},t) = 1$ and ϕ_{lim}, the higher and lower possible density values are obtained, which respectively correspond to $\rho_{max} = \rho_1$ and $\rho_{min} = \rho_2 + \phi_{\text{lim}}(\rho_1 - \rho_2)$. Consequently, the larger attainable density difference at the interface is

$$\Delta\rho = \rho_{max} - \rho_{min} = (1 - \phi_{\text{lim}})(\rho_1 - \rho_2). \tag{5.5}$$

Therefore, as the ϕ_{lim} value gets closer to 1, the range of densities involved in the numerical solution is reduced. This overall reduction leads to a minimization of the spurious currents, resulting in faster and more stable numerical calculations. On the other hand, as grid points

on the interface zone are deactivated, part of the heavy phase inertia is also neglected. Consequently, a correct velocity field extrapolation is needed to ensure a proper interface advection. The accuracy of the extrapolation becomes increasingly important as the value ϕ_{lim} tends to 1, since it is necessary to extract, and approximate, more and more information of the interface movement from the heavy phase [1, 2]. Nevertheless, from previous work [10], this extrapolation is only effective if the velocity presents a stable and predictable profile, as for example, in the case of progressive waves. In other more complex scenarios, such as the collapse of water columns, this approach is not accurate due to the strong variations in the velocity profile.
On the contrary, as the value ϕ_{lim} is shifted towards 0, a smaller amount of inertia is neglected. It has been found that above a certain lower limit, which depends on the particular case, a velocity field extrapolation does not lead to any change in the solution of the heavy phase flow. Indeed, all the information necessary for its proper advection is obtained from the flow motion algorithm. This procedure avoids the extrapolation of the velocity field across the interface, thus, limiting the error on the final solution that can be caused by any erroneous or not accurate velocity extension.
Generally, the adoption of $\phi_{\text{lim}} \leq 0.01$ makes the method effective for all the cases analyzed. However, the numerical tests reported in this work are carried out by choosing the highest possible ϕ_{lim} value such that velocity extrapolations are not required to obtain a correct solution. This helps to maximize the benefits obtained from the single-phase approach in terms of stability and velocity. In the next Section, the adopted value of ϕ_{lim} is specified case by case.

5.3 Numerical tests

This section presents numerical results corresponding to the verification and validation of the proposed single-phase scheme. First, the appearance of spurious currents for the full-domain and single-phase approaches is analyzed for a static liquid column in Sec. 5.3.1. A first comparison between numerical results and analytical data is performed in Sec. 5.3.2 by solving the wave sloshing problem. The possibility of integrating the single-phase strategy with a wave maker is assessed in Sec. 5.3.3, where the evolution of a solitary wave is studied. This topic is further explored in Appendix B, where the generation of generic progressive waves and their dissipation on a numerical beach is analyzed. Finally, the well-established dam break problem is numerically simulated, first for a 2-D configuration, Sec. 5.3.4, and later for a more complex 3-D geometry, Sec. 5.3.5. In both cases, the numerical results are compared to experimental data.

5.3.1 Static liquid column

Large density differences between fluids may result in interfacial spurious currents. This first test analyzes the appearance of such currents and their intensity in the case of utilizing the full-domain (2-P) or the single-phase (1-P) approach. For 1-P cases, the deactivation limit, ϕ_{lim}, is set to 0.1. The UP scheme is used for the discretization of the convective operator in the Navier-Stokes equations. The set-up consists of a unit square of side L, occupied in its lower half by the liquid phase, and subjected to the action of gravity with negligible surface tension. No-slip boundary conditions are imposed on the walls. Given the static nature of this case, the rise of any velocity at the interface corresponds to a non-physical solution. The intensity of the spurious currents is measured by means of the Froude number, Fr, evaluated as

$$\text{Fr} = \frac{|\mathbf{u}|}{\mathbf{g}L}, \tag{5.6}$$

where $|\mathbf{u}|$ is the average velocity norm of the fluid at the interface. Since the analytical solution of the problem is a zero velocity field, the Froude number at steady state constitutes itself the norm of the error.

In a first test, performed on a Cartesian coarse mesh with 1.6×10^3 cells, the same density value is assigned to the two fluids. For this case, the spurious currents intensity turn out to be negligible (of the order of 10^{-16}) for both 1-P and 2-P solvers. As a second test, a large density difference is imposed between the two phases ($\Delta\rho = 1000$), therefore, a larger magnitude of spurious currents is expected. In order to evaluate the accuracy of the method, a mesh convergence analysis is performed on progressively finer Cartesian meshes.

In order to compare the collocated (Coll.) and staggered (Stagg.) mesh schemes, the same tests are performed using the Coll. discretization described in Chapter 1, and the Stagg. discretization described in [7]. The results presented in Fig. 5.2 for the Staggered (Stagg.) discretization show that the error is larger for the 2-P scheme. This demonstrates the effectiveness of the 1-P method in reducing spurious velocities due to the decrease of the density differences, as explained in Sec. 5.2. Moreover, results show that the Stagg. formulation maintains a lower Fr than Coll. both for 1-P and 2-P models, thus, confirming its higher stability. On the other side, the Coll. scheme demonstrates to be more accurate, as the order of accuracy, p, measured in the proposed series of tests is higher. A summary of the orders of accuracy of the analyzed methods is reported in Tab. 5.1.

5.3.2 Wave sloshing

The first validation test consists in the analysis of the oscillating movement of a viscous liquid within a stationary 2-D rectangular vessel closed on all its sides. At time $t = 0$, the wave elevation over the calm liquid column, h_l, is described by the following sinusoidal function

$$\eta(x,0) = \eta_0 \cos\left[\kappa(x + \frac{\lambda}{2})\right], \tag{5.7}$$

Mesh	Model	p
Stagg.	1-P	1.45
Stagg.	2-P	1.55
Coll.	1-P	1.68
Coll.	2-P	1.8

Table 5.1: Order of accuracy of the single-phase (1-P) and full-domain (2-P) models used in this work, in combination with both staggered (Stagg.) and collocated (Coll.) mesh schemes. p is evaluated from a mesh convergence analysis performed on the static liquid column case.

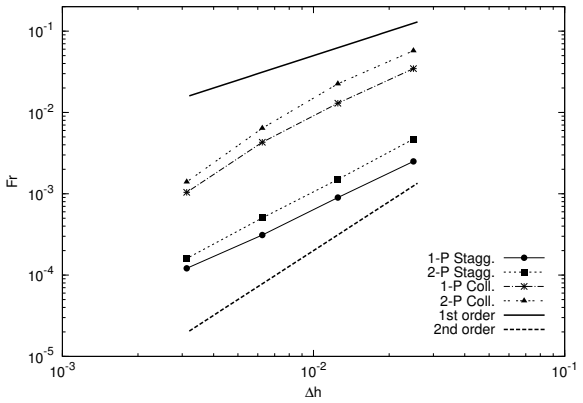

Figure 5.2: Froude number as function of mesh size for the static liquid column problem. The numerical tests are performed by means of the single-phase (1-P) and full-domain (2-P) models, and according to staggered (Stagg.) and collocated (Coll.) discretizations.

where $\kappa = 2\pi/\lambda$ is the wave period, λ is the wavelength and η_0 is the wave amplitude. The results obtained from the analysis of the temporal evolution of the wave height are compared to the analytical function proposed by Wu et al. [13]. If assuming sufficiently high Reynolds number and supposing a negligible influence of the finite depth of the tank, the wave evolution in time and space is described by the following expression

$$\frac{\eta_{ref}(x,t)}{\eta(x,0)} = 1 - \frac{1}{1+4\nu_l^2\frac{\kappa^2}{g}}\left[1 - e^{-2\nu_l\kappa^2 t}\left(\cos\sqrt{\kappa g}t + 2\nu_l\kappa^2\frac{\sin\sqrt{\kappa g}t}{\sqrt{\kappa g}}\right)\right], \tag{5.8}$$

where $\nu_l = \mu_l/\rho_l$ is the kinematic viscosity of the liquid and g is the norm of the gravity acceleration. The analytical solution allows the validation of the model for different values of density and viscosity of the liquid phase. These features are taken into account by means of the Reynolds number, that in free-surface problems can be defined as

$$Re = \frac{h_l\sqrt{h_l g}}{\nu_l}. \tag{5.9}$$

In the simulations, λ is set to 1 in order to obtain a wave with period $\kappa = 2\pi$, while the rectangular vessel is $w = 2\lambda$ in width. The initial wave amplitude, η_0, is 0.02 m, and the calm liquid depth is set to 1 m. The simulations are performed on a Cartesian mesh with 1.7×10^5 cells, distributed more densely in the zone of the interface. No-slip boundary conditions are applied to all the non-periodic boundaries of the domain. From preliminary observations, the deactivation limit ϕ_{lim} value is set to 0.1 —valid for all the cases involving the undulating movement of a liquid reservoir. A pure SP convection scheme is used for the discretization of ψ_f in Eq. (1.17), since the high density of cells in the interface region reduces the amount of spurious currents.

In the first test (High Re), fluid density and viscosity are set to the values of water at room temperature —$\rho_l = 998$ kg/m^3, $\mu_l = 1.003 \times 10^{-3}$ Pa$\cdot$s. The resulting Reynolds number is $Re \simeq 1 \times 10^6$. In Fig. 5.3(a), the time evolution of the relative wave height at the center of the domain, x_c, is shown. Time is indicated in dimensionless form as $t^* = t\sqrt{g/h_l}$. Due to the predominance of inertia forces, the wave oscillates almost undisturbed for a large number of time periods. As shown in the figure, the numerical solution, $\eta(x_c,t)/\eta_0$, agrees with the analytical data, $\eta_{ref}(x_c,t)/\eta_0$. In the next case (Low Re), density and viscosity of the liquid are chosen such that $Re \simeq 1 \times 10^3$. The plot in Fig. 5.3(b) shows a marked reduction of the wave height as the simulation is advanced in time, since viscous forces dominate the physics. In this scenario, the numerical results obtained from the 1-P scheme also agree with analytical data.

5.3.3 Solitary wave

In the following problem, the capability of the single-phase approach to correctly reproduce the viscous damping of water in intermediate or low depth basins is analyzed. Moreover, this

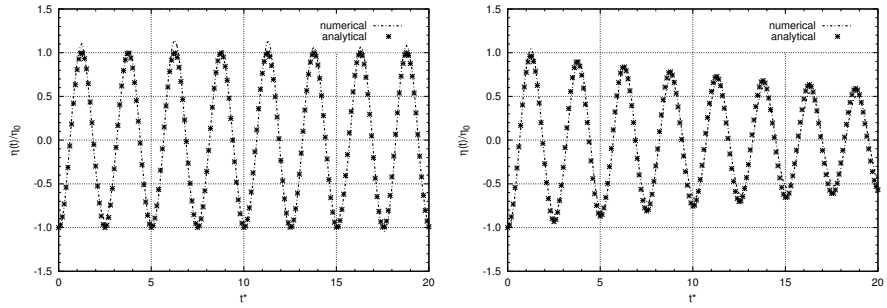

(a) $Re \simeq 1 \times 10^6$ (b) $Re \simeq 1 \times 10^3$

Figure 5.3: Evolution of the wave height at the center of the domain for the wave sloshing experiment: (a) High Re number, (b) Low Re number. Comparison between analytical values and numerical results obtained on a 2-D Cartesian mesh.

test examines the potential of the single-phase scheme in incorporating a wave maker into the simulation. A wave maker consists in analytically forcing the solution of the level-set function and/or the scalar fields on a small part of the domain, such that a specific free-surface profile is numerically obtained. In order to ensure numerical stability in the wave maker zone, the forcing (analytical) function, $\xi_{for}(\mathbf{x},t)$, is coupled to the numerical solution, $\xi_{num}(\mathbf{x},t)$, by means of a relaxation parameter, $\psi(x,t)$, written as

$$\xi(\mathbf{x},t) = \xi_{for}(\mathbf{x},t)(1-\psi(x,t)) + \xi_{num}(\mathbf{x},t), \tag{5.10}$$

where $\psi(x,t)$ varies smoothly in the $x-$axis from 0 at $x = 0$ to 1 at the end of the wave maker zone. The free-surface flow simulated in this test corresponds to a solitary wave traveling from the left to the right part of the domain. It consists in an aperiodic and non-linear displacement of water above the calm water level that can be produced mechanically by an instantaneous impulse. As proposed by Mei et al. [14], the analytical solution of the wave profile takes the form

$$\eta(x,t) = a\cosh^{-1/2}\sqrt{\frac{3a}{4h_w^3}}(x - C\,t), \tag{5.11}$$

with a as the wave amplitude, h_w as the calm water depth, and C as the wave speed defined as

$$C = \sqrt{g(h_w + a)}. \tag{5.12}$$

The motion of a solitary wave is usually characterized by its wave crest advancement and height. The latter caused by the viscous forces and, as given by [14], described by the fol-

lowing expression

$$H(t)^{-1/4} = a^{-1/4} + 0.08356\sqrt{\frac{\nu_w}{(gh_w)^{1/2}h_w^{3/2}}}\frac{C\,t}{h_w}. \tag{5.13}$$

The simulation is carried out with $Re \simeq 1 \times 10^3$, as given by Eq. (5.9), such that the viscous effects increase the amount of wave damping. The computational domain consists in a long, narrow tank (32 m long and 2 m high) initially filled in its lower part by water at rest. The domain is discretized in 4.5×10^5 cells stretched, according to a hyperbolic distribution, at the zone in which the passage of the wave crest is expected. No-slip boundary conditions are imposed at the tank bottom, while Neumann conditions apply on the left, right and top boundaries of the domain. In this test, the UP convection scheme is used to minimize the presence of spurious currents. On the right part of the domain, viscosity is artificially increased in order to provide extra amount of damping before the wave reaches the boundary. Similar to the previous case, ϕ_{lim} is set to 0.1.

The wave —$h_w = 1.0$ m, $a = 0.15$ m— is generated on the left part of the domain, as depicted in Fig. 5.4(a), where it progressively enters the pure numerical zone. Once fully generated, Fig. 5.4(b), the wave continues its path through the domain with an almost constant velocity, Figs. 5.4(c) and 5.4(d), preserving its form, but slowly reducing its height.

The evolution in time of the wave height, $Y = H(t) + h_w$, and advancement on the $x-$axis, X, are shown in Fig. 5.5, as well as its comparison to the analytical solution.

A small number of time steps are required to stabilize the solution when the wave enters the pure numerical zone. Consequently, a slightly difference between the analytical and the numerical solution is noticeable at the initial stage of the simulation, both in Figs. 5.5(a) and 5.5(b). However, once stabilized, the numerical solution closely follows the analytical values of wave height and advancement.

In conclusion, this test is a good demonstration that a wave maker can be coupled to the single-phase scheme. The wave configuration can be easily adapted to model progressive waves, in linear or composed form, which are representative of ocean waves and their interaction with fixed or floating obstacles. For instance, as further demonstrated in Sec. A, the single-phase approach can be used to simulate the interaction between progressive waves and an oscillating water column system for the extraction of energy from sea waves.

5.3.4 Dam break 2-D

The problem of the dam break consists in simulating the collapse of a water column, initially at rest, under the action of gravity. It is one of the most widely used benchmark for the validation of free-surface models, due to its easy set-up, the simplicity of the boundary conditions required, and the presence of several references in the literature, both experimental and numerical. The initial configuration is depicted in Fig. 5.6, where the physical properties of the fluids are also reported, mimicking water and air conditions at room temperature. The initial

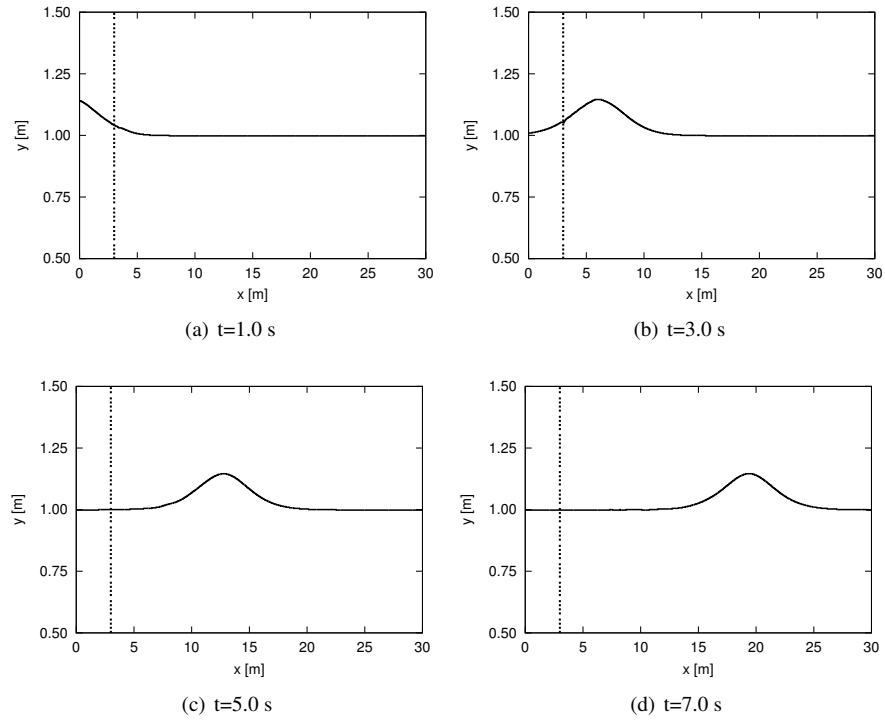

(a) t=1.0 s (b) t=3.0 s

(c) t=5.0 s (d) t=7.0 s

Figure 5.4: Evolution of the 2-D profile of a solitary wave. The dashed line delimits the wave maker zone. The initial time is set equal to the value at which the wave exits ÂâthÂe wave maker zone, t_0.

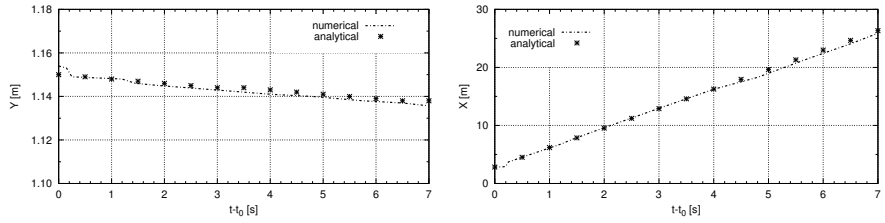

(a) (b)

Figure 5.5: Evolution of wave height and crest position of a solitary wave along time. Comparison between numerical results and analytical values. t_0 indicates the time at which the wave crest enters the pure numerical zone.

Test	Model	Mesh	No. cells
1	2-P	STR	$\sim 3.7 \times 10^4$
2	1-P	STR	$\sim 3.7 \times 10^4$
3	1-P	UNSTR	$\sim 5.0 \times 10^4$

Table 5.2: List of the numerical experiments performed for the 2-D dam break case.

water column presents rectangular shape with side length $a = 4.5$ in, and the proportion f between rectangle height and length is 1. No-slip boundary conditions are imposed at the solid walls of the container, Neumann conditions apply at the top in order to mimic an open boundary, whereas periodic conditions are set on the front and back boundaries.
The numerical results obtained are compared to the experimental data reported in Martin and Moyce [15], in which several experiments were performed on the fall of a water column, considering various options for the initial column shape and proportions. In the experimental set-up of the reference, vacuum conditions were established, thus, making licit the numerical single-phase approximation. Moreover, the independence of the flow from the periodic boundaries is assessed, which allows the 2-D approximation.
The results are presented in dimensionless form. In particular, the magnitudes studied are the dimensionless residual height, H^*, of the water column and the dimensionless leading front, Z^*, of the wave generated by the water collapse, given by

$$H^* = \frac{H}{a \cdot f}, \quad t_H^* = t\sqrt{\frac{g}{a}}, \quad Z^* = \frac{Z}{a}, \quad t_Z^* = t\sqrt{\frac{g \cdot f}{a}}, \tag{5.14}$$

where H is the measured residual height, Z is the measured leading edge, and t_H^* and t_Z^* are the corresponding dimensionless time indicators.
In order to highlight differences due to the air phase deactivation, the simulations are performed by means of the 1-P and 2-P approaches. A pure UP scheme is used for the discretization of the convective term in the momentum equations, such that spurious velocities are efficiently damped. The different simulations performed are listed in Tab. 5.2, where STR corresponds to a Cartesian mesh with $\sim 3.7 \times 10^4$ control volumes ($\Delta h \simeq 1.46 \times 10^{-3}$), while UNSTR refers to an unstructured mesh with $\sim 5 \times 10^4$ triangular elements ($\Delta h \simeq 2 \times 10^{-3}$). In order to accurately capture the advancement of the wave front, the deactivation limit is set to 0.01.
The comparison between numerical results and experimental data is shown in Fig. 5.7, up to the instant in which the wave front reaches the right boundary of the domain. According to the STR mesh results (tests 1 and 2), the numerical simulations faithfully follow the experimental values for H^*. On the other hand, numerical Z^* values are initially higher than the experimental ones. This trend has been reported in similar studies, e.g. by Sheu et al. [8, 16] and by Balcàzar et al. [8, 9] when using the CLS method on fixed unstructured meshes. Its

explanation is probably related to the influence of the mechanical apparatus that releases the water column in the early stages of the experiment. Despite this initial difference, the numerical results agree with the experimental data. In terms of differences between the 1-P and 2-P simulations, it is noticed that: (1) the H^* values practically overlap; (2) the speed of propagation is very similar, and the wave fronts reach the opposite wall almost at the same time —at $t_Z^* = 3.17$ for the 1-P case and at $t_Z^* = 3.2$ for the 2-P one. Hence, no important differences are observed due to the deactivation of the air phase.

In Test 3, H^* is in good agreement with experimental data, though it is noted a lower homogeneity in the fall of the column on the central part of the plot, due to the irregularity of the UNSTR mesh. According to Z^*, the results are very close to the other experiments, and the little mismatch is due to the difficulty of measuring exactly the same point on different meshes.

Snapshots of the liquid-phase time evolution are shown in Fig. 5.8 for Test 2. In detail, Figs. 5.8(a) and 5.8(b) correspond to the initial collapse of the water column, whose front reaches its maximum speed at $t_Z^* \simeq 2.3$. Then, as shown in Fig. 5.8(c), the wave impacts the front wall and, after a transition period, it starts flowing in the opposite direction, Fig. 5.8(d). From this point on, there is a lack of clear references in the literature for the description of the flow evolution. However, the wavefront presented here follows its path without further losses of mass, and continues inverting its flow direction each time it encounters a wall, until the initial potential energy is totally dissipated.

Finally, in order to further assess the mesh convergence of the method, a convergence study on progressively finer Cartesian meshes is performed. The relative Euclidean norm, $\|\varepsilon\|_2$, and infinite norm, $\|\varepsilon\|_\infty$, of the error is evaluated for the H^* and Z^* values, in the form

$$\|\varepsilon\|_2 = \sqrt{\varepsilon_1^2 + \cdots + \varepsilon_t^2}, \quad \|\varepsilon\|_\infty = \max\left(|\varepsilon_1|, \ldots, |\varepsilon_t|\right), \tag{5.15}$$

where the relative error ε_t at point x_c is evaluated at each time t as

$$\varepsilon_t = \frac{|\eta(x_c,t) - \eta_{ref}(x_c,t)|}{|\eta_{ref}(x_c,t)|}, \tag{5.16}$$

with $\eta(x_c,t)$ representing the numerical solution. As no analytical solution is available, the reference values, $\eta_{ref}(x_c,t)$, are taken to be the ones numerically obtained on a very fine mesh with 1.3×10^6 cells ($\Delta h \simeq 0.7 \times 10^{-3}$). The results are plotted in Fig. 5.9, demonstrating a first- to second-order of accuracy as mesh size is decreased. This behavior is consistent with the conclusions extracted in Sec. 5.3.1.

Time savings

The computational savings resulting from the deactivation of the light phase are quantified in this section. These are obtained comparing the simulation time of the dam break problem on

Δh	Δt	ITER	t_{tot}
5.8×10^{-3}	-32%	-80%	-22%
2.9×10^{-3}	+27%	-78%	-38%
1.45×10^{-3}	+25%	-77%	-47%

Table 5.3: Differences in % between the 2-P and 1-P approaches regarding time step, Δt, number of iterations to solve the Poisson linear system, $ITER$, and total simulation time, t_{tot}, when varying the mesh size.

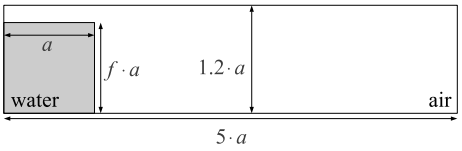

	Water	Air
$\rho\,[\mathrm{kg/m^3}]$	998	1.205
$\mu\,[\mathrm{Pa \cdot s}]$	$1.003 \cdot 10^{-3}$	$1.808 \cdot 10^{-5}$

Figure 5.6: Initial set-up of the 2-D dam break test and properties of the fluids involved in the simulation.

a Cartesian mesh for the 1-P and 2-P approaches, and are expressed in percentage form for three different mesh sizes, Δh. In detail the differences in time step, Δt, number of iterations to solve the Poisson linear system, $ITER$, and the total time-to-solution are given in Tab. 5.3. Three main observations are extracted from the results. The first is that the percentage of reduction in $ITER$ is fairly constant for all cases. The underlying reason is the reduction in ill-posedness of the Poisson linear system as the light phase is deactivated. The second observation is the increase in time step for the fine-mesh cases, which is consequence of the minimization in spurious currents. Last but not least, is that the overall time-to-solution is reduced for all cases, and this difference is larger as the mesh is densified. For instance, a 47% of reduction in time required to solve the dam break problem is obtained for the finest mesh.

Adoption of AMR

The dam break tests is further employed to show the advantages led by the AMR technique —described in Chapter 3— to free-surface configurations. The proposed tests are reported in Tab. 5.4. First, two simulations are carried out on a coarse and a fine mesh. Next, the AMR criteria is applied on the coarse mesh. The computational time needed for the AMR simulation is of the same order of magnitude as that measured with the coarse mesh, while the number of cells increases with the advancement of the wave front. Its value reaches a maximum (around 13500) when the water covers the whole box. The data concerning H^*, depicted in Fig. 5.10(a), show that the results obtained with the fine mesh and the AMR

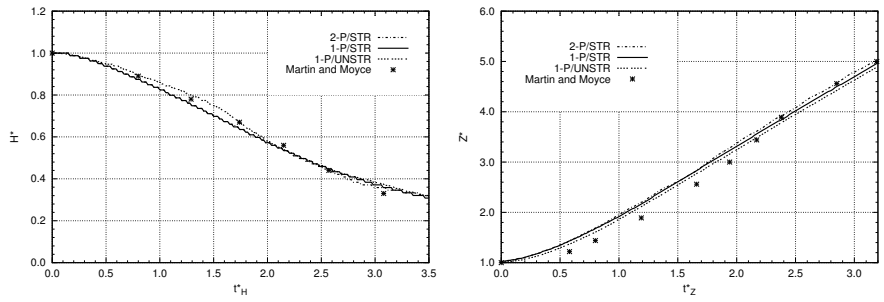

(a) (b)

Figure 5.7: Evolution of residual water column height, H^*, and leading edge, Z^*, along time for the 2-D dam break test. Full-domain (2-P) and single-phase (1-P) numerical results, obtained on Cartesian (STR) and unstructured (UNSTR) grids, are compared to experimental reference values [15].

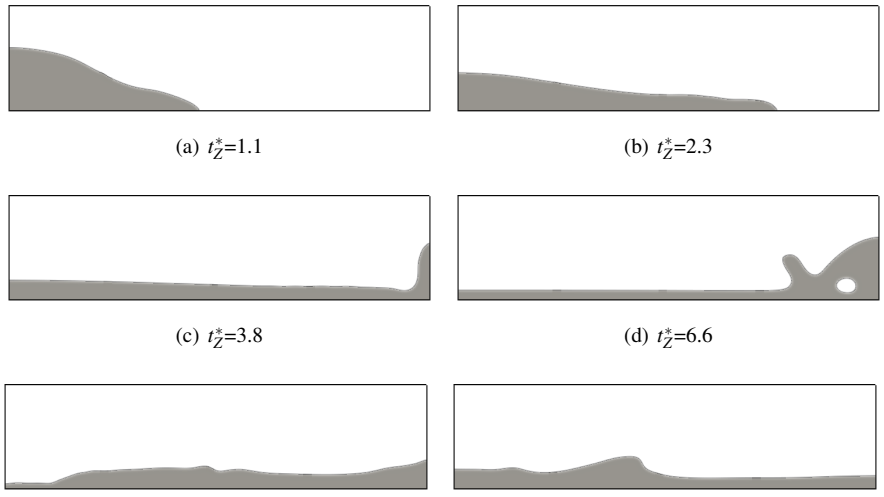

(a) t_Z^*=1.1 (b) t_Z^*=2.3

(c) t_Z^*=3.8 (d) t_Z^*=6.6

(e) t_Z^*=11.6 (f) t_Z^*=18.1

Figure 5.8: Time evolution of the collapsing 2-D water column simulated by means of the single-phase model (Test 2).

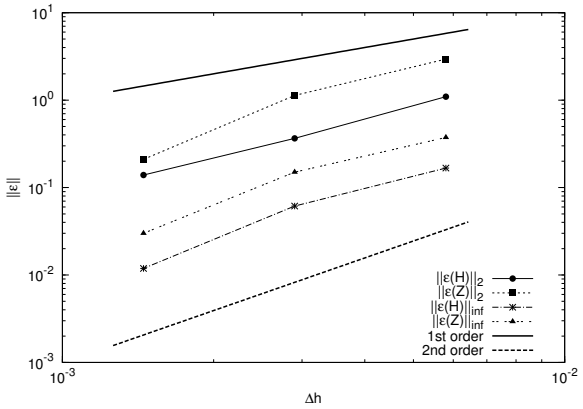

Figure 5.9: Mesh convergence study performed for the 2-D dam break test. Euclidean norm, $\|\varepsilon\|_2$, and infinite norm, $\|\varepsilon\|_{\text{inf}}$, of the error are reported, referring both to Z and H.

Test	clock time [min]	CVs
coarse	360	7920
fine	2120	31680
coarse +AMR	$\sim$500	$\sim$13000

Table 5.4: Mesh data and computational times measured in the dam break tests performed with AMR. The clock time refer to simulationos carried out on 4CPUs in JFF cluster [17].

test are in full agreement and faithfully reflect the benchmark, while the solution obtained on the coarse mesh is clearly poorer. The same is founds as regards Z^*, whose results are showed in Fig. 5.10(b). As explained before, in this plot the numerical data slightly deviate from the experimental ones in the initial part of the simulation, showing a slightly faster front advancement. The success of this test demonstrates the possibility of increasing the efficiency in the simulation of free-surface phenomena with Low Reynolds number, by only increasing the mesh definition in proximity of the interface by means of AMR.

5.3.5 Dam Break 3-D

Once tested on the 2-D dam break problem, the single-phase scheme is further assessed on a 3-D configuration. The problems concerns the evolution of a collapsing water column interacting with a solid box in a 3-D domain. The initial column, depicted in Fig. 5.11, is contained in a tank of 3.2 m with a square cross section of side 1 m, while the solid box —short sides of 0.16 m and long side of 0.4 m—, is placed at $d = 1.17$ m from the initial

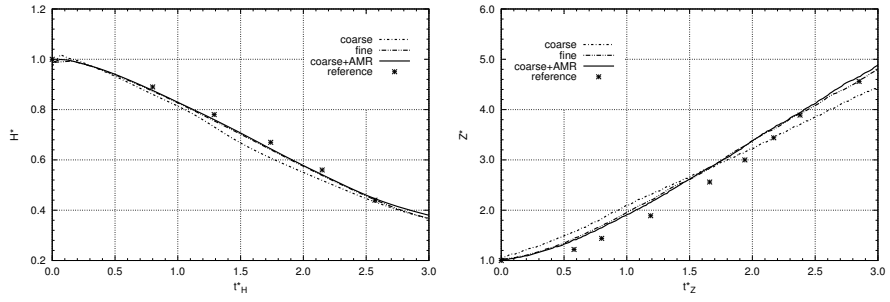

(a) H^* (b) Z^*

Figure 5.10: Evolution of residual water column height, H^*, and leading edge, Z^*, in time in the dam break test. Data obtained with coarse, fine and AMR meshes are compared. The experimental reference [15] is also reported.

water column front.

The results of the simulations are compared to the experimental data obtained at the *Maritime Research Institute Netherlands* (MARIN) [18], and reported by Kleefsman et al. [3]. These refer to the collapse of a water column with dimensions $H = 0.55$ m and $L = 1.22$ m on the described set-up. The available data consists of: (1) the height of the water column at the center of the domain ($z = 0.5$ m) for $x = 0.56$ m (H1) and $x = 2.22$ m (H2); (2) the relative pressure of the water at points P1 $(2.39, 0.025, 0.5)$ m, front of the solid box, and P2 $(2.487, 0.16, 0.5)$ m, top of the box.

The geometry is discretized by means of an unstructured tetrahedral mesh with $\sim 1.1 \times 10^6$ cells, distributed more densely in the zone where the passage of the interface is expected; see Fig. 5.12. The domain presents no-slip boundary conditions at the solid walls, while Neumann conditions are imposed at the top boundary. Once more, a pure UP convection scheme is used for the discretization of ψ_f, while, as in the 2-D case, ϕ_{lim} is set to 0.01.

The evolution in time of the liquid-gas interface is presented in Fig. 5.13. The initial collapse of the column presents a well-defined linear front, until the point in which the obstacle is reached, resulting in a total rupture of the liquid stream. After colliding with the box, the liquid phase encounters the wall of the domain, producing a bounced wave (1^{ST} WAVE) — depicted in Fig. 5.13(c)— that starts flowing in the opposite direction. This 1^{ST} WAVE travels back to the left wall, where it slams and inverts again its direction (2^{ND} WAVE), as shown in Fig. 5.13(d). Finally, the simulation ends at $t = 6$ s, approximately when the 2^{ND} WAVE encounters once more the wall at the right side of the domain.

The numerical results are compared against experimental data in Figs. 5.14 and 5.15. First, the water height for H1 and H2 is plotted in Fig. 5.14, showing its qualitatively good agreement with experiments. In detail, the water height for H1 reduces correctly during the initial

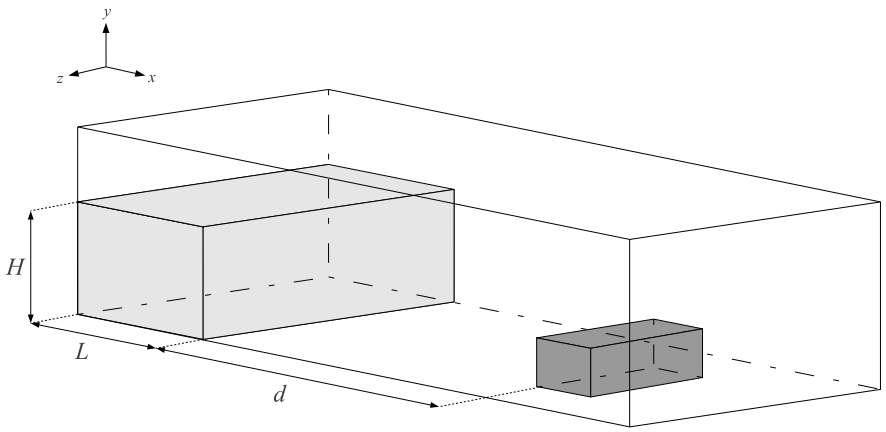

Figure 5.11: Initial set-up of the 3-D dam break simulation.

water column collapse, rises when the 1ST WAVE reaches the H1 location, and results in a second height peak due to the passage of the 2ND WAVE. This is further corroborated by noticing that the water front reaches H2 at the correct time (around $t = 0.33$ s), shows a maximum height during the recombination phase (approximately at $t = 1.8$ s), and shows a second peak corresponding to the passage of the 2ND WAVE (roughly at $t = 5.0$ s), with a short delay in comparison to the experimental solution. Similarly, as demonstrated in Fig. 5.15, the pressure evolution for P1 and P2 is well captured by the numerical simulation. The sudden pressure increase shown for P1 at time $t = 0.2$ s, indicating the instant in which the water front reaches the box, is correctly captured as shown in Fig. 5.15(a). Following this peak value, the pressure slowly reduces, and it only increases again during the passage of the 2ND WAVE (around $t = 5.0$ s). The pressure signal for P2 accurately captures the peak corresponding to the recombination phase that precedes the 1ST WAVE formation (approximately $t = 1.68$ s). The numerical results reported in [3] and plotted in Figs. 5.14 and 5.15, are obtained on a Cartesian mesh with $\sim 1.2 \times 10^6$ cells. These also present differences in comparison to the experimental data when the water column reaches the obstacle zone. This confirms that the small uncertainty between the various results is acceptable when taking into account the complexity and sensibility of the experimental data. Similar conclusions can be extracted from the numerical results recently presented for the same test case by Gu et al. [19].
In summary, the numerical results obtained by means of the single-phase scheme presented in this work are in good agreement with the experimental data. This fact further demonstrates the potential of the method to accurately solve free-surface flows on complex 3-D geometries discretized with fully unstructured meshes.

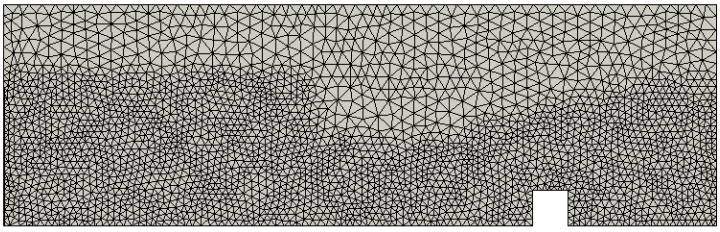

Figure 5.12: Slice of the tetrahedral mesh used for the simulation of the 3-D dam break. The mesh density is increased at the regions in which the passage of the flow is expected.

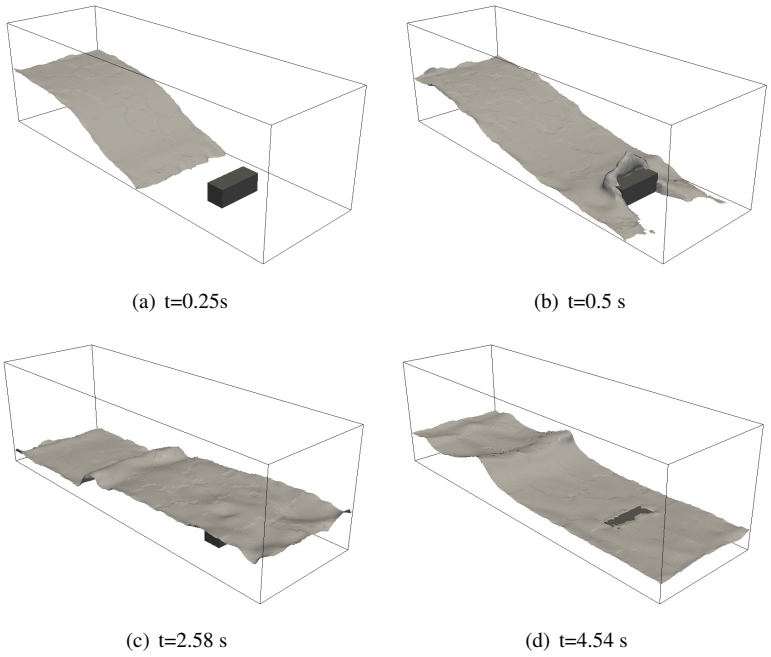

(a) t=0.25s (b) t=0.5 s

(c) t=2.58 s (d) t=4.54 s

Figure 5.13: Instantaneous snapshots of the flow evolution for the 3-D dam break simulation. The represented surfaces correspond to the contour plots of $\phi(\mathbf{x},t) = 0.5$.

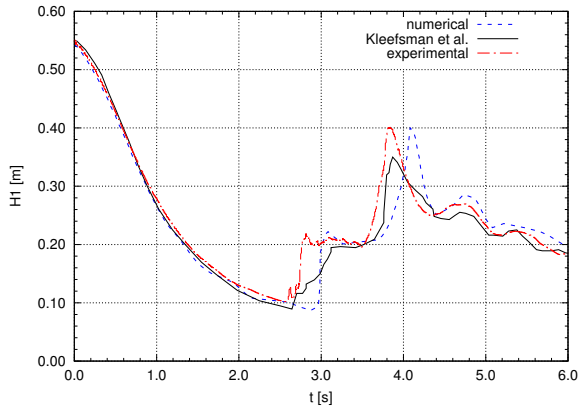

(a)

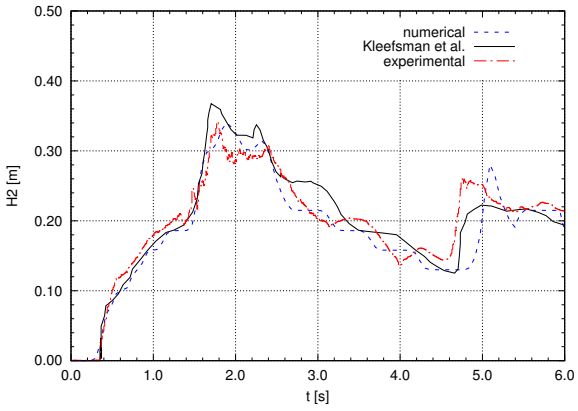

(b)

Figure 5.14: Water column height measured at points H1 and H2 for the 3-D dam break numerical simulation and references, both the numerical [3] and the experimental one [18].

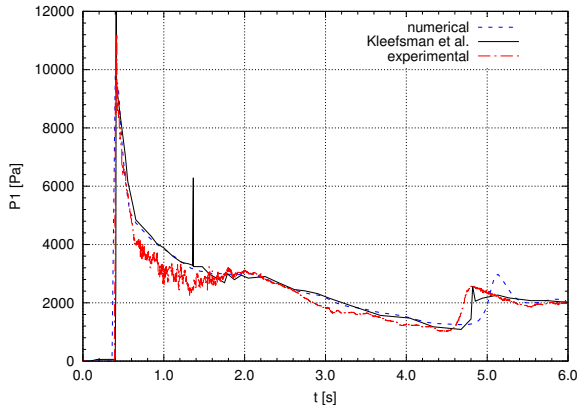

(a)

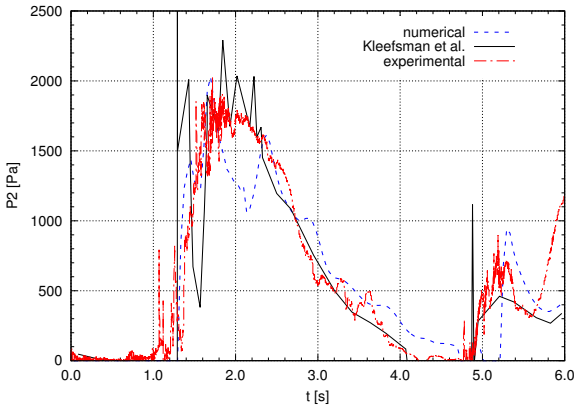

(b)

Figure 5.15: Pressure measured at probe points P1 and P2 for the 3-D dam break numerical simulation and references, both the numerical [3] and the experimental one [18].

5.4 Impulse waves generated by a sliding mass

In this section, a numerical framework for the DNS of a free-surface flow interacting with a solid is used to simulate the practical case of a landslide event inside a water basin.
The simulation of this type of phenomena requires the development of a robust platform that takes into account the mutual interaction of liquid, solid and gaseous phases. Usually, interface-capturing methods proved to be the most efficient and reliable to represent this kind of situations. Some examples are those of Liu et al. [20] which uses a Large-Eddy-Simulation (LES) approach and Volume-of-Fluid algorithms to track the interfaces between phases. Yang et al. [21] introduces the immersed boundary method (IBM) method for the solid tracking while the interface between fluids is captured by a level-set (LS) method. More recently, Sanders et al. [22] and Calderer et al. [23] also solved the interaction between solid and multiphase fluids by means of Fluid Structure Interaction (FSI) methods.
The free-surface approximation described in this Chapter is adopted in order to simulate the movement of the water independently from the air effect, thus, obtaining a more stable and efficient calculation then in classic two-phase computations. The interaction between solid and liquid is solved by means of the Direct Forcing IBM [24, 25] method described in Sec.1.3.5. Neumann boundary conditions are imposed to the volume fractions at the boundary between the fluids and the solid, in order to avoid the diffusion of the phases inside the area occupied by the object. These conditions must be applied to both level-set advection and reinitialization equations, Eqs. 1.6 and 1.9, respectively. The adaptive mesh refinement strategy (AMR) [26] described in Chapter 3 is adopted in order to dynamically improve the mesh definition in the interface region and in zones where the basic mesh size is not sufficient to correctly solve the turbulent scales or the interfacial characteristic lengths. Further details above this work have been recently published in [11].
The method is firstly validated by simulating the entrance of a 2-D object into a still water surface. Next, the case of tsunami generation from a subaerial landslide is studied and the results are validated by comparison to experimental and numerical measurements.

5.4.1 Cylinder entry in water

The numerical method is validated by simulating the entry of a 2-D disk of diameter $D = 1$m within a initially quiet liquid surface. The disk falls with velocity $u =$m/s, and the initial distance from its centre to the water surface is set to $d = 1.5$m. The domain consists of a rectangle of sides $10\,x$ 10m, to which Neumann boundary conditions are applied. The liquid density and viscosity are set to $\rho = 1000$kg/m^3 and $\mu = 1x10^{-3}$ Pa s, respectively,and Earth gravity is assumed. The employment of the free surface method implies the negligibility of the gas influence on the flow. Additionally, the effect of the surface tension is considered irrelevant. The basic mesh has a regular Cartesian grid that accounts for 1×10^4 elements. However, the local definition is increased in the vicinity of the liquid-gas and fluid-solid interfaces thanks to a second level adaptive mesh refinement (the technique is extensively

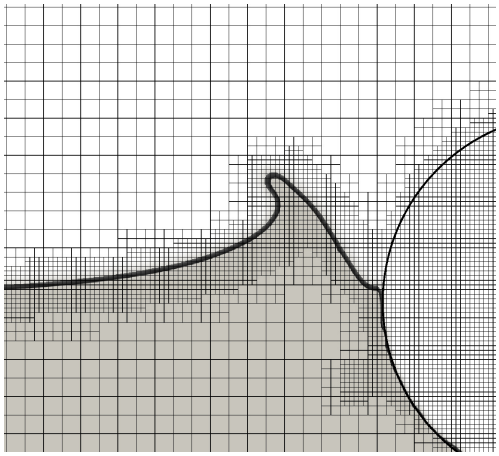

Figure 5.16: Adaptive mesh refinement (level 2) around the interface between gas and liquid and between 2-D cylinder and fluids. The screenshot is taken from the 2-D water entry validation case.

described in Chapter 3), as shown in the screenshot of Fig. 5.16. Consequently, throughout the simulation, the mesh reaches an approximate average of 1×10^5 cells which dynamically adapt to the position of the free-surface. The profiles of the free surface at different instants of dimensionless time, $t^* = tu/h$, are presented in Fig. 5.17. The results are compared with those of Calderer et al. [23], which performed the same test, showing a good agreement.

5.4.2 Subaerial landslide into a water basin

The physical case is introduced by explaining historical causes and consequences. Hence, our numerical set-up is described in detail, followed by the description of the results obtained from the numerical simulations.

Background An impulse -or tsunami wave is a large wave generated by the displacement of a big volume of water. The triggering cause can be an impulsive geophysical event as earthquakes, subaerial/submerged landslides, rock falls, and snow avalanches. On the one side, the knowledge on tsunami generation from sudden impulsive events, as underwater earthquakes, is nowadays considered satisfactory. This was possible thanks to computational advances that led to better modelling of tectonic source mechanisms and coastal inundation models, and, additionally, from large-scale laboratory experiments, analytical results, and post-tsunami field surveys [27]. In such case, because of the deformation speed of the marine bed with respect to the propagation of the wave, it is possible to directly relate the

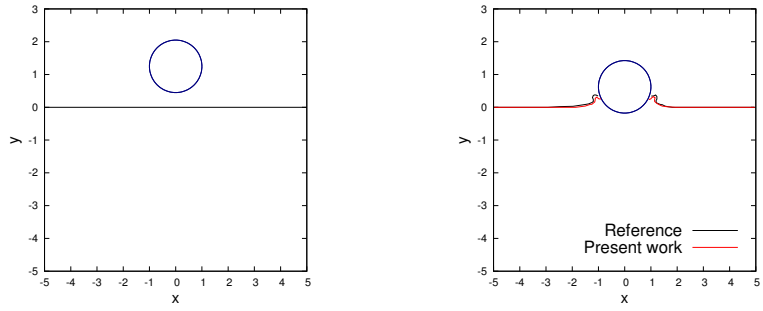

(a) $t^* = 0.0$ (b) $t^* = 0.5$

(c) $t^* = 1.0$ (d) $t^* = 2.0$

Figure 5.17: Snapshots of the 2-D cylinder entry in water. Results obtained in the present work are compared to reference by Calderer et al. [23].

deformation of the soil with the wave characteristics. On the other side, the tsunamigenesis from submarine-subaerial landslides is still considered a not fully understood phenomenon. Indeed, in this case the wave generation process can not be considered impulsive, and the addition of source terms to the equation of motion is needed for the correct modelling [20]. Moreover, the triggering causes may results highly diverse and affected by several factors, as the form and deformation of the sliding mass. Despite many advances have been done in this direction, many researchers still agree that more work is needed to determine how landslide flow processes that involve strong and gradual deformation of subaerial and submarine land are related to tsunami generation [28]. The case of an impulse wave generated by a subaerial landslide is typical of Alpine environments, favored by the presence of steep valleys and large basins at high altitude. A remarkable example is the Vajont dam disaster, occurred in October 1963 in northern Italy [29]: during initial filling, a massive landslide from the surrounding Monte Toc caused a mega-tsunami in the artificial lake. Consequently, 50 million cubic meters of water over-topped the dam and poured into the valley, leading to the complete destruction of several villages and towns, and to 1,917 deaths. On the other hand, one of the clearest and disastrous examples of tsunami generated by submarine landslide is the one occurred in Papua New Guinea in 1998 [30]. The triggering cause was an earthquake of magnitude VII (Mercalli intensity scale), which, despite not leading to significant direct damage, caused a 2 m vertical drop in the pacific plate along 25 miles of shore. This unleashed a huge tsunami, with 10 m average height and a run-up of 7-8 m, that devastated a 30 miles shoreline and led to a total of around 2200 official victims. The run-up is the height reached by the water above the normal sea level, and it is the most important factor to take into account when evaluating the consequences led by tsunamis. Indeed, except for the largest ones, tsunami waves does not break but they come onshore as a rapid rising turbulent surge of water. Consequently, they appear like an endless tide with a maximum run-up that, historically, has reached up to 30 m a.s.l. [31]. The Papua New Guinea event brought to light for the first time the dangerousness of this type of phenomenon, demonstrating how minor earthquakes can lead to disastrous consequences if they produce submarines slips . The prevention of damages caused by impulse waves and the design of countermeasures requires a detailed knowledge of the characteristics of the waves that can be generated in a particular basin. On the one hand, the experimental study by means of small-scale prototypes allows a good understanding of the phenomenon. However, the detailed simulation of large-scale events and the variability of key parameters, is more easily taken into account through the numerical simulation. Relevant parameters that may affect the outcomes are the shore slope, landslide mass and shape, basin depth and configuration.

Description of the case The main objective of this work consists in the validation of our model for the case of a landslide sliding within a water basin. The benchmark for this experiment was developed by Liu et el. [20], while additional details about set-up and results are presented in [32]. In an attempt to evaluate accurately the run-up and run-down generated

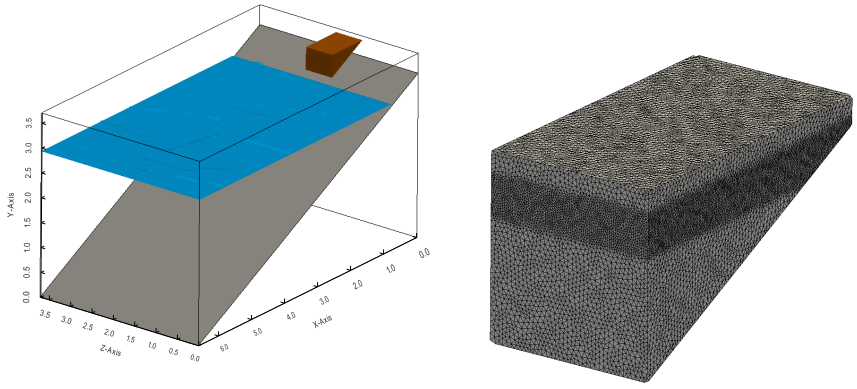

(a) (b)

Figure 5.18: Subaerial landslide simulation: (a) numerical set-up of the sliding mass simulation; (b) tetrahedral mesh used for the simulation performed in this work.

by three dimensional sliding masses, they performed several experiments, both in laboratory and by means of numerical simulations. In particular, we will consider the case of the subaerial wedge-shaped landslide. Experimental data for free-surface fluctuations and run-up/run-down at various locations are taken as reference to validate our numerical model. As shown in Fig. 5.18(a), the domain consists of a rectangular box of sides $6.6 \times 3.7 \times 3.7$ m, cut by a 1:2 slope. The mass is represented by a wedge of sides $0.91 \times 0.455 \times 0.61$ m, which follows the same slope. The object is initially raised by $D = 0.45$ m above the water level, $h_w = 3$ m . In a general case, the equation that describes the movement of a solid body that slips inside a water basin has been proposed by Pelinovsky [33]. For simplicity, in this work we use a simplified version of the profile reported by Wu [32] to prescribe the motion of the body (subaerial case), that was obtained directly from experimental measurements. The complete time history profile is reported in Fig. 5.19, showing both experimental and simplified curves. Fig. 5.20 depicts the position of the sensors (S4 to S13) used to monitor the oscillations of the free surface, while run-up gauges 2 and 3 are used to measure the run-up and run-down in two different points of the coast. Fig. 5.18(b) shows the computational mesh used for the simulation. It consists of an unstructured tetrahedral mesh, with increased cell density in proximity of the free-surface, in order to achieve a better precision in the measurements of surface fluctuations. It accounts for nearly 1.8×10^6 cells.

Numerical results Fig. 5.21 shows the results obtained in the measurement of run-up against simulation time. Run-up 2 demonstrates a good agreement with experimental data

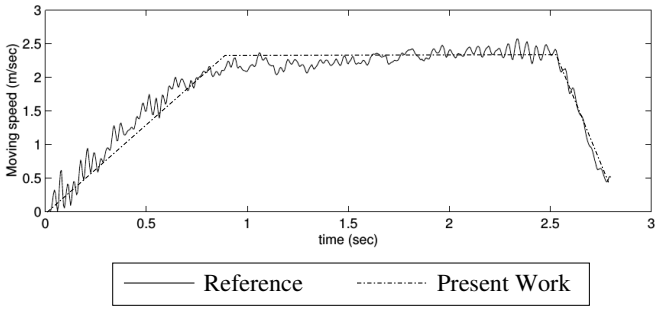

Figure 5.19: Time history of the wedge absolute velocity in the subaerial landslide simulation: reference profile versus approximated profile adopted in this work.

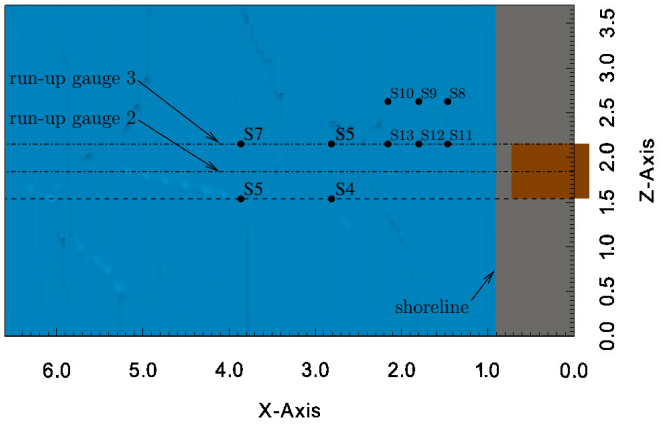

Figure 5.20: Position of Sensors and Run-up gauges on the free surface used in the subaerial landslide simulation.

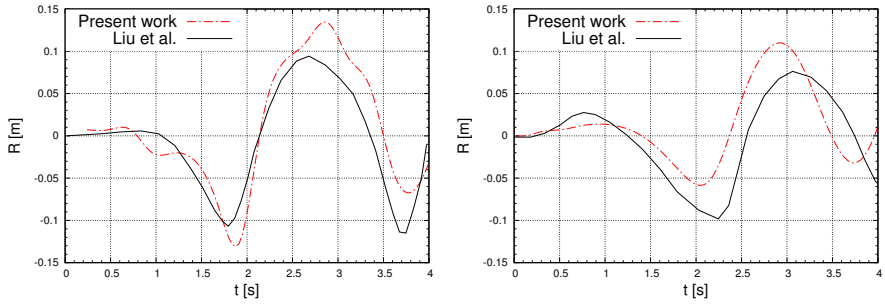

(a) Run-up 2 (b) Run-up 3

Figure 5.21: Run-up and run-down measured at position run-up 2 and 3 for the sliding mass test, Comparison between present work and experimental data [20].

[20], with a maximum run-up slightly over-predicted at $t = 2.7$ s ($R_{num} = 0.13$ m versus $R_{exp} = 0.13$ m). The same trend is reflected in the Run-up 3 plot. However, in this case a short delay can of the numerical solution can be noticed after a few seconds of simulation. The time measurement of relative free-surface fluctuations, h, are shown in Fig. 5.22. For simplicity only S4 to 8 and S10 probes are reported. In this case, in addition to present work and experimental data, we add to the comparison the numerical results by Yang and Stern [21] which performed the same simulation to validate their two-phase numerical model. Also in this case, the measurements satisfactorily follow those of reference. It is possible to notice that present work particularly fits to [21] in some time frames in which they both deviate from the experimental solution. This is clear, for example, in free-surface peaks of S5 and S7. This can lead to the conclusion that part of the mechanical behaviour of the apparatus used in the laboratory experiment lead to spurious effects on the liquid unpredictable by numerical simulations. Finally, in Figure 5.23 the comparison between pictures taken from the flow simulated numerically by [20] and present work are reported for different time instants. Despite the approximated form of the sliding wedge velocity profile adopted in this work, a good overall agreement is found. The model correctly represents the flow from the initial immersion of the object until its stop ($t = 2.7$s) and the subsequent propagation of waves on the free surface and the coast.

5.5 Conclusions

The potential of a new single-phase scheme to accurately reproduce the physics of free-surface flows based on the conservative level-set method has been assessed. The utilization of the level-set function for the identification of the interface allows a straightforward deac-

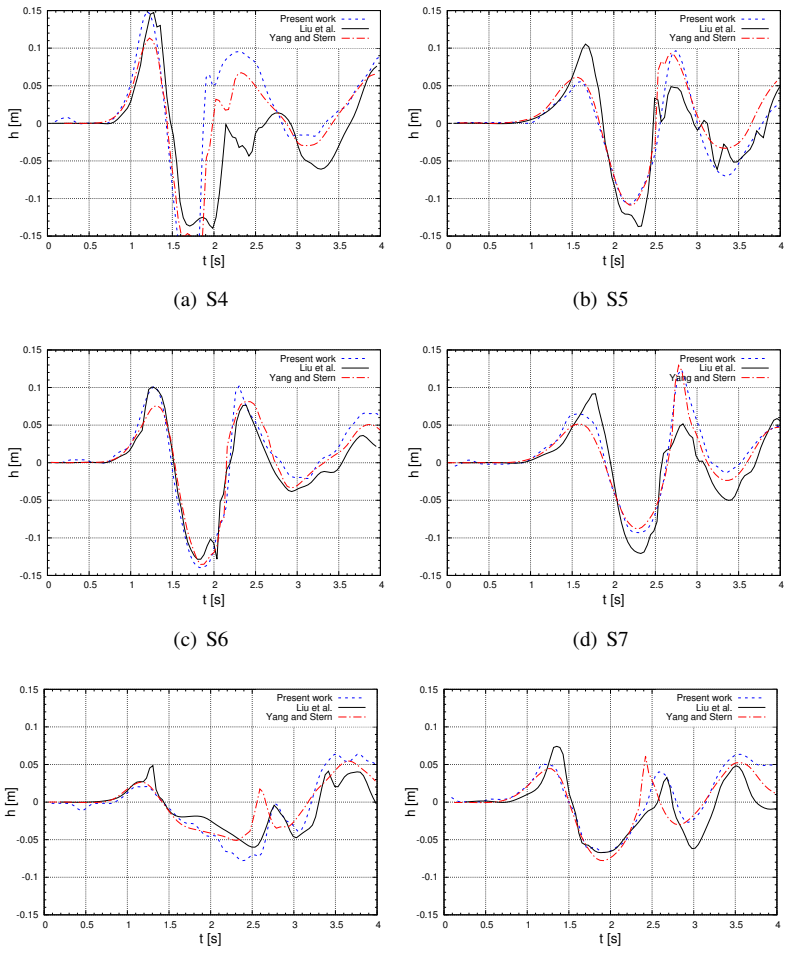

(a) S4 (b) S5

(c) S6 (d) S7

(e) S8 (f) S10

Figure 5.22: Relative free surface elevation, h, measured at different probe location in the sliding mass test. Comparison between present work, experimental data [20] and numerical reference by [21].

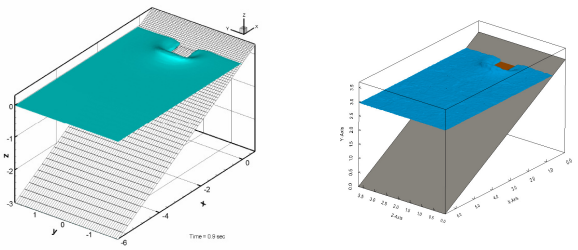

(a) t=0.9s

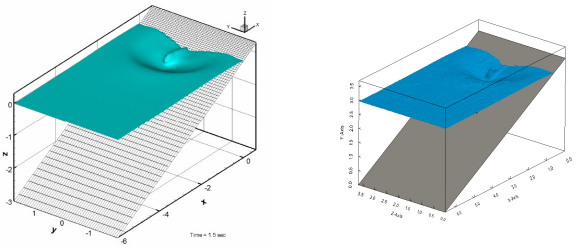

(b) t=1.5s

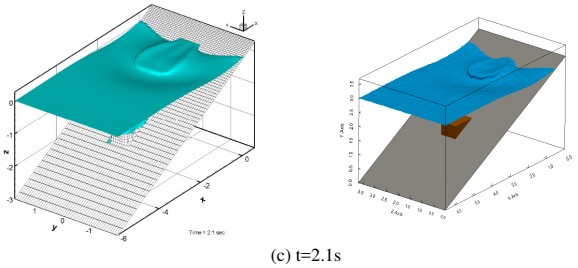

(c) t=2.1s

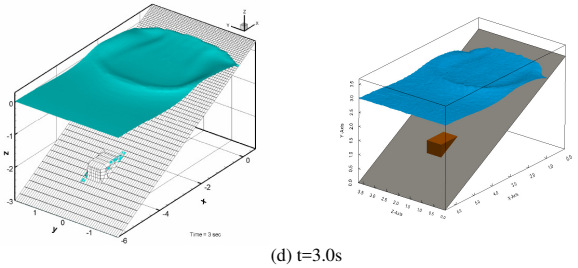

(d) t=3.0s

Figure 5.23: Comparison of the landslide test flow evolution between numerical results computed by Liu et al. [20] (left side) and present work (right side).

tivation of the light phase, and leads to the unnecessity to extend the velocity field for its correct advection.

The method has been demonstrated to work properly on both hexahedral and tetrahedral meshes, since different validation tests are correctly reproduced for both grid types. The hexahedral grid —usually distributed according to a hyperbolic law in the free-surface proximity—, is particularly suitable for the simulation of wave motion. On the other hand, the possibility of using unstructured meshes extends the applicability of the method to very diverse 3-D geometrical configurations. In addition, it allows independent grid densification in particular regions of the domain, for instance, where the passage of the interface or the appearance of turbulence structures is expected.

The adoption of the single-phase solver, instead of a two-phase one, simplifies the resolution of the problem, leading to important advantages in terms of computational time savings. This is due mainly to an increase in time step, as well as a reduction in the number of iterations required to iteratively solve the Poisson's pressure linear system. Moreover, the numerical stability of the simulations is increased due to an overall reduction of the density difference at interfaces.

The scheme has proven to satisfactorily work for the simulation of marine applications. In particular, its capability to reproduce the behavior of solitary and progressive waves, makes it suitable for the numerical simulation of ocean waves interacting with fixed or anchored structures. Possible applications are the analysis of water impact loadings on marine structures, or performance evaluation of offshore devices for energy extraction. Finally, we demonstrate the capability to integrate the level-set aided free surface model with the Immersed Boundary scheme to simulate the interaction of a body with prescribed motion and the surrounding fluids. The platform is altogether suited to the simulation of land sliding into water pools. In fact, the waves induced on the free surface faithfully reproduce those measured through laboratory experiments, allowing the evaluation of the dangerous run-up effect of tsunami waves. Consequently, the tool allows a comprehensive study of this important phenomenon or similar ones, by taking into account several of the many variables that may influence them.

Bibliography

[1] R. Löhner, C. Yang, E. Onate, Simulation of flows with violent free surface motion and moving objects using unstructured grids, International Journal for Numerical Methods in Fluids 53 (2007) 1315–1338.

[2] X. Lv, Q. Zou, Y. Zhao, D. Reeve, A novel coupled level set and volume of fluid method for sharp interface capturing on 3d tetrahedral grids, Journal of Computational Physics 229 (2010) 2573–2604.

[3] K. Kleefsman, G. Fekken, A. Veldman, B. Iwanowski, B. Buchner, A volume-of-fluid based simulation method for wave impact problems, Journal of computational physics 206 (2005) 363–393.

[4] P. Carrica, R. Wilson, F. Stern, An unsteady single-phase level set method for viscous free surface flows, International Journal for Numerical Methods in Fluids 53 (2007) 229–256.

[5] A. Di Mascio, R. Broglia, R. Muscari, On the application of the single-phase level set method to naval hydrodynamic flows, Computers & fluids 36 (2007) 868–886.

[6] D. Enright, D. Nguyen, F. Gibou, R. Fedkiw, Using the particle level set method and a second order accurate pressure boundary condition for free surface flows, in: Proceedings of FEDSM, volume 3, p. 4th.

[7] E. Schillaci, L. Jofre, N. Balcázar, O. Lehmkuhl, A. Oliva, A level-set aided single-phase model for the numerical simulation of free-surface flows on unstructured meshes, Computers & Fluids 140 (2016) 97–110.

[8] N. Balcázar, L. Jofre, O. Lehmkuhl, J. Castro, J. Rigola, A finite-volume/level-set method for simulating two-phase flows on unstructured grids, International Journal of Multiphase Flow 64 (2014) 55–72.

[9] N. V. Balcázar Arciniega, Numerical simulation of multiphase flows: level-set techniques, Ph.D. thesis, Universitat Politècnica de Catalunya, 2014.

[10] E. Schillaci, N. Balcázar Arciniega, L. Jofre Cruanyes, O. Lehmkuhl Barba, J. Castro González, A free surface model for the numerical simulation of oscillating water column systems, in: 11th World Congress on Computational Mechanics (WCCM XI); 5th European Conference on Computational Mechanics (ECCM V); 6th European Conference on Computational Fluid Dynamics (ECFD VI): all sessions and papers, International Association for Computational Mechanics (IACM), pp. 5286–5297.

[11] E. Schillaci, F. Favre, O. Antepara, N. Balcázar, A. Oliva, Numerical study of an impulse wave generated by a sliding mass., International Journal of Computational Methods and Experimental Measurements 6 (2018) 98–109.

[12] M. Kang, R. P. Fedkiw, X.-D. Liu, A boundary condition capturing method for multiphase incompressible flow, Journal of Scientific Computing 15 (2000) 323–360.

[13] G. Wu, R. E. Taylor, D. Greaves, The effect of viscosity on the transient free-surface waves in a two-dimensional tank, Journal of Engineering Mathematics 40 (2001) 77–90.

[14] C. C. Mei, M. Stiassnie, D. K.-P. Yue, Theory and applications of ocean surface waves: nonlinear aspects, volume 23, World scientific, 2005.

[15] J. Martin, W. Moyce, Part iv. an experimental study of the collapse of liquid columns on a rigid horizontal plane, Philosophical Transactions of the Royal Society of London A: Mathematical, Physical and Engineering Sciences 244 (1952) 312–324.

[16] T. W. Sheu, C. Yu, P.-H. Chiu, Development of a dispersively accurate conservative level set scheme for capturing interface in two-phase flows, Journal of computational physics 228 (2009) 661–686.

[17] Webpage: www.cttc.upc.edu.

[18] Maritime research institute netherlands (marin), webpage: www.marin.nl/web/show.

[19] H. Gu, D. Causon, C. Mingham, L. Qian, Development of a free surface flow solver for the simulation of wave/body interactions, European Journal of Mechanics-B/Fluids 38 (2013) 1–17.

[20] P.-F. Liu, T.-R. Wu, F. Raichlen, C. Synolakis, J. Borrero, Runup and rundown generated by three-dimensional sliding masses, Journal of fluid Mechanics 536 (2005) 107–144.

[21] J. Yang, F. Stern, Sharp interface immersed-boundary/level-set method for wave–body interactions, Journal of Computational Physics 228 (2009) 6590–6616.

[22] J. Sanders, J. E. Dolbow, P. J. Mucha, T. A. Laursen, A new method for simulating rigid body motion in incompressible two-phase flow, International Journal for Numerical Methods in Fluids 67 (2011) 713–732.

[23] A. Calderer, S. Kang, F. Sotiropoulos, Level set immersed boundary method for coupled simulation of air/water interaction with complex floating structures, Journal of Computational Physics 277 (2014) 201–227.

[24] E. Fadlun, R. Verzicco, P. Orlandi, J. Mohd-Yusof, Combined immersed-boundary finite-difference methods for three-dimensional complex flow simulations, Journal of computational physics 161 (2000) 35–60.

[25] F. Favre, O. Antepara, O. Lehmkuhl, R. Borrell, On the fast transient spoiler deployment in a naca0012 profile using les techniques combined with amr and imb methods, in: 11th World Congress on Computational Mechanics (WCCM XI); 5th European Conference on Computational Mechanics (ECCM V); 6th European Conference on Computational Fluid Dynamics (ECFD VI), International Association for Computational Mechanics (IACM).

[26] O. Antepara, O. Lehmkuhl, R. Borrell, J. Chiva, A. Oliva, Parallel adaptive mesh refinement for large-eddy simulations of turbulent flows, Computers & Fluids 110 (2014) 48–61.

[27] J.-P. Bardet, C. E. Synolakis, H. L. Davies, F. Imamura, E. A. Okal, Landslide tsunamis: recent findings and research directions, in: Landslide Tsunamis: Recent Findings and Research Directions, Springer, 2003, pp. 1793–1809.

[28] F. Løvholt, G. Pedersen, C. B. Harbitz, S. Glimsdal, J. Kim, On the characteristics of landslide tsunamis, Phil. Trans. R. Soc. A 373 (2015) 20140376.

[29] Webpage: https://en.wikipedia.org/wiki/vajont_dam.

[30] Webpage: https://en.wikipedia.org/wiki/1998_papua_new_guinea_earthquake.

[31] Webpage: http://www.sms-tsunami-warning.com.

[32] T. Wu, A numerical study of three-dimensional breaking waves and turbulence effects, Ph.D. thesis, Cornell University, 2004.

[33] E. Pelinovsky, A. Poplavsky, Simplified model of tsunami generation by submarine landslides, Physics and Chemistry of the Earth 21 (1996) 13–17.

6

Conclusions and future work

This work arises from the desire to pursue the efforts made by previous researchers of the *Heat and Mass Transfer Technological Center* (CTTC) in the field of development regarding the numerical study of multiphase phenomena. The original numerical techniques developed in this thesis, and the physical cases analyzed, were constructed on the robust bases described in Chapter 1, where the general algorithms for the resolution of momentum conservation equations and for interface-tracking implemented by Balcázar et al. [1, 2] are reported. In this section, we summarize the results of my research work, exposed in Chapters 2 to 5. Finally, I will express my opinion above the further arrangements that need to be added to the numerical framework presented in this work, in order to improve its range of applicability.

6.1 Conclusions

In Chapter 2, a low-dissipation and low-dispersion discretization for the numerical simulation of turbulent interfacial flow is analyzed. This section reflects the original work published in Schillaci et al. [3]. In the tests, the scheme is coupled to both Level-Set (LS) and Volume-of-Fluid (VOF) methods for the representation of the interface, demonstrating its versatility. The scheme is designed to minimize the amount of artificial dissipation introduced into the discrete system, while manages to limit the growth of spurious currents. The theoretical analysis presented in Secs. 2.2 and 2.3 confirms that the scheme is conservative except for the subgroup of cells found in the vicinity of the interface, where a controlled amount of dissipation is introduced to diminish spurious flows. This feature is confirmed by the numerical results of a 3-D vortex presented in Sec. 2.4.1. The same test shows that the overall kinetic-energy dissipation is kept to a level well lower than classic dissipative schemes. As demonstrated in the spherical drop test in Sec. 2.4.3, the localized injection of dissipation allows an effective control of the spurious currents, which remain contained to small values in the case of

utilizing the hybrid convection scheme. This behavior is further corroborated by obtaining a proper interface advection when the sphere is placed in a swirling velocity field. The same test shows how spurious flows grow unbounded when using purely conservative discretizations, both in static and swirling set-up, leading to unphysical results. The performance of the numerical framework in a complete multiphase turbulent scenario has been tested by solving a liquid-gas atomizing jet. The case is firstly validated by comparison to the results presented by Fuster et al. [4]. The test demonstrates that the controlled dissipation added to the interfacial region is sufficient to stabilize the numerical simulation, otherwise unfeasible when adopting pure conservative operators. On the other hand, unlike pure dissipative schemes, the hybrid convection approach properly represents the physics of turbulent flow. Indeed, as shown in the analysis of the energy spectra (Sec. 2.4.4) the method is able to resolve correctly the energy cascade and to reproduce the vortex shedding effect.

In Chapter 3, we present a model to improve the efficiency of multiphase flow simulations by integrating the CLS solver introduced by Balcázar et al. [1] with the Adaptive Mesh Refinement (AMR) strategy proposed by Antepara et al. [5]. As demonstrated in the various numerical tests, the method is able to dramatically reduce the computational resources employed compared to static mesh methods, without at the same time losing accuracy in the solution. The method is mainly intended for the simulation of break-up and atomization phenomena, where particularly small characteristics length need to be reached. The refinement criteria designed to follow the interface and to represent the small convective scales in the considered flow are explained in Sec. 3.2. The model accounts for a divergence-free treatment of the refined and coarsened cells, which is analytically demonstrated to ensure the correct transport of mass, momentum and kinetic energy. In a first series of tests, proposed in Sec. 3.3, and accounting for a vortex flow and different rising bubble cases, the convergence of the results obtained in two-phase flows is demonstrated. The sharp decline in computational resources required in comparison to static mesh cases is also highlighted. In the instability phenomena section, Sec. 3.4, we have presented some basic tests aimed at demonstrating the correct capture of instability and break-up phenomena at small scales. First, the Plateau-Rayleigh instability growth ratio was correctly measured on unstable liquid columns. Hence, in the 2-D coaxial jet case, the capability of the CLS-AMR method to yield a convergent solution when increasing the refinement level in two-phase phenomena with interface break-up and turbulent fluctuations is demonstrated.

In Chapter 4, we employ the CLS-AMR solver described in Chapter 3 to carry out the complete DNS of 3D break-up phenomena. In Sec. 4.2, we describe the results obtained when performing the complete simulation of 3-D coaxial jets at Re_l=600 and $Re_l \simeq 1 \times 10^4$, respectively. The simulations are validated by observing the physical features of the flow, and comparing them with experimental sources. In particular, in the near-field test, where the primary instabilities lead to the core break-up, we have measured the wavelengths connected to both Kelvin-Helmholtz and Rayleigh-Taylor instabilities, finding good agreement with the semi-empirical relations proposed by Marmottant and Villermaux [6]. Hence, in a second

test, we focused on the study of the far-field region, where the secondary structures have mostly degraded into droplets. Here we have evaluated the statistical distribution of droplets, obtaining a Sauter Mean Diameter close to that indicated by [6]. In Sec. 4.3, after introducing some theoretical and experimental studies concerning the physics of liquid sprays, we conducted a series of simulations to analyze their physical behavior as function of different input parameters. In a first study we analyzed the variation of the break-up regime according to the input speed, and therefore the Reynolds number ($\mathrm{Re}_l = 227 : 5400$). The characteristics of the various regimes encountered when increasing Re_l are consistent with the literature of the field [7], allowing to qualitatively recognize the four stages of instability of a jet: Rayleigh, 1°an 2°Wind-Induced and Atomization. Further simulations were performed by varying the magnitude of other parameters such as gas density (Tests 3–b, 4–b and 6–b) and surface tension (Tests 2–c, 3–c, 4–c), allowing additional observations. The various simulations have been placed inside the regime maps, such as Re_l vs. Oh, and We_g vs. Oh. We noted that, despite good agreement for most of the analyzed cases, the transition zones observed in the simulations are slightly shifted to the right compared to those found in the literature. The interpretation that we gave to this effect is the absence of an initial jet turbulence in the numerical set-up.

In Chapter 5, reflecting the original research paper by Schillaci et al. [8], the potentiality of a new single-phase scheme to accurately reproduce the physics of free-surface flows based on the conservative level-set method —introduced and implemented by Balcázar et al. [1, 2]— are assessed. The utilization of the level-set function for the identification of the interface allows a straightforward deactivation of the light phase, and leads to the unnecessity to extend the velocity field for its correct advection, as it happens in similar works found in literature. Thanks to the several numerical tests proposed, the method has been demonstrated to work properly on both hexahedral and tetrahedral meshes. In case of Cartesian meshes, the possibility of using a dynamic mesh refinement is also contemplated. The adoption of the single-phase solver, instead of a two-phase one, simplifies the resolution of the problem, leading to important advantages in terms of computational time savings. This is due mainly to an increase in time step, as well as a reduction in the number of iterations required to iteratively solve the Poisson's pressure linear system. Moreover, the numerical stability of the simulations is increased due to an overall reduction of the density difference at interfaces. The scheme has proven to satisfactorily work for the simulation of marine applications. In particular, its capability to reproduce the behavior of solitary and progressive waves —described in Sec. 5.3.3—, makes it suitable for the numerical simulation of ocean waves interacting with fixed or anchored structures. The process of generation and damping of waves inside the numerical domain is further described in Appendix B. Possible applications are the analysis of water impact loadings on marine structures, as demonstrated in the 3-D dam break case, proposed in Sec. 5.3.5. In Appendix A the model is used for the evaluation of the performance of an offshore device for energy extraction, the Oscillating Water Column (OWC) system. In Sec. 5.4, we demonstrate the capability to integrate the level-set aided free surface model

with the Immersed Boundary scheme to simulate the interaction of a body with prescribed motion and the surrounding fluids. The platform is altogether suited to the simulation of land sliding into water pools. In fact, the waves induced on the free-surface faithfully reproduce those measured through laboratory experiments, allowing the evaluation of the dangerous run-up effect of tsunami waves. Consequently, the tool allows a comprehensive study of this phenomenon or similar ones, by taking into account several of the many variables that may influence them.

6.2 Future Work

The numerical techniques developed by CTTC researchers, together with the tools implemented in the context of this thesis, have allowed the study of relatively complex two-phase phenomena through direct numerical simulations. Some examples are the statistical analysis of a 2-D turbulent coaxial jet at $\mathrm{Re}_l \simeq 1.6 \times 10^4$, different cases of 3-D liquid jet injection (Re_l up to $\sim 1 \times 10^4$), and the study of the interaction between a solid object and a free surface flow. Despite the efficacy provided by the proposed solver and numerical techniques, most of these studies were only possible with the use of heavy computational resources, such as the JFF cluster and the RES structures —as explained in Sec 1.1.1. For example, the simulation of the liquid injection at Re= 5100 (Test 7 in Sec. 4.3.2), requires the use of 288 CPUs during 8–10 days only to reach a steady-state condition, having to bear the load of a dynamic mesh of $\sim 1.5 \times 10^7$ elements. The complete turbulent analysis of these kind of flows, requiring the simulation of several shedding cycles, seems to be still out of reach for the computational resources currently available. In their present state, numerical simulations does not seem a reasonable alternative to the experimental analysis of atomizing phenomena.

One of the possible proposals for improving efficiency in multiphase flow simulations is the development and implementation of LEIS (Large Eddy and Interface Simulations) methods, which combine the resolution of filtered Navier-Stokes equations (LES Models) with the tracking of the interface by means of the typical one-fluid formulations, as Level-Set or Volume-of-Fluid. For instance, as in single-phase flows, Sagaut et al. [9] applied a dynamic Smagorinsky model in under-resolved regions of the domain. Therefore, the flow variables in governing equations are considered to be the filtered variables by adding a sub-grid scale (SGS) stress term to the RHS of momentum equations. The main drawback of this method has been the difficulty of combining filtered equations with the representation of source terms, such as surface tension. However, there are recent developments related to the combination of LES with VoF for turbulent free-surface, bubbly flows and break-up phenomena, as discussed by Liovic and Lakehal [10]. The idea consists of grid-filtering each phase separately, and modeling the resulting SGS stresses as if they were isolated. Special treatment may be necessary at the interface though, taking advantage of the fact that the lighter phase perceives the interfaces like deformable walls. Here, Liovic and Lakehal showed that the effect of unresolved surface tension source terms is small compared to classic SGS stress term. Recently,

the advancement in this field have been demonstrated by Behzad et al. [11], which demonstrated the reliability of LEIS models by simulating the physical mechanism underlying the surface break-up of a liquid jet injected transversely on a crossflow at Re= 1200.
Switching now to the topics discussed in Chapter 5, another interesting field of expansion in the CFD of multiphase flow, is the in-depth study of the mutual interaction between fluids and solid. In the cases presented in Sec. 5.4, the interaction is only unilateral, as the movement of the solid is prescribed and results in a forcing term in the RHS of Navier-Stokes equations. Our intention is now to extend this model, considering the mutual interaction between solid and fluid, namely, Fluid-Structure Interaction (FSI). This method requires the resolution of the motion equations of a rigid body, which passes from the integration of fluid pressure forces on the body surface. Therefore, an iterative solver has the function of balancing the movement of the body with the stresses exerted by –or on the fluid. Such a method would allow the study of the hydrodynamics behavior of floating bodies, such as buoys (including floating power generation devices) or boats. As verified in literature, e.g. Calderer et al. [12] and Pathak et al. [13], the most common way to represent the solid object within the flow consists in a Lagrangian description of its motion, and in the tracking of its movement within a fixed mesh through the Immersed Boundary Method (already used in Sec. 5.4). This method allows a good versatility and mobility of the object within the domain, without compromising the stability of the flow-solver. We are currently working on this issue by developing a multiphase FSI model that is capable of granting all the possible degrees of freedom (6 DOF) to an arbitrary object moving inside the fixed mesh, and ensuring the mass conservation of all the phases involved.

Bibliography

[1] N. Balcázar, L. Jofre, O. Lehmkuhl, J. Castro, J. Rigola, A finite-volume/level-set method for simulating two-phase flows on unstructured grids, International Journal of Multiphase Flow 64 (2014) 55–72.

[2] N. V. Balcázar Arciniega, Numerical simulation of multiphase flows: level-set techniques, Ph.D. thesis, Universitat Politècnica de Catalunya, 2014.

[3] E. Schillaci, L. Jofre, N. Balcázar, O. Antepara, A. Oliva, A low-dissipation convection scheme for the stable discretization of turbulent interfacial flow, Computers & Fluids 153 (2017) 102–117.

[4] D. Fuster, A. Bagué, T. Boeck, L. Le Moyne, A. Leboissetier, S. Popinet, P. Ray, R. Scardovelli, S. Zaleski, Simulation of primary atomization with an octree adaptive mesh refinement and vof method, International Journal of Multiphase Flow 35 (2009) 550–565.

[5] O. Antepara, O. Lehmkuhl, R. Borrell, J. Chiva, A. Oliva, Parallel adaptive mesh refinement for large-eddy simulations of turbulent flows, Computers & Fluids 110 (2014) 48–61.

[6] P. Marmottant, E. Villermaux, On spray formation, Journal of Fluid Mechanics 498 (2004) 73–111.

[7] C. Dumouchel, On the experimental investigation on primary atomization of liquid streams, Experiments in fluids 45 (2008) 371–422.

[8] E. Schillaci, L. Jofre, N. Balcázar, O. Lehmkuhl, A. Oliva, A level-set aided single-phase model for the numerical simulation of free-surface flows on unstructured meshes, Computers & Fluids 140 (2016) 97–110.

[9] P. Sagaut, Large eddy simulation for incompressible flows: an introduction, Springer Science & Business Media, 2006.

[10] P. Liovic, D. Lakehal, Multi-physics treatment in the vicinity of arbitrarily deformable gas–liquid interfaces, Journal of Computational Physics 222 (2007) 504–535.

[11] M. Behzad, N. Ashgriz, B. Karney, Surface breakup of a non-turbulent liquid jet injected into a high pressure gaseous crossflow, International Journal of Multiphase Flow 80 (2016) 100–117.

[12] A. Calderer, S. Kang, F. Sotiropoulos, Level set immersed boundary method for coupled simulation of air/water interaction with complex floating structures, Journal of Computational Physics 277 (2014) 201–227.

[13] A. Pathak, M. Raessi, A 3d, fully eulerian, vof-based solver to study the interaction between two fluids and moving rigid bodies using the fictitious domain method, Journal of Computational Physics 311 (2016) 87–113.

Appendix A

2-D Simulation of an Oscillating Water Column device

An OWC device consists of a semi-submerged air chamber, partially filled by sea water and connected to a bidirectional Wells air turbine [1] by means of an air duct. The surface of the water that fills the stucture oscillates when solicited by ocean waves, thus, driving air in and out the duct. The turbine, supplied by the air driven through the duct, is able to produce energy continuously, due to its property of rotating always in the same direction.
In the study proposed in the current work, the OWC device has been represented as a semi-submerged air chamber —placed in the right extreme of the domain, see Fig. A.1—, opened to the environment by means of a small orifice that expulses or sucks air when the water surface is moving. This approximation properly models the ideal behavior of the device, as demonstrated firstly by Evans and Porter [2]. Moreover, the viscous damping caused by the friction of the air through the orifice is used to reproduce numerically the pressure losses caused by the power extraction system —as shown, among others, by Zhang et al. [3]—, thus, providing a tool to determine the pressure of the air inside the chamber. An early version of the current model was presented in Schillaci et al. [4].

A.1 Device characterization

The instantaneous power extracted by the device is evaluated as

$$P_{owc}(t) = A_{ch} p_{air}(t) v_{owc}(t), \tag{A.1}$$

where A_{ch} is the surface of the water at rest inside the air chamber, p_{air} is the pressure of the air in the chamber, and v_{owc} is the mean vertical velocity of the water column inside the air

chamber. While v_{owc} can be evaluated numerically by using both 1-P and 2-P models, the simulation of the case with 1-P implies the necessity of approximating the pressure of the air analytically. Here, its value has been estimated considering the pressure drop through the orifice by means of the ideal Bernoulli theorem

$$p_{air} - p_{air,env} = \frac{1}{2}\rho_{air}(v_{air,or}^2 - v_{air,env}^2), \tag{A.2}$$

and imposing zero air velocity, $v_{air,env}$, and pressure, $p_{air,env}$, at the environment. The velocity of the air at the orifice, $v_{air,or}$, is calculated assuming that the air mass moved from the vertical motion of the wave passes immediately through the hole

$$v_{air,or} = v_{owc}\frac{A_{ch}}{A_{or}}, \tag{A.3}$$

where A_{or} is the orifice cross section. Hence, substituting Eq. A.3 into Eq. A.2, and this one into Eq. A.1, the following expression for the power is obtained

$$P_{owc}(t) = A_{ch}\frac{1}{2}\rho_{air}|v_{air,or}|^3\frac{A_{ch}^3}{A_{or}^2}. \tag{A.4}$$

The norm of the velocity indicates that the device is able to extract energy both if the water level is increasing or decreasing.

The forcing waves are generated in the left part of the domain by means of a wave maker, that —according to the principle already described in Sec. 5.3.3— imposes wave elevation and velocity. The wave elevation, $\eta(x,t)$, follows a sinusoidal function that produces progressive waves, identified by the wavelength, λ, and the amplitude, α, as

$$\eta(x,t) = \alpha sin(\kappa x - \omega t), \tag{A.5}$$

where $\kappa = \frac{2\pi}{\lambda}$ is the wave number, $\omega = \frac{2\pi}{\tau}$ is the angular frequency and τ is the wave period. The linear wave theory [5] gives a tool to relate wavelength and time period by means of the dispersion relation

$$\frac{\omega^2}{g} = \kappa \tanh \kappa h_w, \tag{A.6}$$

and provides an analytical solution for the velocity field. The linear wave theory admits the superposition principle, hence, multiple waves can be created in the wave maker to mimic the real ocean behavior. However, for the scope of this study, only single waves are simulated. In detail, the waves —generated on a free-surface of water depth $h_w \simeq 1.0$—, present $\lambda = 3.7$ m, that corresponds to the maximum power output, and $\alpha = 0.04$ m, in order to obtain a low wave height to water depth ratio —requirement for the application of linear wave theory approximations. The simulations are characterized referring to the output of v_{owc}, p_{air} and P_{owc} values.

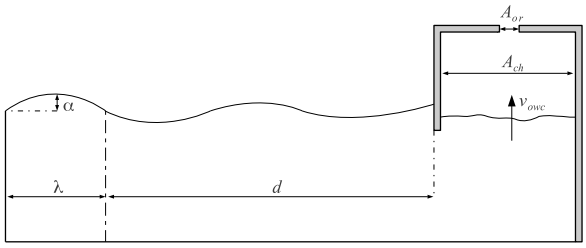

Figure A.1: Schematics of the model used for the OWC numerical simulation. The dashed line on the left bounds the wave maker zone, while the gray structure on the right represents the air chamber. d is chosen to allow the wave travel for a few wavelengths before encountering the air chamber wall.

A.2 Numerical tests

The proposed tests are carried out on a Cartesian mesh, composed of 7.3×10^5 cells, distributed more densely close to the interface. The simulations are performed by using the free-surface (1-P) model, where p_{air} and P_{owc} are evaluated by means of Eqs. A.2 and A.4, and the full-domain (2-P) scheme, where p_{air} is evaluated numerically and Eq. A.1 is used for P_{owc}. The free-surface model is described in detail in Chapter 5, where the differences with the full-domain two-phase model are also highlighted.
An upwind convection scheme is used for the discretization of ψ_f in Eq. 1.17, as the mesh is not sufficiently dense to allow the utilization of the simmetry-preserving sceme. No-slip boundary conditions are imposed at the bottom part of the domain and to the air chamber solid walls, while Neumann conditions are given to the other boundaries. As no outflow condition is provided —due to the fact that the air chamber must behave as a rigid body—, a certain amount of reflection will appear after few time periods of the progressive waves, hence, the collection of data is stopped before the effect of the reflected waves affects excessively the solution.
As shown in Fig. A.2(a), the values of v_{owc} obtained in the 1-P and 2-P simulations are in good agreement, both for transient and steady-state analysis, thus, confirming again the effectiveness of the model in simulating the free-surface movement. On the other hand, the comparison of the air pressure behavior between 1-P and 2-P data, proposed in Fig. A.2(b), shows a clear mismatch. The same tendency is also shown in the power plot, shown in Fig. A.2(c). The marked discrepancy is due to the fact that the model chosen for the pressure evaluation, Eq. A.2, is not reliable, as its simple formulation cannot take into account the contributions of the air dynamic effects inside the chamber. However, the proportionality of the results would allow the use of the model for parametric studies. As further work, the model could be improved to effectively simulate the physics of the device in different ways,

for example: (1) finding an alternative mathematical model for the calculation of pressure, or (2) evaluating numerically the air phase in a sector of the domain, at least in the part that concerns the air chamber.

In this test, the savings in computational time are even more important than those reported for the dam break case, see Sec. 5.3.4, due to the fact that it is avoided the calculation of the air that passes through the orifice after being accelerated by the water vertical movement. This leads to an increase of the time step of 139%, mainly due to the considerably lower overall velocity. Furthermore, the increase of the stability results in a reduction of 75% on the number of iterations required for the resolution of the pressure Poisson's equation. In total, the computational time is reduced by 65%.

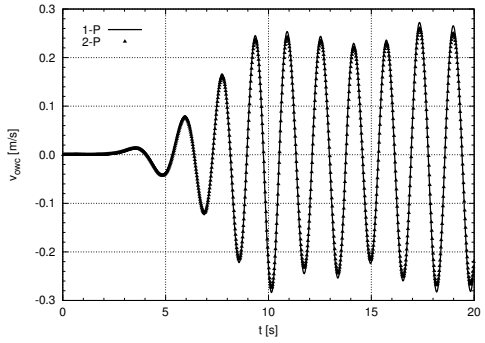

(a)

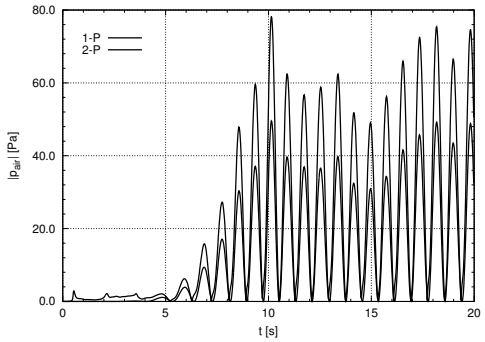

(b)

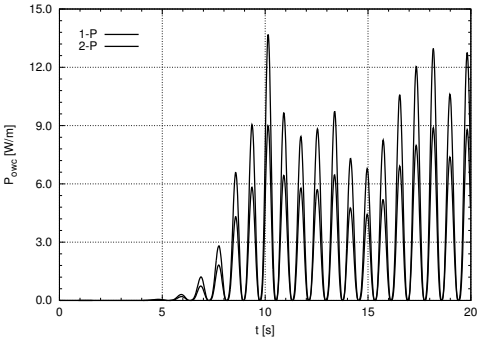

(c)

Figure A.2: Comparison of results obtained with 1-P and 2-P models for the OWC simulation: (a) mean vertical velocity of the water column inside the air chamber; (b) air pressure —1-P from Eq. A.2, 2-P evaluated numerically—; (c) OWC power —1-P from Eq. A.4, 2-P from Eq. A.1.

Bibliography

[1] S.L. Dixon and C. Hall. *Fluid mechanics and thermodynamics of turbomachinery*. Butterworth-Heinemann, 2013.

[2] D.V. Evans and R. Porter. Hydrodynamic characteristics of an oscillating water column device. *Applied Ocean Research*, 17(3):155–164, 1995.

[3] Y. Zhang, Q. Zou, and D. Greaves. Air–water two-phase flow modelling of hydrodynamic performance of an oscillating water column device. *Renewable Energy*, 41:159–170, 2012.

[4] E. Schillaci, N. Balcázar Arciniega, L. Jofre Cruanyes, O. Lehmkuhl Barba, and J. Castro González. A free surface model for the numerical simulation of oscillating water column systems. In *11th World Congress on Computational Mechanics (WCCM XI); 5th European Conference on Computational Mechanics (ECCM V); 6th European Conference on Computational Fluid Dynamics (ECFD VI): all sessions and papers*, pages 5286–5297. International Association for Computational Mechanics (IACM), 2014.

[5] L.M. Milne-Thomson. *Theoretical hydrodynamics*. Courier Corporation, 1996.

Appendix B

Generation and damping of waves generated on a free-surface

In this Appendix, I report all the information related to the numerical simulation of linear progressive waves in water that I collected during my research work.
In some of the set-up analyzed during my experience, I had the necessity to set a numerical domain in which regular or irregular waves reach a steady-state behavior. The model can be successively integrated in more complex domains to simulate, for example, the interaction with floating– or fixed solid objects. The physics of the multi-phase flow, described by means of the Navier-Stokes equations for momentum conservation, can be simulated by using a two-phase model (that considers both air and water) or a free-surface model —as the one described in Chapter 5—, that makes the simulation simpler by considering the interface between fluids as an internal moving boundary and neglecting the air-phase.
The domain used for the simulation, showed in Fig. B.1, consists in a closed tank partially filled with water (initially at rest). No-slip boundary condition are applied to bottom, left and right edges. The waves are generated by a wave maker in the left part and propagate through the whole length of the domain, until entering the damping zone on the right, where they are numerically damped.

B.1 Wave maker

The *wave maker* consists in a small sector of the domain, where a relaxed numerical solution, $\psi_{relaxed}$, is applied for water elevation and some scalar fields. In that small sector, the numerical solution, $\psi_{analytical}$, and the forcing analytical function, $\psi_{numerical}$, are mixed by means

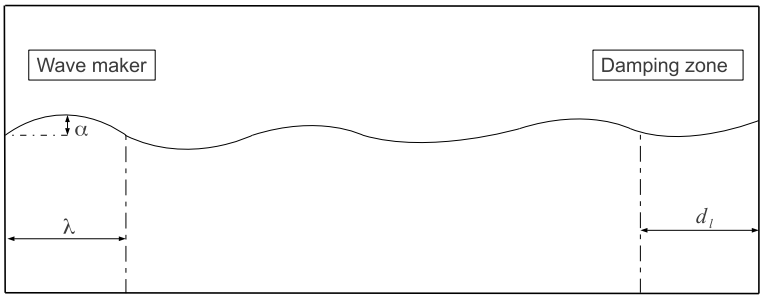

Figure B.1: Domain used for the numerical simulation of progressive linear– or composed waves. The dashed line on the left delimits the wave maker zone while the on the right marks the beginning of the damping zone (numerical beach).

of a relaxing function, $\xi(x)$, in order to assure numerical stability in the generation zone.

$$\psi_{relaxed} = \xi(x)\psi_{analytical} + (1-\xi(x))\psi_{numerical}. \tag{B.1}$$

$\xi(x)$, varies smoothly from 1 to 0 moving from the boundary to the center of the tank. The analytical forcing function that imposes the wave elevation is a sinusoidal function that produces progressive waves, identified by the wavelength and the amplitude

$$\eta(x,t) = \alpha\ sin(\kappa x - \omega t), \tag{B.2}$$

$$\kappa = \frac{2\pi}{\lambda}, \quad \omega = \frac{2\pi}{\tau},$$

where α is the wave amplitude, κ is the wave number, ω is the angular frequency, λ is the wavelength and τ is the wave period. These two quantities (κ-ω or λ-τ) are correlated, according to the dispersion relation [1]

$$\rho_w\omega^2 coth(\kappa h_w) + \rho_a(\omega - \kappa U)^2 coth(\kappa h_a) = (\rho_w - \rho_a)g\kappa, \tag{B.3}$$

where U is the wind velocity, h_w is the calm water depth and h_a is the height of the domain section including air. When the wind velocity is supposed to be zero, an explicit relation can be found between wavelength and wave period

$$\tau = \sqrt{\frac{2\pi\lambda(\rho_a \frac{1}{\tanh\left(\frac{2\pi h_a}{\lambda}\right)} + \rho_w \frac{1}{\tanh\left(\frac{2\pi h_w}{\lambda}\right)})}{(\rho_w - \rho_a)g}}. \tag{B.4}$$

When the air effect is neglected, the dispersion relation simply reduces to

$$\frac{\omega^2}{g} = \kappa \tanh \kappa h_w. \tag{B.5}$$

The velocity field is also imposed in the wave maker zone by means of the analytical solution proposed by Milne [1], that used linear wave theory to evaluate progressive wave velocities

$$u_x = U - B_w \kappa c \alpha \; sin(\kappa x - \omega t) cosh(\kappa(y + h_w)), \tag{B.6}$$

$$u_y = B_w \kappa c \alpha \; cos(\kappa x - \omega t) sinh(\kappa(y + h_w)), \tag{B.7}$$

$$u_y = 0, \tag{B.8}$$

where $c = \lambda / \tau$ is the phase velocity and $B_w = 1/sinh(\kappa h_w)$. Due to the linearity of the waves, the superposition principle can be applied, thus, allowing the generation of composed waves. In this case the forcing functions, water elevation and wave velocities, are given by the sum of all the composite wave components.

B.2 Damping zone

Once generated, the waves travel through the domain until encountering the right boundary. As no outflow condition is provided, they would rebound against the wall, thus, reflecting part of their inertia towards the center of the domain and avoiding the obtention of a steady-state condition. Moreover, the reflected energy can go back up to the generation zone, thus, affecting the wave maker and compromising the stability of the simulation. In order to avoid this drawback, a numerical beach is added in the right part of the domain. It consists of a region, with length d_l (damping length), in which an artificial dissipation of the wave energy is carried out. The dissipation can be performed by means of different strategies, some of which are listed below:

- **Viscous damping**: the viscosity of the water, μ_w, is increased artificially in the damping zone. In particular, it increases linearly from $x_{\text{buffer}} = x_{\text{end}} - d_l$ to x_{end}, proportionally to the damping coefficient c_μ

$$\mu_w = \mu_w \left(1 + c_\mu \frac{x - x_{\text{buffer}}}{x_{\text{end}} - x_{\text{buffer}}} \right) \tag{B.9}$$

- **Gravity damping**: the waves movement is damped by adding an additional body force, $\vec{F}_{\text{damp}}$, acting as an additional gravity force on the free surface. Again, this force rises progressively up to the domain extreme, proportionally to the damping coefficient c_{grav}. Its absolute value is evaluated as

$$|F_{\text{damp}}| = g \rho_c V_c \left(1 + c_{\text{grav}} \frac{x - x_{\text{buffer}}}{x_{\text{end}} - x_{\text{buffer}}} \right) \tag{B.10}$$

  where ρ_c and V_c are the cell density and volume, respectively.

B.3 Numerical tests

In order to assess the effectiveness of these dissipation methods, some tests are realized on rectangular 2-D domain of sides 16 $\times$ 2 m, while the water height is set to $h_w = 1$ m. The Cartesian mesh is composed by $\sim 6.5 \times 10^4$ elements (departed on 8 CPUs), distributed more densely in the zone of the interface. The forcing progressive waves are assigned a single wavelength (simple wave, $\lambda = 2.3$m, $a = 0.04$m), and the simulations are carried out by using a single-phase (1-P) scheme described in Chapter 5. The length of the numerical beach is $d_l = 5$m. Hence, the simulation realized without any damping strategy (UNDAMPED), is compared with the gravity damped simulation (GRAV damping, $c_{\text{grav}} = 100$) and the viscosity damped one (VISC damping, $c_\mu = 1.0 \times 10^5$). The parameters used for the comparison are the vertical velocity of the free surface close to the right boundary, V_{OUT}, showed in Fig. B.2, the vertical velocity of the free surface at the center of the domain, V_{CENTER}, showed in Fig. B.3, and the horizontal mean velocity of the water at the center of the domain, U_{CENTER}, showed in Fig. B.4.

Fig. B.2 shows how VISC damping manages to reduce the oscillations of the surface at the output, compared to the obscillations of the UNDAMPED solution, while GRAV damping produces a very constrained and almost random movement.

In Fig. B.3, it can be noticed that all the solutions reach the same behavior after a few time periods (time needed by the progressive wave to reach the center of the domain). However, after a few steady-state oscillations, the UNDAMPED solution rises its velocity peaks, probably due to the effect of the reflected energy that starts affecting its movement. On the other side, the GRAV damped solution keep on oscillating between the same values, demonstrating that the damping zone is properly performing its function. VISC damping also shows regular oscillations that reach slightly higher peaks than GRAV damping.

The same conclusions can be taken from the analysis of Fig.B.4, that shows how the mean horizontal velocity of the waves is reduced after a few time periods in the UNDAMPED solution —where the reflected waves block the horizontal movement of the forcing waves, also affecting the oscillation time period—, in contrast to the GRAV damped one, where it mantains the same sinusoidal behavior for the whole simulation. VISC damping shows a similar behavior than GRAV damping, even if with reduced values of the peaks, probably because the effect of the reflected energy is still partially present.

Finally, Tab.B.1 resumes some features regarding the computational time of the simulations. In particular, it is remarkable the reduction of the time step in the VISC damping simulation, that causes an important increase in the total computational time. This reduction is due to the fact that the methods for the time step evaluation —here, the self adaptive method proposed by Trias et al. [2] is used— directly depends, in their diffusive contribution, on the maximun value of viscosity present on the domain. Hence, the GRAV damping method results the best one in performing its function, due to its better effectiveness and the avoided weighting of the computational time.

	Iter	Δt	t_{rel} [min/s]
UNDAMPED	553	8.7×10^{-4}	~ 21
VISC damping	513	2×10^{-4}	~ 54
GRAV damping	505	8.5×10^{-4}	~ 21

Table B.1: Time step, Δt, mean number of iterations for Poisson's equation solution, *Iter*, and computation time in minutes per second of simulation, t_{rel}, measured in the proposed tests.

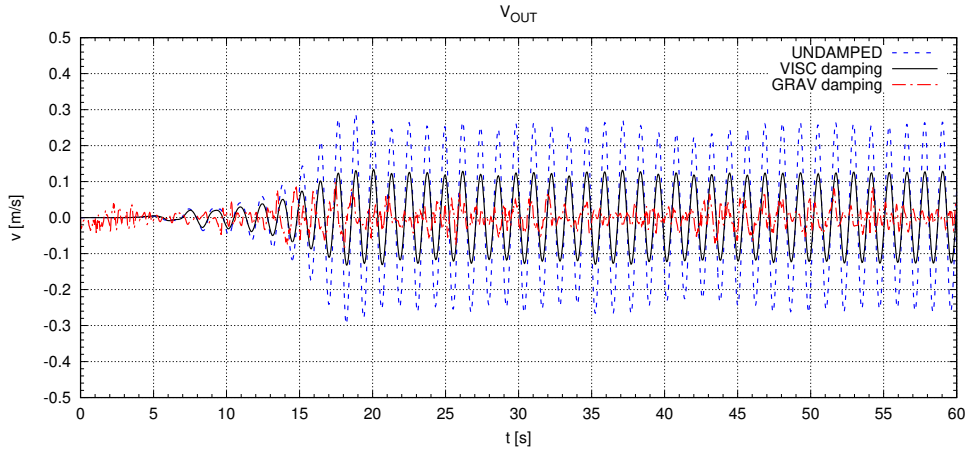

Figure B.2: Mean vertical velocity of the free surface in the wave damping zone.

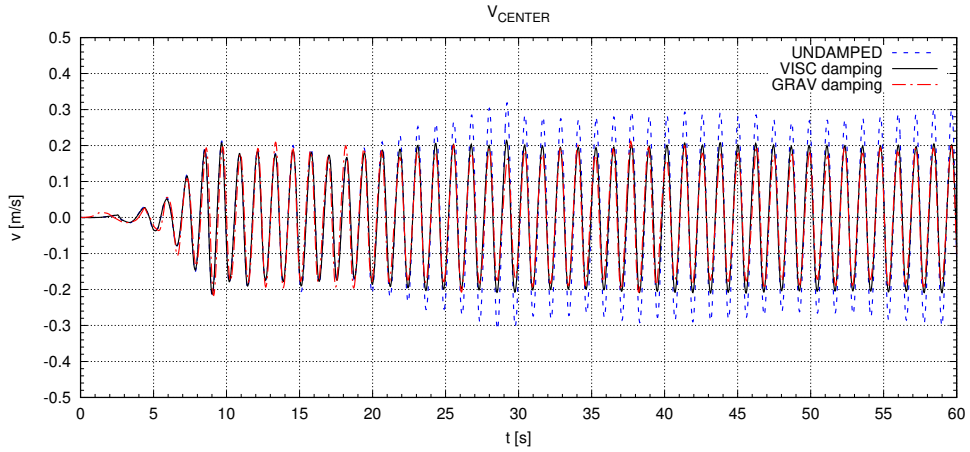

Figure B.3: Mean vertical velocity of the free surface at the center of the domain.

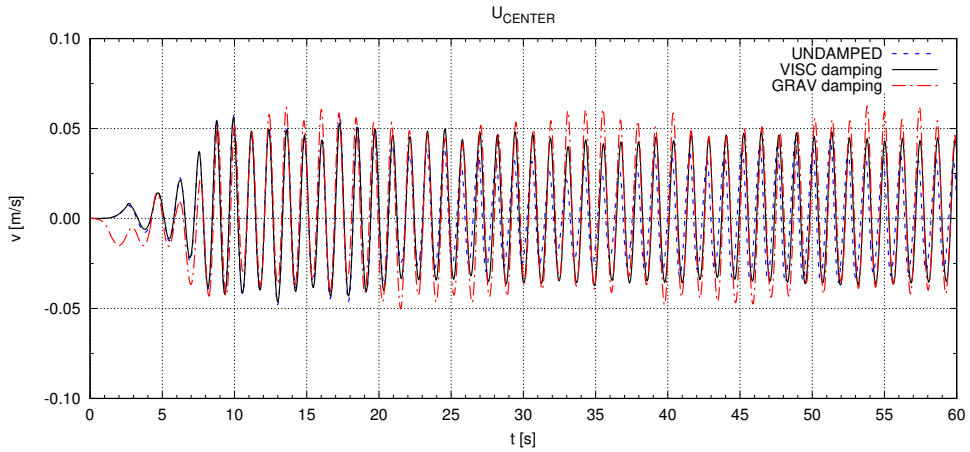

Figure B.4: Mean horizontal velocity of the water at the center of the domain.

Bibliography

[1] L.M. Milne-Thomson. *Theoretical hydrodynamics*. Courier Corporation, 1996.

[2] F.X. Trias and O. Lehmkuhl. A self-adaptive strategy for the time integration of Navier-Stokes equations. *Numerical Heat Transfer, Part B: Fundamentals*, 60(2):116–134, 2011.

Appendix C

List of pubblications and projects

In this Appendix, a comprehensive list af all the publications resulted from the current work is provided. They are divided between research paper and conference proceedings. I also report the competitive projects to which I partecipated, including the ones that gave me the possibility to access the Red Española de Supercomputaciòn (RES) resources.

C.1 Research Papers

- E.Schillaci, L.Jofre, N.Balcázar, O.Lehmkuhl and A. Oliva. A level-set aided single-phase model for the numerical simulation of free-surface flow on unstructured meshes. *Computers & Fluids*, 140:97–110, 2016.
- E.Schillaci, L.Jofre, N. Balcázar, O. Antepara, and A. Oliva. A Low-Dissipation Convection Scheme for the Stable Discretization of Turbulent Interfacial Flow. *Computers & Fluids*, 153:102–117, 2017.
- E.Schillaci, O. Antepara, N. Balcázar, and A. Oliva. A dynamic mesh refinement strategy for the simulation of break-up phenomena in two-phase jets *International Journal of Heat and Fluid Flow*, Under Review.

C.2 Conference Proceedings

- E. Schillaci, N. Balcázar, L.Jofre, O.Lehmkuhl, and J.Castro. A free surface model for the numerical simulation of oscillating water column systems. In 11th World Congress

on Computational Mechanics (WCCM XI); 5th European Conference on Computational Mechanics (ECCM V); 6th European Conference on Computational Fluid Dynamics (ECFD VI): all sessions and papers, pages 5286–5297. International Association for Computational Mechanics (IACM), 2014.

- E.Schillaci, O.Antepara, O.Lehmkuhl, N. Balcázar, and A.Oliva. Effectiveness of adaptive mesh refinement strategies in the DNS of multiphase flows. In: Proceedings of international symposium turbulent heat and mass transfer VIII; 2015 .

- E.Schillaci, O.Lehmkuhl, O.Antepara, and A.Oliva. Direct numerical simulation of multiphase flows with unstable interfaces. *Journal of Physics: Conference Series*, (Vol. 745, No. 3, p. 032114). IOP Publishing. Proceedings of Eurotherm 2016, 7th European Thermal-Sciences Conference, 19–23 June 2016, Krakow, Poland.

- E.Schillaci, F.Favre, O.Antepara, N.Balcázar and A. Oliva. Numerical study of an impulse wave generated by a sliding mass. *International Journal of Computational Methods and Experimental Measurements*, 6:98–109, 2018. Proceedings of Multiphase Flow 2017, 9th International Conference on Computational and Experimental Methods in Multiphase and Complex Flow, 20–22 June 2017, Tallinn, Estonia.

C.3 Competitive projects

- ENE2015-70672-P. Modelización multiescala y simulación numérica directa de flujos multifásicos gas líquido en burbujas, películas y esprays. Ministerio de Economía y Competitividad, Secretaría de Estado de Investigacíon, Desarrollo e Innovacíon, Spain.

- RES-FI-2016-1-0023. Direct Numerical Simulation of turbulent atomizing two-phase jets with an adaptive mesh refinement strategy, Period 1. Awarded with 550k hours of simulation at MareNostrum III —technical support provided by BSC.

- RES-FI-2016-2-0028. Direct Numerical Simulation of turbulent atomizing two-phase jets with an adaptive mesh refinement strategy, Period 2. Awarded with 400k hours of simulation at Finisterrae II—technical support provided by CESGA.

- RES-FI-2016-3-0015. DNS of 3D turbulent sprays with the aid of adaptive mesh refinement and low dissipative advective scheme, Period 1. Awarded with 750k hours of simulation at Finisterrae II—technical support provided by CESGA.

- RES-FI-2017-2-0015. DNS of 3D turbulent sprays with the aid of adaptive mesh refinement and low dissipative advective schemes, Period 2. Awarded with 800k hours of simulation at MareNostrum IV —technical support provided by BSC.